

Doctoral Dissertation

博士論文

Order and Topology in Nonequilibrium Quantum  
Dynamics

(非平衡量子ダイナミクスにおける秩序とトポ  
ロジー)

A Dissertation Submitted for  
the Degree of Doctor of Philosophy

July 2020

令和2年7月博士（理学）申請

Department of Physics, Graduate School of Science,

The University of Tokyo

東京大学大学院理学系研究科  
物理学専攻

Zongping Gong

龔 宗平

## Abstract

In this Thesis, we investigate some fundamental problems concerning dynamical phases of quantum matter out of nonequilibrium, an emergent subject at the interface of atomic, molecular and optical physics, condensed matter physics and statistical physics. It is well-known that spontaneous symmetry breaking and topology provide two universal mechanisms for phase transitions in equilibrium quantum systems. However, it remains poorly understood how we can generalize these notions to the nonequilibrium regime, where not only the quantum many-body states but also their dynamical evolutions become crucial. Here, we address this issue for three of the most common nonequilibrium situations, namely periodic driving, dissipation and quench. For periodically driven (Floquet) systems, we focus on both mechanisms of spontaneous symmetry breaking and topology. We predict that discrete time crystals which spontaneously break the discrete time-translation symmetry can exist in open quantum systems. We also perform a systematic topological classification of locality-preserving unitary operators with symmetries. For dissipative and quenched systems, we focus only on their topological aspects. We classify the dynamical phases for both scenarios and discuss observable signatures of their unique topological structures. The results of this Thesis have strong relevance to the state-of-the-art quantum-simulation experiments, and serve as some basic paradigms for further studies on nonequilibrium phases in more general settings.

# List of Publications

This Thesis is based on the following publications.

1. *Classification of Matrix-Product Unitaries with Symmetries*  
**Zongping Gong**, Christoph S underhauf, Norbert Schuch, and J. Ignacio Cirac,  
Physical Review Letters **124**, 100402 (2020).
2. *Topological Entanglement-Spectrum Crossing in Quench Dynamics*  
**Zongping Gong** and Masahito Ueda,  
Physical Review Letters **121**, 250601 (2018).
3. *Topological Phases of Non-Hermitian Systems*  
**Zongping Gong**<sup>\*</sup>, Yuto Ashida<sup>\*</sup>, Kohei Kawabata, Kazuaki Takasan, Sho Higashikawa,  
and Masahito Ueda (<sup>\*</sup>double corresponding authors),  
Physical Review X **8**, 031079 (2018) [Featured in Physics, see also Physics **11**, 96].
4. *Discrete Time-Crystalline Order in Cavity and Circuit QED Systems*  
**Zongping Gong**, Ryusuke Hamazaki, and Masahito Ueda,  
Physical Review Letters **120**, 040404 (2018).

The following publications are related but are not claimed in this Thesis.

1. *Non-Hermitian Physics*  
Yuto Ashida, **Zongping Gong**, and Masahito Ueda,  
arXiv:2006.01837 (2020) [Review article submitted to Advances in Physics].
2. *Universal Error Bound for Constrained Quantum Dynamics*  
**Zongping Gong**, Nobuyuki Yoshioka, Naoyuki Shibata, and Ryusuke Hamazaki,  
Physical Review Letters **124**, 210606 (2020).
3. *Error bounds for constrained dynamics in gapped quantum systems: Rigorous results and generalizations*  
**Zongping Gong**, Nobuyuki Yoshioka, Naoyuki Shibata, and Ryusuke Hamazaki,  
Physical Review A **101**, 052122 (2020).
4. *Thermodynamic Uncertainty Relation for Arbitrary Initial States*  
Kangqiao Liu, **Zongping Gong**, and Masahito Ueda,  
arXiv:1912.11797 (2019).
5. *Lieb-Robinson Bounds on Entanglement Gaps from Symmetry-Protected Topology*  
**Zongping Gong**, Naoto Kura, Masatoshi Sato, and Masahito Ueda,  
arXiv:1904.12464 (2019).
6. *Second-Order Topological Phases in Non-Hermitian Systems*  
Tao Liu, Yu-Ran Zhang, Qing Ai, **Zongping Gong**, Kohei Kawabata, Masahito Ueda,  
and Franco Nori,  
Physical Review Letters **122**, 076801 (2019).
7. *Topological unification of time-reversal and particle-hole symmetries in non-Hermitian physics*  
Kohei Kawabata, Sho Higashikawa, **Zongping Gong**, Yuto Ashida, and Masahito Ueda,  
Nature Communications **10**, 297 (2019) [Editors' Highlights].

8. *Verification of the quantum nonequilibrium work relation in the presence of decoherence*  
Andrew Smith, Yao Lu, Shuoming An, Xiang Zhang, Jing-Ning Zhang, **Zongping Gong**,  
H. T. Quan, Christopher Jarzynski, and Kihwan Kim,  
New Journal Physics **20**, 013008 (2018).
9. *Fluctuation theorems in feedback-controlled open quantum systems: Quantum coherence and absolute irreversibility*  
Yûto Murashita, **Zongping Gong**, Yuto Ashida, and Masahito Ueda,  
Physical Review A **96**, 043840 (2017).
10. *Zeno Hall Effect*  
**Zongping Gong**, Sho Higashikawa, and Masahito Ueda,  
Physical Review Letters **118**, 200401 (2017) [Editors' Suggestion].
11. *Stochastic Thermodynamics of a Particle in a Box*  
**Zongping Gong**, Yueheng Lan, and H. T. Quan,  
Physical Review Letters **117**, 180603 (2016).
12. *Quantum-trajectory thermodynamics with discrete feedback control*  
**Zongping Gong**, Yuto Ashida, and Masahito Ueda,  
Physical Review A **94**, 012107 (2016).
13. *Quantum-classical correspondence principle for work distributions in a chaotic system*  
Long Zhu, **Zongping Gong**, Biao Wu, and H. T. Quan,  
Physical Review E **93**, 062108 (2016).
14. *Crooks fluctuation theorem and the fluctuation theorems of heat for arbitrary initial states*  
**Zongping Gong** and H. T. Quan,  
Physical Review E **92**, 012131 (2015).
15. *Thermodynamics of information processing based on enzyme kinetics: An exactly solvable model of information pump*  
Yuansheng Cao, **Zongping Gong**, and H. T. Quan,  
Physical Review E **91**, 062117 (2015).
16. *Interference of identical particles and the quantum work distribution*  
**Zongping Gong**, Sebastian Deffner, and H. T. Quan,  
Physical Review E **90**, 062121 (2014).

# Abbreviations

AMO	atomic, molecular and optical
AZ	Altland-Zirnbauer
$dD$ ( $d = 1, 2, 3, \dots$ )	$d$ dimensions ( $d$ -dimensional)
DTC	discrete time crystal (crystalline)
ES	entanglement spectrum
GKSL	Gorini-Kossakowski-Sudarshan-Lindblad
iTEBD	infinite time-evolving block decimation
lhs (rhs)	left-hand side (right-hand side)
MBL	many-body localization (localized)
MPS	matrix-product state
MPU	matrix-product unitary
NV	nitrogen-vacancy
OBC	open boundary condition
PBC	periodic boundary condition
PDPD	probability distribution of the phase difference
PHS	particle-hole symmetry
QED	quantum electrodynamics
SPI	symmetry-protected index
SPT	symmetry-protected topology (topological)
SSB	spontaneous symmetry breaking (broken)
SSH	Su-Schrieffer-Heeger
TRS	time-reversal symmetry

# Contents

<b>1</b>	<b>Overview</b>	<b>8</b>
<b>2</b>	<b>Discrete time-crystalline order in cavity and circuit QED systems</b>	<b>12</b>
2.1	Background and motivation . . . . .	12
2.1.1	Brief review on time crystals . . . . .	12
2.1.2	Motivation and the main achievement . . . . .	13
2.2	Theoretical proposal . . . . .	14
2.3	Numerical simulations . . . . .	17
2.3.1	Mean-field dynamics in the thermodynamic limit . . . . .	18
2.3.2	Open-system dynamics in the few-atom regime . . . . .	25
2.4	General phenomenology . . . . .	29
2.4.1	Floquet-GKSL-Landau theory . . . . .	29
2.4.2	Scaling of the DTC lifetime . . . . .	32
2.5	Experimental implementations . . . . .	34
2.5.1	Cavity QED setup based on four-level atoms . . . . .	34
2.5.2	Circuit QED setup based on inductive coupling . . . . .	38
<b>3</b>	<b>Classification of matrix-product unitaries with symmetries</b>	<b>39</b>
3.1	Introduction . . . . .	39
3.1.1	Background, motivation and the main results . . . . .	39
3.1.2	Brief review on matrix-product states and unitaries . . . . .	40
3.2	Systematic classifications . . . . .	42
3.2.1	Equivalence and the complete classification . . . . .	42
3.2.2	Strong equivalence and the symmetry-protected indices . . . . .	46
3.3	Examples . . . . .	50
3.3.1	MPUs with nontrivial cohomology classes . . . . .	51
3.3.2	Nontrivial MPUs in the trivial cohomology class . . . . .	58
3.4	Experimental probing of SPIs . . . . .	61
3.5	Implications for Floquet topological phases . . . . .	66
<b>4</b>	<b>Topological phases of non-Hermitian systems</b>	<b>70</b>
4.1	Introduction . . . . .	70
4.1.1	Background, motivation and the main results . . . . .	70
4.1.2	Definition of non-Hermitian topological phases . . . . .	73
4.2	Topological non-Hermitian lattices in 1D with no symmetry . . . . .	75
4.2.1	Topological winding number . . . . .	75
4.2.2	Bulk-edge correspondence . . . . .	78
4.2.3	Determining the winding number . . . . .	81
4.2.4	Experimental implementation of asymmetric hopping amplitudes . . . . .	84

4.3	Classification of non-Hermitian topological phases in the Altland-Zirnbauer classes	86
4.3.1	Unitarization under symmetry constraints	86
4.3.2	$K$ -theory and Clifford-algebra extension	88
4.3.3	Explicit classification	89
4.3.4	Discussions	90
4.4	Topological indices for non-Hermitian systems	92
4.4.1	Zero dimension	92
4.4.2	One dimension	96
<b>5</b>	<b>Topological entanglement-spectrum crossing in quench dynamics</b>	<b>99</b>
5.1	Introduction	99
5.2	Parent Hamiltonians and their classifications	100
5.2.1	Parent Bloch Hamiltonian	101
5.2.2	Symmetry constraints and the maximal $K$ -groups	102
5.2.3	Topological numbers and the dynamical realizations	104
5.2.4	Quench dynamics in two-band systems	109
5.3	Entanglement-spectrum dynamics after quenches	113
5.3.1	Case study on the Su-Schrieffer-Heeger model	113
5.3.2	Distinguishing $\mathbb{Z}$ and $\mathbb{Z}_2$ topology	116
5.3.3	Experimental situation	120
<b>6</b>	<b>Summary and outlook</b>	<b>121</b>
<b>Appendix A Topological invariants for inhomogenous locality-preserving uni-</b>		
	<b>taries</b>	<b>123</b>
A.1	Factorization relation	123
A.2	Topological invariants	126
<b>Appendix B Localization and topology in the Hatano-Nelson model</b>		<b>130</b>
B.1	Winding number for disordered systems	130
B.2	Topological and localization transitions	132
<b>Appendix C Proof of the bulk-edge correspondence</b>		<b>138</b>
<b>Appendix D Calculating the entanglement-spectrum dynamics</b>		<b>142</b>
D.1	Numerical method for general noninteracting systems	142
D.2	Analytical results for some flat-band quenches	145

# Chapter 1

## Overview

*C'est*—— 蒼を繋いで... 流れる雲... 蝉の時雨... 夏の追想...

*C'est*—— 大地を包み... 微眠む雪... 時の木枯... 冬の追想... <sup>1</sup>

The beauty of nature is rooted in the diversity of states of matter and their dynamical changes with the flow of time. It is one of the most important tasks in physics to understand the essence underlying the diversity of states of matter, which consist of macroscopic numbers of atoms, electrons and ions that behave following quantum mechanics, the fundamental law in the microscopic world. To this end, it is constructive to group the states of matter that share the same qualitative properties into some universal classes, which are called *phases*. Concerning the classification of phases, a groundbreaking contribution was made in 1930s by Landau [1], who proposed a universal mechanism called *spontaneous symmetry breaking* (SSB), which refers to a situation where the microscopic physical laws that describe a many-body system respect certain symmetries but the state at equilibrium does not. An example of such a phase transition has been given in the opening poetry by the crystalization of rain into snow upon decreasing the temperature, where the continuous spatial translation symmetry is spontaneously broken into a discrete one. In general, different phases of a given system can be distinguished from each other by the different ways in which the symmetries are broken.

For quite a long time, it was believed that all the phases can be understood on the basis of SSB [2]. However, a revolution was triggered by the discovery of the quantum Hall effect in 1980s [3], after which the existence of novel states of matter beyond Landau's SSB paradigm had become clear [4]. These novel phases are qualitatively distinguished from the conventional ones in the sense that the microscopic ingredients are arranged and interacting with each other in a *topologically nontrivial* manner [5]. To gain some intuitive insight into what we mean by topologically nontrivial, one may imagine two linked rings, which cannot be separated into two individual rings unless one of them is cut (corresponding to a singularity in a continuous deformation). When some symmetries are imposed, the topological structure may be further enriched, leading to the notions of *symmetry-protected topological (SPT) phases* [6] and symmetry-enriched topological phases [7]. More precisely, in the language of quantum information, we can say that topologically nontrivial quantum many-body states cannot be disentangled into individual components by any finite-step combinations of local operations by quantum gates (with symmetry constraints, if any) [8]. In light of the recent rapid development of topological material science, a complete classification of topological phases at equilibrium has almost been achieved [9].

It might not be a surprise that the discovery of topological phases is much more delayed than

---

<sup>1</sup>This is part of the lyric of a Japanese-French song “美しきもの (belles choses)”. It describes some scenes with vivid seasonal features, such as a drizzling rain harmonized with the cry of cicadas in summer and a peaceful snow wrapping the earth in winter.



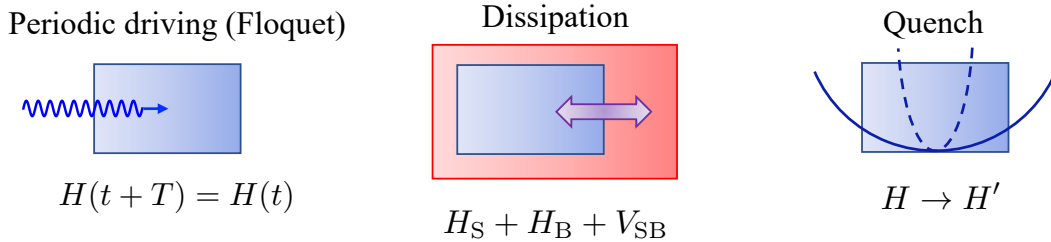


Figure 1.1: Schematic illustration of the three prototypical scenarios for bringing a quantum system out of equilibrium, which are periodic driving, dissipation and quench.

the proposal of SSB, since topological phenomena such as the quantization of the Hall conductance [3] are usually observable only when the quantum effects dominate. This typically requires a low temperature and a nearly perfect isolation from an environment.<sup>2</sup> These experimental situations have been achieved for not only crystalline materials [12], but also artificial quantum many-body systems implemented by various atomic, optical and molecular (AMO) platforms such as ultracold atoms [13], trapped ions [14] and superconducting qubits [15]. Compared to real materials, which inevitably involve some defects and impurities and can only be described by some effective theories after a lot of approximations, such kind of *quantum simulators* have the advantage to mimic a clean and simple system that is faithfully described by the physical theory we wish to investigate [16]. Indeed, various topological phases have been realized in AMO quantum simulators [17–19]. One representative implemented with ultracold atoms is the famous Haldane model that gives a minimal realization of the anomalous quantum Hall effect [20]. Interestingly, this model is expected by Haldane himself to be “unlikely to be directly physically realizable” [21].

It is certainly not the end of the story if we could classify all the phases at equilibrium and realize them in the laboratory. Indeed, nature is intrinsically out of equilibrium, and its beauty can never be fully understood without considering its dynamical aspects. Sometimes it might be good enough to interpret a dynamical change of states of matter as a transition between different equilibrium phases, provided that the transition is driven by some slowly varying parameters. However, things can be qualitatively different if the parameters change as quickly as the internal microscopic dynamics, as is the case of, e.g., optically driven crystalline materials [22]. Similar situations can also be realized in quantum simulators in a highly controllable way [23]. For these quantum many-body systems far from equilibrium, can we have a systematic classification based on their universal dynamical properties? In particular, can we have similar notions like SSB and topological phases? If these notions apply, what are the relations and essential differences between the nonequilibrium dynamical phases and the conventional equilibrium phases? These issues are actually under active discussions in recent years, yet they are poorly understood.

This Thesis is devoted to address the above fundamental questions concerning nonequilibrium dynamical phases. It is certainly too ambitious a goal to establish a complete framework since there is an enormous number of ways to drive a system out of equilibrium. Here, we confine ourselves to three of the simplest scenarios that are widely used in the literature, as illustrated in Fig. 1.1. The first scenario is periodic driving, which means that the parameters of the system are modulated periodically in time. Such a system is usually referred to as a *Floquet system* [24]. In the simplest setup, a Floquet system is still closed in the sense that it does not exchange matter with an environment, but exchanges energy with the work resources

<sup>2</sup>Recently, it has become clear that some topological phenomena occur also in classical wave systems at room temperature, such as photonic lattices [10] and mechanical metamaterials [11].

Table 1.1: Topics discussed in each chapter.

Topic	Order	Topology	Floquet	Dissipation	Quench
Chapter 2	○		○	○	
Chapter 3		○	○		
Chapter 4		○		○	
Chapter 5		○			○

that enable the temporal variations of parameters. We will discuss both SSB and topological phases in Floquet systems [25]. The second scenario is dissipation, which means that the system is coupled to some well-designed reservoirs which are generally not at thermal equilibrium [26]. Accordingly, the system is necessarily open and matter exchange with the reservoirs is generally allowed. The third scenario is quench, which means a sudden change of a parameter such that an original equilibrium state becomes highly excited [27]. This is arguably the simplest setup since the system is isolated after the quench. For the latter two scenarios, we will primarily focus on topological phases.

Let us sketch out the outline of the remaining chapters, which is briefly summarized in Table 1.1. In Chapter 2, we discuss a unique dynamical order associated with the SSB of discrete time-translation symmetry in Floquet open quantum systems. Previously, the so-called *discrete time-crystalline (DTC) order*, which can be considered as the temporal counterpart of the conventional spatial crystalline order in crystals, had been predicted [28–30] and experimentally verified in closed Floquet systems [31, 32], and was expected to be fragile against dissipation [33]. However, we will show that the interplay between some specific dissipation and driving can stabilize and even enrich the unique dynamical order. We will also discuss the possible experimental realization in cavity and circuit QED systems. This chapter is based on the following publication [34]:

- “*Discrete Time-Crystalline Order in Cavity and Circuit QED Systems*”, Zongping Gong, Ryusuke Hamazaki, and Masahito Ueda, *Physical Review Letters* **120**, 040404 (2018).

In Chapter 3, we focus on the topological aspects of Floquet systems. Precisely speaking, we discuss the topological classification of one-dimensional (1D) locality-preserving unitary operators with on-site unitary symmetries. Such kind of unitary operators have elegant tensor-network representations called *matrix-product unitaries* (MPUs) [35], which are the simplest tensor-network operators used to describe nonequilibrium quantum dynamics. MPUs provide efficient descriptions of the single-periodic time-evolution operators (i.e., the Floquet unitary) of 1D Floquet systems [36]. Moreover, it is known that, even in the absence of symmetries, there exist some topologically nontrivial MPUs that appear only as the edge dynamics of 2D intrinsic Floquet topological phases without equilibrium counterparts [37]. We will see that such kind of novel MPUs, as well as the corresponding 2D Floquet topological phases, are further enriched by symmetries. This chapter is based on the following publication [38]:

- “*Classification of Matrix-Product Unitaries with Symmetries*”, Zongping Gong, Christoph S underhauf, Norbert Schuch, and J. Ignacio Cirac, *Physical Review Letters* **124**, 100402 (2020).

In Chapter 4, we turn to discuss the topological phases in dissipative systems. In particular, we focus on the simplest class described by non-Hermitian Hamiltonians in the quadratic

form, which is a natural generalization of free-fermion systems. To our knowledge, the earliest classification of topological phases was done for free-fermion systems in the so-called Altland-Zirnbauer (AZ) classes [39, 40], which feature one or some of the three fundamental symmetries — time-reversal symmetry, particle-hole symmetry and chiral symmetry [41]. Well-known examples of free-fermion topological phases include quantum Hall insulators [3] and the more recently discovered time-reversal symmetric topological insulators [42]. When the Hermiticity constraint on the Hamiltonian is removed due to dissipation, we will see a dramatically changed classification result. For example, a 2D quantum Hall insulator is no longer topological and a prototypical nontrivial system turns out to be a 1D lattice with asymmetric left and right hopping amplitudes, a model originally proposed by Hatano and Nelson in a context irrelevant to topological phases [43]. This chapter is based on the following publication [44]:

- “*Topological Phases of Non-Hermitian Systems*”, Zongping Gong, Yuto Ashida, Kohei Kawabata, Kazuaki Takasan, Sho Higashikawa, and Masahito Ueda, *Physical Review X* **8**, 031079 (2018).

In Chapter 5, we focus on the topological classification of quench dynamics. Somewhat surprisingly, while quantum quenches are the simplest scenario for generating nonequilibrium dynamics, their topological aspects had not been seriously studied until recently. A pioneering work discovered the Hopf link in the  $(2 + 1)$ D momentum-time space after a quench from a trivial two-band insulator to a nontrivial Chern insulator in 2D [45]. Following this line of thought, we will perform a systematic analysis on the  $(1 + 1)$ D spacetime topology underlying the quench dynamics in 1D topological insulators in all the AZ classes. We will also discuss the universal feature of such dynamical topology from an entanglement perspective. This chapter is based on the following publication [46]:

- “*Topological Entanglement-Spectrum Crossing in Quench Dynamics*”, Zongping Gong and Masahito Ueda, *Physical Review Letters* **121**, 250601 (2018).

Finally, in Chapter 6, we summarize the thesis and discuss some possible directions for future studies.

## Chapter 2

# Discrete time-crystalline order in cavity and circuit QED systems

Periodic driving is one of the most common scenarios for bringing a system out of equilibrium. It not only provides a convenient tool to overcome some technical difficulties such as generating long-range hoppings and effective gauge fields, but also opens up the possibility of exploring new phases of matter unique to the nonequilibrium regime. A prototypical example of intrinsic nonequilibrium phases of matter with recent interest is *discrete time crystals*, which can be considered as the time analog of conventional crystals that spontaneously break the spatial translation symmetry. Most of the studies in literature focus on discrete time crystals in closed systems, since dissipation and decoherence are usually thought to destroy the dynamical order in discrete time crystals, the so-called *discrete time-crystalline order*. In this chapter, we argue that the discrete time crystals *do* exist in some open systems, where the discrete time-crystalline order may be stabilized and even enriched. We will not only discuss the theoretical possibilities, but also provide concrete experimental implementations based on driven cavity and circuit QED systems in the ultra-strong coupling regimes.

## 2.1 Background and motivation

### 2.1.1 Brief review on time crystals

Phases and phase transitions of matter are key concepts for understanding complex many-body physics [47, 48]. *Spontaneous symmetry breaking* (SSB) is among the most important mechanisms of phase transitions. Examples that are ubiquitous in nature include the spatial translation symmetry breaking in the liquid-solid phase transition and the spin-rotational symmetry breaking in the paramagnet-ferromagnet phase transition. While the notion of SSB was originally used to physically understand natural phenomena, one can always ask from a purely theoretical point of view whether a symmetric many-body Hamiltonian breaks all or some of the symmetries in certain parameter regimes. Rigorously speaking, here we have assumed the system to be isolated so that its energy is conserved and there is always a *continuous time-translation symmetry* generated by the Hamiltonian itself. Here comes a fundamental question: can this continuous time-translation symmetry be spontaneously broken? In fact, this is a question considered by Nobel laureate Frank Wilczek in 2012, who answered it in the affirmative and proposed plausible realizations in both classical and quantum systems [49, 50]. Meanwhile, a similar proposal with a concrete trapped-ion implementation appeared [51].

However, the original proposal of Wilczek turns out to be defective [52]. Moreover, it is found that the continuous time-translation symmetry breaking never occurs in ground states

and thermal states, provided that the Hamiltonian only involves sufficiently local interactions. In other words, there is a no-go theorem for continuous quantum time crystals [53]. It is not trivial at all to formulate this statement — to judge whether the continuous time-translation symmetry is spontaneously broken, we have to introduce a time-dependent perturbation to see whether a local observable oscillates in time if we first take the thermodynamic limit and then the zero perturbation limit. A more convenient criterion, which does not require a perturbation and is adapted in the proof of the no-go theorem in Ref. [53], is whether there is a long-range spatial-temporal order in a ground state or thermal state. Such a long-range spatial-temporal order turns out to be impossible, although there can be long-range spatial correlations alone, as is the case for conventional SSBs.

The discovery of the no-go theorem is not the end of the story. We recall that an important assumption in the no-go theorem is that the system is at its ground state or thermal equilibrium, so that it stays far from clear what would happen when the system is driven out of equilibrium. Indeed, recent experimental developments in various quantum simulators, such as ultracold atoms [13, 54], trapped ions [14, 55] and superconducting qubits [15, 56], have enabled us to prepare and control non-equilibrium quantum many-body systems [23, 57, 58]. Several unique dynamical phases have been unveiled, such as the many-body localized phases [59–64], whose excited states are non-thermal states with area-law entanglement, and the Floquet topological phases [37, 65–71], which are nonequilibrium topological phases enriched by periodic driving and will be discussed in the next chapter. Indeed, it turns out that we can bypass the no-go theorem by either focusing on excited states [72], or introducing periodic driving [28, 29, 73, 74]. The latter is of much more recent interest [75] and leads to the notion of *discrete time crystals* (DTC) or Floquet time crystals. We also mention that it is possible to realize a continuous time crystal at equilibrium by introducing long-range interactions [76].

To realize DTCs in periodically driven quantum systems, at the very least, we have to circumvent the Floquet eigenstate thermalization hypothesis, which implies that the system will eventually be heated to a featureless infinite-temperature state due to persistent driving [77–79]. One common scenario is the Floquet many-body localization, which requires strong disorder. This idea is adapted in a variety of driven spin-chain models [28, 29, 73, 74] and the trapped-ion experiment [32]. Note that another experiment based on NV-centers [31] does not fall into this category since the spatial dimension is three and the long-range dipole-dipole interactions tend to delocalize the system, leading to critical thermalization [80]. There are also some other scenarios that do not require any disorder such as mean-field models [81, 82] and Floquet prethermalization [83, 84]. In any case, these phases with broken discrete time-translation symmetry exhibit *discrete time-crystalline order* (DTC order) characterized by periodic oscillations of physical observables with period  $nT$ , where  $T$  is the Floquet period and  $n = 2, 3, \dots$ . Moreover, the DTC order is expected to be stabilized by many-body interactions against variations of driving parameters. Such a *rigidity* feature explains why a DTC is called a “crystal”.

### 2.1.2 Motivation and the main achievement

While remarkable progress concerning the DTCs has been made, most studies focus on closed quantum systems. Indeed, as has been experimentally observed [31, 32] and theoretically investigated [33], the DTC order in an open system is usually destroyed by decoherence. On the other hand, it is known that dissipation and decoherence can also serve as resources for quantum tasks such as quantum computation [85] and metrology [86]. From this perspective, it is natural to ask whether the DTC order exists and can even be stabilized in open systems [87]. Such a possibility has actually been pointed out in Ref. [83], but neither a detailed theoretical

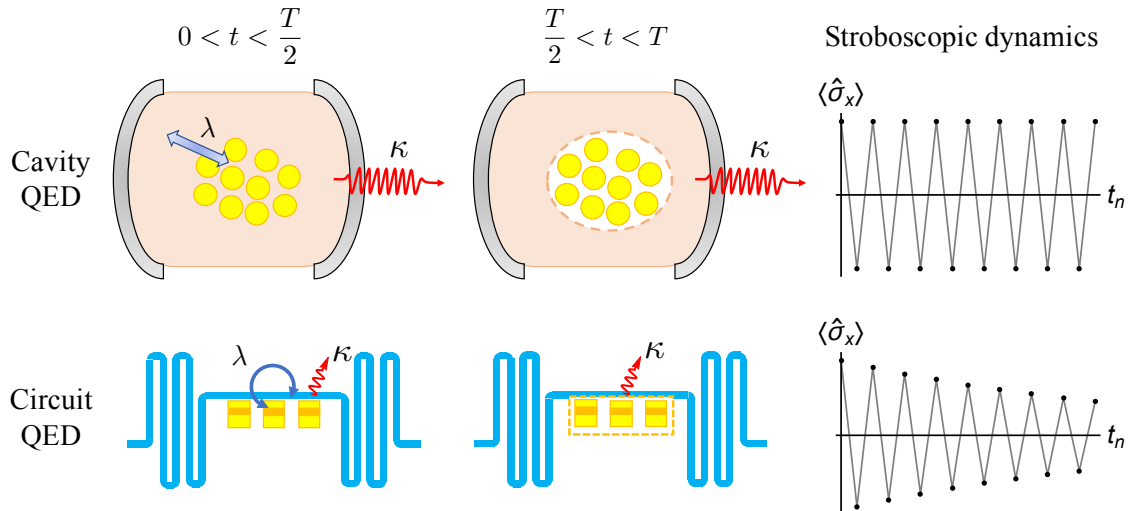


Figure 2.1: Cavity and circuit QED setups for realizing the DTC order. In the first (second) half of a Floquet period  $T$ , we switch on (off) the coupling  $\lambda$  between light and (artificial) atoms. For sufficiently large  $\lambda$ , almost persistent DTC order in the stroboscopic dynamics of a local observable is expected for an ensemble of a large number of atoms in an optical cavity, while transient DTC behavior can be observed for few superconducting qubits coupled to a microwave transmission line. Here  $\kappa$  denotes the loss rate of (microwave) photons. Reproduced from Fig. 1 of Ref. [34]. Copyright © 2018 by the American Physical Society.

model nor a concrete experimental implementation is presented.

Here, we propose a concrete open-system setup for realizing the DTC order by using a prototypical dissipative model — a modified open Dicke model [88–90], which describes a collective light-atom interaction in the presence of interaction modulation and photon loss. This model is relevant to cavity QED systems based on cold atoms [91–94] and circuit QED systems based on superconducting qubits [95–101]. As schematically illustrated in Fig. 2.1, the DTC order manifests itself through periodic switch-on and switch-off of a sufficiently strong light-atom coupling, leading to a period doubling in the stroboscopic dynamics of a physical observable such as the atomic spin polarization. For the cavity QED case, we consider the thermodynamic limit and find unexpectedly rich dynamical phases as the detuning parameter is varied (see Fig. 2.4). For the circuit QED case, we examine a deep quantum regime with few qubits to find a clear transient DTC behavior even for two qubits, a minimal setup of superradiance [98]. We also discuss a phenomenological model which demonstrates the exponentially long lifetime of the DTC order. These predictions should be testable in light of the state-of-the-art experimental developments in atomic, molecular and optical physics.

## 2.2 Theoretical proposal

We consider  $N$  pieces of identical two-level atoms in a single-mode cavity. Neglecting the motional degrees of freedom of atoms, the dynamics of the system can be described by the open

Dicke model [102]:

$$\begin{aligned}\frac{d\rho_t}{dt} &= \mathcal{L}(\lambda)\rho_t = -i[H(\lambda), \rho_t] + \kappa\mathcal{D}[a]\rho_t, \\ H(\lambda) &= \omega a^\dagger a + \omega_0 J_z + \frac{2\lambda}{\sqrt{N}}(a + a^\dagger)J_x,\end{aligned}\tag{2.1}$$

where

$$\mathcal{D}[a]\rho \equiv a\rho a^\dagger - \frac{1}{2}\{a^\dagger a, \rho\}\tag{2.2}$$

is the photon-loss dissipator with  $a$  being the annihilation operator of the photon field and  $\{\cdot, \cdot\}$  being the anticommutator,

$$J_\mu \equiv \frac{1}{2} \sum_{j=1}^N \sigma_j^\mu, \quad \mu = x, y, z\tag{2.3}$$

is the collective atomic pseudospin operator,  $\omega$ ,  $\omega_0$ ,  $\lambda$  and  $\kappa$  are the optical frequency, the resonant frequency of an atom, the coupling strength and the photon-loss rate, respectively. One can check that the GKSL generator respects the combined  $\mathbb{Z}_2$  parity symmetry of atoms and photons, which is represented by

$$P \equiv e^{i\pi(a^\dagger a + J_z + \frac{N}{2})}.\tag{2.4}$$

Here by respecting the parity symmetry, we mean that

$$\mathcal{L}(\lambda)\mathcal{P} = \mathcal{P}\mathcal{L}(\lambda),\tag{2.5}$$

where  $\mathcal{P}\rho \equiv P\rho P$  is the parity superoperator.

Let us first review some basic facts about the phase transition in the static open Dicke model, i.e., the case of a time-independent  $\lambda$ . These results have been derived in Ref. [102] on the basis of a semiclassical approach. Here, we present a quantum treatment as an open-system generalization of the method developed in Ref. [90], which deals with the quantum phase transition in the isolated Dicke model. It is convenient to represent the system using the *Holstein-Primakoff transformation*:

$$J_+ = b^\dagger \sqrt{N - b^\dagger b}, \quad J_- = \sqrt{N - b^\dagger b} b, \quad J_z = b^\dagger b - \frac{N}{2},\tag{2.6}$$

where the bosonic field operator  $b$  describes the atomic collective mode, which has a truncated Fock space up to  $N$  bosons. In particular, the  $N$ -boson Fock state corresponds to the fully spin-up polarized state  $|\uparrow\rangle \equiv \bigotimes_{j=1}^N |\uparrow\rangle$  in the original spin picture. Suppose that the system is in the parity-symmetry-broken superradiant phase, which has a macroscopic coherence in both photon and atom fields. This motivates us to rewrite the photonic and atomic modes as

$$a = c + \alpha, \quad b = d - \beta,\tag{2.7}$$

where  $|\alpha|$  and  $|\beta|$  are of the order of  $\sqrt{N}$ . Using the gauge invariance of a general Gorini-Kossakowski-Sudarshan-Lindblad (GKSL) equation  $\dot{\rho}_t = -i[H, \rho_t] + \sum_j \mathcal{D}[L_j]\rho_t$  under the transformations [87]

$$L_j \rightarrow L_j + C_j, \quad H \rightarrow H + \sum_j \frac{i}{2}(C_j L_j^\dagger - C_j^* L_j),\tag{2.8}$$

where  $C_j$ 's are  $c$ -numbers, we can rewrite the master equation for the open Dicke model (2.1) as

$$\dot{\rho}_t = -i[H'(\lambda), \rho_t] + \kappa \mathcal{D}[c]\rho_t. \quad (2.9)$$

Here, up to small corrections that vanish in the thermodynamic limit  $N \rightarrow \infty$ , the modified Hamiltonian  $H'(\lambda)$  is given by

$$\begin{aligned} H'(\lambda) = & \omega c^\dagger c + \omega_0 d^\dagger d + |\alpha|^2 \omega + \left( |\beta|^2 - \frac{N}{2} \right) \omega_0 - \lambda \sqrt{1 - \frac{|\beta|^2}{N}} (\alpha^* + \alpha)(\beta^* + \beta) \\ & + \left[ \alpha \left( \omega - i\frac{\kappa}{2} \right) - (\beta^* + \beta) \sqrt{1 - \frac{|\beta|^2}{N}} \lambda \right] c^\dagger + \text{H.c.} \\ & + \left\{ \lambda (\alpha^* + \alpha) \sqrt{1 - \frac{|\beta|^2}{N}} \left[ 1 - \frac{(\beta^* + \beta)\beta}{2(N - |\beta|^2)} \right] - \beta \omega_0 \right\} d^\dagger + \text{H.c.} \\ & + \lambda (\alpha^* + \alpha) \sqrt{1 - \frac{|\beta|^2}{N}} \left[ \frac{\beta^* d^2 + \beta d^{\dagger 2}}{2(N - |\beta|^2)} + \frac{(\beta^* + \beta) d^\dagger d}{N - |\beta|^2} + \frac{(\beta^* + \beta)(\beta^* d + \beta d^\dagger)^2}{8(N - |\beta|^2)^2} \right] \\ & + \lambda \sqrt{1 - \frac{|\beta|^2}{N}} \left[ 1 - \frac{(\beta^* + \beta)\beta^*}{2(N - |\beta|^2)} \right] (c^\dagger + c) d + \text{H.c.} \end{aligned} \quad (2.10)$$

To eliminate the terms that are linear in the field operators in Eq. (2.10), we require the parameters  $\alpha$  and  $\beta$  to satisfy

$$\begin{aligned} \alpha \left( \omega - i\frac{\kappa}{2} \right) &= (\beta^* + \beta) \sqrt{1 - \frac{|\beta|^2}{N}} \lambda, \\ \lambda (\alpha^* + \alpha) \sqrt{1 - \frac{|\beta|^2}{N}} \left[ 1 - \frac{(\beta^* + \beta)\beta}{2(N - |\beta|^2)} \right] &= \beta \omega_0, \end{aligned} \quad (2.11)$$

which implies  $\beta^* = \beta$  and

$$\beta \frac{\lambda^2}{\lambda_c^2} \left( 1 - \frac{2\beta^2}{N} \right) = \beta, \quad \alpha = \frac{2\beta\lambda}{\omega - i\frac{\kappa}{2}} \sqrt{1 - \frac{\beta^2}{N}}, \quad (2.12)$$

where the critical value  $\lambda_c$  reads

$$\lambda_c = \frac{1}{2} \sqrt{\frac{\omega_0}{\omega} \left( \omega^2 + \frac{\kappa^2}{4} \right)}. \quad (2.13)$$

It is clear that nontrivial solutions (i.e.,  $|\alpha|, |\beta| \neq 0$ )

$$\beta^2 = \frac{N}{2}(1 - \mu), \quad |\alpha|^2 = \frac{N\omega_0}{4\omega}(\mu^{-1} - \mu), \quad \mu \equiv \frac{\lambda_c^2}{\lambda^2} \quad (2.14)$$

exist if and only if  $\lambda > \lambda_c$  or equivalently  $\mu < 1$ . Substituting Eqs. (2.14) and (2.11) into Eq. (2.10) yields

$$\begin{aligned} H'(\lambda) = & \omega c^\dagger c + \frac{1 + \mu}{2\mu} \omega_0 d^\dagger d + \frac{(3 + \mu)(1 - \mu)}{8\mu(1 + \mu)} \omega_0 (d + d^\dagger)^2 + \lambda \mu \sqrt{\frac{2}{1 + \mu}} (c^\dagger + c)(d^\dagger + d) \\ & - \frac{N(1 + \mu^2) + 1 - \mu}{4\mu} \omega_0. \end{aligned} \quad (2.15)$$

It has been shown in Ref. [90] that, without photon loss ( $\kappa = 0$ ), the ground state of  $H'$  (2.15) is a squeezed (including both single-mode and two-mode squeezed) vacuum with respect to  $c$



and  $d$ . In the presence of photon loss, the steady state becomes not only squeezed but also mixed. However, since  $c$  and  $d$  are obtained by a macroscopic translation of the order of  $\sqrt{N}$  from  $a$  and  $b$ , the expectation values of local observables (e.g., single-atom spin polarization) in the thermodynamic limit are expected to coincide with those of  $|\alpha\rangle \otimes |-\beta\rangle$ , i.e., the direct product of photon and atomic-spin coherent states:

$$|\alpha\rangle = e^{-\frac{|\alpha|^2}{2}} \sum_{n=0}^{\infty} \frac{\alpha^n}{\sqrt{n!}} |n\rangle, \quad |-\beta\rangle = e^{-\frac{|\beta|^2}{2}} \sum_{n=0}^{\infty} \frac{(-\beta)^n}{\sqrt{n!}} |n\rangle. \quad (2.16)$$

So far we have shown that, in the thermodynamic limit and when  $\lambda$  exceeds  $\lambda_c$  given in Eq. (2.13), the open Dicke model exhibits a phase transition that breaks the  $\mathbb{Z}_2$  symmetry characterized by the parity operator in Eq. (2.4) [90, 92]. For  $\lambda > \lambda_c$ , we can actually construct an *exact* period-doubling Floquet dynamics as follows: Starting from one of the symmetry-broken steady states  $\rho_{\text{ss}}$ , in the first-half period, the dynamics is governed by Eq. (2.1), and therefore  $\rho_{\text{ss}}$  stays unchanged by definition. In the second-half period, we perform the parity operation on the system, so that the other steady state

$$\rho'_{\text{ss}} = \mathcal{P} \rho_{\text{ss}} \equiv P \rho_{\text{ss}} P \quad (2.17)$$

is achieved at the end of the Floquet period. If we observe the system stroboscopically at  $t_n = nT$ , we should find  $\rho_{\text{ss}}$  ( $\rho'_{\text{ss}}$ ) for even (odd)  $n$ . This gives the desired period doubling.

However, the exact period doubling under the above specific driving protocols does not necessarily mean that the system is in a DTC phase. Only if we can demonstrate that the period doubling is robust against imperfection such as the deviation of the evolution in the second-half period from the parity operation, we can identify it as a DTC order. A straightforward way to introduce such imperfection is to switch off the atom-light coupling in the second-half period. That is, we modulate  $\lambda$  in Eq. (2.1) periodically as

$$\lambda_{t+T} = \lambda_t = \begin{cases} \lambda & 0 \leq t < \frac{T}{2}; \\ 0 & \frac{T}{2} \leq t < T. \end{cases} \quad (2.18)$$

In the resonant ( $\omega = \omega_0 = \omega_T \equiv 2\pi/T$ ) and isolated ( $\kappa = 0$ ) limit, the time evolution during the second half of the period gives the parity operator up to an unimportant global phase since

$$P = e^{-i\frac{T}{2}H(\lambda=0) + \frac{i\pi}{2}N}. \quad (2.19)$$

If we introduce a detuning between  $\omega$  and  $\omega_0$  as

$$\omega = (1 - \epsilon)\omega_T, \quad \omega_0 = (1 + \epsilon)\omega_T, \quad (2.20)$$

we can control the degree of imperfection by  $\epsilon$ . In addition, there is always a *nonunitary* imperfection due to photon loss ( $\kappa \neq 0$ ) even for  $\epsilon = 0$ . Without loss of generality, we set  $\omega_T = 1$  hereafter.

## 2.3 Numerical simulations

In this section, we perform extensive numerical simulations on the modulated open Dicke model. We focus both on the thermodynamic limit, for which we solve the semiclassical equation of motion using the Runge-Kutta method, and on the few-atom quantum regime, for which we solve the original master equation by using the exact-diagonalization method.

### 2.3.1 Mean-field dynamics in the thermodynamic limit

#### Semiclassical equation of motion

In the thermodynamic limit  $N \rightarrow \infty$ , the relative fluctuation in a local observable becomes negligible, and the semiclassical approach is justified in such a mean-field regime [103–105]. To work out the semiclassical equation of motion, we should adapt the Heisenberg picture. For a general *time-dependent* GKSL equation  $\dot{\rho}_t = \mathcal{L}_t \rho_t = -i[H(t), \rho_t] + \sum_j \mathcal{D}[L_j(t)]\rho_t$ , the corresponding open-system Heisenberg equation for an observable  $O$  is given by [87]

$$\frac{d\langle O \rangle}{dt} = \langle \mathcal{L}_t^\dagger O \rangle = \left\langle i[H(t), O] + \sum_j \left( L_j^\dagger(t) O L_j(t) - \frac{1}{2} \{L_j^\dagger(t) L_j(t), O\} \right) \right\rangle, \quad (2.21)$$

where  $\langle \dots \rangle \equiv \text{Tr}[\dots \rho_t]$  is the instantaneous ensemble average. Applying Eq. (2.21) to the modulated open Dicke model (2.1) and using the commutation relations  $[a, a^\dagger] = 1$  and  $[J_\mu, J_\nu] = i\epsilon_{\mu\nu\sigma} J_\sigma$ , we obtain

$$\begin{aligned} \frac{d\langle a \rangle}{dt} &= -\left(i\omega + \frac{\kappa}{2}\right) \langle a \rangle - \frac{2i\lambda_t}{\sqrt{N}} \langle J_x \rangle, \\ \frac{d\langle J_x \rangle}{dt} &= -\omega_0 \langle J_y \rangle, \quad \frac{d\langle J_y \rangle}{dt} = \omega_0 \langle J_x \rangle - \frac{2\lambda_t}{\sqrt{N}} \langle (a + a^\dagger) J_z \rangle, \quad \frac{d\langle J_z \rangle}{dt} = \frac{2\lambda_t}{\sqrt{N}} \langle (a + a^\dagger) J_y \rangle. \end{aligned} \quad (2.22)$$

We can also check from  $[J^2, J_\mu] = 0$  that

$$\frac{d\langle J^2 \rangle}{dt} = 0, \quad J^2 \equiv \sum_\mu J_\mu^2, \quad (2.23)$$

which means  $\langle J^2 \rangle$  is conserved. In particular, if the atoms are initialized (by, e.g., optical pumping) to be a fully spin-polarized state like  $|\Downarrow\rangle \equiv \bigotimes_{j=1}^N |\downarrow\rangle$ , which is the case in real experiments [91, 94], we have  $\langle J^2 \rangle = \frac{N}{2}(\frac{N}{2} + 1)$  for all the time.

On the mean-field level, we can approximate the crossing terms like  $\langle a J_\mu \rangle$  as  $\langle a \rangle \langle J_\mu \rangle$ , which has an order of magnitude of  $\mathcal{O}(N^{\frac{3}{2}})$ , while the quantum fluctuation is expected to be no more than  $\mathcal{O}(N)$ . Such an approximation should become exact in the thermodynamic limit. In terms of the scaled variables

$$\tilde{\alpha} \equiv \frac{\langle a \rangle}{\sqrt{N}}, \quad j_\mu \equiv \frac{\langle J_\mu \rangle}{N}, \quad \mu = x, y, z \quad (2.24)$$

Eq. (2.22) gives a closed set of semiclassical equations:

$$\begin{aligned} \frac{d\tilde{\alpha}}{dt} &= -\left(i\omega + \frac{\kappa}{2}\right) \tilde{\alpha} - 2i\lambda_t j_x, \\ \frac{dj_x}{dt} &= -\omega_0 j_y, \quad \frac{dj_y}{dt} = \omega_0 j_x - 2\lambda_t (\tilde{\alpha} + \tilde{\alpha}^*) j_z, \quad \frac{dj_z}{dt} = 2\lambda_t (\tilde{\alpha} + \tilde{\alpha}^*) j_y, \end{aligned} \quad (2.25)$$

which can finally be rewritten in the forms of

$$\begin{aligned} \frac{dx}{dt} &= p - \frac{\kappa}{2} x, \quad \frac{dp}{dt} = -\omega^2 x - \frac{\kappa}{2} p - 2\lambda_t \sqrt{2\omega} j_x, \\ \frac{d\mathbf{j}}{dt} &= (\omega_0 \mathbf{e}_z + 2\lambda_t \sqrt{2\omega} x \mathbf{e}_x) \times \mathbf{j}, \quad \mathbf{j} \equiv (j_x, j_y, j_z), \end{aligned} \quad (2.26)$$

after the substitution

$$\tilde{\alpha} \equiv \sqrt{\frac{\omega}{2}} x + \frac{ip}{\sqrt{2\omega}}. \quad (2.27)$$

In terms of the photon fields,  $x$  and  $p$  are expressed as

$$x \equiv \frac{\langle a + a^\dagger \rangle}{\sqrt{2N\omega}}, \quad p \equiv \frac{i\langle a^\dagger - a \rangle}{\sqrt{2N/\omega}}. \quad (2.28)$$

Note that  $j^2 \equiv \sum_\mu j_\mu^2$  continues to be a conserved quantity for Eq. (2.25) and takes on the value of  $1/4$  for  $\langle J^2 \rangle = (N/2)(N/2 + 1)$  when  $N \rightarrow \infty$ . This observation implies that the trajectory of atomic angular momenta is confined on the Bloch sphere. It is also worth mentioning that for a large but finite  $N$  we can systematically calculate the corrections of the order of  $N^{-k}$  by means of the cumulant expansion [106].

One can check that the  $\mathbb{Z}_2$  parity symmetry is inherited by the semiclassical equation of motion, in the sense that Eq. (2.26) is invariant under the simultaneous sign reversal of  $x$ ,  $p$ ,  $j_x$  and  $j_y$ . The dissipative phase transition [107] in the open Dicke model now becomes a dynamical phase transition known as the pitchfork bifurcation [104], where the original unique stable attractor

$$(x_0, p_0) = (0, 0), \quad (j_{x0}, j_{y0}, j_{z0}) = \left(0, 0, -\frac{1}{2}\right) \quad (2.29)$$

becomes unstable and two new stable attractors

$$(x_\pm, p_\pm) = \mp \frac{\sqrt{2\omega(1-\mu^2)}}{\omega^2 + \kappa^2/4} \left(\lambda, \frac{\kappa}{2}\right), \quad (j_{x\pm}, j_{y\pm}, j_{z\pm}) = \frac{1}{2}(\pm\sqrt{1-\mu^2}, 0, -\mu), \quad \mu \equiv \frac{\lambda_c^2}{\lambda^2} \quad (2.30)$$

emerge as the classical reductions from  $\rho_{ss}$  and  $\rho'_{ss}$ . To be specific, we choose the initial state to be the “+” attractor (2.30) in all the following numerical calculations. We solve the nonlinear differential equation given in Eq. (2.26) for up to 5000 periods by using the Runge-Kutta method.

### *Synchronization-based approach to diagnosing dynamical phases*

While it is not so difficult to judge whether the system is in a DTC phase (or other dynamical phases) from the time evolution of some appropriate observables, here we introduce a synchronization-based approach to make an accurate diagnosis. Indeed, the rigidity of the DTC order in closed systems is usually explained as a result of many-body synchronization [74]. As for the Dicke model, while we do have long-range (actually all to all) interactions between atoms mediated by photons [91], it is more convenient to regard the atoms as a rotor that couples nonlinearly to a harmonic oscillator that represents single-mode photons. In this picture, we can quantify the degree of synchronization through the phase difference between the rotor and the oscillator. Similar synchronization quantifiers have been used in several recent studies on nonlinear classical and quantum systems [108–110].

Denoting the phase of photons as  $\phi_a$  and that of atoms as  $\phi_b$ , we have

$$\langle a \rangle \equiv |\langle a \rangle| e^{i\phi_a}, \quad \langle b \rangle \equiv |\langle b \rangle| e^{i\phi_b}, \quad (2.31)$$

where  $b$  is the bosonic mode of collective atomic excitations defined in Eq. (2.6). In the thermodynamic limit, the phases can semiclassically be evaluated through the relations

$$\phi_a = \text{Arg} \left( \sqrt{\omega}x + \frac{ip}{\sqrt{\omega}} \right), \quad \phi_b = \text{Arg}(j_x + ij_y). \quad (2.32)$$

Note that  $\phi_a - \phi_b = \pi \pmod{2\pi}$  for the symmetry-broken ground states of the isolated Dicke model, and that it slightly deviates from  $\pi$  for a small nonzero  $\kappa$ . In the following calculations, we fix  $\lambda = 1$  and  $\kappa = 0.25$  unless otherwise indicated.

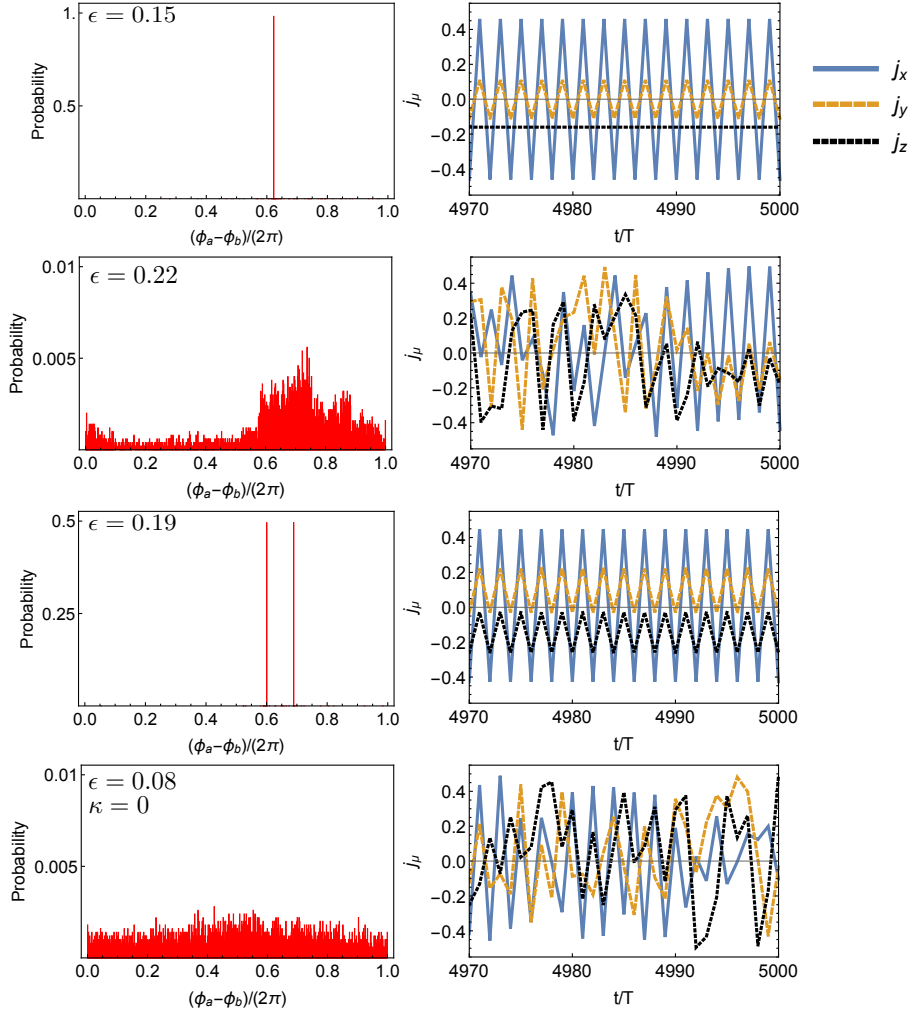


Figure 2.2: Probability distribution of the phase difference (PDPD)  $\phi_a - \phi_b$  over 5000 periods and the stroboscopic dynamics of atomic angular momenta in the last 30 periods for the normal DTC phase ( $\epsilon = 0.15$ ), the asymmetric period-doubling phase ( $\epsilon = 0.19$ ) and the thermal phases ( $\epsilon = 0.22$  and  $\epsilon = 0.08, \kappa = 0$ ). We use  $\lambda = 1$  and  $\kappa = 0.25$  unless indicated otherwise. A single peak in the PDPD splits into two when the doublet becomes asymmetric. For thermal phases, the PDPD spreads almost uniformly in the closed limit ( $\kappa = 0$ ) while inhomogeneously for a nonzero  $\kappa$ . Reproduced from Supplementary Fig. 1 of Ref. [34]. Copyright © 2018 by the American Physical Society.

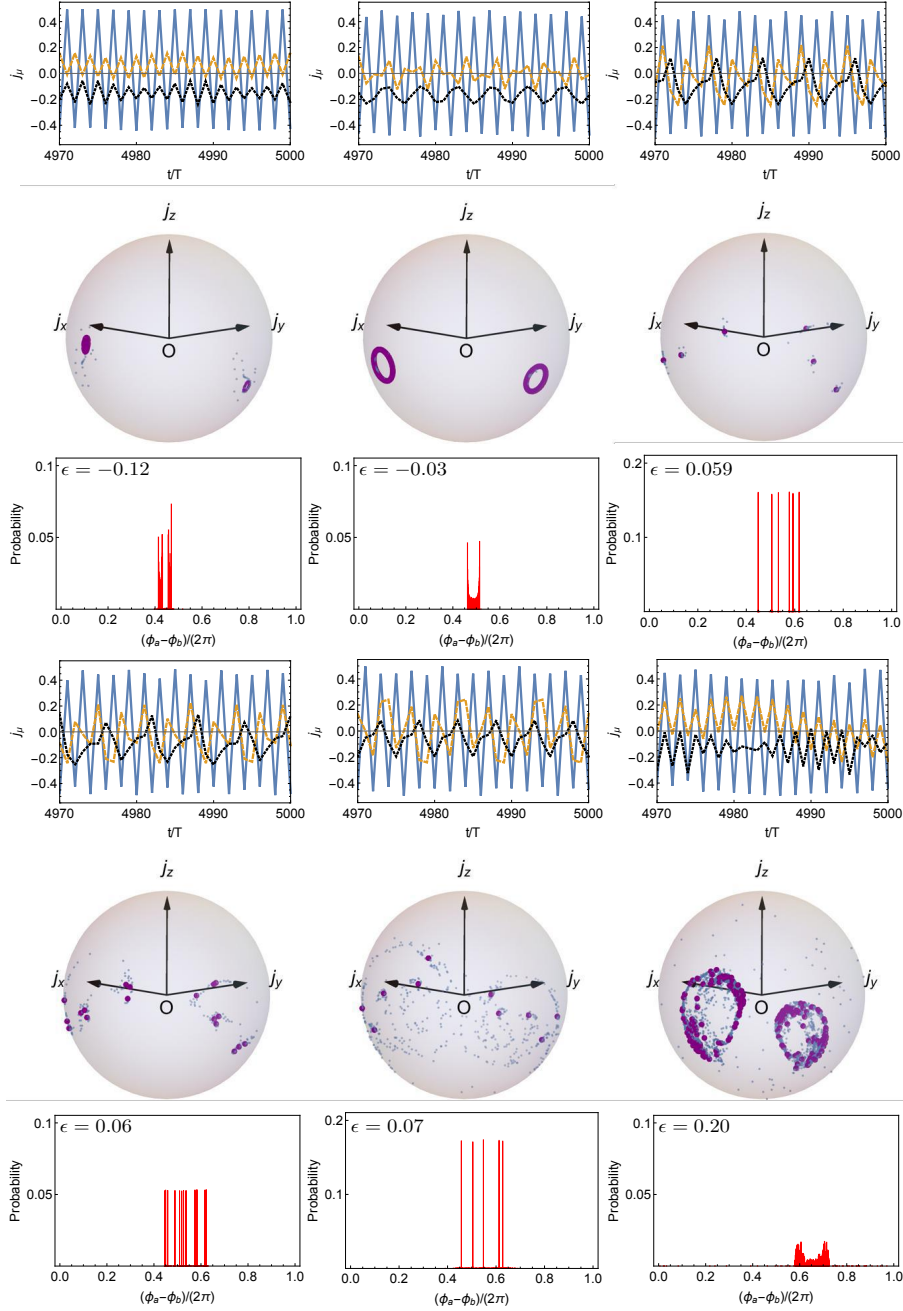


Figure 2.3: Stroboscopic dynamics of the atomic angular momenta over the last 30 periods of the 5000-period evolution (top), the phase-space trajectories of the last 200 periods projected onto the pseudospin Bloch sphere (middle) and the corresponding probability distribution of the phase difference (bottom). The other parameters are chosen to be  $\kappa = 0.25$  and  $\lambda = 1$ . In addition to a limit-cycle pair ( $\epsilon = -0.03$ ), we find new dynamical phases including an asymmetric limit-cycle pair ( $\epsilon = -0.12$ ), an asymmetric sextet ( $\epsilon = 0.059$ ), symmetric ten- ( $\epsilon = 0.07$ ) and asymmetric eighteen-fold ( $\epsilon = 0.06$ ) multiplets, and a locally ergodic phase ( $\epsilon = 0.2$ ). Reproduced from Supplementary Fig. 3 of Ref. [34]. Copyright © 2018 by the American Physical Society.

Let us consider the modulated open Dicke model in the normal DTC phase (symmetric doublet). The states of the system at the end of an odd number of periods and that of an even number of periods are exactly related to each other by the parity operator, implying  $\phi_a \rightarrow \phi_a + \pi \pmod{2\pi}$  and  $\phi_b \rightarrow \phi_b + \pi \pmod{2\pi}$  after each period. Therefore, the photon and atomic phases are perfectly synchronized in the normal DTC phase, as indicated by a single peak in the probability distribution of the phase difference (PDPD)  $\phi_a - \phi_b$  calculated at  $t_n = nT$  ( $n = 1, 2, \dots, 5000$ ). We give an example in the top left two panels in Fig. 2.2.

When the period doubling becomes asymmetric, the PDPD splits into two peaks (see the top right two panels in Fig. 2.2), since the increments of  $\phi_a$  and  $\phi_b$  after each period are no longer the same, although those after every *two* periods are both  $2\pi$ . When the system enters the thermal phase, the PDPD spreads to everywhere over  $[0, 2\pi)$ , implying the loss of synchronization (see the panels in the bottom in Fig. 2.2). The PDPD also becomes continuous for a symmetric limit-cycle pair, but is localized in a finite range with singularities at the boundaries (see the second column from the left in Fig. 2.2). We can see that the behavior of the PDPD sharply distinguishes different dynamical phases.

We apply this powerful approach to further explore the rich dynamical phases. Typical numerical results are presented in Fig. 2.3. For  $\epsilon = -0.12$ , we find a pair of asymmetric limit cycles, indicated by two continuous compact regions in the PDPD. For  $\epsilon = 0.059$ , we find an asymmetric sextet order. For  $\epsilon = 0.06$  (0.07), we find that the period of the stroboscopic dynamics becomes eighteen-fold (ten-fold) in an asymmetric (symmetric) manner, which can be read out from the number of peaks in the PDPD. Furthermore, when  $\epsilon = 0.2$ , we observe a locally ergodic phase where the trajectories cover two separated *areas* on the angular-momentum sphere (in the quadrature plane). This phase is more chaotic than the phase of a limit-cycle pair, for which the trajectories are one dimensional, yet less chaotic than a thermal phase, where there is only a single area covered by the trajectories and the DTC order is destroyed. These features are well captured by the PDPD, which is still localized but the boundary singularities are smeared out.

Finally, we emphasize that once the semiclassical dynamics becomes chaotic, it is in practice impossible to obtain exact numerical results except for an initial short time interval. This is due to the *exponential* amplification of inevitable numerical errors. Nevertheless, we can still observe qualitative behavior of irregular trajectories covering areas, based on which we judge that the system is in the thermal phase.

### *Phase diagram*

By employing the approach in the previous section for different  $\epsilon$  and fixed  $\kappa = 0.05$  and  $\lambda = 1$ , we map out the full dynamical phase diagram in the top row of Fig. 2.4. We find the normal DTC phase (denoted as SD) and the thermal phase (T); the former respects the  $\mathbb{Z}_2$  symmetry in which  $j_x, j_y, x, p$  reverse their signs after one period, and the latter shows irregular trajectories that cover some areas of the pseudospin sphere (or in the quadrature  $(x-p)$  plane). Furthermore, we find symmetric limit-cycle pairs (LC), for which the steady orbit forms two closed loops in the phase space, period sextupling (S), and asymmetric period doubling (AD), with  $j_x, j_y, x, p$  taking on two different values that are not symmetric against inversion. Interestingly, the regions of SD and LC phases are not connected but separated into two parts by other dynamical phases. As we will see in the next subsection, these phases can be systematically understood on the basis of bifurcation theory [111–115].

We note that the dynamics of a generalized *time-independent* open Dicke model, which has an additional Stark-shift term  $(U/N)J_z a^\dagger a$  in  $H(\lambda)$  in Eq. (2.1) (see Eq. (2.70)), has been thoroughly studied in Ref. [104] based on the semiclassical analysis. While there are only

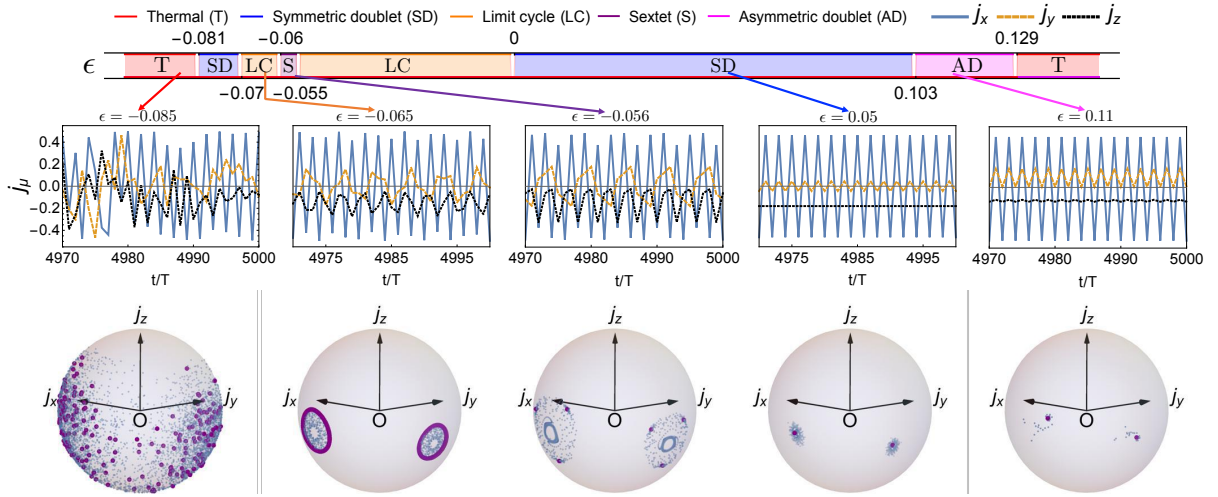


Figure 2.4: Dynamical phase diagram (top), typical stroboscopic dynamics (middle), and trajectories (bottom) of the atomic pseudospin for atom-light coupling  $\lambda = 1$  and photon-loss rate  $\kappa = 0.05$ . Top: As the detuning  $\epsilon$  (see Eq. (2.20)) is varied, five different dynamical phases emerge: thermal (T, red), symmetric period doubling (normal DTC order, SD, blue), limit-cycle pair (LC, orange), period sextupling (S, purple), and asymmetric period doubling (AD, magenta). The phase boundaries are marked in white with resolution  $10^{-3}$ . Middle: Typical stroboscopic dynamics of  $j_\mu \equiv \langle J_\mu \rangle / N$  ( $\mu = x$  (solid blue),  $y$  (dashed orange),  $z$  (dotted black)) for the last 30 periods of the entire 5000-period evolution. Bottom: Full stroboscopic phase-space-point trajectories (light blue) and those of the last 200 periods (purple) projected on the pseudospin Bloch sphere. Reproduced from Fig. 2 of Ref. [34]. Copyright © 2018 by the American Physical Society.

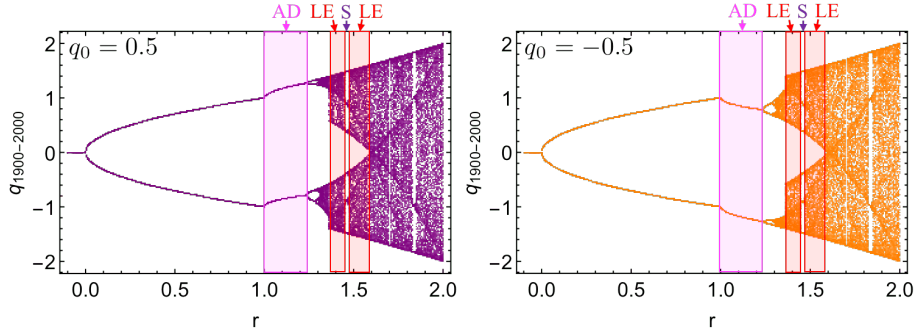


Figure 2.5: Steady orbit  $q_{1900-2000}$  of the recurrence equation (2.33) starting from  $q_0 = 0.5$  (left panel) and  $-0.5$  (right panel) for different values of the parameter  $r$ . Besides the symmetric doublet for  $0 < r < 1$ , we observe the asymmetric doublet (indicated as AD) and even the period sextupling (S) embedded in the locally ergodic phase (LE). Reproduced from Supplementary Fig. 2 of Ref. [34]. Copyright © 2018 by the American Physical Society.

single- (normal) and double- (superradiant) attractor phases for  $U = 0$ , limit-cycle and multiple-attractor phases emerge for  $U \neq 0$ , leading also to a rich dynamical-phase structure. Here, in contrast, the richness of dynamical phases arises from the *time dependence* of  $\lambda$  with  $U = 0$ . Another distinction is that in Ref. [104] the steady state picks up one of the attractors or the unique limit cycle, whereas here the steady state goes around different fixed points or limit cycles in a stroboscopic manner.

### *Understanding the dynamical phases from bifurcation theory*

The richness of the dynamical phases in the modulated open Dicke model arises also from the nonlinearity of the semiclassical dynamics (2.25), which, in turn, originates from the finite-level nature of the atomic spectrum. Here, by the finite-level nature, we mean that the atomic excitations can be saturated for a given  $N$ . Such saturation effects become increasingly more significant, and hence survive even in the thermodynamic limit as the system is excited farther away from the steady state. This is precisely the case of the modulated open Dicke model.

In the language of nonlinear dynamical systems [112], different dynamical phases are caused by certain types of bifurcations. The normal DTC order is essentially an interplay of pitchfork bifurcation and parity symmetry. It appears already in a simple recurrence series:

$$q_{n+1} = -(r+1)q_n + q_n^3, \quad (2.33)$$

which is a combination of a minimal discrete dynamics  $q \rightarrow (r+1)q - q^3$  for supercritical pitchfork bifurcation and the inversion  $q \rightarrow -q$ . Note that this is neither a supercritical pitchfork bifurcation alone, after which the dynamics converges to one of the fixed points, nor a subcritical pitchfork bifurcation, after which no stable fixed point exists. As shown in Fig. 2.5, we see symmetric period doubling for  $0 < r < 1$ . When  $r$  exceeds 1, the symmetric orbit becomes unstable and a local period-doubling bifurcation, which is well-known in the logistic map [111], occurs at the ensemble level, leading to the asymmetric period doubling at the trajectory level. For larger  $r$ , we observe a narrow sextet window embedded in the locally (two-branched) ergodic phase, which resembles the period-sextupling phase sandwiched by limit-cycle pairs shown in the top row of Fig. 2.4. While the toy model (2.33) and the modulated Dicke model share many common features, only the latter shows transitions between limit cycles and fixed points around



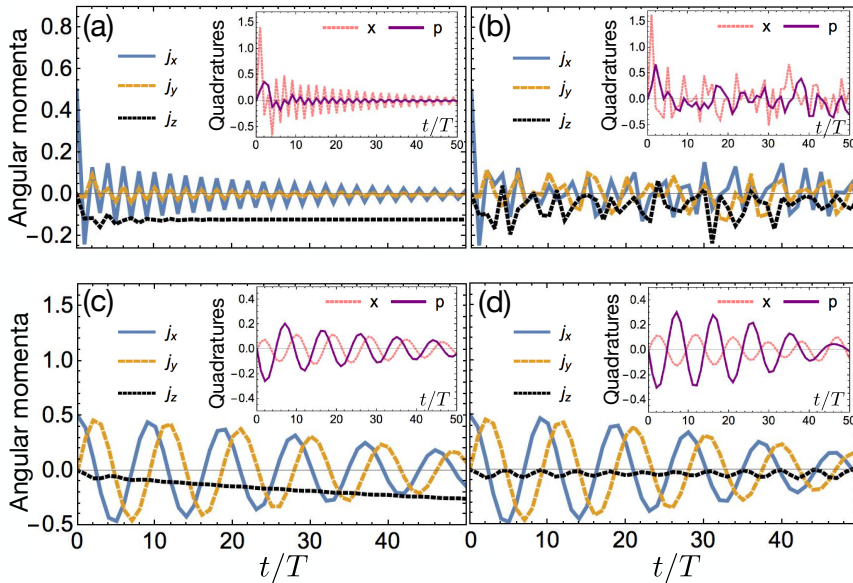


Figure 2.6: (a) Stroboscopic dissipative dynamics of the scaled angular momenta of  $j_x$  (solid),  $j_y$  (dashed), and  $j_z$  (dotted) in the two-qubit Dicke model with  $\kappa = 0.05$ ,  $\epsilon = 0.1$  and  $\lambda = 1$  (strong coupling). The inset shows quadratures, i.e.,  $x$  (dotted) and  $p$  (solid). (b) Stroboscopic dynamics for isolated systems ( $\kappa = 0$ ,  $\epsilon = 0.1$ , and  $\lambda = 1$ ) in the strong-coupling regime. (c) Stroboscopic dissipative dynamics in the weak-coupling regime ( $\kappa = 0.05$ ,  $\epsilon = 0.1$ , and  $\lambda = 0.1$ ). (d) Stroboscopic unitary dynamics in the weak-coupling regime ( $\kappa = 0$ ,  $\epsilon = 0.1$ , and  $\lambda = 0.1$ ). Only (a) shows a DTC transient. The initial state is always  $|\Rightarrow\rangle \otimes |0\rangle$ , where  $|\Rightarrow\rangle$  is the eigenstate of  $J_x$  with eigenvalue  $N/2$  ( $N = 2$ ) and  $|0\rangle$  is the photon vacuum. Reproduced from Fig. 3 of Ref. [34]. Copyright © 2018 by the American Physical Society.

$\epsilon = 0$  and  $-0.07$ . These transitions are a Floquet version of the Hopf bifurcation [114], which requires at least two continuous variables.

### 2.3.2 Open-system dynamics in the few-atom regime

#### *Numerical results from exact diagonalization*

Let us move to the few-atom regime (i.e.,  $N \sim \mathcal{O}(1)$ ), which is the case for circuit QED systems. We first consider the modulated open Dicke model with  $N = 2$  and demonstrate that the interplay between strong coupling and dissipation causes a DTC behavior<sup>1</sup> for unexpectedly long periods even in this deep quantum regime. By unexpectedly long we mean that the DTC transient lasts much longer than the decay time  $\kappa^{-1} \sim 3T$ .

We solve the Floquet-GKSL dynamics governed by Eqs. (2.1) and (2.18) using the exact diagonalization approach under a truncation up to 16 photons. Figure 2.6 (a) shows the obtained stroboscopic dynamics of the scaled angular momenta  $j_\mu$  and quadratures  $x, p$  (inset) in the strong-coupling regime, where  $\kappa = 0.05$ ,  $\epsilon = 0.1$  and  $\lambda = 1$ . The initial state is chosen to be  $|\Rightarrow\rangle \otimes |0\rangle$ , where  $|\Rightarrow\rangle \equiv \bigotimes_{j=1}^N |\rightarrow\rangle$  is the eigenstate of  $J_x$  with eigenvalue  $N/2$  ( $N = 2$ ) and  $|0\rangle$  is the photon vacuum. We clearly see that  $j_x$  and  $x$  start oscillating with a period of  $2T$  after

<sup>1</sup>In this few-body regime, we avoid using the term ‘‘DTC order’’ since an order usually refers to a property in the thermodynamic limit.

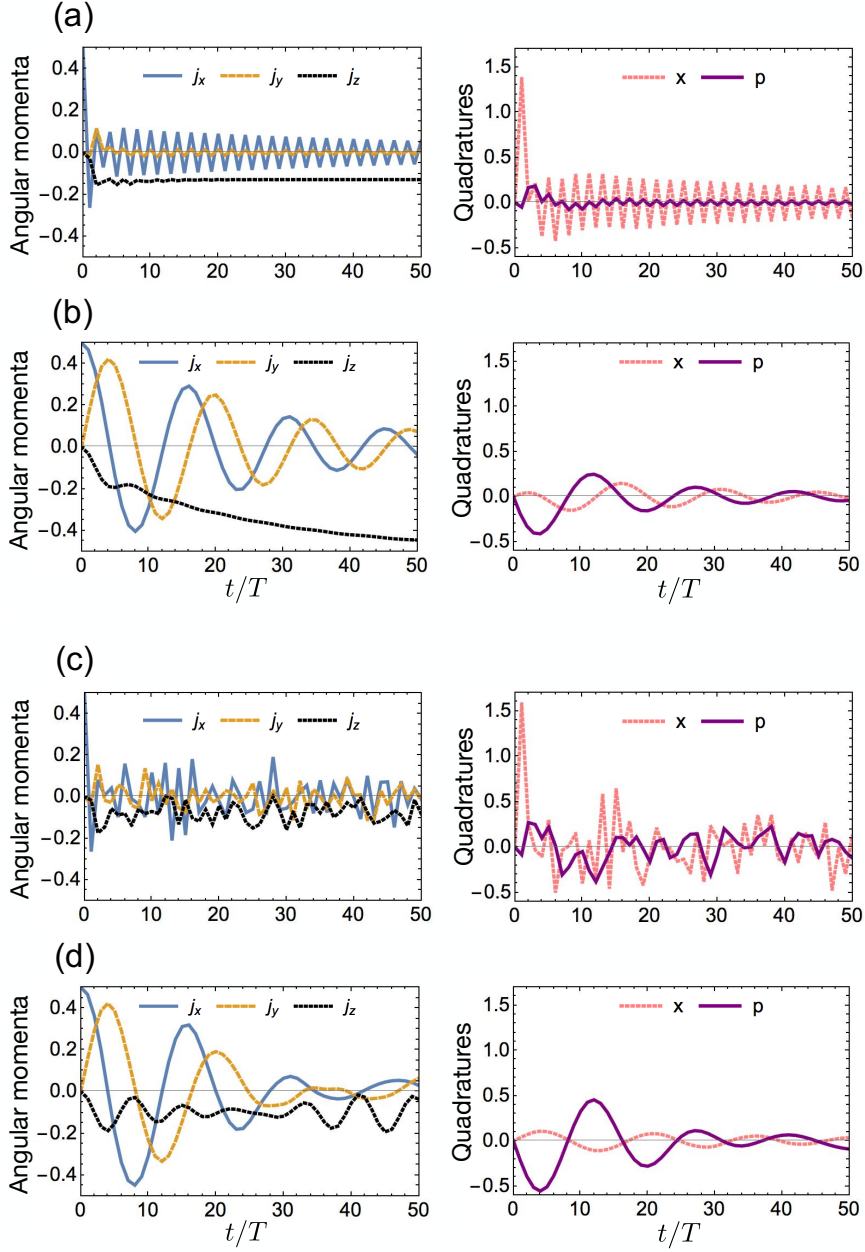


Figure 2.7: (a) Stroboscopic dissipative dynamics of the three-qubit Dicke model with  $\kappa = 0.05$ ,  $\epsilon = 0.05$  and  $\lambda = 1$  (strong coupling). Scaled angular momenta of  $j_x$  (solid),  $j_y$  (dashed),  $j_z$  (dotted), and quadratures  $x$  (dotted) and  $p$  (solid) are shown. We clearly see that the DTC order emerges. (b) Stroboscopic dissipative dynamics in the weak-coupling regime ( $\kappa = 0.05$ ,  $\epsilon = 0.05$  and  $\lambda = 0.1$ ). (c) Stroboscopic unitary dynamics ( $\kappa = 0$ ,  $\epsilon = 0.05$ , and  $\lambda = 1$ ) in the strong coupling regime. (d) Stroboscopic unitary dynamics in the weak-coupling regime ( $\kappa = 0$ ,  $\epsilon = 0.05$  and  $\lambda = 0.1$ ). In (b)-(d), no DTC order appears. The initial state is always chosen to be  $|\Rightarrow\rangle \otimes |0\rangle$ , where  $|\Rightarrow\rangle \equiv \bigotimes_{j=1}^N |\rightarrow\rangle$  is the eigenstate of  $J_x$  with eigenvalue  $N/2$  ( $N = 3$ ) and  $|0\rangle$  is the photon vacuum. Reproduced from Supplementary Fig. 5 of Ref. [34]. Copyright © 2018 by the American Physical Society.

$t \sim 5T$ , which persists even at  $t \sim 50T$ . This result shows that our strong-coupling modulated open Dicke model features a DTC transient even in the deep quantum regime before reaching the stationary state. For the sake of comparison, we show in Fig. 2.6 (b) the stroboscopic dynamics for an isolated Dicke model ( $N = 2, \kappa = 0, \epsilon = 0.1, \lambda = 1$ ) starting from the same initial state. We can see that the expectation value of each observable randomly fluctuates and does not have temporal order in contrast to its dissipative counterpart.

We note that no DTC transient emerges in the weak-coupling regime. Figure 2.6 (c) shows the Floquet dynamics for an open ( $\kappa = 0.05$ ) Dicke model with  $\epsilon = 0.1$  and  $\lambda = 0.1$ . Unlike the DTC transient in Fig. 2.7(a) with a fixed (approximate) period  $2T$  that is robust against small variations of the parameters, the low-frequency oscillation has a period around  $T/\epsilon$  which is sensitive to the detuning  $\epsilon$ . This is similar to the observation that the period doubling is fragile in noninteracting spin systems [32, 74]. A similar dynamics is found in a weakly coupled isolated Dicke system ( $\kappa = 0, \epsilon = 0.1$  and  $\lambda = 0.1$ ) as shown in Fig. 2.6 (d). Thus, neither photon loss nor strong coupling alone gives rise to the DTC transient.

So far, we have seen that, in the strong-coupling regime, the transient DTC behavior is stabilized by dissipation even for two qubits. We here demonstrate that the same feature is shared by the modulated open Dicke models with  $N = 3$ . Figure 2.7 shows time evolutions of the scaled angular momenta and quadratures for three-qubit Dicke models with different parameters (the detuning is fixed to be  $\epsilon = 0.05$ ). As shown in Fig. 2.7 (a), the transient DTC behavior emerges for the dissipative case ( $\kappa = 0.05$ ) in the strong-coupling regime ( $\lambda = 1$ ). On the other hand, no transient DTC behavior appears in the closed counterpart ( $\kappa = 0$  and  $\lambda = 1$ ), as shown in Fig. 2.7 (c). In the weak-coupling regime ( $\lambda = 0.1$ ), the dissipative ( $\kappa = 0.05$ , Fig. 2.7 (b)) and closed ( $\kappa = 0$ , Fig. 2.7 (d)) cases behave similarly to each other, both of which do not exhibit the DTC behavior.

### *Understanding the DTC behavior from the Floquet-GKSL spectrum*

As shown in the previous subsection, the transient DTC behavior of the modulated open Dicke model in the deep quantum regime emerges only in the presence of both dissipation and strong coupling. Here we present further discussions on this issue on the basis of the spectrum analysis of the Floquet-GKSL superoperator

$$\mathcal{U}_F = \hat{T} e^{\int_0^T dt \mathcal{L}(\lambda_t)}, \quad (2.34)$$

where  $\hat{T}$  denotes the time ordering.

Let  $\{u_\alpha\}_\alpha$  and  $\{|u_\alpha\rangle\}_\alpha$  be a set of eigenvalues and that of right (super)eigenvectors of  $\mathcal{U}_F$ , respectively. The vector  $|\rho_0\rangle$  representing the initial state  $\rho_0$  evolves stroboscopically as

$$|\rho_{nT}\rangle = \sum_\alpha u_\alpha^n (\tilde{u}_\alpha | \rho_0) |u_\alpha\rangle, \quad (2.35)$$

where  $|\tilde{u}_\alpha\rangle$  is the left eigenvector corresponding to  $|u_\alpha\rangle$  and the Hilbert-Schmidt inner product is defined as

$$(A|B) \equiv \text{Tr}[A^\dagger B]. \quad (2.36)$$

The eigenvector  $|u_+\rangle$  with  $u_+ = 1$  represents the stationary state of the Floquet-GKSL dynamics. If we assume that the stationary state is unique, the other eigenvectors have eigenvalues with  $|u_\alpha| < 1$  and decay exponentially due to the factor  $u_\alpha^n$ . However, if there exists a single eigenvector  $|u_-\rangle$  whose eigenvalue  $u_-$  is close to  $-1$ ,  $|\rho_{nT}\rangle$  becomes a mixture of two eigenmodes of  $|u_\pm\rangle$  for relatively large  $n$ . In this case, if we approximate the state at time  $t_n \equiv nT$  as

$$|\rho_{nT}\rangle \simeq c_+ |u_+\rangle + c_- |u_-\rangle, \quad (2.37)$$

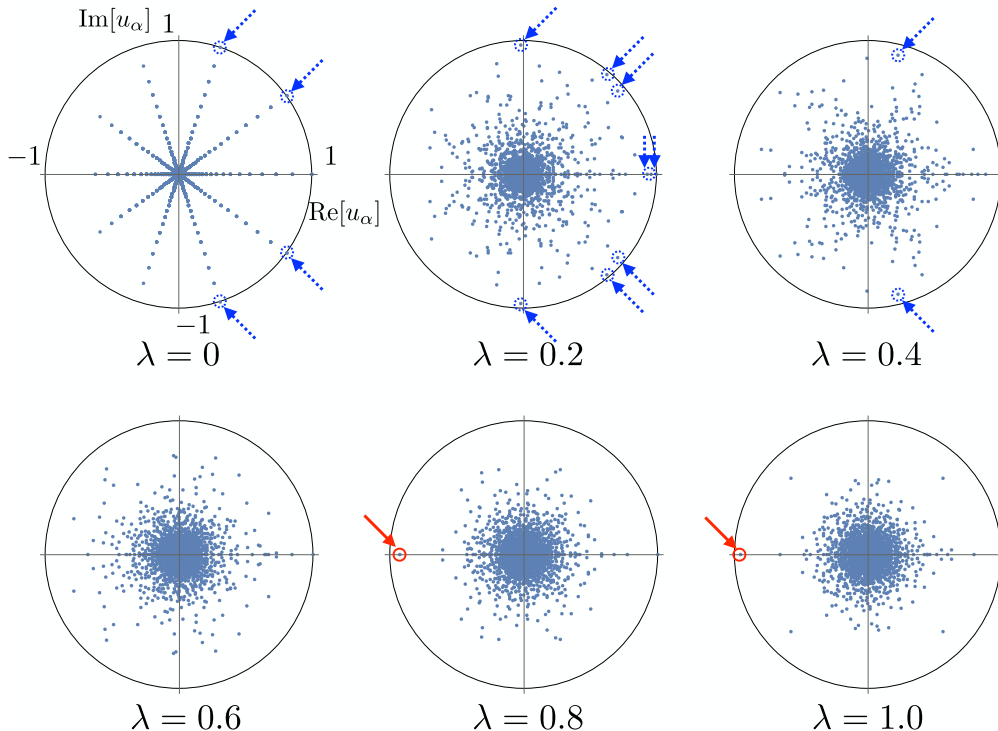


Figure 2.8: Spectra of the Floquet-GKSL superoperator  $\mathcal{U}_F$  for different coupling strength  $\lambda = 0, 0.2, 0.4, 0.6$  and  $0.8$ . Arrows show long-lived eigenmodes whose eigenvalues satisfy  $|u_\alpha| \geq 0.9$  and  $u_\alpha \neq 1$ . Note that such an eigenmode does not exist for  $\lambda = 0.6$ . As indicated by the dotted arrows, such eigenmodes are not close to  $-1$  in the weak-coupling regime ( $\lambda \leq 0.6$ ). On the other hand, in the strong-coupling regime ( $\lambda \geq 0.8$ ), there exists a single real eigenmode whose eigenvalue is close to  $-1$ , as indicated by the solid arrows. The data are obtained by the exact diagonalization method, in which we truncate the Hilbert space up to 16 photons. Reproduced from Supplementary Fig. 4 of Ref. [34]. Copyright © 2018 by the American Physical Society.

we will obtain

$$|\rho_{(n+1)T}\rangle \simeq c_+|u_+\rangle - c_-|u_-\rangle, \quad |\rho_{(n+2)T}\rangle \simeq c_+|u_+\rangle + c_-|u_-\rangle, \quad (2.38)$$

provided that the decay of  $|u_-\rangle$  is neglected. This regime exhibits the DTC behavior with a period of  $2T$ . Note that  $c_+ = 1$  if  $|u_+\rangle$  is a *normalized* steady state with the unit trace.

It is worthwhile to mention that the DTC order manifests only if we look at an *odd-parity* observable  $O$ , such as  $x$ ,  $p$ ,  $J_x$  and  $J_y$ . That is, the DTC order emerges only if we look at those observables satisfying

$$\mathcal{P}O \equiv POP = -O, \quad (2.39)$$

where  $\mathcal{P}$  is the parity operator defined in Eq. (2.4). Note that the parity operation preserves the trace, so that each odd-parity operator must be traceless. By taking the contraposition, we know that the unique steady state  $|u_+\rangle$  must feature even parity, i.e.,

$$\mathcal{P}|u_+\rangle = |u_+\rangle. \quad (2.40)$$

We can also argue that  $|u_-\rangle$  is an odd-parity operator, i.e.,

$$\mathcal{P}|u_-\rangle = -|u_-\rangle, \quad (2.41)$$

from the perspective of continuous deformation of  $\mathcal{U}_F$  from the ideal form  $\mathcal{P}e^{\mathcal{L}(\lambda)T/2}$  and the discrete nature of parity eigenvalues. Therefore,  $|u_+\rangle$  contributes nothing to  $\langle O \rangle$  and only  $|u_-\rangle$  in Eq. (2.38) contributes a finite expectation value and thus gives rise to the DTC order. On the other hand, the expectation of an even-parity operator, such as  $n = a^\dagger a$  and  $J_z$ , stays unchanged during the stroboscopic evolution given by Eq. (2.38), since only  $|u_+\rangle$  contributes a finite value but the coefficient does not flip its sign after a period.

Figure 2.8 shows the spectra of  $\mathcal{U}_F$  for different coupling strength  $\lambda$ . The other parameters are fixed to be  $\kappa = 0.05$  and  $\epsilon = 0.1$ . Arrows in Fig. 2.8 show long-lived eigenmodes whose eigenvalues satisfy  $|u_\alpha| \geq 0.9$  and  $u_\alpha \neq 1$ . As indicated by the dotted arrows, such eigenmodes are not close to  $-1$  in the weak-coupling regime ( $\lambda \leq 0.6$ ). We note that the approximated ten-fold rotation symmetry of the spectrum for  $\lambda = 0$  is due to the specific choice  $\epsilon = 0.1$  ( $\epsilon^{-1} = 10$ ). On the other hand, in the strong-coupling regime ( $\lambda \geq 0.8$ ), there exists a single real eigenmode whose eigenvalue is close to  $-1$ , as indicated by solid arrows. This eigenmode corresponds to  $|u_-\rangle$  above and contributes to the transient DTC behavior.

## 2.4 General phenomenology

With all the obtained numerical results in mind, we are now in a position to establish a general phenomenology for such open-system DTCs. This phenomenological theory, which is derived from the modulated open Dicke model by eliminating the atomic degrees of freedom, turns out to be the Floquet-GKSL generalization of the scalar-field Landau theory in  $0 + 1$  dimension. We call this theory the *Floquet-GKSL-Landau* theory and expect it to capture the general qualitative features of a wide class of Floquet open systems in addition to the Dicke model. We demonstrate within this theory that the lifetime of the DTC order increases *exponentially* with respect to the system size.

### 2.4.1 Floquet-GKSL-Landau theory

#### *Semiclassical derivation*

We first derive the effective dynamics of the photon degree of freedom on the basis of a semiclassical argument. Recall that the semiclassical equation of motion is given by Eq. (2.26). Assuming that  $\omega_0 \gg \omega$ , we expect that the atomic degrees of freedom will soon equilibrate ( $\dot{j}_\mu = 0$ ,  $\mu = x, y, z$ ) upon a small change in the photon degree of freedom. In this case,  $j_x$  can be estimated from  $x$  via

$$j_x = -\frac{\lambda\sqrt{2\omega x}}{\sqrt{\omega_0^2 + 8\omega\lambda^2 x^2}}. \quad (2.42)$$

Note that the minus sign comes from the assumption that  $j_z < 0$ , which can be justified by a low-energy atomic state like  $j_z = -1/2$  at the initial time. Substituting Eq. (2.42) into the first two equations in Eq. (2.26) yields a closed equation of motion in terms of  $x$  and  $p$  alone:

$$\dot{p} = -\omega^2 x - \frac{\kappa}{2} p + \frac{4\lambda^2 \omega x}{\sqrt{\omega_0^2 + 8\omega\lambda^2 x^2}}, \quad \dot{x} = p - \frac{\kappa}{2} x. \quad (2.43)$$

If  $8\omega\lambda^2 x^2 \ll \omega_0^2$ , which turns out to be equivalent to  $\lambda \simeq \lambda_c$  (since  $x \sim (\lambda\omega_0/\lambda_c^2\sqrt{\omega})\sqrt{1 - \lambda_c^4/\lambda^4}$ ), Eq. (2.43) can well be approximated by

$$\dot{p} = -\omega^2 x - \frac{\kappa}{2} p + \frac{4\lambda^2 \omega}{\omega_0} x - \frac{16\lambda^4 \omega^2}{\omega_0^3} x^3, \quad \dot{x} = p - \frac{\kappa}{2} x, \quad (2.44)$$

from which we can infer that the corresponding Lindblad master equation is given by

$$\dot{\rho}_t = -i \left[ \omega a^\dagger a - \frac{\lambda^2}{\omega_0} (a^\dagger + a)^2 + \frac{\lambda^4}{\omega_0^3 N} (a^\dagger + a)^4, \rho \right] + \kappa \mathcal{D}[a] \rho_t. \quad (2.45)$$

With  $\lambda$  replaced by  $\lambda_t = \lambda_{t+T}$ , the above equation describes the dissipative and Floquet counterpart of the well-known Landau theory. In this sense, while derived from the open Dicke model, the general form of Eq. (2.45)

$$\dot{\rho}_t = -i[H_L, \rho_t] + \kappa \mathcal{D}[a] \rho_t, \quad H_L = \omega a^\dagger a - \frac{\Omega_2}{4} (a^\dagger + a)^2 + \frac{\Omega_4}{32N} (a^\dagger + a)^4 \quad (2.46)$$

should widely be applicable to periodically driven single-mode open quantum systems. It is worth mentioning that Eq. (2.46) features a parity symmetry with respect to  $P_a = e^{i\pi a^\dagger a}$ .

### **Consistency check based on adiabatic elimination**

A result consistent with Eq. (2.45) can be obtained by using adiabatic elimination, which is a purely quantum treatment. To do this, we first write down the Dicke Hamiltonian

$$H = \omega a^\dagger a + \omega_0 b^\dagger b + \lambda (a^\dagger + a) \left( b^\dagger \sqrt{1 - \frac{b^\dagger b}{N}} + \sqrt{1 - \frac{b^\dagger b}{N}} b \right) - \frac{N}{2} \omega_0, \quad (2.47)$$

which can be approximated as

$$H = \omega a^\dagger a + \omega_0 b^\dagger b + \lambda (a^\dagger + a) (b^\dagger + b) - \frac{\lambda}{2N} (a^\dagger + a) (b^{\dagger 2} b + b^\dagger b^2) \quad (2.48)$$

if  $b^\dagger b \ll N$ , i.e., almost all the atoms are at their ground states. In the case of  $\omega \ll \omega_0$  and starting from the ground state  $|0\rangle_b$  of the atomic ensemble, the creation of an atomic excitation is expected to be blocked by a large energy discrepancy. The task of adiabatic elimination is nothing but to find out an effective Hamiltonian  $H_a$  of the photon field alone, which satisfies

$$e^{-iH_a t} \simeq {}_b\langle 0 | e^{-iHt} | 0 \rangle_b. \quad (2.49)$$

This problem is more conveniently solved in the frequency domain by using the Green's-function formalism and the Dyson equation

$$G(\Omega)^{-1} = G_0(\Omega)^{-1} - \Sigma(\Omega), \quad (2.50)$$

where  $G(\Omega) = {}_b\langle 0 | (\Omega - H + i0^+)^{-1} | 0 \rangle_b$  is the photon Green's function in the presence of an interaction,  $G_0(\Omega) = (\Omega - \omega a^\dagger a + i0^+)^{-1}$  is the free photon Green's function and  $\Sigma(\Omega)$  is the self-energy, which can be perturbatively computed by summing up the contribution from irreducible virtual processes (see Fig. 2.9). The leading-order contribution arises from the virtual process of single atomic excitation and is given by

$$\Sigma_1(\Omega) = {}_b\langle 0 | V_{01} G_{b0}(\Omega) V_{10} | 0 \rangle_b = \frac{\lambda^2}{\Omega - \omega_0} (a^\dagger + a)^2, \quad (2.51)$$

where  $V_{10} = V_{01}^\dagger = \lambda(a^\dagger + a)b^\dagger$  and  $G_{b0}(\Omega) = (\Omega - \omega_0 b^\dagger b + i0^+)^{-1}$  is the free Green's function of atoms. Note that in Eq. (2.51) the term  $i0^+$  can be neglected since typically  $\Omega \ll \omega_0$ . The

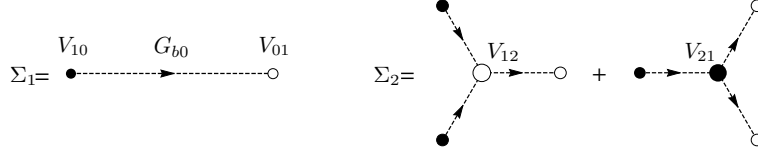


Figure 2.9: Diagrammatic illustration of the single (left) and double (right) atomic excitation virtual processes. The creation, annihilation and free propagation of an atomic excitation are represented as a filled dot, an open dot and a dashed line, respectively. The larger open (filled) dot refers to the coalescence of two atomic excitations (the split of an atomic excitation). Reproduced from Supplementary Fig. 6 of Ref. [34]. Copyright © 2018 by the American Physical Society.

subleading-order contribution arises from the virtual process of two atomic excitation and is given by

$$\begin{aligned}\Sigma_2(\Omega) &= {}_b\langle 0|(V_{01}G_{b0}(\Omega)V_{12}G_{b0}(\Omega)V_{10}G_{b0}(\Omega)V_{10} + V_{01}G_{b0}(\Omega)V_{01}G_{b0}(\Omega)V_{21}G_{b0}(\Omega)V_{10})|0\rangle_b \\ &= -\frac{2\lambda^3}{N(\Omega - \omega_0)^2(\Omega - 2\omega_0)}(a^\dagger + a)^4,\end{aligned}\quad (2.52)$$

where  $V_{21} = V_{12}^\dagger = -\frac{\lambda}{2N}(a^\dagger + a)b^{\dagger 2}b$  and the factor of 2 in the numerator results from

$${}_b\langle 0|b^2b^{\dagger 2}bb^\dagger|0\rangle_b = {}_b\langle 0|bb^\dagger b^2b^{\dagger 2}|0\rangle_b = 2. \quad (2.53)$$

Since  $\Omega \sim \omega \ll \omega_0$ , we can safely approximate  $\Sigma_{1,2}(\Omega)$  by  $\Sigma_{1,2}(0)$  to obtain an effective Hamiltonian

$$H_a = H_{a0} + \Sigma_1(0) + \Sigma_2(0) = \omega a^\dagger a - \frac{\lambda^2}{\omega_0}(a^\dagger + a)^2 + \frac{\lambda^4}{\omega_0^3 N}(a^\dagger + a)^4, \quad (2.54)$$

which coincides with the unitary part in Eq. (2.45).

### Mean-field analysis

On the mean-field level, Eq. (2.46) implies the following equation of motion of  $\alpha \equiv \langle a \rangle$ :

$$i\partial_t \alpha = \left(\omega - i\frac{\kappa}{2}\right)\alpha - \Omega_2 \text{Re } \alpha + \frac{\Omega_4}{N}(\text{Re } \alpha)^3, \quad (2.55)$$

which can be rewritten as

$$i\partial_t \tilde{\alpha} = \left(\omega - i\frac{\kappa}{2}\right)\tilde{\alpha} - \Omega_2 \text{Re } \tilde{\alpha} + \Omega_4(\text{Re } \tilde{\alpha})^3 \quad (2.56)$$

after the rescaling  $\tilde{\alpha} \equiv \alpha/\sqrt{N}$ . In addition to  $\tilde{\alpha}_0 = 0$ , when  $\Omega_2 > \Omega_c = \omega + \frac{\kappa^2}{4\omega}$ , Eq. (2.56) has two fixed points

$$\tilde{\alpha}_0 = \pm \left(1 + \frac{i\kappa}{2\omega}\right) \sqrt{\frac{\Omega_2 - \Omega_c}{\Omega_4}}, \quad (2.57)$$

near which the semiclassical equation of motion (2.56) can be linearized to give

$$i\partial_t \delta\tilde{\alpha} = \left(\omega - i\frac{\kappa}{2}\right)\delta\tilde{\alpha} + [3\Omega_4(\text{Re } \tilde{\alpha}_0)^2 - \Omega_2]\text{Re } \delta\tilde{\alpha}. \quad (2.58)$$

The two eigenvalues of Eq. (2.58) read

$$\lambda_{\pm} = -\frac{1}{2}[\kappa \pm \sqrt{\kappa^2 - 8\omega(\Omega_2 - \Omega_c)}], \quad (2.59)$$

which are both negative when  $\Omega_2 > \Omega_c$ , implying the stability of the two fixed points (2.57). Replacing  $\lambda$  with  $\lambda_t = \lambda_{t+T}$ , we may expect that the lifetime of the damping mode besides the DTC mode is  $\mathcal{O}(\kappa^{-1})$ . After a similar linearization-based analysis, we can obtain the two eigenfrequencies of the damping modes near  $\tilde{\alpha} = 0$  to be

$$\lambda'_{\pm} = -\frac{1}{2}[\kappa \pm \sqrt{\kappa^2 + 4\omega(\Omega_2 - \Omega_c)}]. \quad (2.60)$$

As expected, both of  $\lambda'_{\pm}$  are negative ( $\lambda'_-$  becomes positive) when  $\Omega_2 < \Omega_c$  ( $\Omega_2 > \Omega_c$ ), implying the stability (instability) of the fixed point  $\tilde{\alpha} = 0$ .

We note that Eq. (2.57) can be used to perform a self-consistent check to justify the adiabatic elimination. Substituting  $\Omega_2 = 4\lambda^2/\omega_0$  and  $\Omega_4 = 2\Omega_2^2/\omega_0$  into Eq. (2.57), we obtain

$$|\tilde{\alpha}_0|^2 = \frac{\omega_0}{2\omega}\mu(1 - \mu), \quad (2.61)$$

where  $\mu = \lambda_c^2/\lambda^2$  with  $\lambda_c = (1/2)\sqrt{(\omega_0/\omega)(\omega^2 + \kappa^2/4)}$ . While this result (2.61) differs generally from the order parameter  $|\tilde{\alpha}|^2 = \omega_0(\mu^{-1} - \mu)/(4\omega)$  in the original Dicke model (cf. Eq. (2.14)), they do coincide near  $\lambda = \lambda_c$  or  $\mu = 1$ . This provides a piece of evidence that the effective theory does give a good approximation of the Dicke model in certain limits.

## 2.4.2 Scaling of the DTC lifetime

### *Numerical calculation by exact diagonalization*

The above mean-field analysis should become exact in the large- $N$  limit and can help us map out the dynamical phase diagram, just like what we did for the modulated Dicke model. On the other hand, it cannot tell us how the lifetime of the DTC mode scales with respect to  $N$ , which is a particularly important question of our concern. A natural expectation is that the lifetime becomes *exponentially* long with increasing  $N$ , since the underlying dissipative phase transition features an exponentially small damping gap [116]. However, it is highly nontrivial to find whether this is the case even in a Floquet open system. It turns out to be difficult to handle this problem numerically in the original modulated open Dicke model with both atomic and photonic degrees of freedom. This difficulty emphasizes the importance of scalable circuit-QED-based quantum simulation with up to tens of qubits [117], as we will discuss in the next section. Nevertheless, we can gain qualitative insights by considering the previously derived Floquet-GKSL-Landau theory:

$$\begin{aligned} \frac{d\rho_t}{dt} &= -i[H_L(\Omega_2(t), \Omega_4(t)), \rho_t] + \kappa\mathcal{D}[a]\rho_t, \\ H_L(\Omega_2, \Omega_4) &= \omega a^\dagger a - \frac{\Omega_2}{4}(a^\dagger + a)^2 + \frac{\Omega_4}{32N}(a^\dagger + a)^4. \end{aligned} \quad (2.62)$$

This model is numerically much more tractable since there is only the photon field with no atomic degrees of freedom.

To investigate the lifetime scaling of the DTC mode, we employ the exact diagonalization method, by means of which it is more convenient to rewrite the original GKSL equation in Eq. (2.62) into

$$\dot{\rho}_t = -i(H_{\text{eff}}\rho_t - \rho_t H_{\text{eff}}^\dagger) + \kappa a \rho_t a^\dagger. \quad (2.63)$$



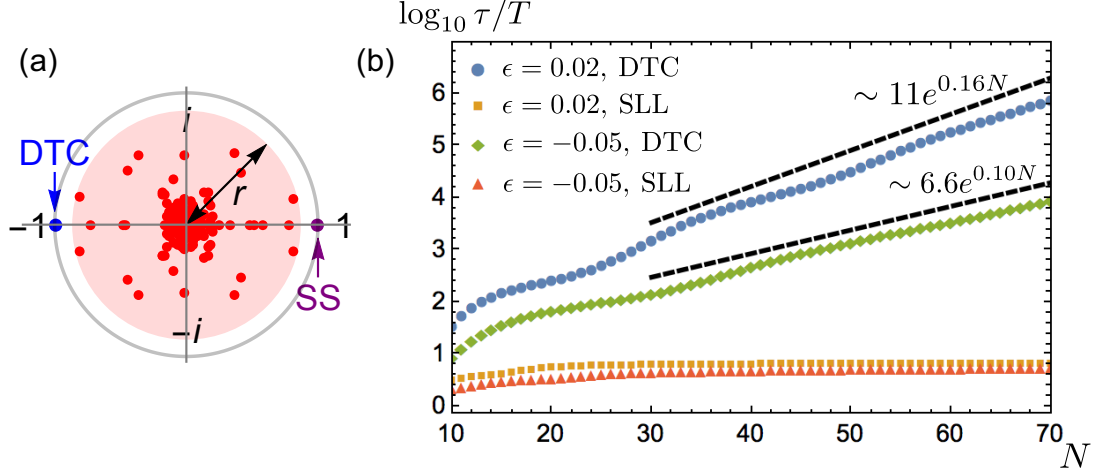


Figure 2.10: (a) Typical Floquet-GKSL spectrum of an open-system DTC. The DTC mode and the steady state (SS) locate at  $-1 + \delta$  and  $1$ , respectively, with  $\delta \sim \mathcal{O}(e^{-cN})$ . The other modes locate in a disk (shaded) with radius  $r < 1$  for  $\forall N$ , so that their lifetime is bounded by a constant  $-T/\ln r$ . (b) Finite-size scaling for the lifetime  $\tau = -T/\ln(1 - \delta)$  of the DTC and the second longest-lived (SLL) modes in the Floquet-GKSL-Landau model (2.62) for  $\epsilon = 0.02$  and  $-0.05$ . Reproduced from Fig. 4 of Ref. [34]. Copyright © 2018 by the American Physical Society.

Here the non-Hermitian effective Hamiltonian is given by

$$\begin{aligned}
 H_{\text{eff}} = & \left( \omega - \frac{\Omega_2}{2} - i\frac{\kappa}{2} \right) n + \frac{3\Omega_4}{16N} n(n+1) + \left( \frac{3\Omega_4}{16N} - \frac{\Omega_2}{4} \right) (a^{\dagger 2} + a^2) \\
 & + \frac{\Omega_4}{8N} (a^{\dagger 2} n + n a^2) + \frac{\Omega_4}{32N} (a^{\dagger 4} + a^4),
 \end{aligned} \tag{2.64}$$

where the time arguments of  $\Omega_2$  and  $\Omega_4$  are dropped for simplicity. In addition, we have to truncate the Hilbert space up to a  $|n_{\text{max}}\rangle$  to make its dimension finite. While we expect that the profile of the Floquet steady state (approximately a Poisson distribution in the Fock space) is reliable as long as  $n_{\text{max}} \gtrsim 2|\alpha_0|^2$ , it is not clear whether the exponentially long lifetime could be reliable. Nevertheless, we can certify the precision by changing  $n_{\text{max}}$  in actual numerical calculations, and we have indeed confirmed the convergence.

In practice, we can perform exact diagonalization independently for the odd and even parity sectors, since Eq. (2.62) respects the parity symmetry. To be concrete, if we choose the basis to be  $|n\rangle\langle m|$  with  $|m\rangle$  and  $|n\rangle$  being photon Fock states, then the GKSL generator in Eq. (2.62) never mixes the sector having odd  $m+n$  (odd parity) with that having even  $m+n$  (even parity). This is true also for the Floquet-GKSL superoperator. In particular, the steady state (DTC mode) can be found by diagonalizing the even-parity (odd-parity) sector. Using this approach, we carry out numerical calculations for a specific protocol

$$\Omega_4(t) = \Omega_2(t) = \Omega_2(t+T) = \begin{cases} 1.5\omega, & 0 \leq t < \frac{\pi}{\omega}; \\ 0, & \frac{\pi}{\omega} \leq t < T = (2 - \epsilon)\frac{\pi}{\omega}, \end{cases} \tag{2.65}$$

and  $\kappa = 0.05\omega$ . The results are presented in Fig. 2.10.

As illustrated in Fig. 2.10 (a), the spectrum of the Floquet-GKSL superoperator for Eq. (2.62) indeed has a DTC mode near  $-1$  under some appropriately chosen parameters, which is similar

to the case of the Dicke model (see Fig. 2.8). In Fig. 2.10 (b), we show the lifetime of the DTC (longest-lived) and that of the second longest-lived mode (except for the steady state). We do find an exponential scaling of the lifetime of the DTC order with respect to  $N$  and the saturation of the lifetime of the second longest-lived mode. Note that the lifetime of a one-dimensional many-body localized DTC obeys the same exponential scaling in the system size [69], although the mechanism of DTC order is different [28, 29, 73, 74].

### *Possible phenomenology for the asymmetric DTC behavior*

We have performed yet another finite-size scaling analysis for a large imperfection  $\epsilon = 0.12$ , the semiclassical dynamics of which exhibits an asymmetric DTC behavior. As shown in Figs. 2.11 (a) and (b), in addition to the exponentially long-lived DTC mode, the second longest-lived mode turns out to possess a relatively long lifetime that scales linearly with respect to  $N$ . In Fig. 2.11 (c) we also present the stroboscopic dynamics of the rescaled quadratures starting from a coherent state (cf. Eq. (2.16))  $\rho_0 = |\alpha\rangle\langle\alpha|$  with  $\alpha = \sqrt{N/5} + \sqrt{N/10}i$ . The dynamics turns out to be the relaxation of an asymmetric DTC (ADTC) behavior to the usual symmetric DTC order. Since the life time of the transient ADTC behavior seems to be consistent with that of the second longest-lived mode, it is natural to expect the latter to give rise to the former. In the thermodynamic limit, the second longest-lived mode persists and so does the ADTC behavior.

To establish a possible phenomenology for the ADTC behavior, it is constructive to look at the full Floquet-GKSL spectrum (see Fig. 2.11 (d)). After an intermediately large number of periods, e.g.,  $n \sim \mathcal{O}(\sqrt{N})$ , we can well approximate the state of the system by

$$|\rho_{nT}\rangle \simeq |\rho_{ss}\rangle + c_D|\sigma_D\rangle + c_O|\sigma_O\rangle + c_E|\sigma_E\rangle, \quad (2.66)$$

where  $|\rho_{ss}\rangle$ ,  $|\sigma_D\rangle$ ,  $|\sigma_O\rangle$  and  $|\sigma_E\rangle$  are the steady state, the DTC mode, the second longest-lived mode in the odd-parity sector parity and the longest-lived mode in the even-parity sector, respectively. As indicated by Fig. 2.11 (d), the eigenvalues of  $|\sigma_O\rangle$  and  $|\sigma_E\rangle$  are almost symmetric with respect to the imaginary axis, implying that their lifetimes are nearly the same. More information of these four eigenmodes is summarized in Table 4.1. After a single period, the state of the system (2.66) evolves into

$$|\rho_{(n+1)T}\rangle \simeq |\rho_{ss}\rangle - c_D|\sigma_D\rangle + c_O|\sigma_O\rangle - c_E|\sigma_E\rangle. \quad (2.67)$$

Note that the coefficient of  $|\sigma_O\rangle$  does not flip the sign and thus serves as a basis for the DTC order resulting from  $|\sigma_D\rangle$  when we look at an odd-parity observable. Furthermore, we can infer from Eqs. (2.66) and (2.67) that the ADTC behavior emerges also in an even-parity observable, lasting for a time of the order of  $N$  before eventually relaxing to a constant instead of an exponentially long symmetric DTC order. In fact, this expectation has already been vindicated in the stroboscopic dynamics of  $j_z$  in the top right panel in Fig. 2.2 as well as that in the rightmost panel in Fig. 2.4.

## 2.5 Experimental implementations

We here discuss concrete experimental implementation of the modulated open Dicke model in a cavity QED setup and its variation in a circuit QED setup. The main ideas are schematically illustrated in Fig. 2.12.

### 2.5.1 Cavity QED setup based on four-level atoms

It is known that, as a result of the Thomas-Reiche-Kuhn sum rule, the Dicke phase transition is always killed by the  $A^2$  term in an equilibrium cavity QED setup [89]. However, the influence of

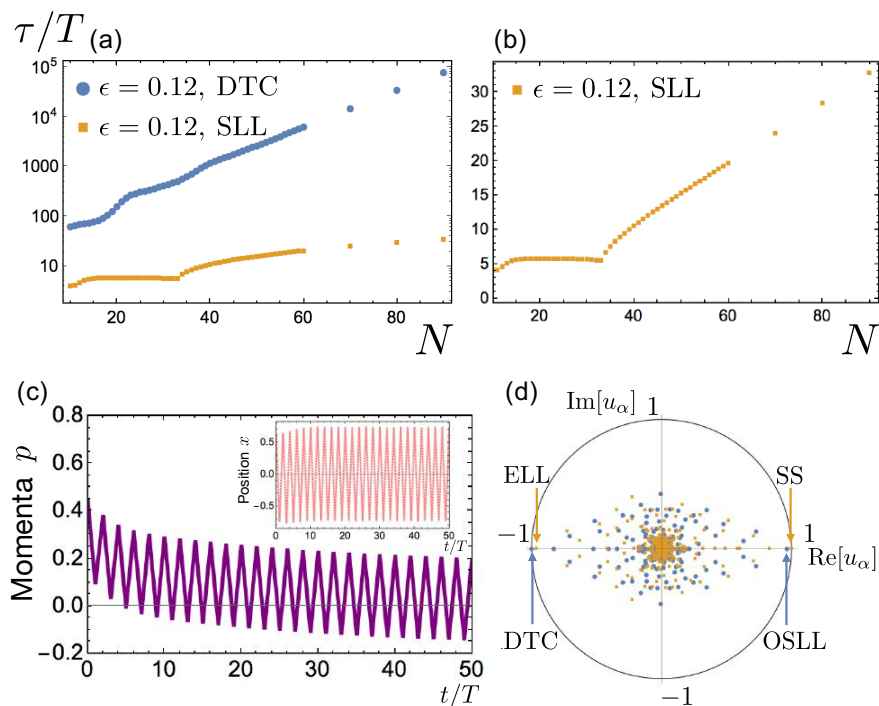


Figure 2.11: (a) Finite-size scaling for the lifetime of the DTC mode and that of the second longest-lived mode in the Floquet-GKSL-Landau model with the protocol in Eq. (2.65) with  $\epsilon = 0.12$ . (b) Same as (a) but the vertical axis is in the normal scale rather than the logarithmic scale. (c) Stroboscopic dynamics of rescaled quadratures  $p = i\langle a^\dagger - a \rangle / \sqrt{2N}$  and  $x = \langle a^\dagger + a \rangle / \sqrt{2N}$  (inset) starting from a coherent state. The parameters are the same as those in (a) but with  $N$  fixed to be 80 and the photon truncation is  $n_{\max} = 81$ . (d) Spectrum of the Floquet-GKSL superoperator for the system in (c). The eigenvalues belonging to the odd (even) sector are marked in blue (orange). Reproduced from Supplementary Fig. 7 of Ref. [34]. Copyright © 2018 by the American Physical Society.

Table 2.1: Properties of several important Floquet-GKSL eigenmodes, including the steady state (SS), the discrete time-crystalline (DTC) mode, the second longest-lived mode in the odd-parity sector (OSLL), and the longest-lived mode in the even-parity sector (ELL). We use the symbol “ $\sim$ ” to indicate the eventual decay of the mode after a long time.

State	Parity	Eigenvalue	Odd-parity observable	Even-parity observable
SS	+	1	0	const.
DTC	-	$-1 + \mathcal{O}(e^{-cN})$	$\sim + - + - \dots$	0
OSLL	-	$1 - \mathcal{O}(N^{-1})$	$\sim \text{const.}$	0
ELL	+	$-1 + \mathcal{O}(N^{-1})$	0	$\sim + - + - \dots$

the  $A^2$  term can be neglected in the rotating frame in an intrinsically nonequilibrium setup based on the Raman transition, as pointed out in Ref. [102]. Such a proposal was first realized by using the atomic motional degrees of freedom [91], which correspond to a fixed  $\omega_0 \sim 2\pi \times 10$  kHz. This is not suitable for our proposal, since  $\omega_0 \ll \omega \sim 2\pi \times 10$  MHz and the parity operator cannot be generated even approximately.<sup>2</sup> Instead, we suggest that the experiment reported in Ref. [94], which is based fully on atomic internal states, might be an appropriate implementation of our proposal, where  $\omega_0$ ,  $\omega$  and  $\lambda$  are all of the same order of magnitude ( $\sim 2\pi \times 1$  MHz).

We first summarize the main results in Ref. [102]. Consider an ensemble of four-level atoms in an optical cavity with frequency  $\omega_c$ . The four levels consist of two ground states  $|\downarrow\rangle$ ,  $|\uparrow\rangle$  and two excited states  $|e_0\rangle$ ,  $|e_1\rangle$ , whose frequencies are 0,  $\omega_1$ ,  $\omega_{a0}$  and  $\omega_{a1}$ , respectively. As shown in the upper half in Fig. 2.12, the cavity mode interacts with the atom via the dipole transitions  $|\downarrow\rangle \leftrightarrow |e_0\rangle$  and  $|\uparrow\rangle \leftrightarrow |e_1\rangle$  with single-photon Rabi frequencies  $g_0$  and  $g_1$ . Two additional classical driving lasers  $(\omega_{L0}, \Omega_0)$  and  $(\omega_{L1}, \Omega_1)$  are applied to couple  $|\uparrow\rangle \leftrightarrow |e_0\rangle$  and  $|\downarrow\rangle \leftrightarrow |e_1\rangle$ , respectively. The frequencies satisfy

$$\omega_{L1} - \omega_{L0} \simeq 2\omega_1, \quad \omega_{L1} + \omega_{L0} \simeq 2\omega_c \quad (2.68)$$

in order to dramatically reduce the effective  $\omega$  and  $\omega_0$  in an appropriately chosen rotating frame. The detunings

$$\Delta_0 \equiv \omega_{a0} - \frac{1}{2}(\omega_{L0} + \omega_{L1}), \quad \Delta_1 \equiv \omega_{a1} - \omega_{L1} \quad (2.69)$$

are assumed to be so large that the excited-state manifold can be adiabatically eliminated. In this case, the effective Hamiltonian reads

$$H_{\text{eff}} = \hbar\omega a^\dagger a + \hbar\omega_0 J_z + \hbar\delta a^\dagger a J_z + \frac{1}{\sqrt{N}}\hbar\lambda(a^\dagger J_- + a J_+) + \frac{1}{\sqrt{N}}\hbar\lambda'(a J_- + a^\dagger J_+), \quad (2.70)$$

where the parameters are given by

$$\begin{aligned} \omega &= \omega_c - \frac{1}{2}(\omega_{L1} + \omega_{L0}) + \frac{N}{2} \left( \frac{g_0^2}{\Delta_0} + \frac{g_1^2}{\Delta_1} \right), \\ \omega_0 &= \omega_1 - \frac{1}{2}(\omega_{L1} - \omega_{L0}) + \frac{1}{4} \left( \frac{\Omega_0^2}{\Delta_0} - \frac{\Omega_1^2}{\Delta_1} \right), \\ \delta &= \frac{g_0^2}{\Delta_0} - \frac{g_1^2}{\Delta_1}, \quad \lambda = \frac{\sqrt{N}g_0\Omega_0}{2\Delta_0}, \quad \lambda' = \frac{\sqrt{N}g_1\Omega_1}{2\Delta_1}. \end{aligned} \quad (2.71)$$

If we take an  $A^2$  term  $D(a + a^\dagger)^2$  into account, the only difference is a small shift in  $\omega$  by  $2D$ , which plays no role since  $\omega$  is tunable via changing  $\omega_{L1}$  and  $\omega_{L2}$ . The Dicke Hamiltonian can be obtained from Eq. (2.70) by fine-tuning the parameters of the external driving lasers such that  $\delta = 0$  and  $\lambda = \lambda'$ . Note that  $N \sim 10^5$  is also a tunable quantity. We therefore have enough degrees of freedom to independently control all the three parameters  $\omega$ ,  $\omega_0$  and  $\lambda$  for the same cavity (with fixed  $g_0$ ,  $g_1$ ,  $\omega_c$  and  $\kappa$ ).

To switch off the interaction in such a setup, we only have to switch off the driving lasers, corresponding to  $\Omega_0 = \Omega_1 = 0$  and thus  $\lambda = \lambda' = 0$ . Note that  $\omega$  and  $\omega_1$  stay unchanged, since  $\omega$  is independent of  $\Omega_{0,1}$  and  $\omega_0 = \omega_1 - (\omega_{L1} - \omega_{L2})/2$ , provided that  $\delta = 0$  and  $\lambda = \lambda'$  are satisfied. Therefore, by simply switching on and off the external driving lasers as shown in the upper half in Fig. 2.12, we can realize the modulated open Dicke model.

<sup>2</sup>However, this regime might be relevant to the Lipkin-Meshkov-Glick model, which also supports the DTC order by periodically switching off the all-to-all coupling [82]. Furthermore, Fig. 4 in Ref. [92] seems to suggest the possibility to realize the DTC order in this regime.

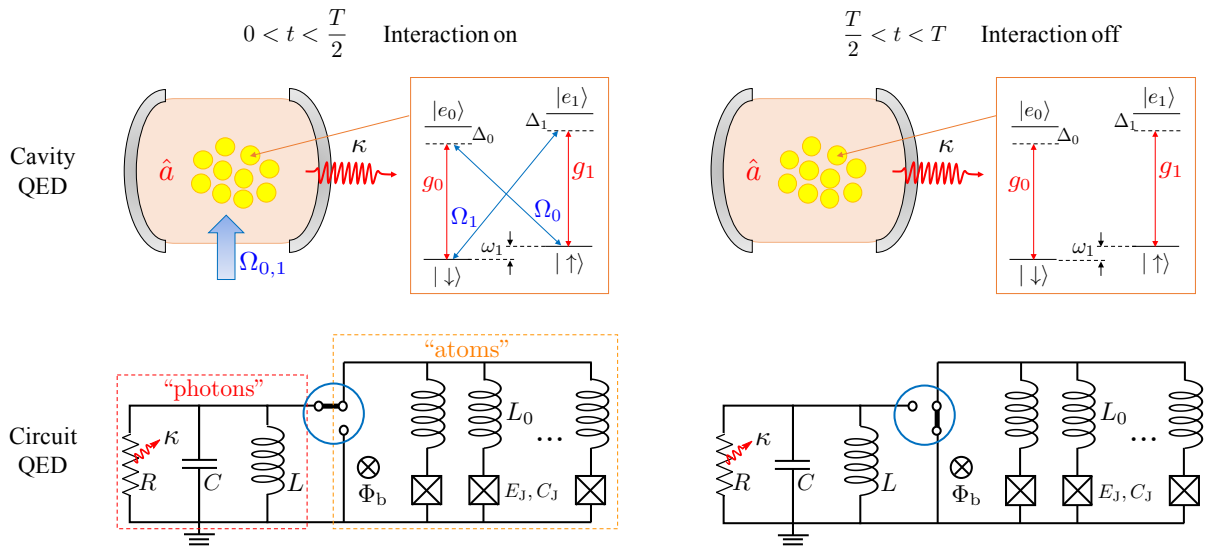


Figure 2.12: Detailed implementations of the modulated Dicke model and its variation in the cavity (upper half) and circuit (lower half) QED systems. In the former case, the light-atom coupling is a Raman process assisted by excited states of four-level atoms. The coupling can be switched off if one stops shining the external driving lasers  $\Omega_{0,1}$ . In the latter case, the light-atom coupling is simulated by inductive coupling between an  $LCR$  circuit (analogy of microwave photons with loss) and an array of Josephson oscillators (artificial atoms). The coupling can be turned off through a three-way switch (marked by blue circles). Reproduced from Supplementary Fig. 8 of Ref. [34]. Copyright © 2018 by the American Physical Society.

### 2.5.2 Circuit QED setup based on inductive coupling

As for the circuit QED setup based on superconducting qubits, we note that, due to the absence of the Thomas-Reiche-Kuhn sum rule for the capacitive coupling, the  $A^2$  term could be negligible in the strong-coupling regime without entering the rotating frame of reference [96] (although still controversial [97, 99]). For the inductive coupling, while the Dicke phase transition has not yet been experimentally observed in superconducting circuits, the beyond-ultrastrong coupling has recently been realized for a single flux qubit [101]. In a similar setup, the transient DTC behavior might be observable by fine-tuning the parameters and scaling up the number of superconducting qubits.

To be concrete, we discuss how to simulate a variation of the modulated open Dicke model by slightly modifying a circuit proposed in Ref. [100], which has been demonstrated to exhibit a superradiant phase transition. As shown in the lower half in Fig. 2.12, an  $LCR$  circuit, which corresponds to a lossy “photon” mode with frequency  $\omega = (LC)^{-\frac{1}{2}}$  and decay rate  $\kappa = (RC)^{-1}$ , is integrated with an array of  $N$  Josephson oscillators sharing the same flux bias  $\Phi_b = \Phi_0/2$  (where  $\Phi_0 \equiv h/(2e)$  is the flux quantum). The “light-atom” coupling can be turned on/off via a three-way switch (marked by blue circles). If the photon-like and atom-like circuits are coupled, the Hamiltonian reads

$$H_1 = \frac{Q^2}{2C} + \frac{\Psi^2}{2L} + \sum_{j=1}^N \left[ \frac{q_j^2}{2C_J} + \frac{(\psi_j - \Psi)^2}{2L_0} + E_J \cos\left(\frac{2\pi\psi_j}{\Phi_0}\right) \right], \quad (2.72)$$

where the charge operator  $Q$  ( $q_j$ ) and the flux operator  $\Psi$  ( $\psi_j$ ) of the  $LCR$  circuit (the  $j$ th artificial atom) satisfy  $[\Psi, Q] = i\hbar$  ( $[\psi_j, q_k] = i\hbar\delta_{jk}$ ),  $C_J$  is the capacity of the Josephson junction and  $E_J$  is the Josephson energy. The *plus* sign before  $E_J$  in Eq. (2.72) is due to the global flux bias  $\Phi_b$ . This is crucial to enable the superradiant transition [100], which we believe would create a transient DTC behavior even for small  $N$ .

Note that even if the  $A^2$  ( $\Psi^2$  from  $(\psi_j - \Psi)^2$ ) term is included,  $H_1$  still has an exact parity symmetry, i.e., the invariance under  $Q \rightarrow -Q$ ,  $\Psi \rightarrow -\Psi$ ,  $q_j \rightarrow -q_j$  and  $\psi_j \rightarrow -\psi_j$ . This symmetry is maintained for the GKSL equation, in which the jump operator is linear in  $Q$  and  $\Psi$ . The parity operator can again be approximated as a time evolution under the following noninteracting Hamiltonian:

$$H_2 = \frac{Q^2}{2C} + \frac{\Psi^2}{2L} + \sum_{j=1}^N \left[ \frac{q_j^2}{2C_J} + \frac{\psi_j^2}{2L_0} + E_J \cos\left(\frac{2\pi\psi_j}{\Phi_0}\right) \right], \quad (2.73)$$

provided the anharmonicity is small so that

$$E_J \cos\left(\frac{2\pi\psi_j}{\Phi_0}\right) \simeq E_J - \frac{\psi_j^2}{2L_J}, \quad L_J = \frac{1}{E_J} \left(\frac{\Phi_0}{2\pi}\right)^2, \quad (2.74)$$

and the parameters satisfy

$$LC \simeq \left(\frac{1}{L_0} - \frac{1}{L_J}\right)^{-1} C_J. \quad (2.75)$$

That is, the detuning between the  $LCR$  circuit and the Josephson oscillators is small.

## Chapter 3

# Classification of matrix-product unitaries with symmetries

In the previous chapter, we have focus on DTCs, which are novel dynamical phases that stroboscopically switch between different spontaneously symmetry-broken states. Having in mind that topology gives yet another fundamental mechanism of phase transitions beyond the SSB paradigm, it is natural to ask whether there exist dynamical phases that stroboscopically switch between different topological states. In this chapter, we answer this question in the affirmative in the context of matrix-product unitaries, the simplest tensor networks used to describe locality-preserving nonequilibrium quantum dynamics in one spatial dimension (1D). Moreover, we perform a systematic classification for the matrix-product unitaries with on-site unitary symmetries and unveil a new type of topological invariants called symmetry-protected indices. Our findings have experimentally verifiable consequences and important implications for 2D Floquet symmetry-protected topological phases.

### 3.1 Introduction

#### 3.1.1 Background, motivation and the main results

Classification of topological phases of matter is a central issue in modern condensed matter physics [9]. A particular recent attention is focused on the classification of topological systems far from thermal equilibrium [44, 46, 65, 69–71, 118–125]. This tendency is largely driven by the remarkable experimental developments in atomic, molecular and optical physics, which have opened up unprecedented flexibility for controlling and probing quantum many-body dynamics [31, 32, 126–129]. Moreover, understanding nonequilibrium phases of matter per se is of fundamental theoretical importance in extending the conventional paradigm of statistical mechanics to the largely unexplored nonequilibrium regime [23, 58, 61].

For equilibrium interacting systems, the arguably most well-understood classification is that of 1D bosonic symmetry-protected topological (SPT) phases [6, 130–132] as ground states of gapped local Hamiltonians with symmetries. Thanks to the entanglement area law [133], these 1D SPT phases are well described by the matrix-product states (MPSs) [134–137], and are completely classified by the second cohomology group [138–141], provided that the symmetries are not spontaneously broken. An analogous minimal setting in the nonequilibrium context is the classification of *matrix-product unitaries* (MPUs) [35, 37, 141, 142], which have been shown to be equivalent to quantum cellular automata [35]. They efficiently approximate finite-time 1D dynamics generated by local Hamiltonians [36], as can be understood from the Lieb-Robinson bound [143]. While an MPU can be regarded as an MPS with an enlarged local Hilbert space, the

classification of MPUs can be very different from that of MPSs due to the unitarity requirement. Indeed, without symmetry protection, MPSs can always be continuously deformed into product states, while MPUs are classified by the (chiral) index quantized as the logarithm of a rational number [35, 37, 142, 144]. Efforts have also been made to classify 1D SPT many-body-localized (MBL) phases, and the result turns out to be the same as that of ground-state SPT MPSs [145].

In stark contrast to the case of MPSs, the problem of classifying MPUs commuting with a local symmetry operation remains unsolved. In this chapter, we address this problem for general on-site unitary symmetries forming a finite group  $G$ . First, we allow adding arbitrary symmetric ancillas (identities) with arbitrary on-site representations of  $G$ . We prove that the combination of the index and the second cohomology class *completely* classifies all the MPUs with given symmetries. This actually proves a conjecture raised by Hastings [146] for quantum cellular automata. Whenever the cohomology class is nontrivial, the MPU transfers a symmetric state in one SPT phase into another, giving rise to a topological analogy of time crystalline oscillation discussed in the previous chapter.

Second, we allow ancillas only with the same symmetry representation as the original system. Here, we unveil a series of quantized *symmetry-protected indices* (SPIs). Nonzero SPIs quantify an imbalance of the left and right transport of each group element in the Heisenberg picture. We identify an observable signature of SPIs as the asymmetries in the two edges of symmetry-string operators evolved by the MPU, and propose an interferometry experiment for probing the SPIs relative to the index. Such an experimental scheme in turn inspires us to show that the SPIs (as well as the indices and cohomology classes) are robust against disorder, i.e., they stay well-defined for inhomogenous locality-preserving unitaries.

Our results should directly impact on the classification of Floquet SPT phases [25]. Given a 2D Floquet system with boundary in the MBL regime, its edge dynamics is well described by an MPU [37]. Here, we construct a class of 2D Floquet systems with edge MPUs characterized by nontrivial SPIs, and provide a unified picture for understanding the edge dynamics of 2D intrinsic Floquet SPT phases as symmetry-charge pumps.

### 3.1.2 Brief review on matrix-product states and unitaries

While we mainly focus on MPUs in this chapter, it is instructive to first review MPSs, which are closely related to MPUs. With the translation-invariance and the periodic boundary condition assumed, an MPS is a quantum many-body state that is defined on a 1D lattice and takes the following form [134, 136, 137]:

$$|\Psi\rangle = \sum_{j_1, j_2, \dots, j_L} \text{Tr}[A_{j_1} A_{j_2} \dots A_{j_L}] |j_1 j_2 \dots j_L\rangle. \quad (3.1)$$

Here  $L$  is the total length of the lattice,  $|j_s\rangle$  denotes a state in a *fixed* basis of the local Hilbert space  $\mathbb{C}^d$  at the  $s$ th site, and  $\{A_j\}$  is a set of  $D \times D$  matrices with  $D$  being the *bond dimension*. Such an MPS can be diagrammatically expressed as

$$\begin{array}{c} \diagup \quad \diagdown \\ \text{A} \quad \text{A} \quad \dots \quad \text{A} \\ \diagdown \quad \diagup \end{array}, \quad (3.2)$$

where the contractions of the horizontal legs correspond to the matrix products and the remaining legs correspond to the local physical states (i.e., the subscript  $j$  in  $A_j$ ). Note that Eq. (3.1) is invariant under the gauge transformation  $A_j \rightarrow X A_j X^{-1} \forall j$ , where  $X$  is an arbitrary invertible  $D \times D$  matrix. Moreover, by multiplying an appropriate normalization factor, we can always associate an MPS with a completely positive map  $\mathcal{E}(\cdot) = \sum_j A_j \cdot A_j^\dagger$  with unit spectral radius.



Such a map can be diagrammatically represented by

$$\mathcal{E} = \begin{array}{c} \overline{\triangle}^{A^*} \\ \diagdown \\ \diagup \\ \triangle^A \end{array} . \quad (3.3)$$

If  $\mathcal{E}$  has a unique and positive-definite (i.e., full-ranked) fixed point, the corresponding MPS is said to be *normal* and necessarily has short-range correlations. In this case, we can always make  $\mathcal{E}$  a quantum (or unital) channel by gauge transforming  $\{A_j\}$ . All the 1D SPT phases<sup>1</sup> are described by normal MPSs subject to certain symmetry constraints [132, 139, 140].

Let us move on to clarify the definition of MPUs and some basic facts. Qualitatively, according to Ref. [35], an MPU is nothing but a 1D quantum cellular automaton defined as a *locality-preserving* unitary transformation on a 1D lattice. By locality-preserving we mean that, with the unitary denoted as  $U$ , any operator  $O$  supported on a finite region  $R$  is transformed into  $U^\dagger O U$  supported on another finite region  $R' \supseteq R$ . This property allows us to define a finite *Lieb-Robinson length* as the minimal length  $l_{\text{LR}}$  such that  $R' \subseteq [j - l_{\text{LR}}, j + l_{\text{LR}}]$  for any on-site operator  $O$  supported on the  $j$ th site for any  $j$ .

Quantitatively, with the local Hilbert-space dimension assumed to be  $d$ , an MPU of length  $L$  is a unitary operator  $U^{(L)} : (\mathbb{C}^d)^{\otimes L} \rightarrow (\mathbb{C}^d)^{\otimes L}$  generated by a rank-four tensor  $\mathcal{U}$ :

$$U^{(L)} = \sum_{i_1, i_2, \dots, i_L, j_1, j_2, \dots, j_L} \text{Tr}[\mathcal{U}_{i_1 j_1} \mathcal{U}_{i_2 j_2} \dots \mathcal{U}_{i_L j_L}] |i_1 i_2 \dots i_L\rangle \langle j_1 j_2 \dots j_L|, \quad (3.4)$$

where the virtual indices are contracted with each other and two physics indices label the local input and output states. Similarly to the case of MPSs (3.1), the dimension  $D$  of the matrices  $\{\mathcal{U}_{ij}\}$  is also called the bond dimension. If we consider  $\mathcal{U}_{ij}$  as a rank-three tensor by combining  $i$  and  $j$  together, then the vectorized MPU is always a normal MPS. Moreover, it is shown in Ref. [35] that, after blocking  $k$  times, i.e., combining multiple physical indices into one index:

$$\boxed{\mathcal{U}_k} \equiv \underbrace{\boxed{\mathcal{U}} \boxed{\mathcal{U}} \dots \boxed{\mathcal{U}}}_k, \quad (3.5)$$

where  $k$  is at most  $D^4$ ,  $\mathcal{U}_k \rightarrow \mathcal{U}$  becomes *simple* in the sense that the blocked tensor satisfies

$$\begin{array}{c} \boxed{\bar{\mathcal{U}}} \quad \boxed{\bar{\mathcal{U}}} \\ | \\ \boxed{\mathcal{U}} \quad \boxed{\mathcal{U}} \end{array} = \begin{array}{c} \boxed{\bar{\mathcal{U}}} \\ | \\ \boxed{\mathcal{U}} \end{array} \begin{array}{c} \boxed{\bar{\mathcal{U}}} \\ | \\ \boxed{\mathcal{U}} \end{array}, \quad (3.6)$$

where  $\bar{\mathcal{U}}_{ij} \equiv \mathcal{U}_{ji}^*$  and  $\Sigma$  is the unique fixed point of the following quantum channel  $\mathcal{E}$ :

$$\mathcal{E} = d^{-1} \begin{array}{c} \boxed{\bar{\mathcal{U}}} \\ | \\ \boxed{\mathcal{U}} \end{array} . \quad (3.7)$$

<sup>1</sup>Here we have actually assumed that no SSB occurs. Accordingly, we have excluded those unconventional topological phases protected by some partially broken symmetries [139, 141].

This property implies that the Lieb-Robinson length  $l_{\text{LR}}$  is bounded from above by  $k$ .<sup>2</sup> The corresponding MPU generated by the blocked tensor acquires the *standard form*

$$\text{---} \begin{array}{c} | \\ \boxed{\mathcal{U}} \\ | \end{array} \text{---} \begin{array}{c} | \\ \boxed{\mathcal{U}} \\ | \end{array} \text{---} \begin{array}{c} | \\ \boxed{\mathcal{U}} \\ | \end{array} \text{---} \begin{array}{c} | \\ \boxed{\mathcal{U}} \\ | \end{array} \text{---} \begin{array}{c} | \\ \boxed{\mathcal{U}} \\ | \end{array} \text{---} = \begin{array}{c} | \\ \boxed{v} \\ | \end{array} \begin{array}{c} | \\ \boxed{v} \\ | \end{array} \begin{array}{c} | \\ \boxed{v} \\ | \end{array} \begin{array}{c} | \\ \boxed{v} \\ | \end{array} \begin{array}{c} | \\ \boxed{v} \\ | \end{array} \begin{array}{c} | \\ \boxed{v} \\ | \end{array} \begin{array}{c} | \\ \boxed{u} \\ | \end{array} \begin{array}{c} | \\ \boxed{u} \\ | \end{array} \begin{array}{c} | \\ \boxed{u} \\ | \end{array} \begin{array}{c} | \\ \boxed{u} \\ | \end{array} \begin{array}{c} | \\ \boxed{u} \\ | \end{array} \begin{array}{c} | \\ \boxed{u} \\ | \end{array} \text{---} \quad (3.8)$$

in terms of unitaries  $u : (\mathbb{C}^{d^k})^{\otimes 2} \rightarrow \mathbb{C}^l \otimes \mathbb{C}^r$  and  $v : \mathbb{C}^r \otimes \mathbb{C}^l \rightarrow (\mathbb{C}^{d^k})^{\otimes 2}$ . Throughout this chapter, we apply operators in the graphical notation from bottom to top. The unitaries  $u$  and  $v$  in the standard form (3.8) are unique up to gauge transformations

$$u \rightarrow (X^\dagger \otimes Y^\dagger)u, \quad v \rightarrow v(Y \otimes X), \quad (3.9)$$

where  $X \in \text{U}(l)$  and  $Y \in \text{U}(r)$  ( $\text{U}(n)$ : set of  $n \times n$  unitaries). Conversely, two arbitrary unitaries  $u$  and  $v$  generate an MPU, possibly with the unit cell doubled.

We will focus our attention on  $G$ -symmetric MPUs which commute with a unitary representation  $\rho_g$  of the finite group  $G$ , i.e.,

$$[\rho_g^{\otimes L}, U^{(L)}] = 0, \quad \forall g \in G. \quad (3.10)$$

Henceforth, we will basically omit the length  $L$  due to the translation-invariance of MPUs. Although that we assume the translation invariance throughout this chapter, all the topological indicators we unveil can be shown to be stable against disorder (see Appendix A). The essential physics behind the stability is the locality-preserving constraint, which is obviously satisfied by the standard form (3.8) even if  $u$  and  $v$  are position-dependent.

## 3.2 Systematic classifications

Even for equilibrium systems, it is known that the topological classifications can be altered depending on the definitions of continuous deformations. For example, a Hopf insulator is topologically nontrivial in the sense of homotopy, but becomes a trivial phase in the more crude  $K$ -theory classification [147]. Similar things happen for the classification of MPUs. In particular, we will define a weak and a strong version of topological equivalence and show that the latter has a much richer classification.

### 3.2.1 Equivalence and the complete classification

We first classify the symmetric MPUs according to the following equivalence relation.

**Definition 1 (Equivalence)** *Two  $G$ -symmetric MPUs  $U_0$  and  $U_1$  are equivalent if we allow for blocking (i.e., treating multiple sites as a single site) and the addition of local ancillas with the identity operator, such that the MPUs can then be continuously connected within the manifold of symmetric MPUs.*

Here, by adding local ancillas to an MPU  $U$ , we mean that we take the enlarged MPU  $U' = U \otimes \mathbb{1}_a^{\otimes L}$  on  $(\mathbb{C}^d \otimes \mathbb{C}^{d_a})^{\otimes L}$ , and consider the representation  $\rho'_g = \rho_g \otimes \sigma_g$ , where  $\sigma$  can be an arbitrary representation of  $G$  on  $\mathbb{C}^{d_a}$ .

<sup>2</sup>We believe that the minimal  $k$  for achieving the simple property is equal to  $l_{\text{LR}}$ , although a rigorous proof is not yet made. Nevertheless,  $l_{\text{LR}} \leq k$  is good enough for deducing that an MPU with a finite bond dimension has a finite Lieb-Robinson length.

An MPU can be considered as a *normal* MPS by bunching the two physical indices of each tensor into one. Whenever inputting a symmetry operator  $\rho_g$  on the physical level, we can identify a unitary  $z_g$  on the virtual level of  $\mathcal{U}$  [138]:

$$\begin{array}{c} \circlearrowleft \rho_g \\ | \\ \boxed{U} \\ | \\ \circlearrowleft \rho_g \end{array} = \begin{array}{c} | \\ \circlearrowleft z_g \\ | \\ \boxed{U} \\ | \\ \circlearrowleft z_g \end{array} . \quad (3.11)$$

Here,  $z_g$  is unique up to a  $U(1)$  phase and forms a *projective representation* of  $G$ :

$$z_g z_h = e^{i\theta(g,h)} z_{gh}, \quad e^{i\theta(g,h)} \in U(1), \quad \forall g, h \in G. \quad (3.12)$$

Accordingly,  $e^{i\theta(g,h)}$  is unique up to a coboundary and satisfies the cocycle condition

$$\theta(g, h) + \theta(gh, k) = \theta(g, hk) + \theta(h, k), \quad \forall g, h, k \in G, \quad (3.13)$$

implying that its cohomology class in  $H^2(G, U(1))$  is well-defined. It is apparent that  $z_g$  does not change upon blocking. When composing or tensoring two symmetric MPUs with representations  $z'_g$  and  $z''_g$ , the projective representation on the MPS level becomes the tensor product  $z_g = z'_g \otimes z''_g$ , implying that the corresponding cohomology classes sum up. In particular, the cohomology class stays unchanged upon adding trivial ancillas.

Alternatively, we can identify the cohomology class from the standard form (3.8). Since

$$U = \rho_g^{\otimes L} U (\rho_g^{\otimes L})^\dagger, \quad (3.14)$$

we know that  $u$  and  $v$  from the standard form of the lhs generate the same MPU as  $u(\rho_g^\dagger \otimes \rho_g^\dagger)$  and  $(\rho_g \otimes \rho_g)v$  from the standard form of the rhs. The gauge freedom (3.9) then immediately results in the existence of unitary  $x_g, y_g$  such that

$$\begin{array}{c} | \\ \boxed{u} \\ | \\ \circlearrowleft \rho_g \quad \circlearrowleft \rho_g \end{array} = \begin{array}{c} \circlearrowleft x_g \quad \circlearrowleft y_g \\ | \\ \boxed{u} \\ | \\ | \end{array} \quad \text{and} \quad \begin{array}{c} \circlearrowleft \rho_g \quad \circlearrowleft \rho_g \\ | \\ \boxed{v} \\ | \\ | \end{array} = \begin{array}{c} | \\ \boxed{v} \\ | \\ \circlearrowleft y_g \quad \circlearrowleft x_g \end{array} . \quad (3.15)$$

Applying the group elements  $g$  and  $h$  separately or jointly, we obtain

$$v(y_g y_h \otimes x_g x_h) = (\rho_{gh} \otimes \rho_{gh})v = v(y_{gh} \otimes x_{gh}), \quad (3.16)$$

which implies that  $y_g \otimes x_g$  forms a linear representation. Hence  $y_g$  and  $x_g$  form projective representations that have opposite phase terms (cocycles)  $e^{i\theta(g,h)} \in U(1)$ :

$$x_g x_h = e^{i\theta(g,h)} x_{gh}, \quad y_g y_h = e^{-i\theta(g,h)} y_{gh}. \quad (3.17)$$

In other words,  $x_g$  and  $y_g$  belong to the opposite cohomology classes. Here we use the same notation  $e^{i\theta(g,h)}$  as in Eq. (3.12) because the cohomology class of  $x_g$  ( $y_g$ ) is indeed the same as (opposite to) that of  $z_g$ . This relation can be understood by considering the singular value decomposition of  $v$

$$\begin{array}{c} | \\ \boxed{v} \\ | \\ | \end{array} = \begin{array}{c} | \\ \boxed{v} \\ | \\ \circlearrowleft x_g \quad \circlearrowleft y_g \end{array}, \quad (3.18)$$

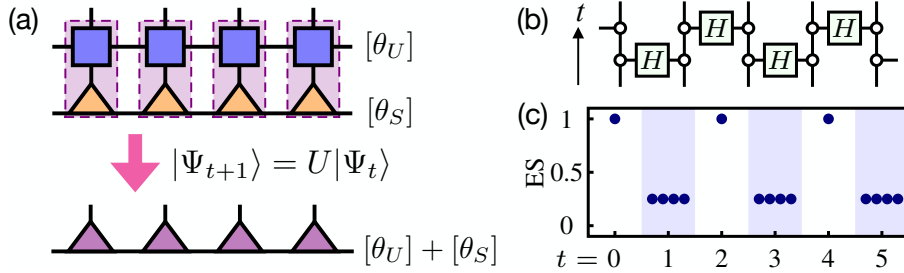


Figure 3.1: (a)  $G$ -symmetric MPS evolved by a  $G$ -symmetric MPU with the cohomology classes summing up. (b)  $\mathbb{Z}_2 \times \mathbb{Z}_2$ -symmetric MPU in the nontrivial cohomology class. Here  $\circ$  is the delta tensor and  $H$  is the Hadamard matrix. (c) Stroboscopic dynamics of the entanglement spectrum (ES) governed by (b) starting from a symmetric product state. Reproduced from Fig. 1 of Ref. [38]. Copyright © 2020 by the American Physical Society.

which, upon the action of  $\rho_g$ , transforms as

$$\begin{array}{c} \circlearrowleft \\ \rho_g \\ \circlearrowright \end{array} = \begin{array}{c} \circlearrowleft \\ z_g^\dagger \\ \circlearrowright \\ x_g \end{array} \quad \text{and} \quad \begin{array}{c} \circlearrowleft \\ \rho_g \\ \circlearrowright \\ \vdots \end{array} = \begin{array}{c} \circlearrowleft \\ z_g \\ \circlearrowright \\ y_g \end{array} . \quad (3.19)$$

Examples of MPUs with nontrivial cohomology classes are already found in Refs. [148, 149] as the edge dynamics of 2D intrinsic Floquet SPT phases.<sup>3</sup> Being initialized as a symmetric state, a nontrivial 1D edge evolves from one SPT phase into another after each Floquet period, reminiscent of the DTCs which toggle between different symmetry-broken phases [28–30, 74]. In the tensor-network picture, we can understand this “topological DTC oscillation” from the virtual level — when a symmetric MPS is evolved by a symmetric MPU, their cohomology classes simply sum up. This is schematically illustrated in Fig. 3.1(a), where the symmetric MPS built from orange triangles denotes the current state  $|\Psi_t\rangle$  at time  $t$  and is evolved by the symmetric MPU  $U$  built from blue squares. The obtained MPS  $|\Psi_{t+1}\rangle = U|\Psi_t\rangle$  marked in purple is again symmetric and its cohomology class is the sum of those of  $|\Psi_t\rangle$  and  $U$ . To diagnose this phenomenon, we may trace the stroboscopic evolution of the entanglement spectrum [46, 122, 123], which is experimentally accessible by many-body-state tomography [150] or interferometric measurement [151]. For the  $G = \mathbb{Z}_N \times \mathbb{Z}_N$  SPT MPU corresponding to the generator of  $H^2(G, U(1)) = \mathbb{Z}_N$  [148], starting from a symmetric trivial state, we will show in Sec. 3.3 that there arises (at least)  $(N/\text{gcd}(N, t))^2$ -fold degeneracy in the entanglement spectrum after  $t$  time steps. See Figs. 3.1(b) and (c) for the simplest case  $N = 2$ . Here the  $\mathbb{Z}_2 \times \mathbb{Z}_2$ -symmetric MPU is built from adjacent controlled Hadamard gates. The stroboscopic dynamics generated by this MPU is a toggle between a trivial direct-product state and a nontrivial 1D cluster state, which have no and 4-fold degeneracies in the entanglement spectrum, respectively. More general examples with nontrivial cohomology classes will be given in the next section.

In addition to the cohomology class, we can always define the (chiral) index for an MPU as [35, 142, 144]

$$\text{ind} \equiv \frac{1}{2} \ln \frac{r}{l}, \quad (3.20)$$

which captures the imbalance between right-propagating quantum information and left-propagating one. Unlike the cohomology class, this topological invariant has no counterpart in MPSs, and

<sup>3</sup>By intrinsic, we mean that they have no equilibrium counterparts and correspond to the  $H^2(G, U(1))$  part in the cohomology classification  $H^3(\mathbb{Z} \times G, U(1)) = H^3(G, U(1)) \times H^2(G, U(1))$  [70].

can thus be considered as being originated in the unitary constraint for MPUs. On the other hand, just like the cohomology class, the index is also stable under blocking and additive under tensoring as well as composition of MPUs [35]. A prototypical example of an MPU with a nontrivial index is a left or right translation unitary, which appears at the boundary of another type of 2D intrinsic Floquet topological phases — anomalous Floquet chiral phase [37, 67].

As Hastings conjectured [146], equivalent phases of MPUs are indeed *completely* classified by the index and cohomology class:

**Theorem 1 (Equivalence)** *Two  $G$ -symmetric MPUs  $U_0$  and  $U_1$  with the same or different symmetry representations are equivalent if and only if they share the same index and cohomology class in  $H^2(G, U(1))$ .*

Note that the necessity of the same indices was shown by Cirac *et al.* [35]; that of the same cohomology classes follows from [139], just as for MPS. We then only have to construct an explicit path that continuously connects  $U_0$  with  $U_1$ . This turns out to be always possible after symmetrization of the on-site symmetry representations of  $U_0$  and  $U_1$  and regularization through attaching ancillas with regular representations, as detailed in the following.

If  $U_0$  and  $U_1$  have different representations  $\rho_0$  and  $\rho_1$  of the symmetry, we may add ancillas (identities) with  $\rho_1$  and  $\rho_0$  to  $U_0$  and  $U_1$ , respectively. The composition  $U_1^\dagger U_0$  is then symmetric with the representation  $\rho_0 \otimes \rho_1$ . Since  $U_0$  and  $U_1$  have the same cohomology class and index, their additivity under composition leads to  $U_1^\dagger U_0$  having trivial cohomology class and zero index. Therefore, we can apply the following lemma to  $U_1^\dagger U_0$ .

**Lemma 1** *Each symmetric MPU  $U$  of zero index and trivial cohomology is equivalent to the identity.*

According to this lemma, we can find a one-parameter class of symmetric MPUs  $V_\lambda$  such that  $V_0 = \mathbb{1}$  and  $U_1^\dagger U_0 = V_1$ . This gives a continuous path  $U_\lambda \equiv U_0 V_\lambda^\dagger$  which is symmetric under  $G$  for  $\forall \lambda \in [0, 1]$  and connects  $U_0$  and  $U_1$ .

We still have to prove Lemma 1. To this end, we may assume that  $U$  is simple, since blocking is allowed in the definition of equivalence. Since  $U$  has trivial cohomology,  $\alpha_g x_g$  and  $\beta_g y_g$  are linear representations for suitable  $\alpha_g, \beta_g \in U(1)$ . We now try to get rid of the phases such that  $x_g$  and  $y_g$  directly are linear representations. To this end, we perform the transformation

$$x'_g = \alpha_g x_g \text{ and } y'_g = (\alpha_g \beta_g)^{-1} \beta_g y_g, \quad (3.21)$$

which does not alter Eq. (3.15) and leaves the linear representation

$$x_g \otimes y_g = x'_g \otimes y'_g = (\alpha_g \beta_g)^{-1} \otimes (\alpha_g x_g) \otimes (\beta_g y_g) \quad (3.22)$$

invariant. On the rhs, the leftmost factor must be a (one-dimensional) linear representation because the other tensor product factors already are linear representations. Therefore, both  $x'_g$  and  $y'_g$  are linear representations. To unclutter notation, we call them  $x_g$  and  $y_g$  in the following.

Now we regularize by adding ancillas (identities) to  $U$ . We are free to choose the regular representation  $\rho_g^{\text{reg}}$  as the action of the symmetry  $G$  on the ancillas. This yields the tensor  $\mathcal{U}_k \otimes \mathbb{1}_{\dim \rho^{\text{reg}}}$ , and the standard form is affected in the following way:

$$\begin{array}{c} \text{---} \square_{\mathcal{U}_k} \text{---} \square_{\mathcal{U}_k} \text{---} \square_{\mathcal{U}_k} \text{---} \square_{\mathcal{U}_k} \text{---} \square_{\mathcal{U}_k} \text{---} \\ \text{---} \square_{\mathcal{U}_k} \text{---} \square_{\mathcal{U}_k} \text{---} \square_{\mathcal{U}_k} \text{---} \square_{\mathcal{U}_k} \text{---} \square_{\mathcal{U}_k} \text{---} \end{array} = \begin{array}{c} \text{---} \square_{\mathcal{U}_k} \text{---} \square_{\mathcal{U}_k} \text{---} \square_{\mathcal{U}_k} \text{---} \square_{\mathcal{U}_k} \text{---} \square_{\mathcal{U}_k} \text{---} \\ \text{---} \square_{\mathcal{U}_k} \text{---} \square_{\mathcal{U}_k} \text{---} \square_{\mathcal{U}_k} \text{---} \square_{\mathcal{U}_k} \text{---} \square_{\mathcal{U}_k} \text{---} \\ \text{---} \square_{\mathcal{U}_k} \text{---} \square_{\mathcal{U}_k} \text{---} \square_{\mathcal{U}_k} \text{---} \square_{\mathcal{U}_k} \text{---} \square_{\mathcal{U}_k} \text{---} \\ \text{---} \square_{\mathcal{U}_k} \text{---} \square_{\mathcal{U}_k} \text{---} \square_{\mathcal{U}_k} \text{---} \square_{\mathcal{U}_k} \text{---} \square_{\mathcal{U}_k} \text{---} \\ \text{---} \square_{\mathcal{U}_k} \text{---} \square_{\mathcal{U}_k} \text{---} \square_{\mathcal{U}_k} \text{---} \square_{\mathcal{U}_k} \text{---} \square_{\mathcal{U}_k} \text{---} \end{array} \quad (3.23)$$

With the original physical legs blocked together with the ancillas, which correspond to the lines over the boxes, the blocked local symmetry is  $\tilde{\rho}_g = \rho_g \otimes \rho_g^{\text{reg}}$ . It acts on the unitaries of the blocked standard form  $\tilde{v} = v \otimes \mathbb{1}_{(\dim \rho^{\text{reg}})^2}$  as

$$(\tilde{\rho}_g \otimes \tilde{\rho}_g)\tilde{v} = \tilde{v}((y_g \otimes \rho_g^{\text{reg}}) \otimes (x_g \otimes \rho_g^{\text{reg}})) \equiv \tilde{v}(\tilde{y}_g \otimes \tilde{x}_g). \quad (3.24)$$

In fact,  $\tilde{\rho}_g$ ,  $\tilde{x}_g$ , and  $\tilde{y}_g$  are equivalent linear representations. To see this, let us demonstrate that  $\tau \otimes \rho^{\text{reg}}$  is equivalent to a  $(\dim \tau)$ -fold copy of  $\rho^{\text{reg}}$  for any linear representation  $\tau$ . Within the character theory of finite groups [152], we can calculate

$$\text{Tr}(\tau_g \otimes \rho_g^{\text{reg}}) = \text{Tr}(\tau_g)(\dim \rho_g^{\text{reg}})\delta_{ge} = (\dim \tau_e) \text{Tr}(\rho_e^{\text{reg}}), \quad (3.25)$$

with the identity  $e \in G$ . Since the MPU is index zero,  $\rho_g, x_g$ , and  $y_g$  have the same dimensions and  $\tilde{\rho}_g, \tilde{x}_g$ , and  $\tilde{y}_g$  are therefore equivalent representations.

The equivalence of representations means that there exist two unitaries  $X$  and  $Y$  such that  $\tilde{x}_g = X\tilde{\rho}_gX^\dagger$  and  $\tilde{y}_g = Y\tilde{\rho}_gY^\dagger$ , implying

$$[\tilde{\rho}_g \otimes \tilde{\rho}_g, \tilde{v}'] = [\tilde{\rho}_g \otimes \tilde{\rho}_g, \tilde{u}'] = 0, \quad \forall g \in G, \quad (3.26)$$

where  $\tilde{v}' = \tilde{v}(Y \otimes X)$  and  $\tilde{u}' = (X^\dagger \otimes Y^\dagger)\tilde{u}$  are related to  $\tilde{v}$  and  $\tilde{u}$  by a gauge transformation, so that they generate the same MPU. Thanks to Eq. (3.26), we can find two Hermitian operators  $h_u$  and  $h_v$  such that  $\tilde{u}' = e^{-ih_u}$  and  $\tilde{v}' = e^{-ih_v}$  and

$$[\tilde{\rho}_g \otimes \tilde{\rho}_g, h_u] = [\tilde{\rho}_g \otimes \tilde{\rho}_g, h_v] = 0, \quad \forall g \in G. \quad (3.27)$$

Defining  $\tilde{u}'(\lambda) \equiv e^{-i\lambda h_u}$  and  $\tilde{v}'(\lambda) \equiv e^{-i\lambda h_v}$ , we immediately know that the generated MPU  $U(\lambda)$  gives a continuous path which respects all the symmetries and interpolates  $U$  and the (global) identity  $\mathbb{1} \equiv \mathbb{1}^{\otimes L}$ .

### 3.2.2 Strong equivalence and the symmetry-protected indices

In real physical systems with symmetries, the representation is usually determined by the microscopic details and cannot be changed freely. This motivates us to ask how the classification will be modified if the representation is fixed. Forbidding arbitrary representations for the ancillas in Def. 1 leads to the following:

**Definition 2 (Strong Equivalence)** *Two  $G$ -symmetric MPUs  $U_0$  and  $U_1$  are strongly equivalent if (i) their on-site representations are (generally different) powers of a single fixed representation  $\rho$  of  $G$  and (ii) they can be continuously connected within the manifold of symmetric MPUs upon blocking and/or adding identities as ancillas with representation  $\rho$ .*

If  $\rho$  is regular, we return to Theorem 1. Otherwise, there is at least one  $g \neq e$  with character  $\chi_g \equiv \text{Tr} \rho_g \neq 0$ . In this case, the notion of strong equivalence refines the phase structure beyond Theorem 1, as revealed by the SPIs which are a natural generalization of the index (3.20), which can be rewritten as

$$\text{ind} = \frac{1}{2} \ln \left| \frac{\text{Tr} y_e}{\text{Tr} x_e} \right|, \quad (3.28)$$

to other group elements other than  $e$  (trivial identity element):

**Definition 3 (Symmetry Protected Index)** *Given a  $G$ -symmetric MPU  $U$  for which we can determine  $x_g$  and  $y_g$  from a standard form, the SPI with respect to  $g \in G$  with  $\chi_g \neq 0$  is defined as*

$$\text{ind}_g \equiv \frac{1}{2} \ln \left| \frac{\text{Tr} y_g}{\text{Tr} x_g} \right|. \quad (3.29)$$

Given a blocking number  $k$ , the SPI is well defined since the absolute value removes the phase ambiguity and the trace is gauge-invariant. Moreover, we can show that, just as in  $\text{ind} = \text{ind}_e$  [35],  $\text{ind}_g$  is invariant under blocking and additive under tensoring and composition:

**Proposition 1** *Given a  $G$ -symmetric MPU generated by  $\mathcal{U}$  and  $g \in G$  with  $\chi_g \neq 0$ , the SPI*

$$\text{ind}_g = \frac{1}{2} \ln \left| \frac{\text{Tr } y_g}{\text{Tr } x_g} \right| \quad (3.30)$$

*is well-defined, although the standard form is not unique.*

*Proof:* Having in mind that the SPI is well-defined for a given blocking number  $k \geq k_0$ , we only have to prove that the SPI does not depend on  $k$ . For  $\forall k > k_0$ , we can always find  $m, m_0 \in \mathbb{Z}^+$  such that  $km = k_0 m_0 \equiv K$ . Denoting the standard form of  $\mathcal{U}_{k_0}$  and  $\mathcal{U}_k$  as  $u_{k_0}, v_{k_0}$  and  $u_k, v_k$ , respectively, by further blocking the former  $m_0$  times (see Fig. 3.2(a)) or the latter  $m$  times, we obtain two equivalent standard forms for  $\mathcal{U}_K$ :

$$\begin{aligned} u_K &= (\mathbb{1}^{\otimes k} \otimes v_k^{\otimes(m-1)} \otimes \mathbb{1}^{\otimes k}) u_k^{\otimes m}, \\ v_K &= \mathbb{1}^{\otimes k(m-1)} \otimes v_k \otimes \mathbb{1}^{\otimes k(m-1)}, \text{ and} \\ u'_K &= (\mathbb{1}^{\otimes k_0} \otimes v_{k_0}^{\otimes(m_0-1)} \otimes \mathbb{1}^{\otimes k_0}) u_{k_0}^{\otimes m_0}, \\ v'_K &= \mathbb{1}^{\otimes k_0(m_0-1)} \otimes v_{k_0} \otimes \mathbb{1}^{\otimes k_0(m_0-1)}, \end{aligned} \quad (3.31)$$

which should be related by a gauge transformation [35]. Accordingly,  $x_g$  and  $y_g$  for  $\mathcal{U}_K$  can be obtained to be

$$\begin{aligned} x_{k,g} \otimes \rho_g^{\otimes k(m-1)}, \rho_g^{\otimes k(m-1)} \otimes y_{k,g}, \text{ and} \\ x_{k_0,g} \otimes \rho_g^{\otimes k_0(m_0-1)}, \rho_g^{\otimes k_0(m_0-1)} \otimes y_{k_0,g}, \end{aligned} \quad (3.32)$$

where  $x_{k,g}, y_{k,g}$  are the projective representations on the virtual level of the standard form of  $\mathcal{U}_k$ . Recalling that  $\text{ind}_g$  is well-defined for a given blocking number, we have

$$\begin{aligned} \text{ind}_g(\mathcal{U}_K) &= \frac{1}{2} \ln \frac{|\text{Tr } y_{k,g}| |\chi_g|^{k(m-1)}}{|\text{Tr } x_{k,g}| |\chi_g|^{k(m-1)}} = \text{ind}_g(\mathcal{U}_k) \\ &= \frac{1}{2} \ln \frac{|\text{Tr } y_{k_0,g}| |\chi_g|^{k_0(m_0-1)}}{|\text{Tr } x_{k_0,g}| |\chi_g|^{k_0(m_0-1)}} = \text{ind}_g(\mathcal{U}_{k_0}). \end{aligned} \quad (3.33)$$

So far, we have confirmed that the SPI is well-defined.  $\square$

**Proposition 2** *The SPI is additive by tensoring and composition.*

*Proof:* The case of tensoring is almost trivial — on the virtual level of the standard form, the projective representations of a tensored MPU  $U = U_1 \otimes U_0$  are given by the tensor product of those of  $U_1$  and  $U_0$ . Using the trace identity  $\text{Tr } x_1 \otimes x_0 = \text{Tr } x_1 \text{Tr } x_0$ , we immediately obtain the additivity of the SPI.

For the case of composition, we consider two  $G$ -symmetric standard-form (after blocking  $k_0$  sites into one) MPUs  $U_0^{(6k_0L)}$  and  $U_1^{(6k_0L)}$  generated by  $u_0, v_0$  and  $u_1, v_1$  and their composition  $U^{(6k_0L)} = U_1^{(6k_0L)} U_0^{(6k_0L)}$ . By further blocking three sites into one, the building blocks  $u, v$  for the standard form of  $U^{(6k_0L)}$  can be related to those for  $U_0^{(6k_0L)}$  and  $U_1^{(6k_0L)}$  via (see Fig. 3.2(b))

$$\begin{aligned} u &= \{x_{0,e} \otimes [(\mathbb{1}^{\otimes k_0} \otimes u_1 \otimes \mathbb{1}^{\otimes k_0}) v_0^{\otimes 2}] \otimes y_{0,e}\} u_0^{\otimes 3}, \\ v &= v_1^{\otimes 3} \{y_{1,e} \otimes [u_1^{\otimes 2} (\mathbb{1}^{\otimes k_0} \otimes v_0 \otimes \mathbb{1}^{\otimes k_0})] \otimes x_{1,e}\}. \end{aligned} \quad (3.34)$$

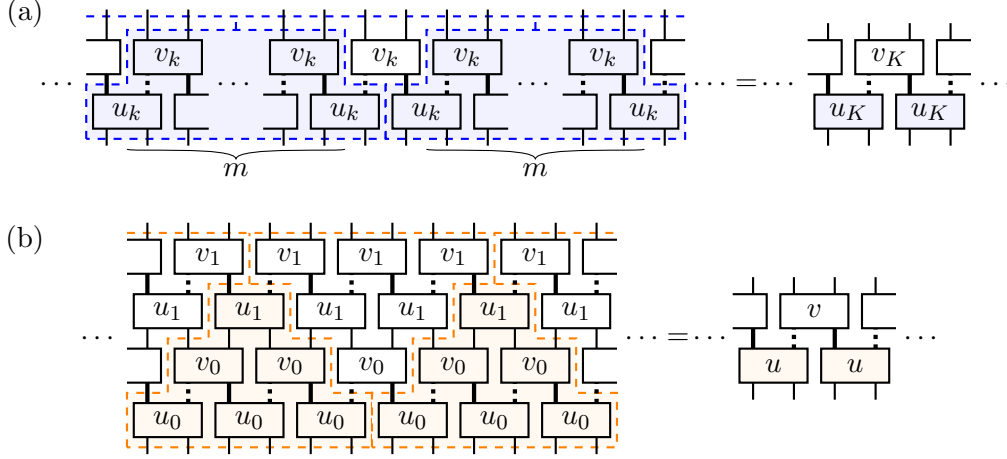


Figure 3.2: Blocking protocols for showing (a) the blocking independence and (b) the additivity of the SPIs. Reproduced from Supplementary Fig. 4 of Ref. [38]. Copyright © 2020 by the American Physical Society.

Therefore, on the virtual level of the standard form of  $U^{(6k_0L)}$ , the projective representations read

$$x = x_0 \otimes \rho^{\otimes k_0} \otimes x_1, \quad y = y_1 \otimes \rho^{\otimes k_0} \otimes y_0, \quad (3.35)$$

which implies that the SPIs are additive.  $\square$

We further claim that the SPI is a topological invariant for strong equivalence. Recall that  $\text{ind}_g$  does not rely on blocking and is obviously invariant if we add identities with the fixed representation. Moreover, it can be shown that  $\text{ind}_g$  is continuous and stays discretized during a continuous deformation. Therefore, the SPI is a quantized topological invariant. A more rigorous statement and the proof can be found in the following:

**Proposition 3** *Given a continuous path of  $\mathcal{U}_\lambda$  generating  $G$ -symmetric MPUs and  $g \in G$  with  $\chi_g \neq 0$ , then  $\text{ind}_g$  stays unchanged along the path.*

*Proof:* According to Corollary 4.7 in Ref. [35], there exists  $k_0 \leq D_m^4$  ( $D_m$ : largest bond dimension of  $\mathcal{U}_\lambda$ ) such that the MPU  $U_\lambda^{(2k_0L)}$  generated by  $\mathcal{U}_\lambda$  has a standard form  $u_\lambda, v_\lambda$  which are continuous with respect to  $\lambda$ . Using  $u_\lambda \rho_g^{\otimes 2k_0} u_\lambda^\dagger = x_{\lambda,g} \otimes y_{\lambda,g} \equiv w_{\lambda,g}$ , we can rewrite the SPI for  $\mathcal{U}_\lambda$  into

$$\text{ind}_g(\mathcal{U}_\lambda) = \frac{1}{2} \ln \frac{\text{Tr}_l[\text{Tr}_r w_{\lambda,g} \text{Tr}_r w_{\lambda,g}^\dagger]}{l |\chi_g|^{2k_0}}, \quad (3.36)$$

where  $\text{Tr}_r$  and  $\text{Tr}_l$  are the partial traces over  $\mathbb{C}^r$  and  $\mathbb{C}^l$  on the virtual level, with  $l$  and  $r$  being the dimensions of  $x_{\lambda,g}$  and  $y_{\lambda,g}$ , respectively. Since  $w_{\lambda,g} \equiv u_\lambda \rho_g^{\otimes 2k_0} u_\lambda^\dagger$  and  $w_\lambda^\dagger$  are both continuous with respect to  $\lambda$ , the continuity of  $\text{ind}_g(\mathcal{U}_\lambda)$  follows. On the other hand, due to the fact that  $x_{\lambda,g} \otimes y_{\lambda,g}$  is a linear representation, we have  $(x_{\lambda,g} \otimes y_{\lambda,g})^{d_g} = \mathbb{1}^{\otimes 2k_0}$  ( $d_g$ : order of  $g$  defined as the smallest integer  $d_g$  such that  $g^{d_g} = e$ ), implying  $x_{\lambda,g}^{d_g} = \mathbb{1}_l$  and  $y_{\lambda,g}^{d_g} = \mathbb{1}_r$  for a certain phase gauge. Accordingly,  $\text{ind}_g(\mathcal{U}_\lambda)$  only takes values over a finite set

$$\left\{ \ln \frac{|\sum_{j \in \mathbb{Z}_{d_g}} n_j \omega_{d_g}^j|}{|\chi_g|^{k_0}} : \sum_{j \in \mathbb{Z}_{d_g}} n_j = r \right\} \quad (3.37)$$



in  $\ln |\mathbb{Q}(\omega_{d_g}) \setminus \{0\}|$ , where  $\omega_{d_g} \equiv e^{2\pi i/d_g}$ . Combining the discrete image of  $\text{ind}_g(\mathcal{U}_\lambda)$  with its continuity, we conclude that  $\text{ind}_g$  is a quantized constant, which is a logarithm of the absolute value of a cyclotomic number, along the continuous path.  $\square$

The above proposition immediately implies the following:

**Theorem 2** *Two symmetric, strongly equivalent MPUs share the same SPI for all group elements with  $\chi_g \neq 0$ .*

The contraposition of Theorem 2 allows us to use SPIs to distinguish topologically different MPUs. For cyclic groups  $G = \mathbb{Z}_N$  with  $N \geq 3$ , the minimal nontrivial example is the bilayer SWAP circuit of qubits [35], in which a single site contains two qubits and

$$\rho_{1_{\mathbb{Z}_N}} = \mathbb{1} \otimes Z_{\omega_N}, \quad Z_{\omega_N} \equiv |0\rangle\langle 0| + e^{2\pi i/N} |1\rangle\langle 1|, \quad (3.38)$$

where  $1_{\mathbb{Z}_N}$  is the generator of  $\mathbb{Z}_N$ . We can check that

$$x_{1_{\mathbb{Z}_N}} = \mathbb{1}^{\otimes 2}, \quad y_{1_{\mathbb{Z}_N}} = Z_{\omega_N}^{\otimes 2}, \quad (3.39)$$

leading to

$$\text{ind}_{1_{\mathbb{Z}_N}} = \ln \left| \cos \frac{\pi}{N} \right| \neq 0, \quad (3.40)$$

which is sufficient to rule out the *strong* equivalence between the bilayer SWAP circuit and the identity. However, having  $\text{ind} = 0$  and trivial cohomology, it is still equivalent to the identity.

Recalling that the index and cohomology class fully classify all the MPUs in the sense of equivalence, we would like to ask whether the SPIs, together with the index and the cohomology class, give a complete classification for strong equivalence. This question can be settled by answering whether an MPU with trivial SPIs, index and cohomology class is always strongly equivalent to the identity. The answer turns out to be *no*, because the SPI can be further refined, at least for those MPUs with trivial cohomology. Let us introduce the definition of such a *refined SPI*:

**Definition 4 (Refined SPI)** *Given a  $G$ -symmetric MPU in the trivial cohomology class, a refined index with respect to any  $g \in G$  with  $\chi_g \neq 0$  is defined as*

$$\text{rind}_g = \left( \frac{\text{Tr } y_g}{\text{Tr } \rho_g} \right)^{d_g}, \quad (3.41)$$

where  $y_g$  is already lifted to a linear representation.

As  $y_g$  is a linear representation, the phase ambiguity is discretized as a 1D representation and thus killed by the power  $d_g$ , implying that the refined SPI is well-defined for a given standard form. We show the following proposition:

**Proposition 4** *Given a  $G$ -symmetric MPU in the trivial cohomology class and  $g \in G$  with  $\chi_g \neq 0$ , the refined SPI given in Eq. (3.41) is well-defined, although the standard form is not unique.*

To show this, we can use almost the same analysis as the one for the blocking-independence of the SPI.

We still have to prove that the refined SPI is not only well-defined but also a topological invariant. To this end, we need the following lemma:

**Lemma 2** *Given a continuous path of projective representation  $z_g(\lambda)$  of a finite group  $G$  in the trivial cohomology class, there exists a continuous function  $\omega_g : \lambda \rightarrow \text{U}(1)$  such that  $\omega_g(\lambda)z_g(\lambda)$  is a continuous path of linear representation.*

*Proof:* By assumption, there exists  $z'_g(\lambda) = \omega'_g(\lambda)z_g(\lambda)$  which is a linear representation but not necessarily continuous with respect to  $\lambda$ . From  $z'_g(\lambda)^{d_g} = \mathbb{1}$ , we know that  $\omega'_g(\lambda)^{d_g} = z_g(\lambda)^{-d_g}$  should be continuous, thus

$$\omega'_g(\lambda) = \omega_g^c(\lambda)\omega_{d_g}^{n_g(\lambda)}, \quad (3.42)$$

where  $\omega_g^c(\lambda)$  is continuous and  $n_g(\lambda) \in \mathbb{Z}_{d_g}$ . Moreover, from  $z'_g(\lambda)z'_h(\lambda) = z'_{gh}(\lambda)$ , we know that

$$\omega'_g(\lambda)\omega'_h(\lambda)\omega'_{gh}(\lambda)^{-1} = [z_g(\lambda)z_h(\lambda)z_{gh}(\lambda)]^{-1} \quad (3.43)$$

is continuous. The combination of Eqs. (3.42) and (3.43) implies that  $\omega_{d_g}^{n_g(\lambda)}\omega_{d_h}^{n_h(\lambda)}\omega_{d_{gh}}^{-n_{gh}(\lambda)}$  is also continuous. On the other hand,  $\omega_{d_g}^{n_g(\lambda)}\omega_{d_h}^{n_h(\lambda)}\omega_{d_{gh}}^{-n_{gh}(\lambda)}$  takes discrete values in  $\{\omega_{d_G}^j : j \in \mathbb{Z}_{d_G}\}$  ( $d_G$ : order of group  $G$  defined as the smallest integer  $d_G$  such that  $g^{d_G} = e \ \forall g \in G$ ), so that

$$\omega_{d_g}^{n_g(\lambda)}\omega_{d_h}^{n_h(\lambda)}\omega_{d_{gh}}^{-n_{gh}(\lambda)} = \omega_{d_g}^{n_g(0)}\omega_{d_h}^{n_h(0)}\omega_{d_{gh}}^{-n_{gh}(0)} \quad (3.44)$$

should be independent of  $\lambda$ . Now defining

$$z''_g(\lambda) \equiv \omega_g^c(\lambda)\omega_{d_g}^{n_g(0)}z_g(\lambda), \quad (3.45)$$

which is obviously continuous, we can check that it is a linear representation.  $\square$

Combining Proposition 4 and Lemma 2, we immediately obtain

**Proposition 5** *The refined SPI is a topological invariant, which is multiplicative by tensoring and composition.*

The generalization of the refined SPI to inhomogeneous locality-preserving unitaries can be done in full analogy to the generalization of the SPI.

Since  $\text{rind}_g$  is a topological invariant, we have the following:

**Theorem 3** *Given two symmetric, strongly equivalent MPUs  $U_0$  and  $U_1$ , then  $U_1^\dagger U_0$  has trivial (unit) refined SPIs.*

A minimal example that is not strongly equivalent to the identity as indicated by Theorem 3 but not captured by Theorem 2 is a  $\mathbb{Z}_3$ -symmetric MPU consisting of qutrits. Denoting  $\rho^{(j)}$  ( $j \in \mathbb{Z}_3$ ) as the irreducible (1D) representation of  $\mathbb{Z}_3$  with  $\rho_{1\mathbb{Z}_3}^{(j)} = \omega_3^j$ , for  $\rho = \rho^{(0)} \oplus 2\rho^{(1)}$ , we can realize  $x = y = \rho^{(0)} \oplus 2\rho^{(2)}$  on the virtual level due to  $\rho \otimes \rho = x \otimes y = \rho^{(0)} \oplus 4\rho^{(1)} \oplus 4\rho^{(2)}$ . Substituting  $\text{Tr } y_{1\mathbb{Z}_3} = 1 + 2\omega_3^2$  and  $\text{Tr } \rho_{1\mathbb{Z}_3} = 1 + 2\omega_3$  into Eq. (3.41), we obtain  $\text{rind}_{1\mathbb{Z}_3} = -1 \neq 1$ , which implies that the MPU *cannot* be deformed into the identity without breaking the  $\mathbb{Z}_3$  symmetry with such a fixed representation. We will see an explicit construction of such an MPU in the following subsection. Finally, we emphasize that while Theorem 3 is undoubtedly an improved criterion for ruling out strong equivalence, we still do not know whether the refined SPI gives the complete classification.

### 3.3 Examples

In this section, we present some examples of MPUs with nontrivial cohomology classes and (refined) SPIs. We will first represent the  $\mathbb{Z}_N \times \mathbb{Z}_N$  SPT edge unitaries in Ref. [148] in the MPU forms followed by discussing the signatures in the entanglement-spectrum dynamics, and then provide a general construction for an arbitrary  $G$ . We will also discuss how to realize nontrivial (refined) SPIs in a systematic manner.

### 3.3.1 MPUs with nontrivial cohomology classes

#### $\mathbb{Z}_N \times \mathbb{Z}_N$ SPT MPUs

For unitary symmetries,<sup>4</sup> the minimal group that admits a nontrivial projective representation is  $\mathbb{Z}_2 \times \mathbb{Z}_2$ , whose cohomology group reads  $H^2(\mathbb{Z}_2 \times \mathbb{Z}_2, \text{U}(1)) = \mathbb{Z}_2$  and a realization of the nontrivial element has been shown in Fig. 3.1(b). In the following, we discuss how to generalize the results to  $\mathbb{Z}_N \times \mathbb{Z}_N$  SPT MPUs corresponding to nontrivial elements in  $H^2(\mathbb{Z}_N \times \mathbb{Z}_N, \text{U}(1)) = \mathbb{Z}_N$ .

Specifying the representation of the  $\mathbb{Z}_N \times \mathbb{Z}_N$  symmetry group as

$$\rho_{(m,n)} = Z^m \otimes Z^n, \quad (m, n) \in \mathbb{Z}_N \times \mathbb{Z}_N, \quad (3.46)$$

where  $Z_{ij} \equiv \langle i|Z|j \rangle = \delta_{ij}\omega_N^j$  with  $\omega_N \equiv e^{i\frac{2\pi}{N}}$ , we can write down the generator of nontrivial SPT MPUs (cohomology group) as [148]

$$U_{\text{SPT}} = e^{-i\frac{2\pi}{d} \sum_j (-)^j N_{j,X} N_{j+1,X}}, \quad (3.47)$$

where  $N_X \equiv \sum_{j=1}^{d-1} (X^j - \mathbb{1}) / (\omega_N^{-j} - 1)$  with  $X_{ij} \equiv \delta_{i+1,j}$ . Note that here the variables in the Kronecker delta are elements in  $\mathbb{Z}_N$ , thus  $\delta_{N,0} = 1$ . One can easily check that

$$XZ = \omega_N ZX. \quad (3.48)$$

With the delta tensor and the generalized Hadamard matrix defined diagrammatically as

$$\begin{array}{c} i \\ | \\ \text{---} j \equiv \delta_{ij} \delta_{jk} \\ | \\ k \end{array}, \quad j \text{---} \boxed{H} \text{---} k \equiv \omega_N^{jk} \quad (3.49)$$

under the eigenbasis of  $\{X_j\}$ , the building block of the  $\mathbb{Z}_N \times \mathbb{Z}_N$  SPT MPU (3.47) can be represented as

$$\boxed{U} = \begin{array}{c} \text{---} \text{---} \text{---} \\ | \quad | \quad | \\ \text{---} \text{---} \text{---} \\ | \quad | \quad | \\ \text{---} \text{---} \text{---} \end{array} \quad (3.50)$$

Note that the delta tensor and the generalized Hadamard matrix satisfy

$$\begin{array}{c} \begin{array}{c} \text{---} \text{---} \\ | \quad | \\ \text{---} \text{---} \\ | \quad | \\ \text{---} \text{---} \end{array} = \begin{array}{c} \text{---} \text{---} \\ | \quad | \\ \text{---} \text{---} \\ | \quad | \\ \text{---} \text{---} \end{array}, \quad \begin{array}{c} \text{---} \text{---} \\ | \quad | \\ \text{---} \text{---} \\ | \quad | \\ \text{---} \text{---} \end{array} = \begin{array}{c} \text{---} \text{---} \\ | \quad | \\ \text{---} \text{---} \\ | \quad | \\ \text{---} \text{---} \end{array}, \\ \\ \begin{array}{c} \text{---} \text{---} \\ | \quad | \\ \text{---} \text{---} \\ | \quad | \\ \text{---} \text{---} \end{array} = \begin{array}{c} \text{---} \text{---} \\ | \quad | \\ \text{---} \text{---} \\ | \quad | \\ \text{---} \text{---} \end{array} = \begin{array}{c} \text{---} \text{---} \\ | \quad | \\ \text{---} \text{---} \\ | \quad | \\ \text{---} \text{---} \end{array}, \\ \\ \text{---} \text{---} \boxed{H} \text{---} = \text{---} \boxed{H} \text{---} \text{---}, \\ \text{---} \text{---} \boxed{X} \text{---} \boxed{H} \text{---} = \text{---} \boxed{H} \text{---} \text{---} \text{---}. \end{array} \quad (3.51)$$

<sup>4</sup>If we allow anti-unitary symmetries, then a time-reversal symmetry ( $\mathbb{Z}_2^T$ ) alone can protect nontrivial topological phases, including both MPSs [132] and MPUs [35].

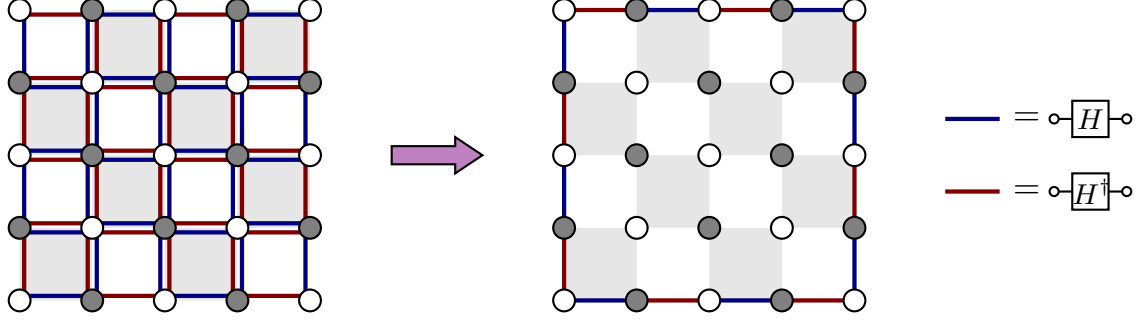


Figure 3.3: 2D Floquet SPT model with a trivial bulk and an anomalous edge dynamics governed by the  $\mathbb{Z}_N \times \mathbb{Z}_N$  SPT MPU (3.47). Reproduced from Supplementary Fig. 1 of Ref. [38]. Copyright © 2020 by the American Physical Society.

Using these relations (3.51), upon inputting  $\rho_{(m,n)} = Z^m \otimes Z^n$  on the physical level, we obtain

$$\begin{aligned}
 & \begin{array}{c} \textcircled{Z^m} \\ | \\ \textcircled{Z^n} \\ | \\ \textcircled{H} \end{array} = \begin{array}{c} \textcircled{Z^{-m}} \\ | \\ \textcircled{Z^m} \\ | \\ \textcircled{H} \end{array} \begin{array}{c} \textcircled{Z^n} \\ | \\ \textcircled{Z^{-n}} \\ | \\ \textcircled{H^\dagger} \end{array} = \omega_N^{mn} \begin{array}{c} \textcircled{Z^{-m}} \\ | \\ \textcircled{X^{-n}} \\ | \\ \textcircled{H} \end{array} \begin{array}{c} \textcircled{Z^n} \\ | \\ \textcircled{X^{-n}} \\ | \\ \textcircled{H^\dagger} \end{array} \\
 & = \omega_N^{mn} \begin{array}{c} \textcircled{Z^{-m} X^{-n}} \\ | \\ \textcircled{Z^m} \\ | \\ \textcircled{H} \end{array} \begin{array}{c} \textcircled{X^{-n}} \\ | \\ \textcircled{H^\dagger} \\ | \\ \textcircled{X^n} \end{array} = \begin{array}{c} \textcircled{X^{-n} Z^{-m}} \\ | \\ \textcircled{Z^m} \\ | \\ \textcircled{H} \end{array} \begin{array}{c} \textcircled{H^\dagger} \\ | \\ \textcircled{Z^m X^n} \end{array}.
 \end{aligned} \tag{3.52}$$

Therefore, the projective representation on the virtual level reads

$$z_{(m,n)} = Z^m X^n. \tag{3.53}$$

According to the building block (3.50), we can write down the standard form as follows:

$$\begin{aligned}
 u &= \begin{array}{c} | \\ | \\ \textcircled{H^\dagger} \\ | \\ \textcircled{H} \end{array}, \\
 v &= \begin{array}{c} | \\ | \\ \textcircled{H^\dagger} \\ | \\ | \end{array}.
 \end{aligned} \tag{3.54}$$

Using Eq. (3.51), we can determine the projective representations  $x_g$  and  $y_g$  on the virtual level of the standard form as

$$\begin{aligned}
 x_{(m,n)} &= \omega_N^{-mn} X^n Z^m \otimes Z^n, \\
 y_{(m,n)} &= Z^m \otimes X^m Z^n.
 \end{aligned} \tag{3.55}$$

It is easy to check  $\omega_x((m,n), (m',n')) = \omega_N^{m'n} = \omega_z((m,n), (m',n'))$ , which is consistent with the general relation that  $x_g$  and  $z_g$  belong to the same cohomology class.

The MPU representation (3.50) in turn gives us an elegant picture of the associated 2D Floquet system with a trivial bulk. As shown in Fig. 3.3, the 2D Floquet unitary is a product of commutative local unitaries  $\square$  and  $\square$  acting on gray and white plaquettes, respectively. Since  $\square$  and  $\square$  are actually small SPT MPU with 2 unit cells, the entire 2D Floquet unitary is locally implemented under the symmetry constraint. While the bulk turns out to be trivial due to the fact that  $\square$  and  $\square$  cancel out, we obtain an anomalous edge as in Eq. (3.47), which is not locally implementable under the symmetry constraint [148].

### Entanglement-spectrum dynamics

As briefly mentioned in the previous section, starting from a trivial symmetric MPS  $|\Psi_0\rangle$ , after  $t$  steps of time evolution by a  $\mathbb{Z}_N \times \mathbb{Z}_N$  SPT MPU with the same cohomology class as Eq. (3.47), the entanglement spectrum (under the periodic boundary condition) must be at least  $(N/\text{gcd}(N, t))^2$ -fold degenerate. To show this, we first point out a useful property that the spectrum of the transfer matrix of an MPS is conserved during the time evolution by an MPU. This result comes from the unitary nature of time evolution, which implies

$$\text{Tr} \left( \sum_j M_j \otimes \bar{M}_j \right)^L = \text{Tr} \left( \sum_j M'_j \otimes \bar{M}'_j \right)^L, \quad \forall L \in \mathbb{Z}^+, \quad (3.56)$$

where  $M_j \in \mathbb{C}^{D \times D}$  and  $M'_j = \sum_{j'} \mathcal{U}_{jj'} M_{j'}$ . In particular, if the transfer matrix of  $|\Psi_0\rangle$  has a unique fixed point, the uniqueness is preserved for  $|\Psi_t\rangle$ . This observation rules out the possibility of spontaneous symmetry breaking during the time evolution of a symmetric MPU. Moreover, let  $\Lambda$  be the unique fixed point of the transfer matrix of  $|\Psi_t\rangle$ ; it is known that the entanglement spectrum is given by  $\{\lambda_\alpha \lambda_\beta\}_{\alpha, \beta=1}^D$ , where  $\{\lambda_\alpha\}_{\alpha=1}^D$  are the eigenvalues of  $\Lambda$  [136]. In addition, the cohomology-class sum rule applies to an MPS evolved by an MPU (see Fig. 3.1(a)), just as does to composed MPUs.

Denoting the projective representation on the virtual level of  $|\Psi_t\rangle \equiv U_{\text{SPT}}^t |\Psi_0\rangle$  as  $V_{(m,n)}$ , we know from the additivity of the cohomology class that

$$V_{(m,n)} V_{(m',n')} = \omega_N^{tm'n} V_{(m+m',n+n')} \quad (3.57)$$

for some phase gauge. Moreover, due to the uniqueness of the fixed point, we have  $[V_{(m,n)}, \Lambda] = 0$  for  $\forall (m,n) \in \mathbb{Z}_N \times \mathbb{Z}_N$ . Noting  $V_{(1,0)}^N = \mathbb{1}_v$  ( $\mathbb{1}_v$ : the identity on the virtual level), we can define a set of projectors

$$P_n \equiv N^{-1} \sum_{j \in \mathbb{Z}_N} \omega_N^{-jn} V_{(1,0)}^j, \quad n \in \mathbb{Z}_N \quad (3.58)$$

that satisfy  $P_n P_m = \delta_{mn} P_n$ ,  $\sum_{n \in \mathbb{Z}_N} P_n = \mathbb{1}_v$  and  $P_n V_{(1,0)} = V_{(1,0)} P_n = \omega_N^n P_n$ . Now consider an arbitrary eigenstate  $|\lambda\rangle_v$  of  $\Lambda$  with eigenvalue  $\lambda$ ; there should be at least one  $P_{n_0}$  such that  $P_{n_0} |\lambda\rangle_v \neq 0$  and thus  $|\lambda_{n_0}\rangle_v \equiv P_{n_0} |\lambda\rangle_v / \|P_{n_0} |\lambda\rangle_v\|$  is a common eigenstate of  $\Lambda$  and  $V_{(1,0)}$  with eigenvalues  $\lambda$  and  $\omega_N^{n_0}$ , respectively. Using Eq. (3.57), we have

$$V_{(1,0)} V_{(0,1)}^n |\lambda_{n_0}\rangle_v = \omega_N^{-tn+n_0} V_{(0,1)}^n |\lambda_{n_0}\rangle_v, \quad (3.59)$$

so that  $V_{(0,1)}^n |\lambda_{n_0}\rangle_v$  are also common eigenstate of  $\Lambda$  and  $V_{(1,0)}$  with eigenvalues  $\lambda$  and  $\omega_N^{-tn+n_0}$ , respectively. Since  $\omega_N^{-tn+n_0}$  takes  $N/\text{gcd}(N, t)$  pieces of different values, the degeneracy in the entanglement spectrum should be at least  $(N/\text{gcd}(N, t))^2$ .

Let us verify the above conclusion both analytically and numerically. We first consider an analytically solvable case in which  $|\Psi_0\rangle = |0_Z\rangle^{\otimes 2L}$  ( $|j_Z\rangle$  defined from  $Z|j_Z\rangle = \omega_N^j |j_Z\rangle$ ) is

evolved by the MPU in Eq. (3.47). With the local basis chosen as the eigenstates of  $X$ , the MPS building block for  $|\Psi_t\rangle$  is given by

$$[M_{(a,b)}^X]_{\alpha\beta} = d^{-1} \delta_{\alpha\beta} \omega_N^{tb(\alpha-\beta)}, \quad (3.60)$$

where we have used  $\langle j_X | j'_Z \rangle = \omega_N^{-j'j} / \sqrt{N}$  with  $j' = 0$  ( $|j_X\rangle$  defined from  $X|j_X\rangle = \omega_N^j |j_X\rangle$ ). To make the representation matrix of the  $\mathbb{Z}_N \times \mathbb{Z}_N$  symmetry diagonal, we prefer to use the  $Z$ -basis, under which

$$\begin{aligned} [M_{(a,b)}^Z]_{\alpha\beta} &= N^{-1} \sum_{a',b' \in \mathbb{Z}_N} \omega_N^{a'a+b'b} [M_{(a',b')}^X]_{\alpha\beta} \\ &= N^{-1} \omega_N^{\alpha a} \delta_{(\beta-\alpha)t, b}. \end{aligned} \quad (3.61)$$

One can check that  $M_{(a,b)}^Z$  is zero unless  $q \equiv \gcd(N, t) | b$ , i.e.,  $q$  divides  $b$ . When  $q|b$ , defining  $\tilde{b} \equiv b/q$ ,  $\tilde{N} \equiv N/q$  and  $\tilde{t} \equiv t/q$ , we have

$$M_{(a,b)}^Z = \tilde{N}^{-1} Z^a X^{\tilde{b}\tilde{t}^{-1}} P, \quad (3.62)$$

where  $\tilde{t}^{-1}$  is the well-defined inverse (due to  $\gcd(\tilde{N}, \tilde{t}) = 1$ ) of  $\tilde{t}$  on  $\mathbb{Z}_{\tilde{N}}$  and

$$P \equiv q^{-1} \sum_{j \in \mathbb{Z}_q} X^{j\tilde{N}} \quad (3.63)$$

is a projector with rank  $\text{Tr } P = N/q = \tilde{N}$ . Since  $P^2 = P$ ,  $\tilde{M}_{(a,b)}^Z \equiv P M_{(a,b)}^Z$  gives the same MPS and the bond dimension is  $\tilde{N}$ . This result already implies that the extreme case of  $(N/\gcd(N, t))^2 = \tilde{N}^2$ -fold degeneracy is achievable. Moreover, defining  $X_P \equiv P X P$  and  $Z_P \equiv P Z^q P$ , we can check that  $X_P^{\tilde{N}} = Z_P^{\tilde{N}} = P$ ,  $X_P Z_P = \omega_{\tilde{N}} Z_P X_P$  and  $P Z^a P = 0$  unless  $a = q\tilde{a}$ , in which case  $P Z^a P = Z_P^{\tilde{a}} P = P Z_P^{\tilde{a}}$ . Therefore, we obtain  $\tilde{M}_{(a,b)}^Z = 0$  except for

$$\tilde{M}_{q(\tilde{a}, \tilde{b})}^Z = \tilde{N}^{-1} Z_P^{\tilde{a}} X_P^{\tilde{b}\tilde{t}^{-1}}. \quad (3.64)$$

Under the  $Z$ -basis, the action of  $Z^m \otimes Z^n$  on  $|a_Z b_Z\rangle$  is just a phase  $\omega_N^{am+bn}$ , so that the projective representation on the virtual level can be determined as

$$V_{(m,n)} = Z_P^{\tilde{m}\tilde{t}} X_P^{-m}, \quad (3.65)$$

which satisfies

$$V_{(m,n)} V_{(m',n')} = \omega_N^{-mn'\tilde{t}} V_{(m+m', n+n')}. \quad (3.66)$$

Since  $\omega_N^{-mn'\tilde{t}} = \omega_N^{-mn't} = \omega_N^{m'nt} \omega_N^{-t(mn'+m'n)}$  with

$$\omega_N^{-t(mn'+m'n)} = \frac{\omega_N^{-(m+m')(n+n')t}}{\omega_N^{-mnt} \omega_N^{-m'n't}} \quad (3.67)$$

being a coboundary, Eq. (3.66) can be related to Eq. (3.57) by a gauge transformation.

If  $U_{\text{SPT}}$  in Eq. (3.47) is perturbed in a symmetry-preserving manner, the strict  $N$ -fold period multiplication generally disappears but the constraint on the entanglement-spectrum degeneracy should still be valid. For simplicity, we consider the following  $\mathbb{Z}_N \times \mathbb{Z}_N$ -symmetric MPU which belongs to the same phase as  $U_{\text{SPT}}$ :

$$U_{\text{F}} = e^{-ih \sum_j N_{j,Z} U_{\text{SPT}}}, \quad (3.68)$$

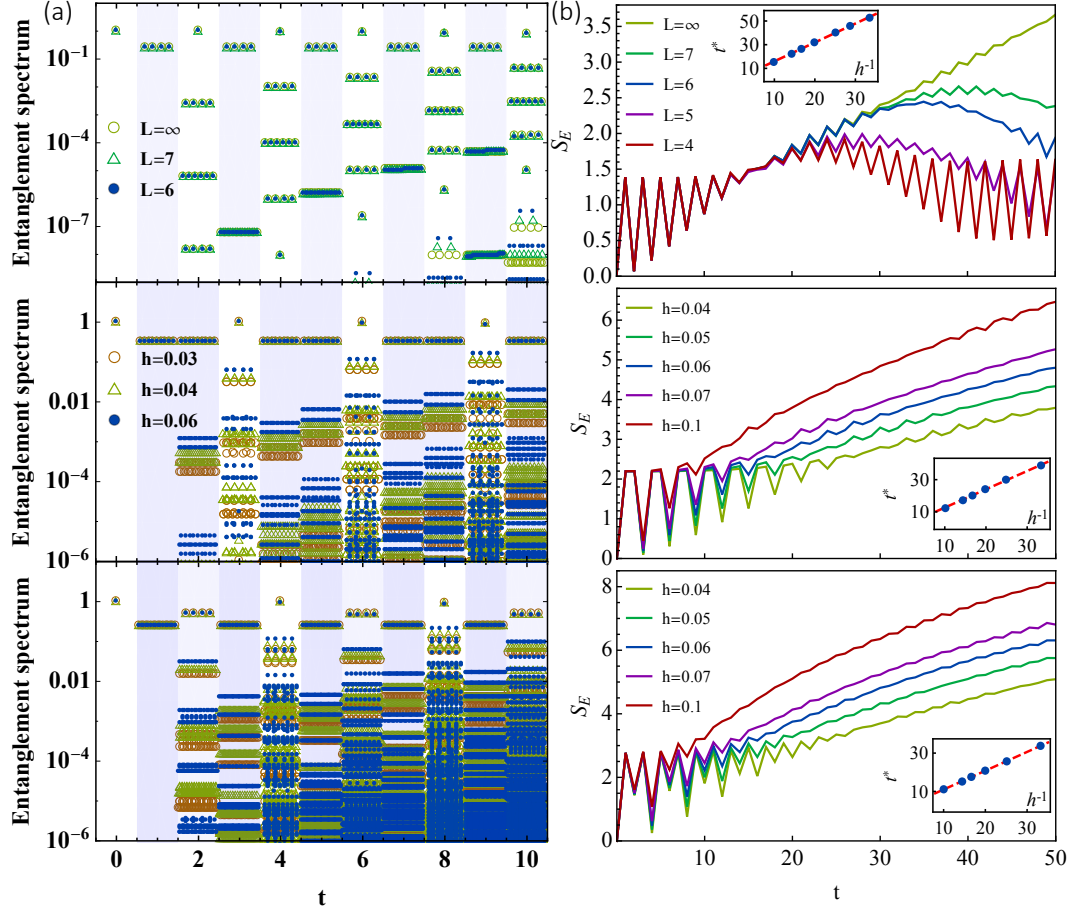


Figure 3.4: Stroboscopic dynamics of (a) the entanglement spectrum and (b) the entanglement entropy governed by the Floquet unitary in Eq. (3.68) starting from  $|\Psi_0\rangle = |0_Z\rangle^{\otimes 2L}$ . The top, middle and bottom rows show the cases of  $N = 2$  (qubit),  $N = 3$  (qutrit) and  $N = 4$  (ququard), respectively. Times steps with SPT-enforced entanglement-spectrum degeneracy are shaded in (a). The Insets in (b) show the  $h$  dependence of the crossover time  $t^*$  determined from Eq. (3.69). The entanglement dynamics in finite qubit systems are obtained by exact diagonalization while those in infinite qutrit and ququard systems are obtained by iTEBD with varying bond dimension  $\chi = 100 \sim 1500$  such that the numerical results converge. Reproduced from Supplementary Fig. 2 of Ref. [38]. Copyright © 2020 by the American Physical Society.

where  $N_Z \equiv \sum_{j=1}^{d-1} (Z^j - \mathbb{1}) / (\omega_d^{-j} - 1)$ . We perform numerical studies on the stroboscopic dynamics of both the entanglement spectrum and entropy for  $N = 2, 3$  and 4 with varying  $h$ . In particular, we study the finite-size effect using exact diagonalization for  $N = 2$  (with  $h = 0.1$  only) while we focus on infinite systems for  $N = 3$  and 4 using the infinite time-evolving block decimation (iTEBD) method [153]. While the growing (with oscillation) entanglement entropy shown in Fig. 3.4(b) indicates that the system will eventually thermalize, we do observe in Fig. 3.4(a) the (at least)  $(N/\gcd(N, t))^2$ -fold degeneracy in the entanglement spectrum. Even in a qubit system with  $L = 6$ , the (at least) 4-fold degeneracy at odd time steps is only slightly lifted (not visible in Fig. 3.4(a)), implying that the SPT DTC oscillation is, in principle, observable in small systems.

It is also worth mentioning that the entanglement entropy  $S_E$  exhibits a crossover between two dynamical regimes with large and small oscillations accompanied by the growth. As shown in the insets in Fig. 3.4(b), the crossover time  $t^*$ , which we determine from

$$t^* = \frac{1}{N-1} \sum_{s=1}^{N-1} t_s^*, \quad t_s^* \equiv \min\{t : S_E^{(s)}(t) = S_E^{(0)}(t)\}, \quad (3.69)$$

where  $S_E^{(s)}(t)$  is a continuation of  $S_E(t = nN + s)$  ( $s \in \mathbb{Z}_N$ ), turns out to be proportional to  $h^{-1}$  for small  $h$ . We can understand the crossover from the SPT-enforced entanglement-spectrum degeneracy, which implies a lower bound  $2 \ln(N/\gcd(N, t))$  on the entanglement entropy. When  $h$  is small, according to the Magnus expansion as used in Ref. [148], the continuation  $S_E^{(s)}(t)$  is expected to be well approximated by the entanglement entropy of  $|\Psi_\lambda^{(s)}\rangle = e^{-i\lambda H_{\text{eff}}^s} U_{\text{SPT}}^s |\Psi_0\rangle$  with  $\lambda = ht$  and

$$H_{\text{eff}} \simeq \frac{1}{N} \sum_j \sum_{a \in \mathbb{Z}_N} U_{\text{SPT}}^a N_{j,Z} U_{\text{SPT}}^{-a}. \quad (3.70)$$

The initial strong oscillation and the  $h^{-1}$  scaling follow.

### General constructions for arbitrary finite groups

So far we have focused on  $\mathbb{Z}_N \times \mathbb{Z}_N$  SPT MPUs. From a general perspective of topological DTC oscillations, we can seek for MPUs with nontrivial cohomology classes by considering bilayer unitary circuits (i.e., standard forms of MPUs, cf. Eq. (3.8)) that transform trivial states, such as product states, into SPT MPSs. Indeed, the  $\mathbb{Z}_N \times \mathbb{Z}_N$  MPU transforms  $|0_Z\rangle^{\otimes L}$  into a 1D cluster state of qudits [154].

In general, an SPT state can be constructed from a path integral of a cocycle action on a triangulated spacetime manifold [155]. This construction might be regarded as a sort of the matter-field dual of the Dijkgraaf-Witten theory for gauge fields [156]. In 1D, given a symmetry group  $G$  and a 2-cocycle  $e^{i\theta(g,h)}$  representing an element in  $H^2(G, \mathbb{U}(1))$ , we can easily identify the underlying MPU as [149]

$$U = \sum_{\{g_j\}_{j=1}^L} e^{-i \sum_{j=1}^L \theta(g_j^{-1} g_{j+1}, g_{j+1}^{-1})} |g_1 g_2 \dots g_L\rangle \langle g_1 g_2 \dots g_L|. \quad (3.71)$$

Here the symmetry representation on a local Hilbert space  $\mathbb{C}^{|G|}$  is assumed to be regular, i.e.,  $\rho_g |h\rangle = |gh\rangle$  for  $\forall g, h \in G$ , and the sum of each  $g_j$  runs over  $G$ . To confirm that Eq. (3.71) is topologically nontrivial, we first identify  $u, v$  in the standard form as

$$u = v = \sum_{g_l, g_r} e^{-i\theta(g_l^{-1} g_r, g_r^{-1})} |g_l g_r\rangle \langle g_l g_r|. \quad (3.72)$$



Accordingly, we can identify  $x_g$  and  $y_g$  from

$$\begin{aligned} (\rho_g \otimes \rho_g)v &= \sum_{g_l, g_r} e^{-i\theta(g_l^{-1}g_r, g_r^{-1})} |gg_l, gg_r\rangle \langle g_l g_r| = \sum_{g_l, g_r} e^{-i\theta(g_l^{-1}g_r, g_r^{-1}g)} |g_l g_r\rangle \langle g^{-1}g_l, g^{-1}g_r| \\ &= \sum_{g_l, g_r} e^{i[\theta(g_r^{-1}, g) - \theta(g_l^{-1}g_r, g_r^{-1}) - \theta(g_l^{-1}, g)]} |g_l g_r\rangle \langle g^{-1}g_l, g^{-1}g_r| = v(y_g \otimes x_g), \end{aligned} \quad (3.73)$$

where we have used the defining property of cocycles (see also Eq. (3.13)):

$$\theta(g_l^{-1}g_r, g_r^{-1}) + \theta(g_l^{-1}, g) = \theta(g_l^{-1}g_r, g_r^{-1}g) + \theta(g_r^{-1}, g). \quad (3.74)$$

Similarly, we can show that  $\rho_g^{\otimes 2}u^\dagger = u^\dagger(x_g \otimes y_g)$ . The expressions of  $x_g$  and  $y_g$  are given by

$$x_g = y_g^* = \sum_k e^{i\theta(k^{-1}, g)} |k\rangle \langle g^{-1}k| = \sum_k e^{i\theta(k^{-1}g^{-1}, g)} |gk\rangle \langle k|, \quad (3.75)$$

according to which we obtain

$$\begin{aligned} x_g x_h &= \sum_k e^{i[\theta(k^{-1}h^{-1}g^{-1}, g) + \theta(k^{-1}h^{-1}, h)]} |ghk\rangle \langle k| \\ &= \sum_k e^{i[\theta(k^{-1}h^{-1}g^{-1}, gh) + \theta(g, h)]} |ghk\rangle \langle k| = e^{i\theta(g, h)} x_{gh}, \end{aligned} \quad (3.76)$$

implying that  $\{x_g\}$  form a projective representation with factor set  $e^{i\theta(g, h)}$ . Since  $y_g = x_g^*$ , the factor set for  $\{y_g\}$  is  $e^{-i\theta(g, h)}$ .

The nontrivial cohomology class can alternatively be confirmed by looking at the building-block tensor  $\mathcal{U}$ , which is given by

$$\mathcal{U} = \sum_{j, r} e^{-i\theta(j^{-1}r, r^{-1})} |j\rangle |j\rangle (r| \langle j|. \quad (3.77)$$

Here, we use  $|\cdot\rangle$  and  $|\cdot\rangle$  to refer to physical and virtual states, respectively. We can identify the projective representation on the virtual level through

$$\begin{aligned} \rho_g \mathcal{U} \rho_g^\dagger &= \sum_{j, r} e^{-i\theta(j^{-1}r, r^{-1})} |gj\rangle |j\rangle (r| \langle gj| = \sum_{j, r} e^{-i\theta(j^{-1}r, r^{-1}g)} |j\rangle |g^{-1}j\rangle (g^{-1}r| \langle j| \\ &= \sum_{j, r} e^{i[\theta(r^{-1}, g) - \theta(j^{-1}r, r^{-1}) - \theta(j^{-1}, g)]} |j\rangle |g^{-1}j\rangle (g^{-1}r| \langle j| = z_g^\dagger \mathcal{U} z_g, \end{aligned} \quad (3.78)$$

where we have again used the cocycle property and  $z_g$  on the virtual level turns out to be

$$z_g = \sum_h e^{i\theta(h^{-1}, g)} |h\rangle (g^{-1}h| = \sum_h e^{i\theta(h^{-1}g^{-1}, g)} |gh\rangle (h|, \quad (3.79)$$

whose entries are the same as those in  $x_g$  (3.75). This result is consistent with the fact that  $z_g$ ,  $x_g$  and  $y_g^*$  belong to the same cohomology class.

Finally, let us construct the parent 2D Floquet system of the general SPT MPU (3.71). In fact, such a construction naturally extends to arbitrary dimensions and realizes all the intrinsic Floquet SPT phases in the cohomology classification [149]. To make the notations concise, we introduce  $\alpha(g_1, g_2, g_3) \equiv e^{-i\theta(g_1^{-1}g_2, g_2^{-1}g_3)}$ , which satisfies  $\alpha(gg_1, gg_2, gg_3) = \alpha(g_1, g_2, g_3)$  for  $\forall g \in G$  and the cocycle property

$$\frac{\alpha(g_2, g_3, g_4)\alpha(g_1, g_2, g_4)}{\alpha(g_1, g_3, g_4)\alpha(g_1, g_2, g_3)} = 1. \quad (3.80)$$

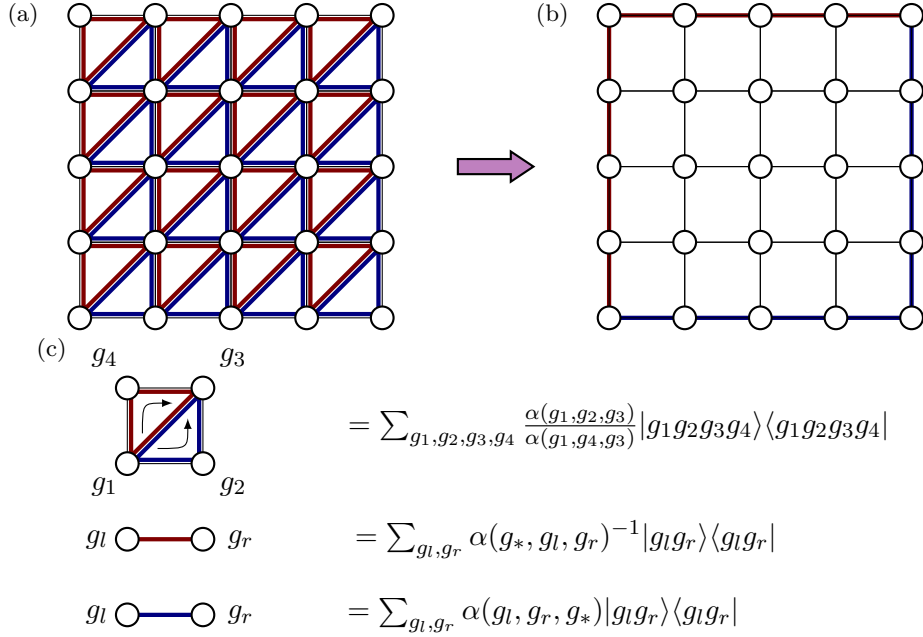


Figure 3.5: (a) 2D Floquet SPT phase built from a 2-cocycle (3.81). (b) Such a Floquet system has a trivial bulk and a nontrivial edge dynamics described by an SPT MPU (3.71). (c) Building blocks of the 2D Floquet unitary and the SPT MPU as its edge dynamics. Reproduced from Supplementary Fig. 3 of Ref. [38]. Copyright © 2020 by the American Physical Society.

As shown in Fig. 3.5, the Floquet unitary is simply a product of commutative four-site unitaries acting on each plaquettes:

$$U_F = \prod_{\square} U_{\square}, \quad U_{\square} = \sum_{\{g_j\}_{j=1}^4} \frac{\alpha(g_1, g_2, g_3)}{\alpha(g_1, g_4, g_3)} |g_1 g_2 g_3 g_4\rangle \langle g_1 g_2 g_3 g_4|. \quad (3.81)$$

Due to the topological nature of the action (especially the cocycle property given in Eq. (3.80)), the  $U(1)$  phase before any  $|\{g_j\}\rangle\langle\{g_j\}|$  (eigenstate of  $U_F$ ) should not depend on the explicit way of triangulation [155, 156]. In particular, we can put a single point into the bulk and assign an arbitrary group element  $g_* \in G$  to determine the phase. This observation implies a trivial bulk dynamics, i.e.,  $U_F = \mathbb{1}_{\text{bulk}} \otimes U_{\text{edge}}$  with  $\mathbb{1}_{\text{bulk}}$  being the bulk identity [149]. For  $g_* = e$ , the bottom edge dynamics is described by the SPT MPU given in Eq. (3.71).

### 3.3.2 Nontrivial MPUs in the trivial cohomology class

Let us move on to construct MPUs with nontrivial (refined) SPIs. We first point out that a nontrivial cohomology class may enforce the projective representation matrices for some group elements to be traceless, implying that the SPIs cannot be defined for these elements. To make the SPI well defined, a necessary condition turns out to be the *c-regularity*. For the cohomology class represented by a 2-cocyle  $c: G \times G \rightarrow U(1)$ ,  $g \in G$  is said to be *c-regular* if

$$c(g, h) = c(h, g), \quad \forall h \in N_g \equiv \{h \in G : gh = hg\}, \quad (3.82)$$

where  $N_g$  is the stabilizer group of  $g$ . We can show that *c-regularity* is actually a property for conjugacy classes, since  $N_{kgk^{-1}} = kN_gk^{-1}$  and  $c(kgk^{-1}, khk^{-1})$  is related to  $c(g, h)$  via a

$k$ -dependent 2-coboundary [157]:

$$c(kgk^{-1}, khk^{-1}) = c(g, h) \frac{\beta_k(gh)}{\beta_k(g)\beta_k(h)}, \quad (3.83)$$

where  $\beta_k(g) = c(k, gk^{-1})c(g, k^{-1})/c(k^{-1}, k)$  is a 1-cochain. Now let us consider an arbitrary projective representation  $z$  with factor set  $c$  together with a group element  $g$  that is not  $c$ -regular. By assumption, there exists  $h \in N_g$  such that  $c(g, h) \neq c(h, g)$ . From the definitions of projective representations  $z_g z_h = c(g, h) z_{gh}$  and  $z_h z_g = c(h, g) z_{hg}$ , we obtain

$$\begin{aligned} \text{Tr } z_g &= c(g, h) \text{Tr}(z_{gh} z_h^{-1}) = c(h, g) \text{Tr}(z_h^{-1} z_{hg}) \\ &= c(h, g) \text{Tr}(z_{gh} z_h^{-1}), \end{aligned} \quad (3.84)$$

where we have used  $\text{Tr}(AB) = \text{Tr}(BA)$  and  $gh = hg$  in the second line. Since  $c(g, h) \neq c(h, g)$ , the only possibility is  $\text{Tr } z_g = \text{Tr}(z_{gh} z_h^{-1}) = 0$ . Similarly, we have  $\text{Tr } z_h = \text{Tr } z_{gh} = 0$ . This completes the proof that the SPI cannot be defined for  $g$  whenever  $g$  is not  $c$ -regular.

In particular, the trivial cohomology class, for which  $c$  is a coboundary, always validates the  $c$ -regular condition. For simplicity, here we only focus on this situation. Given an MPU in the trivial cohomology class, all the projective representations  $z_g$ ,  $x_g$  and  $y_g$  on the virtual level can be lifted to linear representations, which are all elements in the *representation ring* [152]:

**Definition 5 (Representation Ring)** For a finite group  $G$  with in total  $r$  different irreducible representations denoted by  $\rho^{(1)}, \rho^{(2)}, \dots, \rho_r$ , the representation ring  $R(G)$  is defined as  $\{\rho = \bigoplus_{\alpha=1}^r n_\alpha \rho^{(\alpha)} : n_\alpha \in \mathbb{Z}\}$ , on which the addition between two elements  $\rho = \bigoplus_{\alpha=1}^r n_\alpha \rho^{(\alpha)}$  and  $\rho' = \bigoplus_{\alpha=1}^r n'_\alpha \rho^{(\alpha)}$  is defined as

$$\rho \oplus \rho' \equiv \bigoplus_{\alpha=1}^r (n_\alpha + n'_\alpha) \rho^{(\alpha)}, \quad (3.85)$$

while their multiplication is defined as

$$\rho \otimes \rho' \equiv \bigoplus_{\alpha=1}^r \left( \sum_{\beta, \gamma=1}^r N_{\beta\gamma}^\alpha n_\beta n'_\gamma \right) \rho^{(\alpha)}, \quad (3.86)$$

where the nonnegative integer (Littlewood-Richardson) coefficients  $N_{\beta\gamma}^\alpha$  are determined from

$$\rho^{(\beta)} \otimes \rho^{(\gamma)} = \bigoplus_{\alpha=1}^r N_{\beta\gamma}^\alpha \rho^{(\alpha)}, \quad (3.87)$$

the decomposition of the tensor-product representation.

According to the character theory, there is an injective map  $\chi : R(G) \rightarrow \mathbb{C}^r$  ( $r$  is also the number of conjugacy classes)

$$\chi(\rho) \equiv (\text{Tr } \rho_{g_1}, \text{Tr } \rho_{g_2}, \dots, \text{Tr } \rho_{g_r}), \quad (3.88)$$

where  $\text{Tr } \rho_{g_j} = \sum_\alpha n_\alpha \chi_{\alpha j} \in \mathbb{Z}[\omega_{d_{g_j}}]$  (Kummer ring),  $g_j$  is a representative element of the  $j$ th conjugacy class and  $\chi_{\alpha j} \equiv \text{Tr } \rho_{g_j}^{(\alpha)}$  is an entry in the character table. From the injectivity of  $\chi$ , we know that  $N_{\beta\gamma}^\alpha = N_{\gamma\beta}^\alpha$  and thus  $R(G)$  is commutative. Note that  $\mathbb{Z}$  can be regarded as the representation ring of the trivial group  $G = \{e\}$ .

With the notion of representation ring in mind, we can systematically construct MPUs with nontrivial SPIs through finding nontrivial solutions to

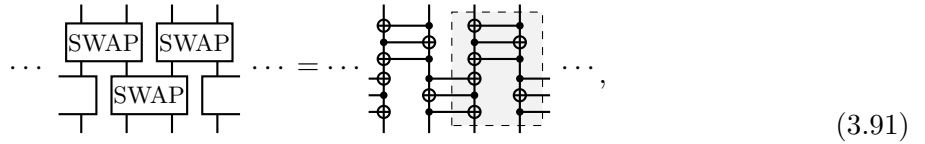
$$\rho^{\otimes 2} = x \otimes y, \quad x, y, \rho \in R^+(G), \quad (3.89)$$

where  $R^+(G)$  is a subset of  $R(G)$  consisting of all the linear representations (i.e.,  $n_\alpha \geq 0$  and  $\sum_{\alpha=1}^r n_\alpha \geq 1$ ),  $\rho$  is on the physical level and  $x$  and  $y$  are on the virtual level of the standard form (3.8). By nontrivial, we mean that  $x \neq \rho_{1D} \otimes \rho$  for any one-dimensional representation  $\rho_{1D}$  of  $G$ ; otherwise the MPU can be trivialized into the identity. In practice, we may alternatively focus on the nontrivial decomposition of the character vector, of which each component is decomposed on the Kummer ring.

For the simplest Abelian group  $G = \mathbb{Z}_N$ , we have  $r = N$  and  $N_{\beta\gamma}^\alpha = \delta_{\alpha, \beta+\gamma}$ ; a minimal example of nontrivial decomposition

$$(2\rho^{(0)} \oplus 2\rho^{(1)})^{\otimes 2} = 4\rho^{(0)} \otimes (\rho^{(0)} \oplus 2\rho^{(1)} \oplus \rho^{(2)}) \quad (3.90)$$

has already been mentioned in Sec. 3.2.2 and can be realized by the bilayer SWAP circuit on two qubits via  $2\rho^{(0)} \oplus 2\rho^{(1)} = (2\rho^{(0)}) \otimes (\rho^{(0)} \oplus \rho^{(1)})$ :



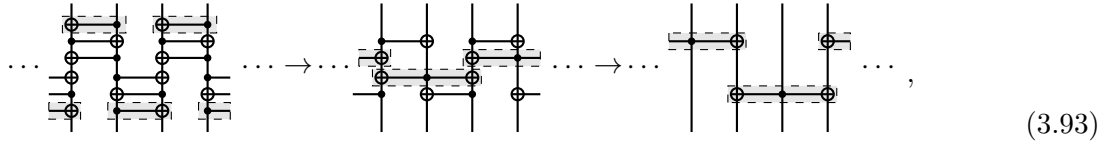
$$\dots \text{ [Bilayer SWAP] } \dots = \dots \text{ [CNOTs and } \mathcal{U} \text{] } \dots, \quad (3.91)$$

where  $\bullet \text{---} \oplus$  is the CNOT gate  $|0\rangle\langle 0| \otimes \mathbb{1} + |1\rangle\langle 1| \otimes X$  and the part marked in the gray rectangle is the building block  $\mathcal{U}$ . The equivalence between the left and right hand sides in Eq. (3.91) can be understood from



$$\text{[SWAP]} = \text{[CNOTs]} = \text{[CNOTs]}. \quad (3.92)$$

For  $N = 2$ , however, such an apparently nontrivial decomposition (3.90) is not stable against blocking since  $\rho \otimes x = \rho \otimes \rho$ . Indeed, we can trivialize the bilayer SWAP circuit as follows:



$$\dots \text{ [Circuit with gray boxes] } \dots \rightarrow \dots \text{ [Deformed circuit] } \dots \rightarrow \dots \text{ [Local identities] } \dots, \quad (3.93)$$

where the local quantum gates in the gray boxes can be continuously deformed into local identities without breaking the  $\mathbb{Z}_2$  symmetry (represented by  $\mathbb{1} \otimes Z$ ). When  $N \geq 3$ , the stability of the nontrivial MPU against blocking (and disorder) is ensured by the nontrivial SPI.

To construct a  $\mathbb{Z}_2$ -symmetric MPU with zero index and nonzero SPI, we first write down the general representation-decomposition relation

$$(d_0\rho^{(0)} \oplus d_1\rho^{(1)})^{\otimes 2} = (m_0\rho^{(0)} \oplus m_1\rho^{(1)}) \otimes (n_0\rho^{(0)} \oplus n_1\rho^{(1)}), \quad (3.94)$$

which is equivalent to

$$(d_0 \pm d_1)^2 = (m_0 \pm m_1)(n_0 \pm n_1). \quad (3.95)$$

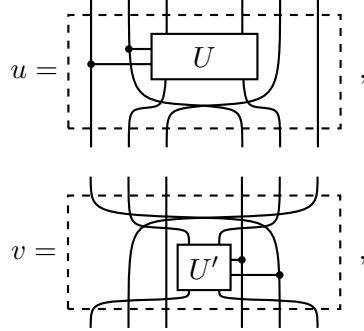
To make the SPI nontrivial, we would like to find a solution with  $d = d_0 + d_1 = m_0 + m_1 = n_0 + n_1$  and  $m_0 - m_1 \neq n_0 - n_1$ ,  $d_0 \neq d_1$ . After some trials, a minimal solution with the smallest local Hilbert-space dimension  $d = 8$  is found to be

$$(6\rho^{(0)} \oplus 2\rho^{(1)})^{\otimes 2} = (5\rho^{(0)} \oplus 3\rho^{(1)}) \otimes 8\rho^{(0)}. \quad (3.96)$$

Regarding  $d = 8 = 2^3$  as three qubits, we can implement Eq. (3.96) with

$$\begin{aligned}\rho_{1z_2} &= (|1\rangle\langle 1| \otimes Z + |0\rangle\langle 0| \otimes \mathbb{1}) \otimes \mathbb{1}, \\ x_{1z_2} &= |00\rangle\langle 00| \otimes \mathbb{1} + (\mathbb{1}^{\otimes 2} - |00\rangle\langle 00|) \otimes Z, \quad y_{1z_2} = \mathbb{1}^{\otimes 3},\end{aligned}\tag{3.97}$$

which can be realized by



$$\begin{aligned}u &= \text{Circuit with gate } U, \\ v &= \text{Circuit with gate } U' \text{ and swap } S.\end{aligned}\tag{3.98}$$

where the two-qubit-controlled gate in  $u$  is given by

$$|11\rangle\langle 11| \otimes (X \otimes |0\rangle\langle 0| + \mathbb{1} \otimes |1\rangle\langle 1|) + |01\rangle\langle 01| \otimes S + \mathbb{1} \otimes |0\rangle\langle 0| \otimes \mathbb{1}^{\otimes 2},\tag{3.99}$$

and that in  $v = \mathcal{S}u^\dagger\mathcal{S}$  ( $\mathcal{S}$  swaps two adjacent sites, either of which consists of three qubits) is given by

$$(|0\rangle\langle 0| \otimes X + |1\rangle\langle 1| \otimes \mathbb{1}) \otimes |11\rangle\langle 11| + S \otimes |01\rangle\langle 01| + \mathbb{1}^{\otimes 3} \otimes |0\rangle\langle 0|.\tag{3.100}$$

Finally, we present an explicit construction that realizes

$$(\rho^{(0)} \oplus 2\rho^{(1)})^{\otimes 2} = (\rho^{(0)} \oplus 2\rho^{(2)})^{\otimes 2}\tag{3.101}$$

on  $R(G = \mathbb{Z}_3)$ , which is the minimal example with trivial SPIs but a nontrivial refined SPI, as mentioned in Sec. 3.2.2. We consider a qutrit system and specify the representations on the physical and virtual levels as

$$\rho_{1z_3} = |0\rangle\langle 0| + \omega_3(|1\rangle\langle 1| + |2\rangle\langle 2|), \quad x_{1z_3} = y_{1z_3} = \rho_{1z_3}^2 = \rho_{2z_3}.\tag{3.102}$$

To transform  $\rho \otimes \rho$  into  $x \otimes y$ , we can use



$$u = v = \text{Circuit with controlled gate } \bullet \oplus,\tag{3.103}$$

where  $\bullet \oplus \equiv \sum_{j \in \mathbb{Z}_3} |j\rangle\langle j| \otimes X^{-j}$  ( $X \equiv \sum_{k \in \mathbb{Z}_3} |k-1\rangle\langle k|$ ) is a natural generalization of the CNOT gate. We can easily check that  $v|00\rangle = |00\rangle$ ,  $v(|01\rangle, |12\rangle, |02\rangle, |21\rangle) = (|12\rangle, |02\rangle, |21\rangle, |01\rangle)$  and  $v(|10\rangle, |11\rangle, |20\rangle, |22\rangle) = (|11\rangle, |20\rangle, |22\rangle, |10\rangle)$ , implying

$$\rho_{1z_3}^{\otimes 2} v = v \rho_{2z_3}^{\otimes 2}, \quad \rho_{2z_3}^{\otimes 2} v = v \rho_{1z_3}^{\otimes 2}.\tag{3.104}$$

### 3.4 Experimental probing of SPIs

#### Observable signatures of SPIs

Similarly to the cohomology character, the SPI (3.29) is defined on the virtual level, so that its physical meaning is not clear at first glance. Having in mind that SPT phases with nontrivial cohomology classes usually exhibit exotic edge physics [158], we are naturally led to think

about a similar situation for SPIs, which depend on  $g$ . In fact, we can consider a sufficiently long string operator  $\rho_g^{\otimes N}$  evolved by the MPU and show that the  $g$ -string operator will almost stay unchanged, except that near the left and right edges two  $2k$ -site unitaries  $L_g$  and  $R_g$  emerge (see Fig. 3.6(a)). These two unitaries on the physical level turn out to be related to  $x_g$  and  $y_g$  on the virtual level via

$$L_g = u^\dagger(x_e \otimes y_g)u, \quad R_g = u^\dagger(x_g \otimes y_e)u, \quad (3.105)$$

leading to (cf. Eqs. (3.28) and (3.29))

$$\text{ind}_g - \text{ind} = \frac{1}{2} \ln \left| \frac{\text{Tr } L_g}{\text{Tr } R_g} \right|. \quad (3.106)$$

It is now clear from Eq. (3.106) that  $\text{ind}_g$  gives a measure of the *edge imbalance* in the  $g$ -string operator evolved by the MPU.

Let us provide the detailed derivation of Eq. (3.105). Without loss of generality, we first assume  $\mathcal{U}$  to be simple (otherwise block and, if so, redefine  $\mathcal{U}_k$  as  $\mathcal{U}$  and correspondingly  $\rho_g^{\otimes k} \rightarrow \rho_g$ ) so that Eq. (3.6) may be satisfied. Applying Eqs. (3.6) and (3.11) to an evolved  $g$ -string operator  $U^\dagger \rho_g^{\otimes l} U$ , we identify  $L_g$  and  $R_g$  to be

$$L_g = \text{circuit diagram}, \quad R_g = \text{circuit diagram}. \quad (3.107)$$

Substituting the singular-value decomposed forms

$$\text{circuit diagram} = \text{circuit diagram} = \text{circuit diagram}. \quad (3.108)$$

into Eq. (3.107), we obtain

$$L_g = \text{circuit diagram} = \text{circuit diagram}, \quad (3.109)$$

and

$$R_g = \text{circuit diagram} = \text{circuit diagram}. \quad (3.110)$$

Here we have used the definition properties of singular-value decomposition

$$\begin{array}{c} \text{---} \\ | \\ \text{---} \end{array} = \begin{array}{c} | \\ \text{---} \\ | \end{array}, \quad \begin{array}{c} \text{---} \\ | \\ \text{---} \\ | \\ \text{---} \\ | \\ \text{---} \end{array} = \begin{array}{c} \text{---} \\ | \\ \text{---} \\ | \\ \text{---} \\ | \\ \text{---} \end{array} \quad (3.111)$$

and the symmetry constraint (complementary to Eq. (3.19))

$$\begin{array}{c} \text{---} \\ | \\ \text{---} \end{array} = \begin{array}{c} \text{---} \\ | \\ \text{---} \\ | \\ \text{---} \end{array}, \quad \begin{array}{c} \text{---} \\ | \\ \text{---} \end{array} = \begin{array}{c} \text{---} \\ | \\ \text{---} \\ | \\ \text{---} \end{array}. \quad (3.112)$$

Note that Eqs. (3.109) and (3.110) are nothing but Eq. (3.105). It is worth mentioning that, by evolving a more general string operator  $\rho_g^{\otimes N} \otimes \rho_h^{\otimes L-l}$  with  $g, h \in G$ , we will obtain  $D_{g,h} = u^\dagger(x_g \otimes y_h)u$  near the domain wall whose left is  $\rho_g$  and right is  $\rho_h$ . Note that  $L_g = D_{e,g}$  and  $R_g = D_{g,e}$ .

As a byproduct of Eq. (3.107), we can compute the relative SPI from a single  $\mathcal{U}$ , which is not necessarily simple. For  $\forall g \in G$  with  $\chi_g \neq 0$ , replacing  $\mathcal{U}$  and  $\rho_g$  in Eq. (3.107) with  $\mathcal{U}_k$  (which is simple) and  $\rho_g^{\otimes k}$ , respectively, followed by taking the trace and using

$$\begin{array}{c} \text{---} \\ | \\ \text{---} \end{array} = d \begin{array}{c} \text{---} \\ | \\ \text{---} \end{array} \quad (3.113)$$

$k$  times, we obtain

$$\text{Tr } L_g = d^k \chi_g^k \text{Tr } \Sigma_g, \quad (3.114)$$

where  $\Sigma_g \equiv \mathcal{E}_g^k(z_g^\dagger \Sigma)$  and

$$\mathcal{E}_g \equiv \chi_g^{-1} \begin{array}{c} \text{---} \\ | \\ \text{---} \end{array}. \quad (3.115)$$

Using the fact that for  $\forall k \geq k_0$  ( $k_0$ : smallest integer such that  $\mathcal{U}_{k_0}$  is simple)

$$\begin{array}{c} \text{---} \\ | \\ \text{---} \end{array} = \begin{array}{c} \text{---} \\ | \\ \text{---} \end{array}, \quad (3.116)$$

which can be obtained from contracting the rightmost  $k_0$  identities in

$$\begin{array}{c} \text{---} \\ | \\ \text{---} \end{array} = \begin{array}{c} \text{---} \\ | \\ \text{---} \end{array} = \begin{array}{c} \text{---} \\ | \\ \text{---} \end{array} = \begin{array}{c} \text{---} \\ | \\ \text{---} \end{array} = \begin{array}{c} \text{---} \\ | \\ \text{---} \end{array} \quad (3.117)$$

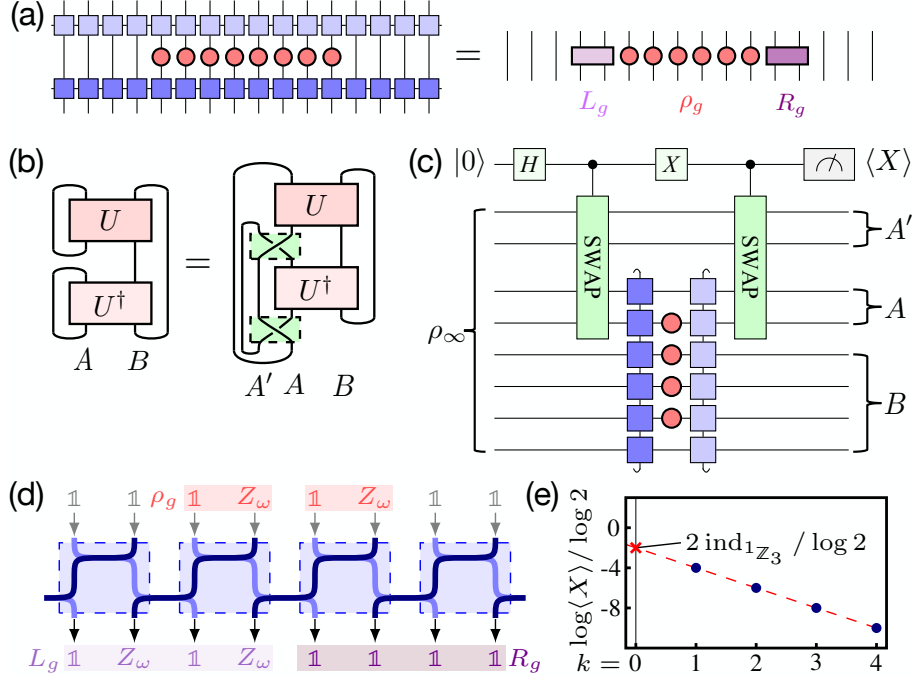


Figure 3.6: (a) Symmetry string operator evolved by a symmetric MPU. Only the left and right edges are modified into  $L_g$  and  $R_g$ , respectively. (b) Tensor-network representation of  $\text{Tr}_B[\text{Tr}_A U \text{Tr}_A U^\dagger] = \text{Tr}[USU^\dagger S]$ , where  $S$  (green rectangles) is the SWAP operator between subsystem  $A$  and its copy  $A'$ . (c) Interferometric approach to probing the relative SPI (3.106). Initially, the qubit is set to be  $|0\rangle$  while the remaining part is prepared in the infinite-temperature state  $\rho_\infty$ . Here  $H$  is the Hadamard gate and the controlled-SWAP gate reads  $U_{CS} = |0\rangle\langle 0| \otimes \mathbb{1}_{A'A} + |1\rangle\langle 1| \otimes S$ . The final expectation value  $\langle X \rangle$  of the qubit is related to  $|\text{Tr} L_g|$  and thus the relative SPI. (d) Bilayer SWAP circuit subject to  $\mathbb{Z}_N$  symmetry. (e) SPI of (d) with respect to  $1_{\mathbb{Z}_{N=3}}$  determined by linear fitting (3.127). Reproduced from Fig. 2 of Ref. [38]. Copyright © 2020 by the American Physical Society.

with  $k' = k + k_0$ , as well as the symmetry requirement, we know that  $\Sigma_g = \mathcal{E}_g^{k_0}(z_g^\dagger \Sigma)$  and satisfies  $\mathcal{E}_g(\Sigma_g) = \Sigma_g$ . On the other hand, due to  $\text{Tr} \mathcal{E}_g^n = 1$  for  $\forall n \in \mathbb{Z}^+$ , the fixed point of  $\mathcal{E}_g$  is unique (just like  $\mathcal{E} = \mathcal{E}_e$ ). Therefore, we can determine  $\Sigma_g$  by solving  $\mathcal{E}_g(\Sigma_g) = \Sigma_g$  subject to  $\text{Tr} z_g \Sigma_g = 1$ , where both  $\mathcal{E}_g$  and  $z_g$  can be obtained from a single  $\mathcal{U}$ . According to Eq. (3.114) and  $\text{Tr} L_g \text{Tr} R_g = d^{2k} \chi_g^{2k}$ , the relative SPI is directly related to  $\Sigma_g$  by

$$\text{ind}_g - \text{ind} = \ln |\text{Tr} \Sigma_g|. \quad (3.118)$$

Recalling that the index  $\text{ind}$  does not rely on blocking, according to Eq. (3.118), we again confirm the blocking independence of  $\text{ind}_g$ .

### Implementation of the measurement

Equation (3.106) opens up the possibility for practically measuring the SPI relative to the index. Noting that

$$\text{Tr} L_g \text{Tr} R_g = d^{2k} \chi_g^{2k}, \quad (3.119)$$

we suffice to measure either  $|\text{Tr} L_g|$  or  $|\text{Tr} R_g|$ . This problem can be simplified into how to measure  $|\text{Tr} U_A|$  for a subsystem unitary  $U_A$  embedded in  $U_{AB} = U_A \otimes U_B$ , where the Hilbert-



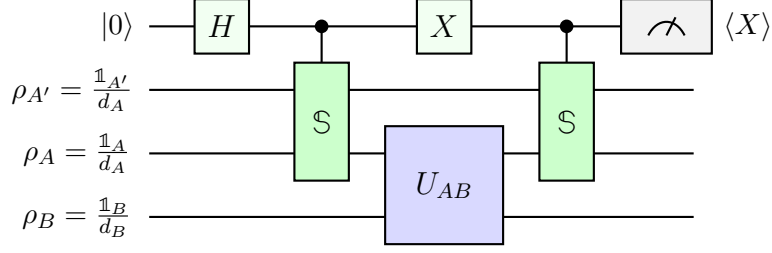


Figure 3.7: Interferometric scheme for measuring  $\text{Tr}_B[\text{Tr}_A U_{AB} \text{Tr}_A U_{AB}^\dagger]$ . Reproduced from Supplementary Fig. 5 of Ref. [38]. Copyright © 2020 by the American Physical Society.

space dimension  $d_B$  of subsystem  $B$  can be much larger than  $d_A$ , which is the dimension of subsystem  $A$ . Combining  $|\text{Tr} U_A|^2 = d_B^{-1} \text{Tr}_B[\text{Tr}_A U_{AB} \text{Tr}_A U_{AB}^\dagger]$  with the identity in Fig. 3.6(b), we obtain

$$|\text{Tr} U_A|^2 = d_A^2 \text{Tr}[U_{AB} \mathbb{S} \rho_\infty U_{AB}^\dagger \mathbb{S}], \quad (3.120)$$

where  $\mathbb{S}$  is the SWAP operator acting on  $A$  and a copy  $A'$  while  $\rho_\infty \equiv d_A^{-2} d_B^{-1} \mathbb{1}_{A'AB}$  is the infinite-temperature state of the entire system including  $A'$ . Since eventually we rewrite  $|\text{Tr} U_A|^2$  into the form of a Loschmidt echo, we can measure it by means of the standard interferometric approach in the following (see also Refs. [159–162]).

We claim that the rhs of Eq. (3.120) can be read out from the expectation value  $\langle X \rangle$  of an auxiliary qubit in Fig. 3.7 for a general bipartite unitary  $U_{AB}$ . To show this, we first recall that the controlled-SWAP gate reads

$$U_{\text{CS}} = |0\rangle\langle 0| \otimes \mathbb{1}_{A'A} + |1\rangle\langle 1| \otimes \mathbb{S}, \quad (3.121)$$

where  $\mathbb{S} \equiv \sum_{j,j'=1}^{d_A} |j_A j_{A'}\rangle \langle j'_A j_{A'}| = \mathbb{S}^\dagger$ , we obtain the unitary evolution of the entire system, including the bipartite physical system  $A \cup B$  with interest, a copy  $A'$  and an auxiliary qubit, as (for simplicity, several subsystem identities are omitted)

$$U_{\text{tot}} = U_{\text{CS}}(X \otimes U_{AB})U_{\text{CS}}H = |1\rangle\langle +| \otimes \mathbb{S}U_{AB} + |0\rangle\langle -| \otimes U_{AB}\mathbb{S}, \quad (3.122)$$

where  $|\pm\rangle \equiv (|0\rangle \pm |1\rangle)/\sqrt{2}$ ,  $X \equiv |1\rangle\langle 0| + |0\rangle\langle 1|$ , and  $H \equiv (X + Z)/\sqrt{2}$  (namely the Hadamard gate) with  $Z \equiv |0\rangle\langle 0| - |1\rangle\langle 1|$ . At the initial time, we prepare the qubit in the pure state  $|0\rangle$  and the remaining systems in the infinite-temperature state  $\rho_\infty \equiv d_A^{-2} d_B^{-1} \mathbb{1}_{A'AB}$ . After evolving the entire system by  $U_{\text{tot}}$  (3.122), we measure the qubit under the  $X$  basis, so that the expectation value  $\langle X \rangle$  should be

$$\begin{aligned} \langle X \rangle &= \text{Tr}[X U_{\text{tot}}(|0\rangle\langle 0| \otimes \rho_\infty)U_{\text{tot}}^\dagger] = \text{Re} \text{Tr}[X U_{\text{tot}}(|+\rangle\langle -| \otimes \rho_\infty)U_{\text{tot}}^\dagger] \\ &= d_A^{-2} d_B^{-1} \text{Tr}[U_{AB} \mathbb{S} U_{AB}^\dagger \mathbb{S}], \end{aligned} \quad (3.123)$$

where we have used  $|0\rangle\langle 0| = \frac{1}{2}(\mathbb{1}_{\text{qubit}} + |-\rangle\langle +| + |+\rangle\langle -|)$  and  $\text{Tr}[\mathbb{S}U_{AB}\mathbb{S}U_{AB}^\dagger] = \text{Tr}[U_{AB}\mathbb{S}U_{AB}^\dagger\mathbb{S}]$ . Combining Eqs. (3.123) and (3.120), we end up with

$$|\text{Tr} U_A| = d_A \sqrt{\langle X \rangle}. \quad (3.124)$$

Let us return to discuss how to measure the relative SPI, for which we should implement  $U_{AB}$  as  $U^\dagger \rho_g^{\otimes l} U$ . See Fig. 3.6(c) for a schematic illustration. Thanks to the locality-preserving property of MPUs, we can choose  $A$  to be as small as  $2k_0 \sim \mathcal{O}(1)$  sites, where  $k_0$  is the smallest  $k$  such that  $\mathcal{U}_k$  is simple, across the left domain wall between  $\rho_g$  and  $\mathbb{1}$ . The controlled-SWAP

gate between  $A$  and its copy can be decomposed into  $2k_0$  individual two-site controlled-SWAP gates acting only on the  $j$ th site of  $A$  and that of the copy. Once we succeed in measuring  $\langle X \rangle$ , we obtain

$$|\mathrm{Tr} L_g| = d^{2k_0} \sqrt{\langle X \rangle}, \quad (3.125)$$

so that the relative SPI reads

$$\mathrm{ind}_g - \mathrm{ind} = \ln \frac{|\mathrm{Tr} L_g|}{d^{k_0} |\chi_g|^{k_0}} = \frac{1}{2} \ln \langle X \rangle + k_0 \ln \frac{d}{|\chi_g|}. \quad (3.126)$$

By choosing  $A$  as  $2k$  sites with  $k \geq k_0$  across the left edge of the symmetry string operator, following a similar analysis, we can obtain Eq. (3.126) with  $k_0$  replaced by  $k$ :

$$\mathrm{ind}_g - \mathrm{ind} = \frac{1}{2} \ln \langle X \rangle + k \ln \frac{d}{|\chi_g|}. \quad (3.127)$$

Note that  $\langle X \rangle$  also depends on  $k$ . Equation (3.127) implies that, even if  $d$  and  $\chi_g$  are unknown, we are still able to measure  $\langle X \rangle$  with increasing length  $2k$  of  $A$  and then extract  $\mathrm{ind}_g$  from a linear fitting. See Figs. 3.6(d) and (e) for the example of the bilayer SWAP circuit subject to  $\mathbb{Z}_3$  symmetry and the linear fitting for determining its SPI.

### 3.5 Implications for Floquet topological phases

Recalling the relation between MPUs and Floquet systems, we can deduce that the (strong) equivalence between MPUs are *necessary* for the (strong) equivalence between the corresponding  $G$ -symmetric 2D MBL Floquet systems – they are continuously connected without crossing a delocalization point [37, 148, 149]. This is because MBL implies a spatial factorization of the bulk Floquet unitary and its separation from the boundary unitary, which is 1D, locality-preserving and thus well described by an MPU [37]. A continuous deformation of the Floquet system thus gives rise to that of the edge MPU. Conversely, two inequivalent MPUs *sufficiently* distinguish their parent Floquet systems.

It is thus natural to ask whether an MPU with nontrivial SPIs can be embedded into a parent Floquet system, just like those with nontrivial indices [37] and cohomology classes [148, 149]. Since topologically different MPUs distinguish different MBL parent Floquet systems, the embeddability would imply a new class of 2D SPT Floquet phases characterized by SPIs. We answer in the affirmative by giving a general construction shown in Fig. 3.8(a), whose bulk is trivial and thus many-body localizable [163], while the edge dynamics is governed by an MPU generated by  $u$  and  $v = u^\dagger \mathbb{S}_v$ , where  $\mathbb{S}_v$  exchanges the virtual Hilbert spaces  $\mathbb{C}^l$  and  $\mathbb{C}^r$ . This construction is inspired by the standard form (3.8) and the four-step SWAP model [37, 67, 164] — we compose two four-step SWAP processes, one on the left virtual Hilbert spaces and pulled back by  $u$ , and the other on the physical level.

The above general construction of parent Floquet systems in turn gives a simple *symmetry-charge-pump* picture for topological MPUs. Here a  $G$ -symmetry charge refers to a Hilbert space on which  $G$  acts as a linear (integer charge) or projective representation (fractional charge). These charges can fuse or split following the fusion rules set by the group structure. With the physical and the left virtual charge in the standard form denoted as  $q_\rho \equiv kq_\rho$  and  $q_x$ ,<sup>5</sup> an MPU segment coupled to two symmetry reservoirs  $R_{l,r}$  right-translates  $q_\rho$  and left-translates

<sup>5</sup>Technically speaking, according to the character theory of projective representations [157],  $q_x$  is specified by a 2-cocycle  $\theta : G \times G \rightarrow 2\pi\mathbb{R}/\mathbb{Z}$  and a vector  $\eta : G \rightarrow \mathbb{C} \cup \{-\infty\}$ ,  $\eta(g) = \ln \mathrm{Tr} x_g$  (we take  $\ln$  to make  $q$  additive) subject to the gauge transformation  $\theta(g, h) \rightarrow \theta(g, h) + \tau(g) + \tau(h) - \tau(gh)$ ,  $\eta(g) \rightarrow \eta(g) + i\tau(g)$  for  $\forall \tau : G \rightarrow 2\pi\mathbb{R}/\mathbb{Z}$ .

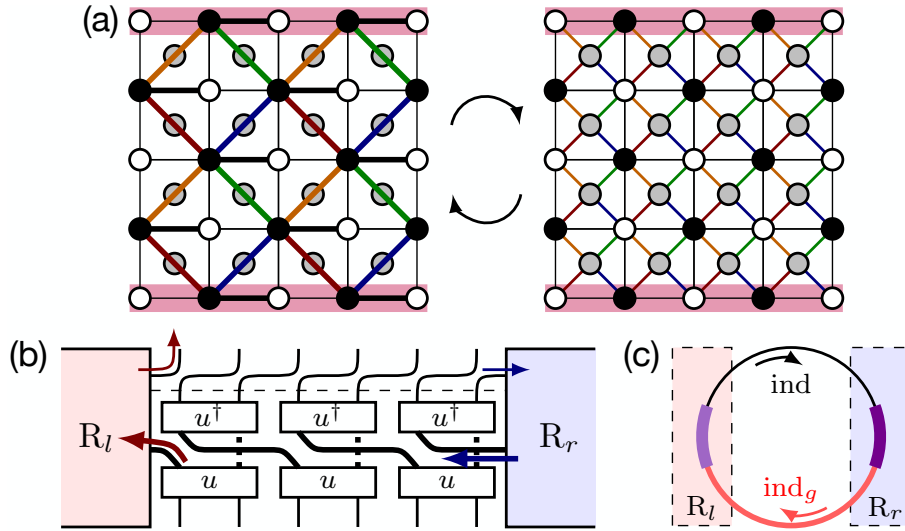


Figure 3.8: (a) 2D Floquet system with a trivial bulk and a nontrivial edge dynamics (shaded in magenta) governed by an MPU. The open (periodic) boundary condition is imposed on the vertical (horizontal) direction. In the first (left panel)/second (right panel) half period, we apply  $u$ -conjugated (thick black bonds) SWAP gates (thick color bonds)/physical-level SWAP gates (color bonds) sequentially as red→blue→green→orange. (b) MPU segment as a symmetry-charge pump that transfers  $q_\phi$  from  $R_l$  to  $R_r$  and  $q_x$  from  $R_r$  to  $R_l$ . The circuits above/below the dashed line are generated by the left/right panel in (a). (c) Edge imbalance (light/dark purple) in an evolved  $g$ -string operator (pink) from current imbalance (3.106). Reproduced from Fig. 3 of Ref. [38]. Copyright © 2020 by the American Physical Society.

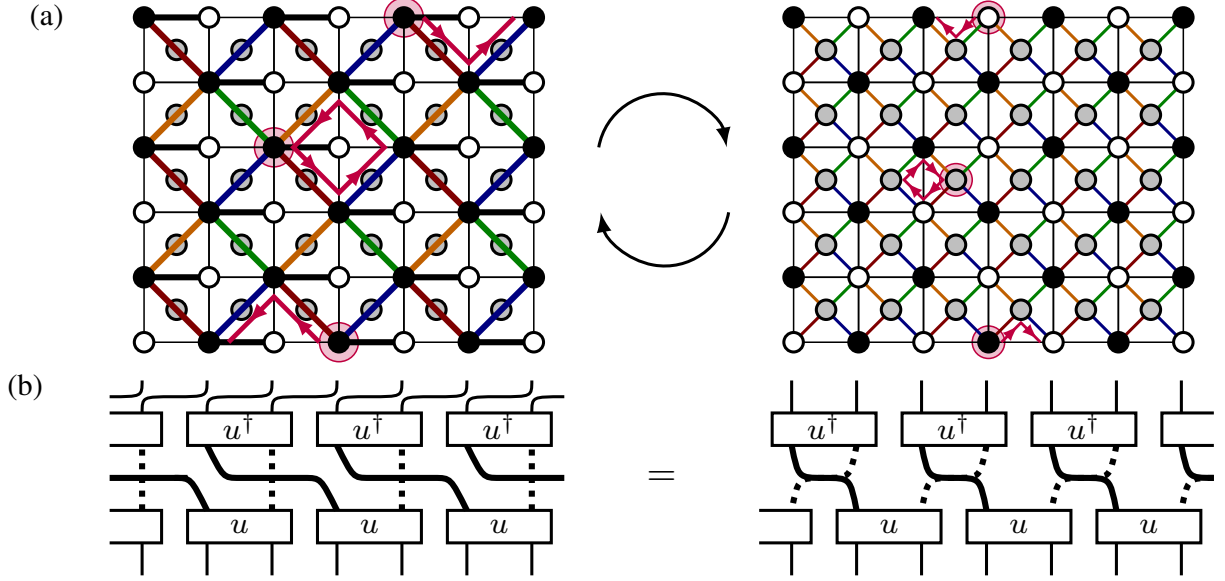


Figure 3.9: (a) General construction of a 2D symmetric Floquet system whose edge dynamics is characterized by a nontrivial SPI. (Left) The thick black lines denote the conjugation by  $u : \mathbb{C}^{d^k} \otimes \mathbb{C}^{d^k} \rightarrow \mathbb{C}^l \otimes \mathbb{C}^r$  and all the colored lines are the SWAP gates on two copies of  $\mathbb{C}^l$  (left virtual Hilbert space). After  $u$  conjugations, the SWAP gates are pulled back to the physical level. (Right) Each colored line corresponds to a SWAP gate on two copies of  $\mathbb{C}^d$  (physical Hilbert space). In both figures, the SWAP gates are switched on sequentially as red  $\rightarrow$  blue  $\rightarrow$  green  $\rightarrow$  orange. The bulk dynamics of the Floquet system is trivial, as indicated by the arrows forming loops. (b) Tensor-network representation (standard form) of the (bottom) edge dynamics. The lhs corresponds directly to the action by (a) Left followed by (a) Right, while it is clear from the rhs that  $v = u^\dagger \mathbb{S}_v$ , where  $\mathbb{S}_v$  is the SWAP gate  $\mathbb{C}^l \otimes \mathbb{C}^r \rightarrow \mathbb{C}^r \otimes \mathbb{C}^l$  that exchanges the left and right virtual Hilbert spaces. Reproduced from Supplementary Fig. 8 of Ref. [38]. Copyright © 2020 by the American Physical Society.

$q_x$  (see Fig. 3.8(b)). In fact, the cohomology class and the SPIs (including the index) are all characters of the net symmetry-charge current  $q_\varrho - q_x$ . This picture unifies all the related previous works as special situations, such as  $G = \{e\}$  [37, 164] and  $\text{Tr } x_g = \text{Tr } \varrho_g = \delta_{ge} \dim \varrho$  [148, 149]. Remarkably, this picture gives an intuitive insight into Eq. (3.106): We regard two equally long segments centered at the edges of a  $g$ -string operator as  $R_{l,r}$ , which are connected by two pumps with inputs  $g$  and  $e$  (see Fig. 3.8(c)). We can then interpret Eq. (3.106) as an *equation of continuity*, with the left- and right-hand sides being the current and the change of charge, respectively. There is a factor 1/2 since a net flow of charge  $q$  causes  $2q$  charge imbalance.

Finally, let us explain the details of the Floquet system in Fig. 3.8(a), which would be helpful for understanding why its bulk is trivial while its edge dynamics is described by a nontrivial MPU. We extend this lattice model in Fig. 3.9(a), where black and white sites live on the vertices of square plaquettes while gray sites live in the centers. Regardless of the color, each site is assigned with a local Hilbert space  $\mathbb{C}^{d^k}$ , where the symmetry is linearly represented as  $\varrho \equiv \rho^{\otimes k}$ . We impose the same boundary conditions as in Fig. 3.8(a). In the first half of a Floquet period, we sequentially apply direct products of  $u$ -conjugated SWAP gates of black

sites as follows (see Fig. 3.9(a) Left):

$$U_{2D} = U_{\leftarrow} U_{\leftarrow} U_{\leftarrow} U_{\leftarrow}, \quad (3.128)$$

where

$$U_{\leftarrow} = \bigotimes_{\leftarrow} u_{\leftarrow}^{\dagger \otimes 2} \mathbb{S}_{\leftarrow} u_{\leftarrow}^{\otimes 2}, \quad (3.129)$$

with  $\mathbb{S}_{\leftarrow}$  acting on two copies of  $\mathbb{C}^l$ , on which the symmetry is represented as  $x$ . Here the identities on the virtual Hilbert space  $\mathbb{C}^r$ , where the symmetry representation is  $y$ , are omitted for simplicity. Other unitaries in Eq. (3.128) are defined similarly. One can check that  $U_{2D}$  is trivial in the bulk, while the left virtual Hilbert spaces  $\mathbb{C}^l$  are left(right)-translated to the nearest one (separated by two physical sites) at the lower (upper) boundary (see the arrows at the edges of Fig. 3.9(a) Left). In the second half of a Floquet period, we sequentially apply direct products of SWAP gates on the physical level as follows (see Fig. 3.9(a) Right):

$$U'_{2D} = (U'_{\leftarrow} \otimes U'_{\leftarrow})(U'_{\rightarrow} \otimes U'_{\rightarrow})(U'_{\leftarrow} \otimes U'_{\leftarrow})(U'_{\rightarrow} \otimes U'_{\rightarrow}), \quad (3.130)$$

where

$$U'_{\rightarrow} \otimes U'_{\rightarrow} = \bigotimes_{\rightarrow} \mathbb{S}_{\rightarrow} \otimes \bigotimes_{\rightarrow} \mathbb{S}_{\rightarrow}, \quad (3.131)$$

with  $\mathbb{S}_{\rightarrow}$  and  $\mathbb{S}_{\leftarrow}$  acting on two copies of  $\mathbb{C}^d$ . This is exactly the model studied in Refs. [37] and [164], which is the bosonic counterpart of the anomalous Floquet insulator of free fermions [67]. Such a unitary is also trivial in the bulk, while the dynamics at the lower (upper) edge is the one-site right (left) translation (see the arrows at the edges of Fig. 3.9(a) Right). The entire Floquet operator is given by  $U'_{2D} U_{2D}$ , which again has a trivial bulk, but exhibits nontrivial edge dynamics described by the MPU given in Fig. 3.9(b).

## Chapter 4

# Topological phases of non-Hermitian systems

In the preceding two chapters, we mainly focused on the unique dynamical phases in periodically driven systems including discrete time crystals and Floquet topological phases. On top of periodic driving, dissipation provides yet another widely used tool for bringing a system out of equilibrium. In this chapter, we discuss the topological phases in the simplest class of dissipative systems described by non-Hermitian Hamiltonians. These systems are of increasing recent interest due partially to their strong experimental relevance to a large variety of open classical and quantum systems such as photonic lattices with gain and loss, active mechanical metamaterials, electrical circuits, exciton-polariton systems and dissipative Bose-Einstein condensates. Unlike the topological phases at equilibrium, non-Hermitian topological phases are generally dynamical phases in the sense that not only the eigenstates but also the complex eigenenergies can play crucial roles and have important dynamical consequences. With the help of the techniques developed for classifying Floquet topological phases, we obtain a systematic classification of non-Hermitian topological phases with Altland-Zirnbauer (AZ) symmetries in all dimensions, in analogy with the periodic table for topological insulators and superconductors. Here, the most fundamental example of a topological phase that does not require any symmetry protection and hence may be considered as the counterpart of 2D quantum Hall insulators in Hermitian physics, turns out to be the 1D Hatano-Nelson model.

### 4.1 Introduction

#### 4.1.1 Background, motivation and the main results

Topological phases of matter [21, 130, 165–167] have attracted growing interest over the last decade in many subfields of physics, including condensed matter physics [4, 9, 12, 42, 168–170], ultracold atomic gases [13, 17, 20, 171–176], quantum information [177–180], photonics [10, 19, 181–188] and mechanics [189–192]. Topological phase transitions lie outside the Landau paradigm of spontaneous symmetry breaking [48]; instead, they are sometimes protected by certain symmetries and become trivial once the symmetries are broken [193]. Among such SPT phases, free-fermion systems, which are usually referred to as topological insulators and superconductors, are arguably the most well-understood class. Their systematic topological classifications have been achieved for various setups ranging from the fundamental AZ classes [39–41, 194, 195] to complicated crystalline materials [196–202]. These novel states of matter exhibit robust edge modes localized at open boundaries [203, 204] and degenerate or gapless entanglement spectra for subsystems [205]. The gapped bulks are characterized by highly nonlocal topological indices, which

Table 4.1: Periodic table for non-Hermitian Hamiltonians. The Altland-Zirnbauer ten-fold classes [39, 40, 194] are grouped into six such that classes A, DIII and CI, classes AI and D, and classes AII and C are unified. The Bott periodicity of classifying (cl.) space  $\mathcal{C}_1$  ( $\mathcal{C}_1 \times \mathcal{C}_1$ ) is 2, and that of  $\mathcal{R}_s$  ( $\mathcal{R}_s \times \mathcal{R}_s$ ,  $s = 1, 5$ ) is 8. Note that all the classes are nontrivial (trivial) in  $d = 4n + 1$  ( $d = 4n + 2$ ) dimensions, where  $n = 0, 1, 2, \dots$ .

AZ class	Cl. space	$d = 0$	1	2	3	4	5	6	7
A, DIII, CI	$\mathcal{C}_1$	0	$\mathbb{Z}$	0	$\mathbb{Z}$	0	$\mathbb{Z}$	0	$\mathbb{Z}$
AIII	$\mathcal{C}_1 \times \mathcal{C}_1$	0	$\mathbb{Z} \oplus \mathbb{Z}$	0	$\mathbb{Z} \oplus \mathbb{Z}$	0	$\mathbb{Z} \oplus \mathbb{Z}$	0	$\mathbb{Z} \oplus \mathbb{Z}$
AI, D	$\mathcal{R}_1$	$\mathbb{Z}_2$	$\mathbb{Z}$	0	0	0	$2\mathbb{Z}$	0	$\mathbb{Z}_2$
BDI	$\mathcal{R}_1 \times \mathcal{R}_1$	$\mathbb{Z}_2 \oplus \mathbb{Z}_2$	$\mathbb{Z} \oplus \mathbb{Z}$	0	0	0	$2\mathbb{Z} \oplus 2\mathbb{Z}$	0	$\mathbb{Z}_2 \oplus \mathbb{Z}_2$
AII, C	$\mathcal{R}_5$	0	$2\mathbb{Z}$	0	$\mathbb{Z}_2$	$\mathbb{Z}_2$	$\mathbb{Z}$	0	0
CII	$\mathcal{R}_5 \times \mathcal{R}_5$	0	$2\mathbb{Z} \oplus 2\mathbb{Z}$	0	$\mathbb{Z}_2 \oplus \mathbb{Z}_2$	$\mathbb{Z}_2 \oplus \mathbb{Z}_2$	$\mathbb{Z} \oplus \mathbb{Z}$	0	0

can give rise to quantized transport phenomena immune to disorder [206]. More recently, the notion of SPT phases has been generalized to periodically driven (Floquet) systems [69–71, 119], which accommodate new topological phases with no static counterparts [65–67]. Indeed, we have discussed some examples in the previous chapter.

In recent years, considerable efforts have been devoted to explore topological phases in *non-Hermitian* systems [207–215], which are open and out of equilibrium. This burgeoning research arena is largely driven by the experimental progress on atomic, optical and optomechanical systems [216–224], where experimentalists are able to controllably introduce gain and loss. Controlled dissipation can be utilized to engineer an effective non-Hermitian Hamiltonian  $H \neq H^\dagger$ , represented by parity-time ( $PT$ )-symmetric systems [225–231], whose spectra stay real in the  $PT$ -unbroken regimes [232, 233]. In contrast to Hermitian systems, in general, the eigenenergies of a non-Hermitian Hamiltonian are complex, and the right eigenstates are neither orthogonal to each other nor equivalent to the corresponding left ones. Furthermore, the right eigenstates can coalesce and become orthogonal to the corresponding left ones at an exceptional point [234], where  $H$  cannot be diagonalized. Previous works have mostly focused on topological properties associated with the exceptional point. Some unique topological objects with no Hermitian counterparts are identified, such as anomalous edge modes characterized by half-integers [212] and Weyl exceptional rings with both the quantized Chern number and the quantized Berry phase [214]. Non-Hermitian systems emerge ubiquitously in a variety of situations including open quantum systems [87, 235–242], mesoscopic physics [243–245], biological physics [246–248] and chemistry [249–251], where topology can play important roles [235, 241, 248, 249].

Nevertheless, a systematic understanding of topological phases of non-Hermitian systems is still elusive. Inspired by the periodic table for Hermitian topological insulators and superconductors [39, 40, 194], we are naturally led to the following questions:

- (i) Can we classify non-Hermitian systems in analogy with the topological phases in closed quantum systems (i.e., Hermitian systems)?
- (ii) If yes, then what is the non-Hermitian counterparts of AZ classes?
- (iii) Is there a quantum-Hall-like non-Hermitian system which has no symmetry yet is topologically nontrivial?
- (iv) Is there a bulk-edge correspondence in non-Hermitian systems?

Regarding these fundamental questions, it seems that exceptional points, while unique to non-Hermitian systems, may not be a good starting point for a systematic classification, since

they imply band touching in the bulk and seem incompatible with a non-Hermitian generalization of gap. We note that two very recent works [252, 253] have made efforts to build a general framework following the methodology for gapped Hermitian systems. In particular, Ref. [252] focuses on 1D lattices with on-site loss and no dark states, and identifies a topological winding number relevant to particle displacement; Ref. [253] mainly discusses 2D non-Hermitian lattices with separable bands in the complex-energy plane, and identifies a Chern number for individual bands. However, these results are rather specific in spatial dimensions and/or the structure of the Hamiltonian.

Here, we present a systematic framework for studying the topological phases of generic non-Hermitian systems. For the sake of comparison with Hermitian free-fermion systems, we focus primarily on lattice systems described by non-Hermitian Bloch Hamiltonians  $H(\mathbf{k})$ . Our framework is based on two guiding principles:

- (I) Topological phases of non-Hermitian systems can be understood as *dynamical* phases, where not only the eigenstates but also the *full complex spectra* should be taken into account;
- (II) The non-Hermitian generalization of the concept of the band gap is the *prohibition* of touching a base energy, which is typically zero but can generally be complex, in the spectrum.

We show that (I) and (II) are well justified both physically and mathematically. On the basis of these two guiding principles, we find that a 1D lattice with *asymmetric* hopping amplitudes, known as the Hatano-Nelson model [43, 254], turns out to be the most prototypical example comparable to the quantum Hall insulator, in the sense that an integer topological number can be defined without any symmetry protection. We also unveil a bulk-edge correspondence which is qualitatively different from the Hermitian case: There is a *continuum* of (quasi-)edge modes in the *semi-infinite* space (open chain), with the winding number being the degeneracy at a given base energy. These findings answer the last two questions (iii) and (iv) raised in the preceding paragraph.

Our guiding principles also enable a systematic application of the *K-theory* [255], a technique widely used in classifying Hermitian topological systems [40, 195, 200], to the non-Hermitian AZ classes, leading to a complete classification in all spatial dimensions. We introduce a *unitarization* procedure as a non-Hermitian generalization of band flattening, followed by a *Hermitianization* procedure to represent the classifying space as a Clifford-algebra extension [119]. The classification problem turns out to be mathematically equivalent to that of the Hermitian AZ classes with an additional chiral symmetry, leading to a dramatically different periodic table as shown in Table 4.1. We identify the underlying topological numbers implied by the *K-theory* classification for all the non-Hermitian AZ classes in 1D. These results answer the first two questions (i) and (ii) raised above, and can further be generalized to, e.g., systems with crystalline symmetries and especially to *PT*-symmetric systems.

Finally, we should point out that question (ii) was not completely answered in Ref. [44]. Since transposition is not equivalent to complex conjugation for a general matrix, fundamental symmetry classes are actually richer than the ten-fold AZ classes for non-Hermitian systems. These symmetric classes are called Bernard-LeClair classes, which were first proposed in the context of random matrices [256], and the complete classifications for all these classes were completed in Refs. [257, 258]. Nevertheless, the main ideas and techniques of Ref. [44] can straightforwardly be applied to deal with the additional symmetry classes.



### 4.1.2 Definition of non-Hermitian topological phases

Before discussing the topological aspects of non-Hermitian systems, it is instructive to give a short introduction to non-Hermitian systems themselves. Formally, a non-Hermitian system is described by the following nonunitary Schrödinger equation:

$$i\partial_t|\psi_t\rangle = H|\psi_t\rangle, \quad (4.1)$$

where  $|\psi_t\rangle$  is the state vector of the system at time  $t$  and  $H$  is a non-Hermitian linear operator. While Eq. (4.1) is almost the same as the conventional Schrödinger equation except for the absence of Hermiticity constraint on  $H$ , the underlying system may not necessarily be quantum mechanical. Indeed, there are various classical systems, such as mechanical metamaterials with frictions or active feedback controls [259–261] and electric circuits with resistors or/and nonreciprocal devices [262–264], whose equations of motion take the form of Eq. (4.1) [265]. On the other hand, it is possible to realize a non-Hermitian quantum system on the basis of reservoir engineering [26, 266–269]. Generally speaking, by engineering a GKSL master equation [270, 271]

$$\dot{\rho}_t = -i[H, \rho_t] + \sum_j \mathcal{D}[L_j]\rho_t, \quad (4.2)$$

where  $\mathcal{D}[L]\rho \equiv L\rho L^\dagger - \{L^\dagger L, \rho\}/2$ , we can obtain an effective non-Hermitian Hamiltonian

$$H_{\text{eff}} = H - \frac{i}{2} \sum_j L_j^\dagger L_j \quad (4.3)$$

under postselection of no-jump trajectories [238, 239, 272] or for loss processes of a coherent condensate [214, 216, 241].

We are now in a position to address the main issue of this chapter. We begin by discussing how to define topological phases. In a gapped Hermitian system, a topological phase can be analyzed from the many-body ground-state wave function  $|\Psi\rangle$ . In particular, for free-fermion systems,  $|\Psi\rangle = (\prod_{E_j < E_F} f_j^\dagger)|\text{vac}\rangle$  has a one-to-one correspondence to the projector

$$P_- = \sum_{E_j < E_F} |\varphi_j\rangle\langle\varphi_j| \quad (4.4)$$

that projects the state onto all the single-particle eigenstates  $|\varphi_j\rangle = f_j^\dagger|\text{vac}\rangle$  below the Fermi energy  $E_F$ . Note that the spectrum plays no role here, since the Hamiltonian  $H$  on the single-particle level can be flattened by means of the projector (4.4) into  $1 - 2P_-$  [39, 40, 194] without closing the band gap, as schematically illustrated in Fig. 4.1 (a). Two gapped Hamiltonians  $H$  and  $H'$  differ topologically if and only if  $|\Psi\rangle$  ( $P_-$ ) cannot continuously be deformed into  $|\Psi'\rangle$  ( $P'_-$ ) under the constraint of the energy gap and certain symmetries. Such a topological distinction between wave functions accords with the “states of matter” interpretation of equilibrium topological phases [4].

However, the very notion of the ground state, be it single- or many-body, breaks down for a non-Hermitian system, since its eigenenergy belongs to the complex-number field  $\mathbb{C}$ , where, unlike the real-number field  $\mathbb{R}$ , an order relation cannot be defined [273]. Indeed, from a physical point of view, non-Hermitian systems are intrinsically nonequilibrium and even unstable. According to the nonunitary Schrödinger equation given in Eq. (4.1), only the single-particle eigenstate with the largest imaginary energy survives in the long-time limit, a phenomenon well known in photonics experiments [230]. It thus cannot be justified to interpret non-Hermitian topological phases simply as topological states of matter.

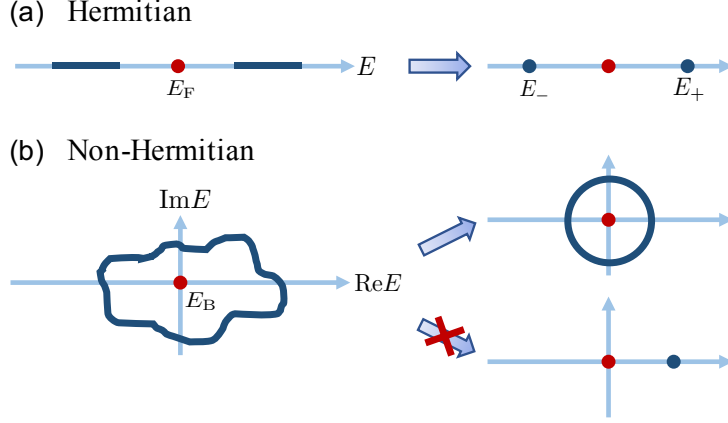


Figure 4.1: (a) Energy spectrum (thick lines and dots) of a Hermitian insulator. We can always perform band flattening, i.e., continuously deform the spectrum into  $\{E_-, E_+\}$  with  $E_- < E_F < E_+$ , where  $E_F$  (red dot) is the Fermi energy. In particular, we can choose  $E_{\pm} = \pm 1$  for  $E_F = 0$ . (b) Energy spectrum of a non-Hermitian system forming a loop that encircles a base point  $E_B \in \mathbb{C}$ . (In the figure we set  $E_B = 0$  for simplicity.) While the shape can be continuously deformed, the loop can never shrink to a single point without crossing or touching the base point. Reproduced from Fig. 1 of Ref. [44]. Copyright © 2018 by the American Physical Society.

Here we argue that the topological phases of non-Hermitian systems can be understood as topological *dynamical* phases, for which not only the eigenstates but also the *full complex spectra* play important roles. In fact, such a dynamical perspective has widely been adopted in the context of thermalization and many-body localization [61], as well as Floquet systems [58]. Examples include the Wigner-Dyson (Poisson) level-spacing statistics in chaotic (integrable) systems [274] and quasi-energy pairing in discrete time crystals [28, 29, 73]. As for non-Hermitian systems, we can immediately identify a unique topological object arising solely from the complex spectrum — a *loop* constituted from eigenvalues that encircles a prescribed base point (see Fig. 4.1 (b)). Here by unique we mean that the topological object discussed here never occurs in a Hermitian system with a real spectrum; by topological we mean that the loop can never be removed without crossing the base point at  $E = E_B$ . If the base point is chosen to be zero, a loop ensures the existence of amplifying ( $\text{Im}E > 0$ ) and attenuating ( $\text{Im}E < 0$ ) modes. Such a topologically enforced dynamical instability (dynamical property) can be compared to topologically protected edge states (state property) in Hermitian systems. Note that the converse is not true, since instability or edge modes may not have a topological origin.

While only the complex spectrum is relevant in the above example, in general, however, both states and the spectrum are important in the complicated transient dynamics governed by Eq. (4.1). Since the full information of dynamical behavior is encoded in the non-Hermitian Hamiltonian  $H$  in Eq. (4.1), we can generally define that two non-Hermitian systems differ topologically if and only if their Hamiltonians cannot continuously be deformed into each other under certain constraints. Here the minimal constraint follows the guiding principle (II), which will be justified in the next section.

Remarkably, by imposing the constraints of Hermiticity and a finite gap, we can reproduce the states-of-matter interpretation in Hermitian systems, at least for noninteracting SPT phases.

Without loss of generality,<sup>1</sup> assuming that  $E_F = 0$  lies in the band gap, the real spectrum can always be trivialized to  $\pm 1$ , leaving the only difference arising from  $P_-$  given in Eq. (4.4). In this sense, the dynamical viewpoint on topological phases is a generalization of the static one.

We would like to recall that Eq. (4.1) should not necessarily be interpreted as a nonunitary equation of motion for a wave function. Indeed, it can be any linear dynamics, such as a classical Markovian process, where  $|\psi_t\rangle$  is a probability distribution [275], or a quantum master equation, where  $|\psi_t\rangle$  is a density operator or a supervector in the Liouville space [276]. In some cases, we may consider a discrete version of Eq. (4.1):

$$|\psi_{t+1}\rangle = U_F |\psi_t\rangle, \quad (4.5)$$

which can be any linear stroboscopic dynamics or even a single input-output process, such as nonunitary quantum walk [229, 277] or quantum channels [278] (see also Sec. 4.4.1). A recent work [118] on classifying Gaussian nonequilibrium steady states  $\rho_{\text{ss}}$  can be regarded as a specific case of Eq. (4.5) with  $\mathcal{U}_\infty(\rho) = \rho_{\text{ss}}$  for all  $\rho$ , where  $\mathcal{U}_\infty = \lim_{t \rightarrow \infty} e^{\mathcal{L}t}$ , and  $\rho_{\text{ss}}$  is the unique (under the periodic boundary condition) kernel of a quadratic GKSL generator  $\mathcal{L}$  with a finite damping gap.

The remainder of this chapter is organized as follows. In Sec. 4.2, we first justify the guiding principle (II) and then discuss the topological properties of non-Hermitian lattices in 1D, including the definition of the winding number, edge physics and experimentally observable signatures. In Sec. 4.3, we employ the  $K$ -theory to achieve a complete classification of non-Hermitian AZ classes in all dimensions, as shown in Table 4.1. The identification of topological numbers and some topologically nontrivial examples in zero and 1Ds are given in Sec. 4.4. While we will primarily discuss translation-invariant systems described by Bloch Hamiltonians, some preliminary results concerning the interplay between topology and disorder can be found in Appendix B.

## 4.2 Topological non-Hermitian lattices in 1D with no symmetry

Before performing a general classification, it is instructive to start from the most illustrative case — 1D lattices without any symmetry. These systems are found to be classified by a topological winding number, provided that a base energy  $E_B$  is not involved in the energy spectrum. We show that such a winding number corresponds to the number of edge states at  $E_B$  in a *semi-infinite* space and is measurable from the wave-packet dynamics.

### 4.2.1 Topological winding number

Let us first clarify the allowed continuous deformation. Note that all the matrices  $M$  can be continuously deformed to zero matrices via the path  $M_\lambda = (1 - \lambda)M$ ,  $\lambda \in [0, 1]$  if there is no constraint. To avoid the situation in which all non-Hermitian systems in all dimensions are trivial, we must impose at least one constraint. In the Hermitian case, such a constraint is the existence of an energy gap near the Fermi energy  $E_F$ , which is equivalent to the condition that  $E_F$  does not belong to the energy spectrum of the Hamiltonian. As a possible generalization to the non-Hermitian case, we impose the condition that a base energy  $E_B \in \mathbb{C}$  does not belong to the energy spectrum of  $H(k)$  for all  $k \in [-\pi, \pi]$ , where  $k$  is the wave number. In analogy with the

---

<sup>1</sup>In the absence of a particle-hole or chiral symmetry, the classification of all the Hermitian Hamiltonians with a given  $E_F$  is equivalent to that with  $E_F = 0$ , since we have a time-reversal-symmetry-preserved one-to-one map  $H \rightarrow H - E_F$  between two sets of Hamiltonians. In the presence of a particle-hole or/and chiral symmetry, although  $E_F$  has arbitrariness for a given system, the only choice of  $E_F$  is zero when considering the set of all such Hermitian Hamiltonians.

Hermitian case where  $E_F$  is typically set to be zero, we assume without loss of generality  $E_B = 0$  such that  $H(k) \in \text{GL}(\mathcal{V})$ , where  $\text{GL}(\mathcal{V})$  is the general linear group on the Hilbert space  $\mathcal{V}$  at a given wave number  $k$ . Such a minimal constraint is not only natural from a mathematical viewpoint, but also physically reasonable, since breaking the invertibility of a Hamiltonian usually requires fine-tuning of parameters. In other words, the constraint should easily be satisfied under random perturbations, as is typically the case with experimental imperfection. Indeed, as will be detailed from now on, our setup does bring fruitful physical insights into non-Hermitian systems.

Mathematically, our minimal constraint reads

$$\det H(k) \neq 0, \quad \forall k \in [-\pi, \pi], \quad (4.6)$$

which allows one to define a topological winding number:

$$w \equiv \int_{-\pi}^{\pi} \frac{dk}{2\pi i} \partial_k \ln \det H(k). \quad (4.7)$$

We note that the generalization to the case of  $E_B \neq 0$  can be achieved by simply replacing  $H(k)$  by  $H(k) - E_B$  in Eqs. (4.6) and (4.7). Let  $E_1(k), E_2(k), \dots, E_N(k) \in \mathbb{C}/\{0\}$  be the eigenenergies of  $H(k)$ , where  $N = \dim \mathcal{V}$  is the total number of bands. Then the winding number (4.7) can be expressed as

$$w = \sum_{n=1}^N \int_{-\pi}^{\pi} \frac{dk}{2\pi} \partial_k \arg E_n(k), \quad (4.8)$$

where  $\arg E_n(k)$  is the argument of the complex energy  $E_n(k)$ . Note that  $w$  always vanishes for Hermitian Hamiltonians because the real energy spectrum implies  $\arg E_n(k)$  is pinned at 0 or  $\pi$ . In this sense, a nontrivial winding number, which counts how many times the complex eigenenergies encircle  $E_B$ , is unique to non-Hermitian systems. Mathematically, the existence of this winding number is ensured by the fact that the fundamental group of  $\text{GL}(\mathcal{V})$  is isomorphic to  $\mathbb{Z}$ . In the next section, we will show that the  $K$ -theory approach also gives the same  $\mathbb{Z}$  classification for 1D systems in class A, which imposes no symmetries. In contrast, class A is topologically trivial in 1D Hermitian systems [39].

As a minimal setup to observe a topological phase transition, we consider a ring geometry with *asymmetric* hopping amplitudes  $J_R, J_L \in \mathbb{C}$  (see Fig. 4.2(a)):

$$H = \sum_j (J_R c_{j+1}^\dagger c_j + J_L c_j^\dagger c_{j+1}). \quad (4.9)$$

Fourier transforming Eq. (4.9) to moment space, we obtain the Bloch Hamiltonian as

$$H(k) = J_R e^{-ik} + J_L e^{ik}, \quad (4.10)$$

whose winding number is evaluated to give

$$w = \begin{cases} 1, & |J_R| < |J_L|; \\ -1, & |J_R| > |J_L|. \end{cases} \quad (4.11)$$

The topological phase-transition point thus locates at  $|J_R| = |J_L|$  (see Fig. 4.2(b)), where  $H(k) = 0$  for  $k = [\arg(J_R/J_L) \pm \pi]/2$  and thus  $H(k)$  is not invertible.

Note that Eq. (4.10) becomes  $H(k) = e^{-ik}$  for the specific choice of  $J_R = 1$  and  $J_L = 0$ , which is known as the one-way model [279]. In this case, the non-Hermitian Hamiltonian

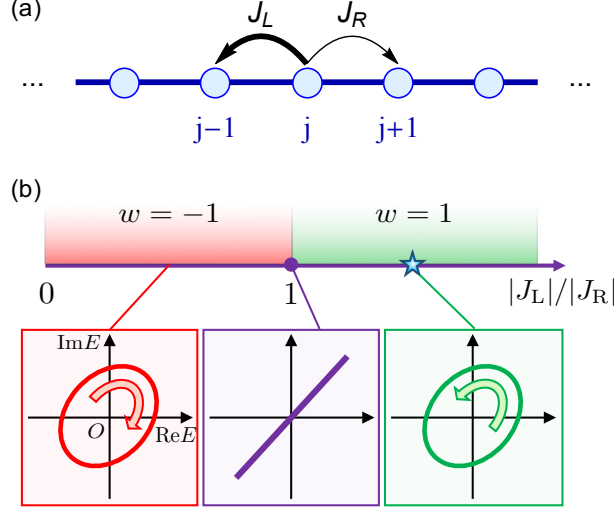


Figure 4.2: (a) 1D lattice with asymmetric hopping amplitudes  $J_L \neq J_R^*$ . Here, we illustrate the case in which  $|J_L| > |J_R|$ , as indicated by the thickness of the arrows. (b) Phase diagram and typical complex energy spectra for the model in (a), where  $w$  is the winding number. A topological phase transition occurs at  $|J_L| = |J_R|$  (purple dot), where the spectrum touches the origin, while the specific case of (a) (blue star) belongs to the  $w = 1$  phase, where the energy spectrum forms a loop encircling the origin. An arrow inside each loop indicates the direction of increasing  $k$  which corresponds to the sign of the winding number  $w$ . Reproduced from Fig. 2 of Ref. [44]. Copyright © 2018 by the American Physical Society.

becomes unitary. Then, if we regard  $H(k)$  as the Floquet operator  $U_F(k)$ , we obtain a Thouless pump [280], which is characterized by the winding number proposed in Ref. [65]:

$$w = \int_{-\pi}^{\pi} \frac{dk}{2\pi i} \text{Tr}[U_F^{-1}(k) \partial_k U_F(k)]. \quad (4.12)$$

In fact, Eq. (4.12) reduces to Eq. (4.7) if we replace  $U_F(k)$  by  $H(k)$ . To see this, it suffices to show the following identity for an invertible matrix with a single parameter:

$$\partial_k \ln \det H(k) = \text{Tr}[H^{-1}(k) \partial_k H(k)]. \quad (4.13)$$

By definition, the lhs of Eq. (4.13) reads

$$\partial_k \ln \det H(k) \equiv \lim_{\epsilon \rightarrow 0} \frac{\ln \det H(k + \epsilon) - \ln \det H(k)}{\epsilon}. \quad (4.14)$$

We only have to take care of the leading-order term in the numerator of the rhs:

$$\begin{aligned} \ln \det H(k + \epsilon) - \ln \det H(k) &= \ln \{ \det [H(k) + \epsilon \partial_k H(k)] / \det H(k) \} + \mathcal{O}(\epsilon^2) \\ &= \ln \det [I + \epsilon H^{-1}(k) \partial_k H(k)] + \mathcal{O}(\epsilon^2) = \epsilon \text{Tr}[H^{-1}(k) \partial_k H(k)] + \mathcal{O}(\epsilon^2), \end{aligned} \quad (4.15)$$

where we have used the identity  $\det e^A = e^{\text{Tr}A}$  and  $\ln(1+x) = x + \mathcal{O}(x^2)$ . Compared to Eq. (4.7), Eq. (4.12) does not seem to have a clear physical meaning but has the advantage of being able to be readily generalized to higher dimensions [194]. Despite some formal similarities, there are also essential differences between non-Hermitian Hamiltonians and Floquet operators, as will be clarified in Sec. 4.3.4.

Remarkably, without symmetry constraints, non-Hermitian systems can support topological phases and transitions even for a single-band lattice like Eq. (4.9). Indeed, we can easily write down a single-band Bloch Hamiltonian  $H(k) = e^{ink}$ , which corresponds to a unidirectional  $|n|$ -site hopping (leftward when  $n > 0$  and rightward when  $n < 0$ ) and features an arbitrary winding number  $n \in \mathbb{Z}$ . This makes a sharp contrast with Hermitian topological systems which require at least two bands. Such a sharp distinction can be understood as follows: According to Eq. (4.8), the winding numbers in non-Hermitian systems are determined solely from complex energies. On the other hand, winding numbers (or Chern numbers) in Hermitian systems are usually related to the Berry phase, which automatically becomes trivial if there is only a single band. We will return to these crucial points in Sec. 4.2.3.

## 4.2.2 Bulk-edge correspondence

As is well known in Hermitian systems, a nontrivial topological number in the bulk usually implies the existence of edge states, such as chiral edge modes in a quantum (anomalous) Hall state with open boundaries [203]. It is thus natural to ask whether the bulk-edge correspondence still holds true in non-Hermitian topological systems. We answer this question in the affirmative, at least for the single-band case. However, the correspondence turns out to be very different from that in Hermitian systems — given a base energy  $E_B$ , a positive (negative) winding number  $w$  implies  $w$  ( $-w$ ) independent edge modes with energy  $E = E_B$  and localized at the left (right) boundary in the *semi-infinite* space.

Let us first focus on the minimal model described by Eq. (4.9). By assuming  $|J_L| > |J_R|$ , we expect an edge state at the left boundary. Indeed, in the limiting case of  $J_R = 0$ ,  $\psi_j = \delta_{j,1}$  is a zero mode localized at the first site. More generally, by imposing the right-half-infinite boundary condition, a state localized at the left boundary can be obtained by solving

$$J_R\psi_{j-1} + J_L\psi_{j+1} = E\psi_j, \quad j = 1, 2, \dots \quad (4.16)$$

subject to

$$\psi_0 = 0, \quad \lim_{j \rightarrow \infty} \psi_j = 0. \quad (4.17)$$

This is a standard problem on a recursive sequence. Denoting  $z_1$  and  $z_2$  as the roots of

$$E = J_R z^{-1} + J_L z, \quad (4.18)$$

which is the characteristic equation of Eq. (4.16), the general form of the wave function can be written as<sup>2</sup>

$$\psi_j = c_1 z_1^j + c_2 z_2^j. \quad (4.19)$$

Accordingly, the conditions in Eq. (4.17) become

$$c_1 + c_2 = 0, \quad |z_1| < 1, \quad |z_2| < 1. \quad (4.20)$$

These conditions lead to a *continuum* of solutions  $\psi_j \propto z_1^j - z_2^j$  with energies that fill the interior of the bulk energy spectrum — a closed loop (see Fig. 4.3 (a)) specified by Eq. (4.10) or Eq. (4.18) with  $|z| = |e^{ik}| = 1$ . Note that  $w = 1$  for any base energy within this loop, including  $E_B = 0$ .

<sup>2</sup>If  $z_1 = z_2$ , we have  $\psi_j = c_1 z_1^j + c_2 j z_1^{j-1}$ . Here the emergence of  $j z_1^{j-1}$  can be understood from the fact that the transfer matrix of  $[\psi_{j+1}, \psi_j]^T$  becomes similar to a  $2 \times 2$  Jordan block with eigenvalue  $z_1$ , whose power has such an off-diagonal entry. See, e.g., Ref. [265] for the calculation of a general analytic function (including power functions) of an arbitrary matrix possibly having a nontrivial Jordan form.

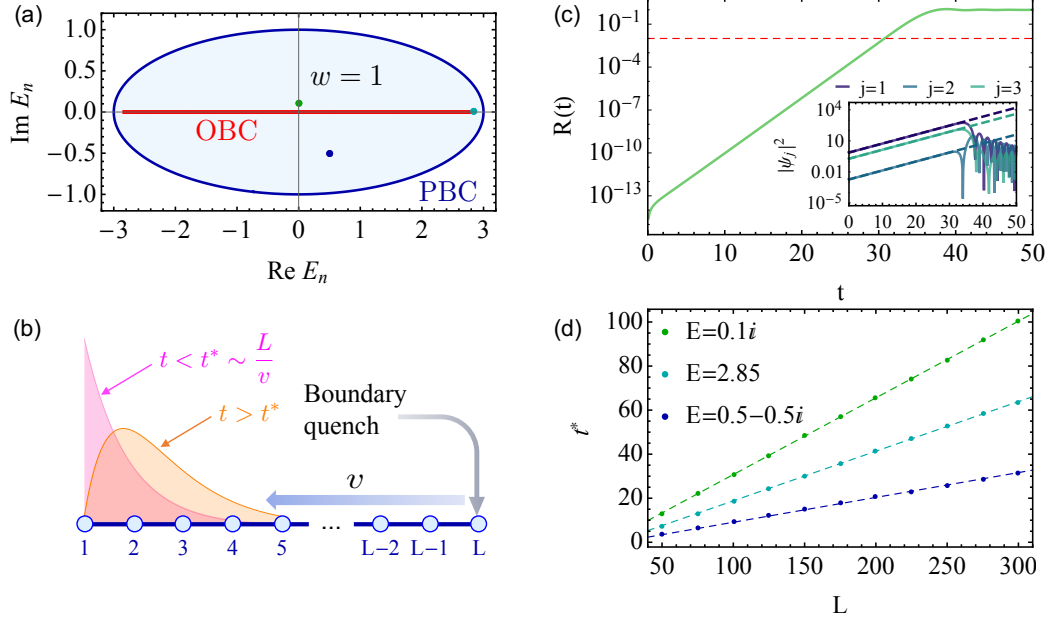


Figure 4.3: (a) Energy spectrum of Eq. (4.9) with  $J_L = 2$  and  $J_R = 1$  under the periodic boundary condition (PBC, blue ellipse) and the open boundary condition (OBC, red line). For each energy  $E$  inside the ellipse (light-blue region) there exists a  $w = 1$  edge state localized at the left boundary in the semi-infinite space. Three colored points show energies of the three quasi-edge modes in (d). (b) An edge state in the semi-infinite space (magenta wave packet) will eventually become unstable (orange wave packet) in a finite open chain with length  $L$  after a time  $t^* \sim L/v$ , where  $v$  is the Lieb-Robinson velocity. (c) Time evolution of the relative deviation  $R(t) \equiv \|[e^{-i(H-E)t} - 1]|\psi\rangle\|$  for the edge state  $|\psi\rangle$  with  $E = 0.1i$  in an open chain with  $L = 100$ . Inset: Time evolution (solid curves) of  $|\psi_j(t)|^2$  at the leftmost three sites ( $j = 1, 2, 3$ ) in comparison with that of  $|\psi_j(t)|^2 = e^{2\text{Im}Et}|\psi_j(0)|^2$  (dashed lines). (d) Finite-size scaling of  $t^*$  for three different quasi-edge states with energies  $E = 0.1i, 2.85$  and  $0.5 - 0.5i$  (marked in (a)). We define  $t^*$  by  $R(t^*) = 10^{-2}$ , as indicated by the dashed red line in (c). Reproduced from Fig. 4 of Ref. [44]. Copyright © 2018 by the American Physical Society.

With the above concrete example in mind, we are ready to generalize the conclusion to arbitrary single bands with positive winding numbers. While the full proof is a bit technical (see Appendix C), the key idea is simply the argument principle [273]

$$\oint_{|z|=1} \frac{dz}{2\pi i} \frac{f'(z)}{f(z)} = Z - P, \quad (4.21)$$

where  $E = f(z)$  is the characteristic equation and  $Z(P)$  denotes the number of zeros (poles) of  $f(z)$  in the area  $|z| < 1$ . Replacing  $z$  with  $e^{ik}$ , we find that the left-hand side of Eq. (4.21) gives nothing but the winding number  $w$  introduced in Eq. (4.8). A general form of the wave function can be written as  $\psi_j = \sum_{l=1}^Z c_l z_l^j$ , where  $\{z_l\}$  are the zeros and  $\{c_l\}$  are subject to  $P$  pieces of different constraints stemming from the inhomogeneity at the edge. These are straightforward generalizations of Eqs. (4.19) and (4.20). As a result, there are  $(Z - P = w)$ -fold degeneracies of edge states at  $E = 0$ , or generally at  $E = E_B$  if we replace  $f(z)$  with  $f(z) - E_B$  in Eq. (4.21). A similar analysis for negative winding numbers can be made by interchanging  $z$  and  $z^{-1}$ .

In realistic 1D systems, such as photonic lattices [230], open boundaries always appear in pairs. In the presence of two edges, only a 1D part is picked out from the edge-state continuum, making the topological degeneracy generally invisible for a given base energy. For example, the spectrum of an open chain described by Eq. (4.9) with length  $L$  can be determined as  $E_n = 2\sqrt{J_L J_R} \cos[n\pi/(L+1)]$  ( $n = 1, 2, \dots, L$ ) which distributes over an interval  $(-2\sqrt{J_L J_R}, 2\sqrt{J_L J_R})$  on the real-energy axis in the thermodynamic limit (see the red line in Fig. 4.3 (a)). A sudden change in the spectrum under different boundary conditions has also been found in Ref. [281]. Precisely speaking, it is found in Ref. [281] for a chiral-symmetric<sup>3</sup> model that an *exponentially small* (in terms of the system size) modification of the boundary condition can lead to an order-one change in the spectrum. This is also the case for the Hatano-Nelson model. Interestingly, we can have a topological interpretation for such an extreme spectral sensitivity by considering an open chain as a special disordered system. See Appendix B.1 for details.

As stated above, an energy eigenstate localized at the edge of a semi-infinite space generally disappears if the system size is finite. Nevertheless, *quasi-edge modes* may exist for finite-size systems. By quasi-edge modes, we mean that they are not exact eigenstates, yet their dynamics seem just as eigenstates do up to a time scale that increases with the system size and diverges in the thermodynamic limit. To investigate them, suppose that an edge state with energy  $E$  for the semi-infinite condition is prepared in a finite lattice with length  $L$ , whose spectrum does not include  $E$ . Then the time evolution can be obtained to a good approximation simply by multiplying  $e^{-iEt}$  up to a time scale (at least) proportional to  $L$  (see Figs. 4.3(c) and (d)). Note that this quasi-eigenstate of a finite chain becomes exact in the semi-infinite limit  $L \rightarrow \infty$ . We can intuitively interpret this linear scaling as a manifestation of the Lieb-Robinson bound [143] after a boundary-condition quench is made roughly  $L$  sites away from the edge mode, as illustrated in Fig. 4.3 (b).

The dramatic changes in the spectra for different boundary conditions have already been investigated in a purely mathematical context regarding non-Hermitian Toeplitz matrices (i.e., the matrices satisfying  $M_{jl} = M_{j-l}$ ) and operators [282]. A generalization of the conventional eigenvalues and eigenvectors, which is called the  $\epsilon$ -pseudo-eigenvalues and eigenvectors, was made to explain the apparent inconsistency. The exact definition is as follows: Given a matrix or operator  $H$ , if there exists  $V$  such that the operator norm satisfies  $\|V\| \leq \epsilon$  and  $(H+V)\psi = E\psi$ , then  $E$  and  $\psi$  constitute a pair of  $\epsilon$ -pseudo-eigenvalue and eigenvector of  $H$ . In our language, Toeplitz matrices and operators correspond to finite and semi-infinite chains, respectively, and a pseudo-eigenvector is nothing but a quasi-edge mode. The spectrum of a Toeplitz operator

<sup>3</sup>According to Ref. [257], it is more precise to say sublattice symmetry.



must be obtained by first taking the thermodynamic limit  $L \rightarrow \infty$  followed by  $\epsilon \rightarrow 0$ , which is generally *inequivalent* to the limit  $\epsilon \rightarrow 0$  followed by  $L \rightarrow \infty$  [282]. This fact is reminiscent of quantum phase transitions [48], where spontaneous symmetry breaking occurs only by first taking the thermodynamic limit and then making the symmetry breaking perturbations vanish.

### 4.2.3 Determining the winding number

In Hermitian systems, the only direct signature of  $w$  in 1D seems to be the number of edge states. Due to the subtlety of the bulk-edge correspondence discussed above, it is highly nontrivial to identify  $w$  simply from the energy spectrum of a finite non-Hermitian system under open boundaries. In this subsection, we introduce both numerical and experimental schemes to determine the winding number.

#### *Numerical scheme*

We can numerically extract the winding number by counting the zero modes of the following enlarged *Hermitian* Hamiltonian constructed from  $H$ :

$$H_{\text{H}} \equiv \sigma_+ \otimes H + \sigma_- \otimes H^\dagger, \quad (4.22)$$

where  $\sigma_\pm \equiv (\sigma_x \pm i\sigma_y)/2$ , with  $\sigma_x$  and  $\sigma_y$  being the Pauli matrices. Such an idea of Hermitianization (4.22) actually lies at the heart of the  $K$ -theory classification discussed in the next section. Using the bulk-edge correspondence of  $H$ , we can show that the number of zero modes of Eq. (4.22) equals to  $2|w|$  (see Appendix C). This result is actually nothing but the bulk-edge correspondence for Hermitian systems with chiral symmetry alone (class AIII). If the chiral symmetry stems from the sublattice degrees of freedom, the sign of  $w$  determines in which sublattice the edge state is localized. Note that the generalization to arbitrary base energies can be done through replacement of  $H$  by  $H - E_{\text{B}}$  in Eq. (4.22).

#### *Experimental scheme*

In practice, we can measure the winding number from the wave-packet dynamics. For Hermitian lattice systems, the semiclassical equations of motion of a particle in a single band are given by [283]

$$\frac{d\mathbf{k}}{dt} = \mathbf{F}, \quad \frac{d\mathbf{r}}{dt} = \nabla_{\mathbf{k}} E(\mathbf{k}) - \frac{d\mathbf{k}}{dt} \times \boldsymbol{\Omega}(\mathbf{k}), \quad (4.23)$$

where  $\mathbf{F}$  is the potential gradient,  $E(\mathbf{k})$  is the band dispersion, and  $\boldsymbol{\Omega}(\mathbf{k}) = i\langle \nabla_{\mathbf{k}} u(\mathbf{k}) | \times | \nabla_{\mathbf{k}} u(\mathbf{k}) \rangle$  is the Berry curvature, which requires at least two dimensions and two bands (as mentioned in Sec. 4.2.1) to be nonzero. In two dimensions, it suffices to determine the Chern number directly from the transverse motion of particles [172]. However, in a 1D lattice, rather sophisticated operations are needed to measure the winding number or the Zak phase [171]. That is, we have to isolate the geometric phase from the dynamical phase [284]. In a non-Hermitian 1D system, however, the winding number (4.8) is determined solely from the eigenenergies, which are relevant to the *dynamical* phase. It turns out that  $w$  can be measured simply from the nonunitary Bloch oscillations [285, 286], whose semiclassical equation of motion is given by

$$\frac{dk}{dt} = F, \quad \frac{dx}{dt} = \text{Re} \frac{dE(k)}{dk}, \quad \frac{d \ln \mathcal{N}_t}{dt} = 2\text{Im} E(k), \quad (4.24)$$

where  $\mathcal{N}_t \equiv \langle \psi_t | \psi_t \rangle$  is not, in general, equal to unity due to the nonunitary nature of the dynamics. The above semiclassical equation of motion will be derived at the end of this subsection. By simultaneously tracing the center of mass and the total weight of the wave packet, we can

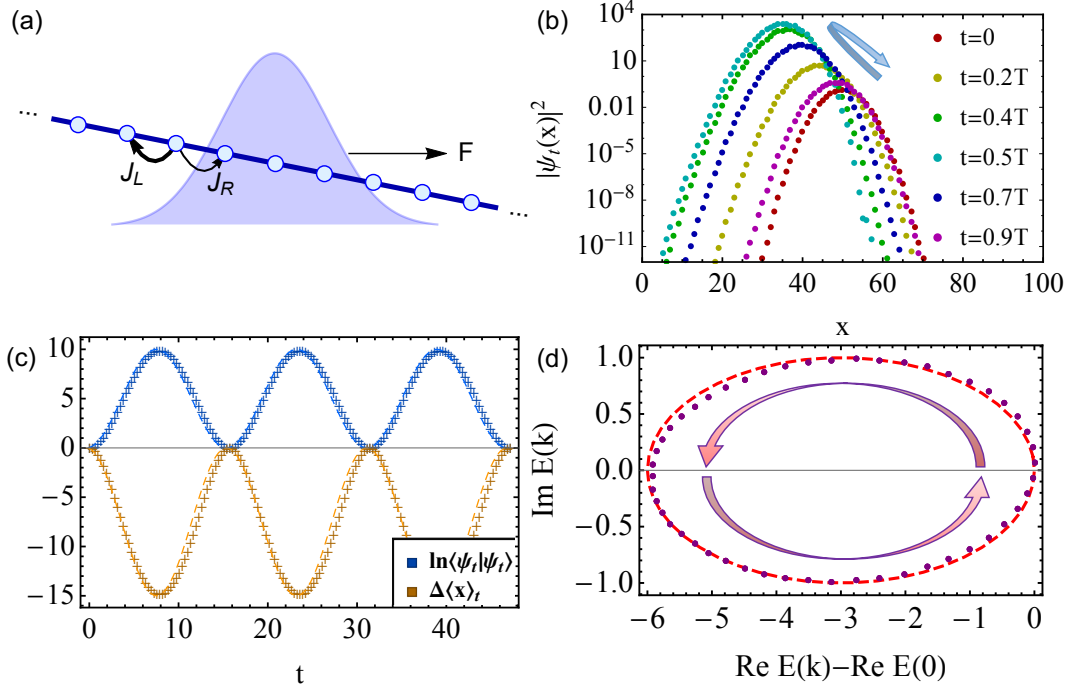


Figure 4.4: (a) Gaussian wave packet in a lattice with asymmetric hopping amplitudes  $J_L = 2$  and  $J_R = 1$  and tilted by a potential gradient  $F = 0.4$ . (b) Profiles of the wave packet in real space at  $t = 0, 0.2T, 0.4T, 0.5T, 0.7T$  and  $0.9T$ , with  $T = 2\pi/F$  for the lattice length  $L = 100$ . (c) Numerical (“+” marks) and semiclassical (dashed curves, obtained from Eq. (4.24)) results for the wave-packet dynamics in real space. Here  $\Delta\langle x \rangle_t \equiv \langle x \rangle_t - \langle x \rangle_0$  denotes the center-of-mass displacement at time  $t$ . (d) Complex eigenenergies reconstructed from (c) (dots) in comparison with the theoretical results (dashed curve). The arrows in (b) and (d) show the direction of time. Since the data are taken stroboscopically, the imaginary energies  $\text{Im}E$  are estimated from  $\ln(\langle \psi_{t+\Delta t} | \psi_{t+\Delta t} \rangle / \langle \psi_t | \psi_t \rangle) / (2\Delta t)$ . Reproduced from Fig. 5 of Ref. [44]. Copyright © 2018 by the American Physical Society.

reconstruct the energy spectrum when the wave number runs over the Brillouin zone. The winding number  $w$  can thus be determined by counting how many times the complex-energy trajectory encircles the base point. Such a simple scenario can be implemented in photonic lattices [287] with asymmetric backscattering [221, 222] or by using auxiliary microresonators with gain and loss [288, 289]. In the next subsection, we propose another implementation based on ultracold atoms in optical lattices with engineered dissipation. Compared with photonic lattices, ultracold atoms have the advantage in controlling interactions flexibly and thus are promising for exploring non-Hermitian quantum many-body physics [238–240].

As a simple example, we consider the wave-packet dynamics in a Hatano-Nelson lattice (4.9) with  $J_L = 2$ ,  $J_R = 1$  and  $L = 100$ . While the open-boundary condition is imposed, we have checked that the difference from the periodic-boundary condition is negligible. At the initial time, we prepare a Gaussian packet in the middle of the lattice with dispersion  $\sigma_r = \sqrt{L}/(4\pi)$  and located at  $k = 0$  in the Brillouin zone (see Fig. 4.4(a)). After applying a potential gradient  $F = 0.4$  in the positive  $x$  (right) direction, both the center of mass and the intensity starts to oscillate. As shown in Fig. 4.4(c), the numerical results (dots) agree quite well with the semiclassical predictions (dashed curves). Thus, the reconstructed complex energies based on Eq. (4.24) accurately reproduce those of the ideal dispersion relation (see Fig. 4.4(d)). We have

also plotted the wave-packet densities at several different times in Fig. 4.4(b) and confirmed that the profile stays approximately Gaussian during the time evolution. The initial direction of motion is opposite to  $F$  due to the negative effective mass  $m_{\text{eff}} = -(J_L + J_R)$  at  $k = 0$ .

Let us return to the derivation of Eq. (4.24). In the continuous limit, the Schrödinger equation (generally nonunitary) in momentum space is given by

$$i\partial_t\psi_t(k) = [E(k) - iF\partial_k]\psi_t(k), \quad (4.25)$$

where  $E(k)$  is the dispersion relation of the band and  $F$  is a potential gradient. Starting from an arbitrary initial state  $\psi_0(k)$ , we can write down a formal solution to Eq. (4.25) as

$$\psi_t(k) = e^{-i\int_0^t dt' E(k-F(t-t'))}\psi_0(k-Ft), \quad (4.26)$$

which satisfies the quasi-periodicity  $\psi_{t+2\pi/F}(k) = e^{-2\pi i\bar{E}/F}\psi_t(k)$  with  $\bar{E} = (2\pi)^{-1}\int_{-\pi}^{\pi} dk E(k)$ . Note that no approximation is made so far except for the continuous limit. We note that a similar semi-classical analysis on nonunitary wave-packet dynamics is made in Ref. [290].

If we focus on the semiclassical regime,  $\psi_0(k)$  should be highly localized in the Brillouin zone, as a Gaussian packet

$$\psi_0(k) = (\sqrt{2\pi}\sigma_k)^{-\frac{1}{2}} e^{-\frac{k^2}{2\sigma_k^2}} \quad (4.27)$$

near  $k = 0$  does, with a small dispersion  $\sigma_k \ll 1$ . In this case, we can expand  $E(k - F(t - t'))$  in Eq. (4.26) near  $Ft'$  (in terms of  $k - Ft \sim \sigma_k$ ) up to  $(k - Ft)^2$ , such that the wave packet  $\psi_t(k)$  stays (approximately) Gaussian:

$$\psi_t(k) \simeq (\sqrt{2\pi}\sigma_k)^{-\frac{1}{2}} e^{-i\int_0^t dt' E(Ft')} e^{-i\frac{E(Ft)-E(0)}{F}(k-Ft) - \left[\frac{1}{4\sigma_k^2} + i\frac{E'(Ft)-E'(0)}{2F}\right](k-Ft)^2}, \quad (4.28)$$

where  $E'(k)$  means  $dE(k)/dk$ . We can thus calculate the normalization  $\mathcal{N}_t \equiv \langle \psi_t | \psi_t \rangle$  as  $\int_{-\pi}^{\pi} dk |\psi_t(k)|^2$ , which turns out to be

$$\mathcal{N}_t = \frac{1}{\sqrt{1 - \frac{2\sigma_k^2}{F} [\text{Im}E'(Ft) - \text{Im}E'(0)]}} e^{2\int_0^t dt' \text{Im}E(Ft') + \frac{2[\text{Im}E(Ft) - \text{Im}E(0)]^2 \sigma_k^2}{F^2 - 2\sigma_k^2 F [\text{Im}E'(Ft) - \text{Im}E'(0)]}}. \quad (4.29)$$

By taking the limit  $\sigma_k \rightarrow 0$ , we obtain the rightmost equation in Eq. (4.24). The center of mass in the Brillouin zone can also be read out from Eq. (4.28) as

$$\langle k \rangle_t = Ft + \frac{2[\text{Im}E(Ft) - \text{Im}E(0)]\sigma_k^2}{F - 2\sigma_k^2 [\text{Im}E'(Ft) - \text{Im}E'(0)]}, \quad (4.30)$$

which reduces to  $Ft$  in the  $\sigma_k \rightarrow 0$  limit. After the Fourier transform  $\psi_t(x) = (2\pi)^{-1/2} \int_{-\pi}^{\pi} dk \times \psi_t(k) e^{ikx}$ , we can obtain the real-space wave function and determine the center of mass in real space as

$$\langle x \rangle_t = \frac{\text{Re}E(Ft) - \text{Re}E(0)}{F} - \frac{2\sigma_k^2}{F^2} \text{Im}[(E^*(Ft) - E^*(0))(E'(Ft) - E'(0))], \quad (4.31)$$

which reduces to the middle equation in Eq. (4.24) in the limit of  $\sigma_k \rightarrow 0$ .

It is worthwhile to consider the special case of free diffusion with  $F = 0$ . Taking the limit of  $F \rightarrow 0$  in Eqs. (4.29), (4.30) and (4.31), we obtain

$$\mathcal{N}_t = \frac{e^{2\text{Im}E(0)t + \frac{2[\sigma_k \text{Im}E'(0)t]^2}{1 - 2\sigma_k^2 \text{Im}E''(0)t}}}{\sqrt{1 - 2\sigma_k^2 \text{Im}E''(0)t}}, \quad \langle k \rangle_t = \frac{2\sigma_k^2 \text{Im}E'(0)t}{1 - 2\sigma_k^2 \text{Im}E''(0)t}, \quad (4.32)$$

$$\langle x \rangle_t = \text{Re}E'(0)t - 2\sigma_k^2 \text{Im}[E'^*(0)E''(0)]t^2.$$

Applying the last equation to a wave packet with the momentum-space spread of  $\sigma_k^2 = \pi/L$  in the clean Hatano-Nelson model (4.9) with  $J_L, J_R \in \mathbb{R}$ , we have

$$\langle x \rangle_t = -\frac{2\pi}{L}(J_L^2 - J_R^2)t^2. \quad (4.33)$$

This result implies that the shift of the center of mass due to asymmetric hopping amplitudes is a finite-size effect. In other words, a wave packet in the classical limit does not move in spite of the asymmetry in hopping amplitudes.

#### 4.2.4 Experimental implementation of asymmetric hopping amplitudes

As mentioned in Sec. 4.1.2, an effective non-Hermitian Hamiltonian appears naturally in the time evolution of a Markovian open quantum system between quantum jumps or on the mean-field level. In particular, if we choose

$$H = -J \sum_j (c_{j+1}^\dagger c_j + \text{H.c.}), \quad L_j = \sqrt{\kappa}(c_j \pm ic_{j+1}) \quad (4.34)$$

in Eq. (4.2), where  $\{L_j\}$  describe a *collective* one-body loss [241], the effective non-Hermitian Hamiltonian in Eq. (4.3) will involve asymmetric hopping amplitudes:

$$H_{\text{eff}} = \sum_j (J_R c_{j+1}^\dagger c_j + J_L c_j^\dagger c_{j+1}) - i\kappa N. \quad (4.35)$$

Here  $J_R = -J \mp \kappa/2$  differs from  $J_L = -J \pm \kappa/2$  and  $N = \sum_j c_j^\dagger c_j$  is the total particle-number operator, so that the last term corresponds to a background loss. Unlike Fig. 4.4(d), the energy spectrum is now below the real axis due to atom loss, and the imaginary part of its center is located at  $-i\kappa$ .

It is not straightforward to engineer a nonlocal one-body loss like  $\{L_j\}$  in Eq. (4.34), since the usual loss process occurs locally [216]. However, we can effectively engineer such a novel nonlocal loss by using a nonlocal Rabi coupling to some auxiliary degrees of freedom which undergo rapid local loss. After adiabatically eliminating the fast decay modes [291], we end up with an effective dynamics with target degrees of freedom alone, which now effectively undergo nonlocal loss.

As illustrated in Fig. 4.5, we consider a system of two-level atoms with internal states  $|g\rangle$  and  $|e\rangle$  in a 1D optical lattice with lattice constant  $a$ . Because the opposite Stark shifts are opposite for  $|g\rangle$  and  $|e\rangle$ , the potential minima for  $|e\rangle$  locate in the middles of each of those for  $|g\rangle$ . The excited state  $|e\rangle$  is assumed to be unstable and rapidly escape from the lattice at a rate  $\gamma$ . Parallel to the optical lattices, we further apply a running-wave laser with frequency  $\omega_R$ , which is detuned from the atomic frequency  $\omega_{eg}$  by  $\Delta = \omega_R - \omega_{eg}$ . The strength of the laser-atom dipole coupling is characterized by a Rabi frequency  $\Omega_R$ . Within the tight-binding approximation and neglecting the interactions between atoms, we can write down the master equation in the rotating frame of reference as

$$\dot{\rho}_t = -i \sum_j [H_0 + V, \rho_t] + \mathcal{D}[c_{je}] \rho_t, \quad (4.36)$$

where  $H_0$  includes the bare tunneling and  $V$  couples different internal states:

$$\begin{aligned} H_0 &= -J \sum_{j,\alpha=g,e} (c_{j+1,\alpha}^\dagger c_{j\alpha} + \text{H.c.}) - \sum_j \Delta c_{je}^\dagger c_{je}, \\ V &= \frac{1}{2} \sum_j [\Omega e^{\pm ik_R j a} c_{je}^\dagger (c_{jg} + e^{\pm \frac{i}{2} k_R a} c_{j+1,g}) + \text{H.c.}]. \end{aligned} \quad (4.37)$$

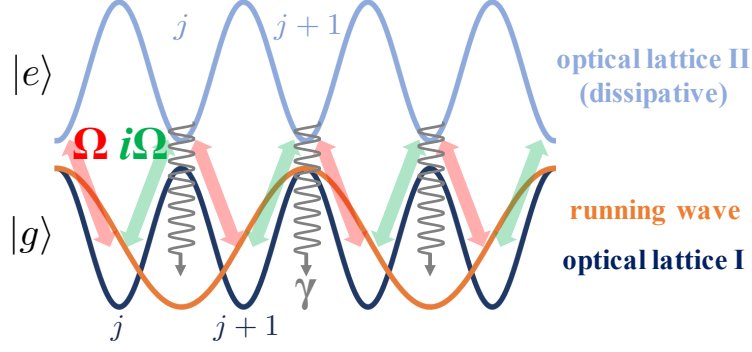


Figure 4.5: Implementation of asymmetric hopping amplitudes in optical lattices. A stable (dissipative) optical lattice is applied to the ground (excited) state  $|g\rangle$  ( $|e\rangle$ ). A running wave parallel to an optical lattice couples  $|g\rangle$  to  $|e\rangle$ , which undergoes rapid on-site loss at a rate  $\gamma$ . By making the wavelength of the running wave equal to the lattice constant, the phases of Rabi couplings can be adjusted to change by  $\pi/2$  compared with the left adjacent ones. Reproduced from Fig. 17 of Ref. [44]. Copyright © 2018 by the American Physical Society.

Here  $+$  ( $-$ ) corresponds to the right (left) propagating wave and the Rabi coupling  $\Omega$  can be determined from  $\Omega = \Omega_R \int dx e^{\pm ik_R x} W(x) W(x - \frac{a}{2})$ , with  $W(x)$  being the Wannier function. In the regime of  $\max\{\Delta, \gamma\} \gg J, \Omega$ , we can adiabatically eliminate  $c_{je}$  in Eq. (4.36) to obtain Eq. (4.2) with the same  $H$  as in Eq. (4.34) and a more general  $L_j$ :

$$L_j = \frac{\sqrt{\gamma}|\Omega|}{\sqrt{\gamma^2 + 4\Delta^2}}(c_{jg} + e^{\pm \frac{i}{2}k_R a} c_{j+1,g}), \quad (4.38)$$

which gives the second equation in Eq. (4.34) if  $k_R a = \pi$  or  $\lambda_R = 2a$ . Note that even if  $\lambda_R$  differs from  $\lambda_L = 2a$ , which is the wavelength of the optical lattice laser, we can still obtain Eq. (4.34) by tilting the running wave from the optical lattice by an angle  $\theta_R = \arccos(\lambda_R/\lambda_L)$  as long as  $\lambda_R < \lambda_L$ .

In a realistic experiment, we can, for example, use  $^{174}\text{Yb}$  atoms and 1117 nm-wavelength lasers to create the anti-magic optical lattice with opposite Stark shifts for  $g = ^1\text{S}_0$  and  $e = ^3\text{P}_0$  [292]. We choose a relatively shallow (yet the tight-binding approximation still works well) lattice depth  $V_0 = 5E_r$ , with  $E_r \equiv \hbar^2/(2m\lambda_L^2) = 2\pi \times 0.92$  kHz being the recoil energy. The bare hopping amplitude is thus estimated to be  $J = 0.066E_r = 2\pi \times 60$  Hz [54]. The on-site loss rate  $\gamma$  of  $|e\rangle$  can be controlled by a 1285 nm laser that couples  $^3\text{P}_0$  to  $^1\text{P}_1$  resonantly, and we can still make  $\kappa = \gamma|\Omega|^2/(\gamma^2 + 4\Delta^2)$  as small as, e.g.,  $0.2J = 2\pi \times 12$  Hz by tuning  $\gamma$ ,  $|\Omega|$  or/and  $\Delta$ . Here, we should make  $\gamma$  much less than the band gap  $4.6E_r$  of the optical lattice to justify the tight-binding approximation for  $|e\rangle$  (e.g., we can choose  $\Delta = 0$  and  $\gamma = 5\Omega = 0.33E_r = 2\pi \times 0.30$  kHz). The wavelength of the running-wave laser is fixed at 578.42 nm (clock transition [293]) and the tilting angle should be  $\theta_R = 58.8^\circ$ . The potential gradient can be made from an optical dipole force via an additional laser beam [172], and may be chosen to be, e.g.,  $F = 4\kappa = 2\pi \times 48$  Hz, which is much smaller than the band gap and thus justifies the single-band treatment. The maximum displacement can thus be evaluated to be  $2J/F = 5$  lattice sites, which is enough to be measured by single-site resolved quantum gas microscopy [294]. The period of Bloch oscillations is  $T_B = 2\pi/F = 21$  ms, after which the survival fraction of atoms is given by  $e^{-2\kappa T_B} = 4.3\%$ , which should be sufficiently large for reconstructing the complex energy spectrum if there are at least thousands of atoms at the initial time.

## 4.3 Classification of non-Hermitian topological phases in the Altland-Zirnbauer classes

The non-Hermitian systems discussed in the previous section are special in the sense that the spatial dimension is  $d = 1$  and no symmetry requirement is imposed. Such a non-Hermitian counterpart of class A in 1D, however, exhibits an integer topological winding number (4.7) reminiscent of Floquet systems [65] and Hermitian systems belonging to class AIII [39]. These observations suggest a connection between a non-Hermitian Hamiltonian and a unitary operator, the latter of which has a one-to-one correspondence to an involutory Hermitian Hamiltonian with a prescribed chiral symmetry [119]. In this section, we establish such a connection, which enables a systematic classification of non-Hermitian Bloch Hamiltonians in all dimensions and in the presence of additional symmetries. In particular, we show that the topological classification of non-Hermitian AZ classes differs significantly from those of Hermitian AZ classes [39, 40, 194, 195].

### 4.3.1 Unitarization under symmetry constraints

In the previous sections we have already clarified that two Hamiltonians are topologically equivalent if they can continuously be deformed into each other under certain constraints. Without symmetries, the only constraint is that a base point  $E_B$  cannot be touched by the energy spectrum. Such a constraint is imposed to satisfy the condition of invertibility of the Hamiltonian for  $E_B = 0$ , which we primarily assume in the following discussions. This gap condition is now called a *point gap* in literature [257]. For a given AZ class, which involves one or some of the time-reversal symmetry  $T$ , particle-hole symmetry  $C$  and chiral symmetry  $\Gamma$ , we have to further impose these symmetry constraints. These considerations lead to the following definition of topological equivalence:

**Definition 6 (Homotopy equivalence)** *Two non-Hermitian Bloch Hamiltonians  $H_0(\mathbf{k})$  and  $H_1(\mathbf{k})$  in the same AZ class are homotopically equivalent, denoted as  $H_0(\mathbf{k}) \simeq H_1(\mathbf{k})$ , if there exists a path  $H_\lambda(\mathbf{k})$  ( $0 \leq \lambda \leq 1$ ) in the space of invertible matrices (i.e., the  $\text{GL}(\mathcal{V})$  group, where  $\mathcal{V}$  is the Hilbert space) such that*

$$SH_\lambda(\mathbf{k})S^{-1} = \eta_S H_\lambda(\epsilon_S \mathbf{k}), \quad \forall \lambda \in [0, 1], \quad (4.39)$$

where  $S = T$  (anti-unitary,  $\eta_T = 1$ ,  $\epsilon_T = -1$ ),  $C$  (anti-unitary,  $\eta_C = \epsilon_C = -1$ ) or  $\Gamma$  (unitary,  $\eta_\Gamma = -1$ ,  $\epsilon_\Gamma = 1$ ).

We emphasize again that the condition of  $H_\lambda(\mathbf{k})$  being invertible is equivalent to the condition that the system stays gapped in the Hermitian case, if we prescribe the Fermi energy to be 0. When generalizing to non-Hermitian systems, the concepts of upper and lower bands disappear since we cannot establish an order relation for complex energies.

Definition 6 implies the following theorem:

**Theorem 4** *For an arbitrary invertible Bloch Hamiltonian  $H(\mathbf{k})$ , which has a unique polar decomposition  $H(\mathbf{k}) = U(\mathbf{k})P(\mathbf{k})$  with  $U(\mathbf{k})$  being unitary and  $P(\mathbf{k}) = \sqrt{H(\mathbf{k})^\dagger H(\mathbf{k})}$  being positive-definite and Hermitian, we have  $H(\mathbf{k}) \simeq U(\mathbf{k})$ .*

*Proof:* To prove  $H(\mathbf{k}) \simeq U(\mathbf{k})$ , we have to first confirm that  $U(\mathbf{k})$  belongs to the same symmetry class of  $H(\mathbf{k})$ . For an arbitrary anti-unitary symmetry or anti-symmetry  $S = U_S K$  ( $U_S$  is unitary and  $K$  denotes complex conjugation) such that

$$U_S H(\mathbf{k})^* U_S^\dagger = \eta_S H(-\mathbf{k}), \quad \eta_A = \pm 1, \quad (4.40)$$

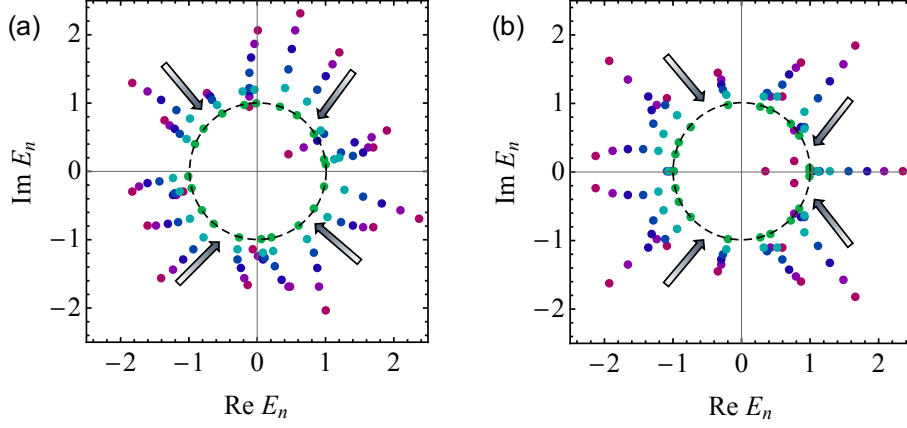


Figure 4.6: (a) Spectral flow (from red to green, guided by the arrows) in the course of the unitarization process of an invertible complex matrix with size 20. Note that the spectrum of the unitarized matrix locates on a unit circle (black dashed). (b) The same as in (a) but for a time-reversal-symmetric matrix. The time-reversal symmetry, which manifests itself as the mirror symmetry of the spectrum with respect to the real axis, is kept in the unitarization process. Reproduced from Fig. 6 of Ref. [44]. Copyright © 2018 by the American Physical Society.

by performing the polar decomposition  $H(\mathbf{k}) = U(\mathbf{k})P(\mathbf{k})$ , we obtain

$$\begin{aligned} U_S U(\mathbf{k})^* P(\mathbf{k})^* U_S^\dagger &= \eta_S U(-\mathbf{k}) P(-\mathbf{k}) \quad \Rightarrow \quad U_S P(\mathbf{k})^* U_S^\dagger = P(-\mathbf{k})^2 \\ \Rightarrow [P(-\mathbf{k}) + U_S P(\mathbf{k})^* U_S^\dagger][P(-\mathbf{k}) - U_S P(\mathbf{k})^* U_S^\dagger] &= 0, \end{aligned} \quad (4.41)$$

where the unitarity of  $U_S$  and  $U(\mathbf{k})$  ( $U(\mathbf{k})^*$ ) and the Hermiticity of  $P(\mathbf{k})$  ( $P(\mathbf{k})^*$ ) are used. Recalling that  $P(\mathbf{k})$  ( $P(\mathbf{k})^*$ ) is positive-definite, we know that  $P(-\mathbf{k}) + U_S P(\mathbf{k})^* U_S^\dagger$  should also be positive-definite and thus invertible. This fact implies

$$P(-\mathbf{k}) = U_S P(\mathbf{k})^* U_S^\dagger \quad \Rightarrow \quad U_S U^*(\mathbf{k}) U_S^\dagger = \eta_S U(-\mathbf{k}). \quad (4.42)$$

Following a similar procedure, we can prove that  $U(\mathbf{k})$  and  $H(\mathbf{k})$  share the same unitary or transpose symmetry or anti-symmetry. This is why we use the term *symmetry class* in the beginning, which is much wider than the AZ class. For example, we can consider crystalline symmetries and Bernard-LeClair symmetries [258].

We can now construct the following path

$$H_\lambda(\mathbf{k}) = (1 - \lambda)H(\mathbf{k}) + \lambda U(\mathbf{k}) = U(\mathbf{k})[(1 - \lambda)P(\mathbf{k}) + \lambda], \quad (4.43)$$

which satisfy  $H_0(\mathbf{k}) = H(\mathbf{k})$  and  $H_1(\mathbf{k}) = U(\mathbf{k})$ . Furthermore, as a linear combination of  $H(\mathbf{k})$  and  $U(\mathbf{k})$ ,  $H_\lambda(\mathbf{k})$  shares all the symmetries of  $H(\mathbf{k})$  and  $U(\mathbf{k})$ , and is indeed invertible due to the fact that  $(1 - \lambda)P(\mathbf{k}) + \lambda$  is positive-definite.  $\square$

We provide two examples of unitarization from  $H$  to  $U$  in Fig. 4.6. According to this theorem, it suffices to consider the classification of all the *unitary* matrices. Note that this result is consistent with band flattening in the Hermitian case [39, 40, 194]. By diagonalizing a Hermitian Hamiltonian as

$$H = V \begin{pmatrix} \Lambda_{p \times p}^+ & 0 \\ 0 & \Lambda_{q \times q}^- \end{pmatrix} V^\dagger, \quad (4.44)$$

where  $\Lambda_{p \times p}^+$  ( $\Lambda_{q \times q}^-$ ) is the diagonal block of all the positive (negative) energies, we find the polar decomposition to be  $H = UP$  with

$$U = V \begin{pmatrix} 1_{p \times p} & 0 \\ 0 & -1_{q \times q} \end{pmatrix} V^\dagger, \quad P = V \begin{pmatrix} \Lambda_{p \times p}^+ & 0 \\ 0 & -\Lambda_{q \times q}^- \end{pmatrix} V^\dagger, \quad (4.45)$$

where  $U$  is nothing but the flattened Hamiltonian.

It is worthwhile to mention that there are also other generalizations of the energy gap, such as the band separability [253] and the line gap [257]. In the latter case, one can prove that the Bloch Hamiltonian can always be continuously deformed into a flattened (anti-)Hermitian Hamiltonian under the constraint of fundamental symmetries (i.e., Bernard-LeClair symmetries), provided that the imaginary (real) energy axis does not cross the energy spectrum [257, 265]. This result implies that the topological classification for line gapped non-Hermitian systems is the same as that for Hermitian systems. As we will see in the following, as for point-gapped non-Hermitian systems, we have a very different classification.

### 4.3.2 $K$ -theory and Clifford-algebra extension

The classification based on the homotopy equivalence is appropriate for a given Hilbert space, but is not so if the operations of inserting extra bands are also allowed. These operations are indeed possible in experiments of ultracold atoms, where we can, for example, couple two or more individual 1D chains [295]. In this case, the correct classification should be carried out on the basis of the  $K$ -theory [40, 195, 199, 200, 296], i.e., all we have to do is to figure out the  $K$ -group of the map from the Brillouin zone  $M = T^d$  ( $d$ : spatial dimension) to a (non-Hermitian) matrix space subject to specific symmetry requirements. If we are only interested in the strong topological numbers [40], the manifold is  $M = S^d$ . From now on, we may omit the variable  $\mathbf{k}$  for simplicity, but we should remember that there is a base manifold.

Let us first review some basics of the  $K$ -theory, so as to understand why it is compatible with band-inserting operations. The  $K$ -group is an Abelian group consisting of equivalence classes, denoted as  $[H_0, H_1]$ , of Hamiltonian *pairs*  $(H_0, H_1)$ , where  $H_0$  and  $H_1$  act on the same Hilbert space. For  $(H_0, H_1)$ , we define an addition structure as

$$(H_0, H_1) + (H'_0, H'_1) = (H_0 \oplus H'_0, H_1 \oplus H'_1). \quad (4.46)$$

We also impose  $(H_0, H_1) = (H'_0, H'_1)$  if  $H_0 \simeq H'_0$  and  $H_1 \simeq H'_1$  (we recall that “ $\simeq$ ” means homotopy equivalence as defined in Definition 6). To specify the equivalence classes, we require that  $(H_0, H_1)$  should be identified as  $(H_0 \oplus H, H_1 \oplus H)$  for all  $H$ , i.e.,  $[H_0 \oplus H, H_1 \oplus H] \equiv [H_0, H_1]$ . By naturally defining the addition between equivalence classes as

$$[H_0, H_1] + [H'_0, H'_1] = [H_0 \oplus H'_0, H_1 \oplus H'_1], \quad (4.47)$$

we can deduce that they form an Abelian group, which is called the  $K$ -group and denoted as  $K(M)$ , with zero element  $[H, H] = 0$  and the inverse of  $[H_0, H_1]$  being  $[H_1, H_0]$ . We say that  $H_0$  and  $H_1$  belong to the same topological phase if and only if  $[H_0, H_1] = 0$ .

A crucial observation here is that although  $H_0 \simeq H_1$  implies  $[H_0, H_1] = 0$ , the converse is *not* true. A prototypical example is the Hopf insulator [147], which is a two-band system in three dimensions and has no symmetry. While a Hopf insulator differs homotopically from a trivial insulator by a nonzero Hopf charge, it becomes trivial in the  $K$ -theory classification since we can insert additional bands into the system to trivialize the homotopy from  $S^3$  to the entire Hilbert space. In other words, nontrivial topological phases emerge in class A in three dimensions only if there are two bands.



While it is not easy to calculate the  $K$ -group for general symmetry constraints [297], well-developed techniques are available if the Hamiltonian space subjected to specific symmetry constraints is an extension of a *Clifford algebra* [40], which is generated by a set of *anti-commutative* elements  $\{e_j\}_{j=1}^n$ :

$$e_j e_{j'} = -e_{j'} e_j, \quad \forall j \neq j'. \quad (4.48)$$

If  $e_j^2 = 1$  for all  $j = 1, 2, \dots, n$ , the algebra generated by  $\{e_j\}_{j=1}^n$  over the complex-number field  $\mathbb{C}$  is called a complex Clifford algebra  $\mathcal{C}l_n$ . If  $e_j^2 = -1$  for  $j = 1, 2, \dots, p$  ( $p \leq n$ ) and  $e_j^2 = 1$  for  $j = p+1, p+2, \dots, n$ , the algebra generated by  $\{e_j\}_{j=1}^n$  over the real-number field  $\mathbb{R}$  is called a real Clifford algebra  $\mathcal{C}l_{p,q}$ , where  $q = n - p$ . For a flattened Hermitian Hamiltonian  $H$ , we naturally have  $H^2 = 1$ , which can already be regarded as an element of a Clifford algebra  $\mathcal{C}l_H$  generated by  $H$  and its two-fold symmetry operators (as well as  $i$ , if there is an anti-unitary symmetry). Noting that the two-fold symmetry operators themselves generate another Clifford algebra  $\mathcal{C}l_S$ , we can thus represent the Hamiltonian space by the Clifford-algebra extension  $\mathcal{C}l_S \rightarrow \mathcal{C}l_H$ . In particular, we denote  $\mathcal{C}l_s \rightarrow \mathcal{C}l_{s+1}$  and  $\mathcal{C}l_{0,s} \rightarrow \mathcal{C}l_{0,s+1}$  as  $\mathcal{C}_s$  and  $\mathcal{R}_s$ , respectively, which satisfy the Bott periodicity [298]:

$$\mathcal{C}_{s+2} = \mathcal{C}_s, \quad \mathcal{R}_{s+8} = \mathcal{R}_s. \quad (4.49)$$

It is well known for Hermitian systems that the two complex AZ classes correspond to  $\mathcal{C}_s$  with  $s = 0, 1$  and the eight real AZ classes correspond to  $\mathcal{R}_s$  with  $s = 0, 1, \dots, 7$  [40]. Denoting the  $K$ -group for a complex or real AZ class parametrized by  $s$  and in  $d$  dimensions as  $K_{\mathbb{C}}(s; d)$  or  $K_{\mathbb{R}}(s; d)$ , we have

$$K_{\mathbb{C}}(s; d) = \pi_d(\mathcal{C}_s) = \pi_0(\mathcal{C}_{s-d}), \quad K_{\mathbb{R}}(s; d) = \pi_d(\mathcal{R}_s) = \pi_0(\mathcal{R}_{s-d}), \quad (4.50)$$

where  $\pi_d$  is the  $d$ th homotopy group.

For a unitarized non-Hermitian Hamiltonian  $U$ , we do not have  $U^2 = \pm 1$  in general. Nevertheless, we can introduce the corresponding Hermitian Hamiltonian

$$H_U \equiv \sigma_+ \otimes U + \sigma_- \otimes U^\dagger = \begin{bmatrix} 0 & U \\ U^\dagger & 0 \end{bmatrix}, \quad (4.51)$$

which now satisfies  $H_U^2 = 1$ . Remarkably, by such construction, we naturally have a chiral symmetry  $\Sigma \equiv \sigma_z \otimes 1$ , which satisfies  $\Sigma^2 = 1$  and

$$\Sigma H_U = -H_U \Sigma. \quad (4.52)$$

It has been proved (see, e.g., Appendix D in Ref. [119]) that  $H_U$  must take the form of Eq. (4.51) if we impose Eq. (4.52). Therefore, one can find properties of  $U$  from those of  $H_U$ .

### 4.3.3 Explicit classification

Now let us study how the non-Hermiticity changes the topological classification for each AZ class. We start from the two complex AZ classes A and AIII, which correspond to  $\mathcal{C}_0$  and  $\mathcal{C}_1$  in the Hermitian case. Due to the emergent chiral symmetry (4.52), class A is shifted to class AIII, which is characterized by  $\pi_d(\mathcal{C}_1) = \mathbb{Z}$  (0) for odd (even)  $d$ . As for class AIII with an intrinsic chiral symmetry  $\Gamma$ , due to  $[\Sigma, \sigma_0 \otimes \Gamma] = 0$  ( $\sigma_0 \equiv 1_{2 \times 2}$ ), the topological number simply duplicates, i.e., it becomes  $\pi_d(\mathcal{C}_1 \times \mathcal{C}_1) = \mathbb{Z} \oplus \mathbb{Z}$  (0) for odd (even)  $d$ .

Let us move on to the real AZ classes with only a single anti-unitary (anti-)symmetry  $S = U_S K$ , including AI ( $T^2 = 1$ ), D ( $C^2 = 1$ ), AII ( $T^2 = -1$ ) and C ( $C^2 = -1$ ). By using the

fact that

$$\begin{aligned} SUS^{-1} = \eta_S U &\Leftrightarrow SU^\dagger S^{-1} = \eta_S U^\dagger \\ \Leftrightarrow \begin{bmatrix} S & 0 \\ 0 & S \end{bmatrix} \begin{bmatrix} 0 & U \\ U^\dagger & 0 \end{bmatrix} &= \eta_S \begin{bmatrix} 0 & U \\ U^\dagger & 0 \end{bmatrix} \begin{bmatrix} S & 0 \\ 0 & S \end{bmatrix}, \end{aligned} \quad (4.53)$$

we find that the action of an anti-unitary (anti-)symmetry  $\sigma_0 \otimes S$  on  $H_U$  is the same as that on  $U$ . Since  $[\sigma_0 \otimes S, \Sigma] = 0$ , such a chiral symmetry  $\Sigma$  implies another anti-unitary symmetry whose square is the same as  $S^2$ . Therefore, classes AI and D (classes AII and C), which correspond to  $\mathcal{R}_0$  and  $\mathcal{R}_2$  ( $\mathcal{R}_4$  and  $\mathcal{R}_6$ ) in the Hermitian case, are unified into BDI (CII) described by  $\mathcal{R}_1$  ( $\mathcal{R}_5$ ).

Finally, let us discuss the AZ classes with two anti-unitary (anti-)symmetries, including DIII ( $T^2 = -1, C^2 = 1$ ), CI ( $T^2 = 1, C^2 = -1$ ), BDI ( $T^2 = 1, C^2 = 1$ ) and CII ( $T^2 = -1, C^2 = -1$ ). For the former two classes, we can construct  $i\Sigma(\sigma_0 \otimes \Gamma) = i\sigma_z \otimes \Gamma$ ; this operator gives  $-1$  upon squaring and commutes with all the elements in the original Clifford algebra excluding  $\Sigma$ . This implies that DIII and CI, which correspond to  $\mathcal{R}_3$  and  $\mathcal{R}_7$  in the Hermitian case, are unified into AIII ( $\mathcal{C}_1$ ), since  $i\sigma_z \otimes \Gamma$  behaves like a complex unit that changes the real AZ classes into the complex ones [199]. For the latter two classes, we can construct  $\Sigma(\sigma_0 \otimes \Gamma) = \sigma_z \otimes \Gamma$ ; this operator gives  $1$  upon squaring and commutes with all the elements in the original Clifford algebra excluding  $\Sigma$ . This implies that the topological number of classes BDI and CII simply gets doubled, since  $\sigma_z \otimes \Gamma$  has two different subspaces of eigenstates with eigenvalues  $\pm 1$  [199].

We list all the results in Table 4.1. To summarize, the effect of non-Hermiticity is equivalent to adding a chiral symmetry that commutes with all the original symmetries. As a result, classes A, DIII and CI are unified into AIII, AI and D are unified into BDI, AII and C are unified into CII, and AIII, BDI and CII become duplicated.

#### 4.3.4 Discussions

A few remarks are in order here. First, the unification of classes AI and D, AII and C as well as that of classes DIII and CI, can be understood as a consequence of the one-to-one mapping between a time-reversal symmetric Hamiltonian and a particle-hole symmetric Hamiltonian which are transformed to each other by simple multiplication of one or the other by  $i$  [299]. Such a unification holds true for very general requirements of continuous deformation other than maintaining invertibility, such as the existence of a complex band gap [253].

Second, despite the fact that the classification of non-Hermitian matrices is equivalent to that of unitary matrices, the periodic table (Table 4.1) differs significantly from that of Floquet systems [119]. This is partly due to the different meanings of symmetries in the context of Hamiltonians and time-development operators. In the former case, we require  $SH(\mathbf{k})S^{-1} = \eta_S H(\epsilon_S \mathbf{k})$ , while in the latter case we require  $SU(\mathbf{k})S^{-1} = U(\epsilon_S \mathbf{k})^{\pm \eta_S}$ , where  $+/-$  corresponds to a unitary/anti-unitary (anti-)symmetry [121]. Another reason is that, rather than a Floquet operator alone, the full information of  $U(\mathbf{k}, t) = \hat{T} e^{-i \int_0^t dt' H(t')}$  from  $t = 0$  to  $t = T$  is important in a Floquet system. A good illustration is the anomalous edge states [67], which exist in spite of a trivial  $U(\mathbf{k}, T) = 1$ , as has been mentioned in the previous chapter. In contrast, here we focus on time-independent non-Hermitian Hamiltonians, so that the base manifold for classification only contains  $\mathbf{k}$  but not  $t$ .

Third, a 2D non-Hermitian system turns out to be always trivial in our classification. This does not contradict a recently discovered Chern number for separable non-Hermitian bands [253], since all the bands can be deformed to touch each other without hitting a base energy. For example, let us show how to trivialize a Chern insulator without the spectrum touching at

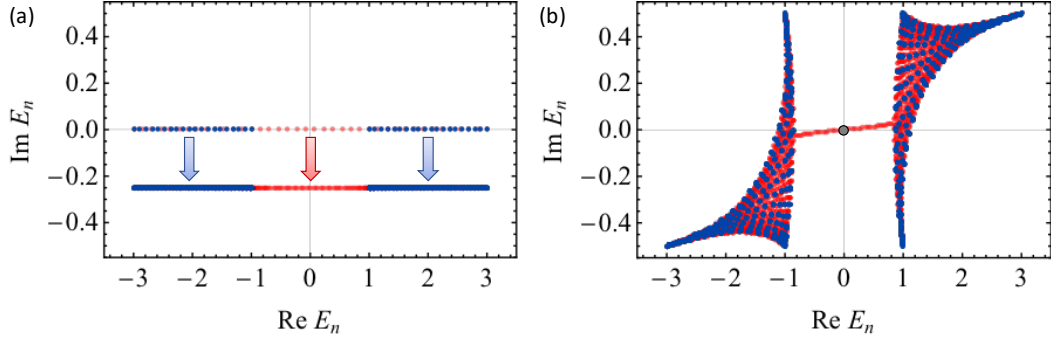


Figure 4.7: (a) Spectrum of Eq. (4.54) with  $(\gamma, m) = (0.25, 1)$ . The zero mode in the  $\gamma = 0$  limit (sparse dots) disappears due to the global spectrum shift along the imaginary energy axis (indicated by the arrows). (b) Same as (a) but with  $(\gamma, m) = (0, 1 + 0.5i)$ . The symmetry constraint given in Eq. (4.55) enforces the spectrum to be inversion symmetric, leading to a robust zero mode (grey dot). In both (a) and (b), the blue (red) dots correspond to the periodic (open) boundary condition, and the system size is  $40 \times 40$ . Reproduced from Fig. 7 of Ref. [44]. Copyright © 2018 by the American Physical Society.

the origin (here, we assume  $E_B = 0$ ). We consider a two-band system

$$H(k_x, k_y) = -i\gamma\sigma_0 + \sin k_x\sigma_x + \sin k_y\sigma_y + (m - \cos k_x - \cos k_y)\sigma_z, \quad (4.54)$$

and start from  $(\gamma, m) = (0, 1)$ , which describes a Hermitian Chern insulator [193]. We can first gradually introduce a global loss up to, e.g.,  $\gamma = 0.25$  (see Fig. 4.7(a)), and then change  $m$  into, e.g.,  $m = 3$ , and finally remove the global loss by reducing  $\gamma$  to zero. It is clear that the origin is not touched by the spectrum of  $H(k_x, k_y)$  during the whole process. Such continuous deformation is, however, forbidden in Ref. [253], because a band touching occurs at  $m = 2$ .

Although the AZ classes are always trivial in two dimensions in our framework, nontrivial topological phases *do* exist in other symmetry classes. For example, by setting  $\gamma = 0$  in Eq. (4.54), we have

$$\sigma_x H(k_x, k_y) \sigma_x = -H(-k_x, k_y) \quad (4.55)$$

even for a complex  $m$ . With the symmetry constraint in Eq. (4.55) alone, we know that the Hermitianized Hamiltonian (4.22) exhibits not only a chiral symmetry  $\Sigma$  but also a *mirror* symmetry (with respect to the  $y$  axis)  $\sigma_z \otimes \sigma_x$  that commutes with  $\Sigma$ , leading to a  $\mathbb{Z}$  classification [198]. In Fig. 4.7(b), we plot the spectrum for  $m = 1 + 0.5i$  with a nontrivial mirror winding number 1 [198], and find a mode with *zero* energy under the open boundary condition. Such a zero-energy mode should be robust due to the interplay of a nontrivial non-Hermitian Chern number [253] and the inversion symmetry of the spectrum enforced by Eq. (4.55). This observation, together with the bulk-edge correspondence found in 1D, suggests that a topologically nontrivial bulk with respect to a base energy  $E_B$  implies one or more robust edge modes *at*  $E_B$  (or crossing  $E_B$  upon the change of boundary condition). This is much stronger a requirement than the existence of robust edge modes (that may appear anywhere), which can be ensured by a nontrivial non-Hermitian Chern number as discussed in Ref. [253]. From this viewpoint, it may not be so incomprehensible that 2D non-Hermitian systems in AZ classes are always trivial — *these systems may exhibit robust edge modes, but they are not expected to exhibit an edge mode at the base energy in general.*

Finally, we again emphasize that weak topological numbers [40] are not shown in Table 4.1.

Indeed, we can define two winding numbers

$$w_\mu \equiv \int_{-\pi}^{\pi} \frac{dk_\mu}{2\pi i} \partial_{k_\mu} \ln \det H(k_x, k_y), \quad \mu = x, y \quad (4.56)$$

for any 2D lattices, but they inherit from the lower dimension ( $d = 1$ ) and are not genuinely 2D topological invariants. On the other hand, a nontrivial weak topological number can lead to a dramatic change in the spectrum under different boundary conditions, just like the 1D case shown in Fig. 4.3(a).

## 4.4 Topological indices for non-Hermitian systems

In this section, we identify the topological indices and provide some concrete examples for all the nontrivial non-Hermitian AZ classes in zero and one dimension.

### 4.4.1 Zero dimension

According to the  $K$ -theory classification (see Table 4.1), if we impose either time-reversal or (and) particle-hole symmetry, we obtain two (four) types of topologically different matrices. Since a matrix of class BDI is made from two independent matrices of class AI (or D), it suffices to focus on a single  $\mathbb{Z}_2$  topological number. Furthermore, class AI and class D can be mapped into each other by simply multiplying the imaginary unit  $i$  [299]; therefore we will primarily discuss the case of class AI without loss of generality.

Note that an involutory ( $T^2 = 1$ ) time-reversal symmetry can always be represented as  $T = K$  (we recall that  $K$  denotes complex conjugation) in an appropriate basis [300], under which all the time-reversal symmetric matrices are real. In this case, the polar decomposition becomes  $H = OR$ , where  $O$  is orthogonal and  $R$  is real, symmetric and positive-definite. Since  $H \simeq O$ , we conclude that the  $\mathbb{Z}_2$  topological number characterizes the two disconnected sectors of an orthogonal group. In terms of  $H$ , this topological number can be defined as

$$s \equiv \text{sgn}(\det H), \quad (4.57)$$

which takes on 1 (−1) if there is an even (odd) number of eigenvalues on the negative real axis (see Fig. 4.8). Using the correspondence between classes AI and D, the  $\mathbb{Z}_2$  index of a particle-hole symmetric Hamiltonian can be defined as

$$s' \equiv \text{sgn}(\det iH), \quad (4.58)$$

which takes on 1 (−1) if there is an even (odd) number of eigenvalues on the positive imaginary axis.

### *PT*-symmetric systems

As mentioned in Sec. 4.1.1, *PT*-symmetric systems are an important class of non-Hermitian systems whose spectra stay real for sufficiently small non-Hermiticity [232, 233]. When the balanced gain and loss in a *PT*-symmetric system exceeds a threshold, complex eigenenergies emerge and such a spectral transition is called the *PT*-symmetry breaking. Remarkably, in the sense of Eq. (4.57) (Eq. (4.58)), a *PT*-symmetry-breaking (or an anti-*PT*-symmetry-breaking [219]) transition across an exceptional point can be identified as a topological transition. While the *PT* symmetry physically differs from the  $T$  symmetry, as long as the symmetry operator is

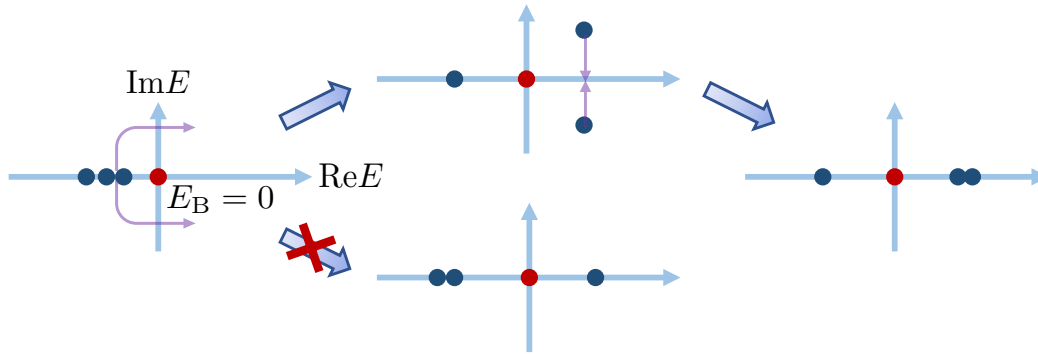


Figure 4.8: Spectrum deformation in a class AI system described by a  $3 \times 3$  matrix in zero dimension. The spectrum is always symmetric with respect to the real axis. Without touching  $E_B = 0$ , the number of eigenvalues on the negative or positive real axis can only change by an even number; therefore, a  $\mathbb{Z}_2$  index ( $s = -1$ ) can be defined as in Eq. (4.57). Reproduced from Fig. 8 of Ref. [44]. Copyright © 2018 by the American Physical Society.

involutionary and anti-unitary, the topological classification in zero dimension is the same as class AI. As a minimal example, we consider a non-Hermitian two-level system [225]

$$H = \Omega\sigma_x + i\gamma\sigma_z, \quad \Omega, \gamma \in \mathbb{R}, \quad (4.59)$$

which features a  $PT$  symmetry  $\sigma_x K$ . We can check that  $\det H = \gamma^2 - \Omega^2$  and thus  $s = -1$  ( $s = 1$ ) in the  $PT$ -unbroken ( $PT$ -broken) phase. A topological transition with anti- $PT$ -symmetry breaking (class D) can similarly be constructed by multiplying Eq. (4.59) by  $i$ .

At first glance, the conclusion that a  $PT$ -symmetry breaking transition is topological seems rather odd, since in Hermitian systems the concept of SPT is complementary to spontaneous symmetry breaking. As for non-Hermitian systems, this is possible due to the conceptual difference in defining topological phases as dynamical phases instead of states of matter, so that the eigenstates do not necessarily respect the symmetry. In particular, the  $\mathbb{Z}_2$  topological number (4.57) for class AI in zero dimension is solely determined by the energy spectrum. The emergence of  $E$  and  $E^*$  is indeed topologically forbidden if they originate from two real energies with opposite signs. This is because in  $PT$ -symmetric systems a pair of complex conjugate eigenvalues emerges when two real eigenenergies coalesce; if these real eigenenergies have opposite signs, they have no alternative but to meet at the origin which, however, is forbidden by our assumption. The sign of the product of the two eigenvalues, which gives the  $\mathbb{Z}_2$  index in Eq. (4.57), is negative before the  $PT$ -symmetry breaking and positive after it. Thus the  $PT$  transition is topologically forbidden unless the origin is touched.

### Quantum channels

Another important example is *quantum channels* or completely positive (CP) and trace-preserving (TP) maps. A CPTP map always has a Kraus representation [301]

$$\mathcal{E}(\rho) = \sum_{\alpha} K_{\alpha} \rho K_{\alpha}^{\dagger}, \quad (4.60)$$

where the Kraus operators  $K_\alpha$  satisfy  $\sum_\alpha K_\alpha^\dagger K_\alpha = I$ . Alternatively,  $\mathcal{E}$  can be represented as an enlarged non-Hermitian matrix

$$\mathcal{E} = \sum_\alpha K_\alpha \otimes K_\alpha^* \quad (4.61)$$

on the Liouville space  $\mathfrak{V} \equiv \mathcal{V} \otimes \mathcal{V}^*$ . Remarkably, defining  $\mathcal{K}(\rho) \equiv \rho^\dagger$  as the Hermitian-conjugate superoperator, which is anti-unitary<sup>4</sup> and involutory ( $\mathcal{K}^2(\rho) = \rho$ ), we have

$$\mathcal{E}\mathcal{K}(\rho) = \mathcal{K}\mathcal{E}(\rho) = \sum_\alpha K_\alpha \rho^\dagger K_\alpha^\dagger, \quad (4.62)$$

which is actually the Hermiticity-preserving property of  $\mathcal{E}$  [274]. Such an inherent symmetry is absolutely robust, unlike the  $PT$  symmetry which can hardly be exact due to experimental imperfection. Therefore, a CPTP map  $\mathcal{E}$  always belongs to the AI class and is classified by a  $\mathbb{Z}_2$  topological index, determined by the sign of  $\det \mathcal{E} \in \mathbb{R}$ . We note that the same classification applies to a CP map, which can also be represented by Eq. (4.60) with no constraints on  $\{K_\alpha\}$ . With the TP property imposed, the eigenvalues of  $\mathcal{E}$  are enforced to be on or inside the unit circle in the complex plane [302].

It is natural to define a trivial map if it is connected to the identity channel  $\mathcal{I}$ . It then follows that  $\mathcal{E}$  is trivial as long as  $\det \mathcal{E} > 0$ . In this sense, each invertible quantum dynamical map  $\Phi_t$  is trivial since  $\Phi_t$  can continuously be deformed into  $\Phi_0 = \mathcal{I}$ , irrespective of whether  $\Phi_t$  is Markovian or not [303]. Conversely, we can conclude that a topologically nontrivial quantum channel with  $\det \mathcal{E} < 0$  can never be continuously generated by a Markovian dynamics. It is nevertheless easy to construct a nontrivial channel via random unitary transformations which take the following form:

$$\mathcal{E}(\rho) = \sum_j p_j U_j \rho U_j^\dagger, \quad \sum_j p_j = 1. \quad (4.63)$$

A prototypical example is the isotropic depolarization channel for a single qubit [278]:

$$\mathcal{E}_d(\rho) = p\rho + \frac{1-p}{3} \sum_{\mu=x,y,z} \sigma_\mu \rho \sigma_\mu, \quad (4.64)$$

whose extension  $\mathcal{E}_d \otimes \mathcal{I}$  has widely been used to introduce imperfection into a maximally entangled qubit pair [304]. We can check that  $\det \mathcal{E}_d = [(4p-1)/3]^3$ , so that a topological transition occurs at  $p = 1/4$ , where the channel becomes a constant (fully depolarized) map  $\mathcal{E}_d(\rho) = \sigma_0/2$ .

If the quantum channel plays a role of a Floquet superoperator for a periodically driven open system [44], the stroboscopic evolution is governed by  $\rho_{n+1} = \mathcal{E}(\rho_n)$ . If we look at the long-time dynamics, the topological index  $\text{sgn}(\det \mathcal{E})$  might become meaningless since only the long-lived modes with eigenvalues with nearly unit norm are relevant. Denoting the superprojector onto such a metastable manifold  $\mathfrak{V}_{\text{ms}}$  as  $\mathcal{P}$ , which can always be made Hermiticity-preserving [305], we expect the sign of  $\det_{\mathfrak{V}_{\text{ms}}} \mathcal{P}\mathcal{E}\mathcal{P}$ , denoted by  $s_{\text{ms}}$ , to be important for the long-time dynamics. If  $s_{\text{ms}} = -1$ , there must be an odd number of long-lived modes near  $-1$ . When the system is perturbed, we expect that at least one long-lived mode stays on the real axis near  $-1$ . This cannot be ensured by  $s_{\text{ms}} = 1$ , since all the long-lived modes near  $-1$  can leave the real axis in a pairwise manner. The above discussion is parallel to the  $\mathbb{Z}_2$  topological insulators [12, 42, 167], on the surface of which at least one Dirac cone survives under time-reversal symmetric perturbations.

<sup>4</sup>This should be understood with respect to the Hilbert-Schmidt inner product  $\langle A|B \rangle \equiv \text{Tr}[A^\dagger B]$  defined in Eq. (2.36) in Chapter 2. We can check that  $\langle \mathcal{K}A|\mathcal{K}B \rangle = \text{Tr}[AB^\dagger] = \text{Tr}[B^\dagger A] = \langle B|A \rangle$ .

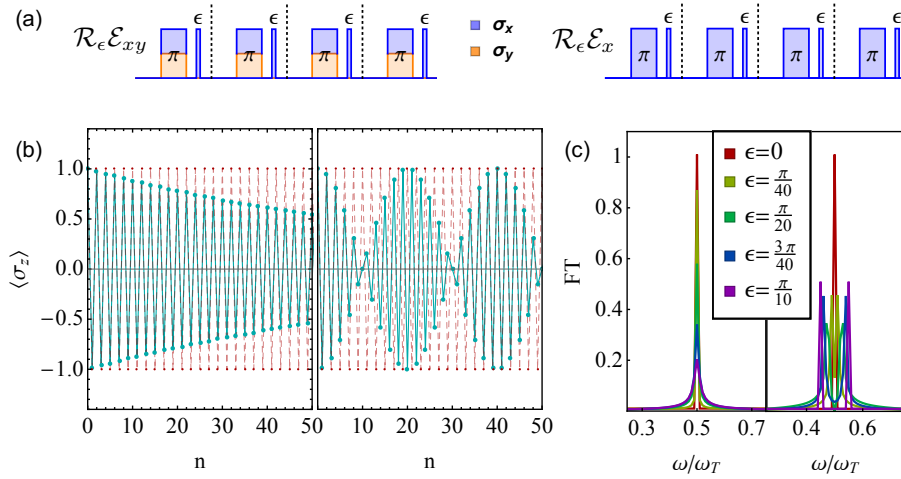


Figure 4.9: (a) Pulse sequence of the stroboscopic qubit dynamics governed by two types of operations  $\mathcal{R}_\epsilon \mathcal{E}_{xy}$  and  $\mathcal{R}_\epsilon \mathcal{E}_x$ . In the former case,  $\pi$ -pulses are applied randomly in the  $x$  and  $y$  directions with equal probability, leading to  $s_{\text{ms}} = -1$ . In the latter case,  $\pi$ -pulses are applied in the  $x$  direction, leading to  $s_{\text{ms}} = 1$ . (b) Starting from  $\rho_0 = |\uparrow\rangle\langle\uparrow|$ , the dynamics of  $\langle\sigma_z\rangle$  for  $\epsilon = 0$  (red dots) are the same between the two cases. As for  $\epsilon = 0.05\pi$  (green dots), the dynamics governed by  $\mathcal{R}_\epsilon \mathcal{E}_{xy}$  (left) exhibit a discrete time-crystalline-like behavior [31, 32, 74], but the dynamics governed by  $\mathcal{R}_\epsilon \mathcal{E}_x$  do not. (c) Fourier transform of  $\langle\sigma_z\rangle_{t=n}$  into the frequency domain. The single peak located at  $\omega = 0.5\omega_T$  ( $\omega_T$  is the fundamental frequency determined by the driving period) stays robust for  $\mathcal{R}_\epsilon \mathcal{E}_{xy}$  (left), but splits into two peaks for  $\mathcal{R}_\epsilon \mathcal{E}_x$  (right). Reproduced from Fig. 9 of Ref. [44]. Copyright © 2018 by the American Physical Society.

As a minimal illustration, let us consider a critical (zero full determinant) quantum channel

$$\mathcal{E}_{xy}(\rho) = \frac{1}{2}(\sigma_x \rho \sigma_x + \sigma_y \rho \sigma_y), \quad (4.65)$$

which has a single long-lived mode  $\sigma_z$  with eigenvalue  $-1$  in addition to the steady state  $\sigma_0/2$ , so that  $s_{\text{ms}} = -1$ . Starting from  $|\uparrow\rangle$ , we find an antiferromagnetic ( $\uparrow\downarrow\uparrow\downarrow \dots$ ) stroboscopic dynamics (see red dots in Fig. 4.9(b)). The same dynamics can be realized by unitary  $\pi$ -rotation along the  $x$  axis, i.e.,

$$\mathcal{E}_x(\rho) = \sigma_x \rho \sigma_x, \quad (4.66)$$

which has two modes with eigenvalues  $-1$  so that  $s_{\text{ms}} = s = 1$ . Now let us disturb the temporal antiferromagnetic pattern by inserting a sudden pulse

$$\mathcal{R}_\epsilon(\rho) = e^{-i\pi\epsilon\sigma_x} \rho e^{i\pi\epsilon\sigma_x} \quad (4.67)$$

at the end of each evolution period (see Fig. 4.9(a)). As clearly shown by the Fourier transform of  $\langle\sigma_z\rangle_{t=nT}$  in Fig. 4.9(c), the antiferromagnetic pattern is robust against perturbation to  $\mathcal{E}_{xy}$  with  $s_{\text{ms}} = -1$ , but is fragile for  $\mathcal{E}_x$  with  $s_{\text{ms}} = 1$ . This observation is reminiscent of discrete time crystals [28, 29, 31, 32, 73, 74], which are Floquet systems that spontaneously break the discrete time-translation symmetry. Akin to intrinsic topological order that does not need any symmetry protection [177], long-range correlation has been identified as the origin of the rigidity of unitary discrete time crystals in 1D [306]. It would be interesting to study whether a nontrivial  $\mathbb{Z}_2$  topological index, which emerges from the inherent time-reversal-like symmetry (4.62), can lead to the absolute rigidity of the 0D dissipative discrete time crystal discussed in Chapter 2 [44].

#### 4.4.2 One dimension

We discuss the general structures of non-Hermitian Hamiltonians in 1D and the corresponding topological numbers in addition to class A (cf. Sec. 4.2).

For class DIII (CI), we can always find a basis under which  $\Gamma = \sigma_z \otimes 1$  and  $T = \sigma_x \otimes i\sigma_y K$  ( $C = \sigma_x \otimes i\sigma_y K$ ). The symmetry requirements  $\Gamma H(k) = -H(k)\Gamma$  and  $TH(k) = H(-k)T$  ( $CH(k) = -H(-k)C$ ) lead to the following general form of the Hamiltonian:

$$H(k) = \begin{bmatrix} 0 & h(k) \\ \pm\sigma_y h(-k)^* \sigma_y & 0 \end{bmatrix}, \quad (4.68)$$

where  $h(k)$  can be an arbitrary invertible matrix, and  $+$  and  $-$  correspond to class DIII and CI, respectively. Due to the arbitrariness of  $h(k)$ , the topological classification coincides with class A and the topological number is determined by  $w_h \in \mathbb{Z}$ , i.e., the winding number of  $h(k)$ .

For class AIII, we can always find a basis under which  $\Gamma = \sigma_z \otimes 1$ . A general form of the Hamiltonian reads

$$H(k) = \begin{bmatrix} 0 & h_1(k) \\ h_2(k) & 0 \end{bmatrix}, \quad (4.69)$$

with  $h_{1,2}(k)$  being arbitrary invertible matrices. Note that there are two independent winding numbers  $w_{h_1}$  and  $w_{h_2}$  in accordance with the classification  $\mathbb{Z} \oplus \mathbb{Z}$ . We can generally have  $w_{h_2} \neq -w_{h_1}$ , implying different numbers of (quasi-)zero modes localized at the two open boundaries. As shown in Fig. 4.10(a), a two-band model with  $h_1(k) = J_1 e^{2ik}$  and  $h_2(k) = J_2 e^{-ik}$  in Eq. (4.69) has two and one zero modes at the left and right boundaries, respectively, as a consequence of asymmetric hopping amplitudes. It is interesting to note that for the Hermitian case the non-Hermitian  $\mathbb{Z} \oplus \mathbb{Z}$  group degenerates into its subset  $\{(n, -n) : n \in \mathbb{Z}\}$  due to the Hermitian



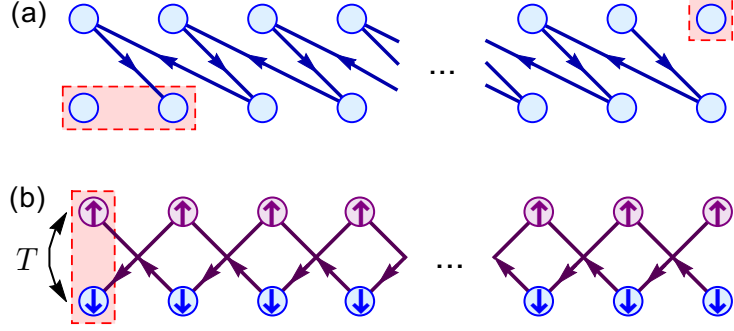


Figure 4.10: Non-Hermitian open chains with unidirectional hoppings (indicated by the arrows) belonging to (a) class AIII and (b) class AII. In (a), the number of zero modes at the left boundary (enclosed by a red rectangle) is not the same as that on the right boundary. In (b), the zero modes form Kramers pairs, which interchange via the time-reversal operator  $T$ , and therefore the total number of the edge modes must be even. Reproduced from Fig. 10 of Ref. [44]. Copyright © 2018 by the American Physical Society.

constraint ( $w_{h_2} = -w_{h_1}$ ), which is nothing but the  $\mathbb{Z}$  classification of class AIII. It is worth mentioning that the Hamiltonian studied in Ref. [212], which can be expressed as  $H(k) = (v + r \cos k)\sigma_x + r(\sin k - i)\sigma_y$  ( $v, r \in \mathbb{R}$ ), gives an example of the two generators of  $\mathbb{Z} \oplus \mathbb{Z}$  by taking  $0 < v/r < 2$  and  $-2 < v/r < 0$ . The  $\mathbb{Z}$  topological number identified therein turns out to be  $(w_{h_1} - w_{h_2})/2$ , which can be a half-integer only if the system is non-Hermitian.

For class AI (D), we can always find a basis under which  $T = K$  ( $C = K$ ), so that  $H(k)^* = H(-k)$  ( $H(k)^* = -H(-k)$ ). This requirement enforces the matrix elements of  $H(k)$  to be  $\sum_{n \in \mathbb{Z}} c_n e^{ink}$ , with  $\{c_n\}$  being real (purely imaginary) numbers, yet the winding number of  $H(k)$  does run over  $\mathbb{Z}$ . All the different topological phases can be realized in a single-band model  $H(k) = e^{ink}$  ( $H(k) = ie^{ink}$ ) with  $n \in \mathbb{Z}$ .

For class BDI, we can always find a basis under which  $\Gamma = \sigma_z$ ,  $T = K$  and  $C = \sigma_z K$ . The general form of the Hamiltonian is again given by Eq. (4.69), but  $h_{1,2}(k)^* = h_{1,2}(-k)$  is required. Similar to class AIII, we have two independent winding numbers  $w_{h_1}$  and  $w_{h_2}$  and the topological classification is  $\mathbb{Z} \oplus \mathbb{Z}$ .

For class AII (C), we can always find a basis under which  $T = i\sigma_y K$  ( $C = i\sigma_y K$ ), so that  $\sigma_y H(k)^* = H(-k)\sigma_y$  ( $\sigma_y H(k)^* = -H(-k)\sigma_y$ ). This symmetry requirement restricts the form of the Hamiltonian to be

$$H(k) = \begin{bmatrix} h_1(k) & h_2(k) \\ \mp h_2(-k)^* & \pm h_1(-k)^* \end{bmatrix}, \quad (4.70)$$

where  $h_1(k)$  and  $h_2(k)$  can be arbitrary (but  $H(k)$  should be invertible after all) and the upper (lower) signs correspond to class AII (C). In this case, we can prove that the winding number of a Hamiltonian must be even, as indicated by the  $2\mathbb{Z}$  classification. To this end, let us first unitarize  $H(k)$  into  $U(k)$  and show that  $\text{Tr}[U(k)^\dagger \partial_k U(k)]$  is an even function of  $k$ . From Eq. (4.42) we know that

$$\begin{aligned} & -\text{Tr}[U(-k)^\dagger \partial_k U(-k)] = -\eta_S^2 \text{Tr}[U_S U(k)^\dagger U_S^\dagger \partial_k (U_S U(k)^* U_S^\dagger)] \\ & = -\text{Tr}[U(k)^\dagger \partial_k U(k)^*] = -\text{Tr}[(\partial_k U^\dagger(k))U(k)] \\ & = -\partial_k \text{Tr}[U^\dagger(k)U(k)] + \text{Tr}[U^\dagger(k)\partial_k U(k)] = \text{Tr}[U^\dagger(k)\partial_k U(k)], \end{aligned} \quad (4.71)$$

where we have used  $\text{Tr}[A^\dagger] = \text{Tr}[A]$ ,  $\partial_k(AB) = (\partial_k A)B + A\partial_k B$  and  $U^\dagger(k)U(k) = 1$ . Using the

fact that  $\text{Tr}[U^\dagger(k)\partial_k U(k)]$  is even in terms of  $k$ , the winding number can be expressed as

$$w = \int_{-\pi}^{\pi} \frac{dk}{2\pi i} \text{Tr}[U^\dagger(k)\partial_k U(k)] = 2 \int_0^\pi \frac{dk}{2\pi i} \text{Tr}[U^\dagger(k)\partial_k U(k)] = 2 \int_0^\pi \frac{dk}{2\pi i} \partial_k \ln \det U(k). \quad (4.72)$$

However, this is not sufficient to ensure  $w \in 2\mathbb{Z}$  since  $\int_0^\pi \frac{dk}{2\pi i} \partial_k \ln \det U(k)$  may be a half-integer. Indeed, Eq. (4.72) is applicable also to classes AI and D. To rule out this possibility, we should show that  $\det U(0)$  and  $\det U(\pi)$  share the same argument. To show this, it is convenient to look at the individual eigenvalues. Note that  $TU(\Gamma)T^{-1} = U(\Gamma)$  ( $CU(\Gamma)C^{-1} = -U(\Gamma)$ ) at  $\Gamma = 0, \pi$ , and  $T^2 = -1$  ( $C^2 = -1$ ) enforce the eigenvalues to appear in pairs like  $e^{\pm i\theta_\alpha}$  ( $\pm e^{\pm i\theta_\alpha}$ ), leading to  $\det U(0) = \det U(\pi) = 1$  ( $\det U(0) = \det U(\pi) = (-1)^{\dim \mathcal{V}/2}$ ). This fact ensures that  $w = 2 \int_0^\pi \frac{dk}{2\pi i} \partial_k \ln \det U(k)$  is quantized as an even integer. An important physical implication is that there must be an even number of (quasi)-edge modes, which actually form Kramers pairs. In Fig. 4.10(b), we present a minimal model of spin- $\frac{1}{2}$  fermions with  $h_1(k) = 0$  and  $h_2(k) = J e^{ik}$  in Eq. (4.70).

For class CII, we can always find a basis under which  $\Gamma = \sigma_z \otimes 1$  and  $T = \sigma_0 \otimes i\sigma_y K$  ( $C = \sigma_z \otimes i\sigma_y K$ ). A general form of the Hamiltonian in this case is again given by Eq. (4.69); however, we do not have  $\sigma_y h_{1,2}(k)^* = h_{1,2}(-k)\sigma_y$ , that is, both  $h_1(k)$  and  $h_2(k)$  belong to class AII. The topological characterization is thus given by two even integers  $w_{h_1}$  and  $w_{h_2}$ , consistent with the  $2\mathbb{Z} \oplus 2\mathbb{Z}$  classification.

## Chapter 5

# Topological entanglement-spectrum crossing in quench dynamics

In the previous chapter, we have known that if the Floquet unitary of a Thouless pump (e.g., the left or right translation operator) is reinterpreted as a non-Hermitian Hamiltonian (e.g., the Hatano-Nelson model with unidirectional hopping), then such a non-Hermitian system has a nontrivial spectral winding number. Here, we would like to ask another fundamental question: can we realize a Thouless pump by a quantum quench, i.e., a sudden change of the Hamiltonian, which is the arguably simplest way of generating nonequilibrium quantum dynamics? While the time periodicity can be ensured by a flat-band quench, the answer turns out to be negative because there obviously exists a global section of the vector bundle over the momentum-time manifold. On the other hand, it is still unclear whether we can realize some SPT pumps by quench dynamics. In this chapter, we address this question in  $(1 + 1)$ D spacetime. We perform a systematic analysis for all the AZ classes and identify those that support topologically nontrivial quench dynamics. We also propose using the entanglement-spectrum crossing to detect a nontrivial spacetime topology underlying quench dynamics.

### 5.1 Introduction

Topological quantum systems have attracted growing interest theoretically and experimentally [168, 169], due partly to their fundamental importance in phase transitions beyond the conventional symmetry-breaking paradigm [2] and applications to quantum computation [178, 179, 307, 308]. For gapped free-fermion systems at equilibrium, a systematic classification has been established for the Altland-Zirnbauer (AZ) classes [39–41, 194, 195] and with additional crystalline symmetries [9, 198, 200, 201, 309]. Topological phases are characterized by topological invariants, some of which, such as the Zak phase and the Chern number, have been measured in ultracold atomic gases [18, 171, 172]. Entanglement measures, which are related to the full *entanglement spectrum* (ES) [310], provide yet another powerful tool to detect (symmetry-protected) topological order. In particular, 1D SPT phases exhibit degeneracy in the ES [132], while 2D topologically ordered phases have a nonzero topological entanglement entropy [311–313].

Recently, studies on topological systems have been extended to various nonequilibrium regimes [23]. As discussed in the previous two chapters, both Floquet systems [25, 58] and non-Hermitian systems [265, 314] have been demonstrated to exhibit intrinsically nonequilibrium topological phases with no static counterparts, including but not restricted to anomalous Floquet chiral phases [37, 65, 67, 68], intrinsic Floquet SPT phases [28, 66, 69, 71] (cf. Chapter 3), point-gapped non-Hermitian topological phases [44, 212, 257, 258] (cf. Chapter 4) and excep-

tional non-Hermitian topological semimetals [214,315–318]. In this chapter, we focus on another important topic about *quantum quenches* in topological systems [45,122,319–328]. Compared with dissipation and periodic driving, this is probably the simplest scenario for bringing a system out of equilibrium: We just start from the ground state  $|\Psi\rangle$  of an initial or prequench Hamiltonian  $H$  and then suddenly change the Hamiltonian to  $H'$ , the postquench Hamiltonian. The wave function subsequently undergoes a nontrivial unitary evolution

$$|\Psi(t)\rangle = e^{-iH't}|\Psi\rangle. \quad (5.1)$$

Previous studies have unveiled the stability of spatial topological numbers [122,320,321], topological dynamical phase transitions [322–324], a nonequilibrium Hall response which is not associated with the Chern number [325–327] and momentum-time Hopf links upon quenches between two 2D insulators with different Chern numbers [45,328].

Despite many previous studies mentioned above, it stays an open problem to *systematically* identify and detect the *spacetime* topology of quench dynamics. This issue is closely related to adiabatic topological pumps, such as the renowned Thouless pump [280] and the more recently proposed  $\mathbb{Z}_2$  topological pumps protected by time-reversal or particle-hole symmetries [195,329]. These topological pumps can be considered as a special type of Floquet systems [65] and are also characterized by the topological number of the wave function dynamics over the momentum-time manifold [195,280,329]. However, there are also several crucial differences. First, unlike adiabatic pumps, the quench dynamics governed by Eq. (5.1) are highly nonadiabatic. Second, even if the pre- and postquench Hamiltonians respect the same symmetries, which we assume throughout this chapter, the symmetries might be partially or even completely broken in the quench dynamics. This phenomenon was pointed out in Ref. [122] and is termed *dynamical symmetry breaking*. This never happens in an adiabatic pump, provided that initially there is no spontaneous symmetry breaking and the time-dependent Hamiltonian stays gapped. Third, compared to quench dynamics, adiabatic pumps actually have much greater degrees of freedom in the time-dependent wave function, since the former is fully determined by an initial state and the (time-independent) postquench Hamiltonian while the latter has a continuous time dependence in the Hamiltonian.

As briefly mentioned above, Ref. [45] has identified the Hopf-link structure in  $(2+1)$ D quench dynamics. However, this is not a stable topological structure since it is well-defined only for a clean system with two bands [147]. In contrast, here we would like to identify the stable topological structures of quench dynamics that survive additional bands and disorder. As the first step to achieve a complete understanding of this issue, we confine ourselves to  $(1+1)$ D quench dynamics. We employ the  $K$ -theory to identify *all* the AZ classes that accommodate stable nontrivial dynamical topology (see Table 5.1), and propose the time evolutions of ES as their universal indicators. In particular, we demonstrate the ES crossing can help us distinguish the  $\mathbb{Z}$  topological number for class BDI from the  $\mathbb{Z}_2$  for class D. These results should be testifiable in the state-of-the-art experiments of ultracold atoms [128,151,330–332] and trapped ions [129,333–335], where many-body tomography has become possible [150,328,336–339].

## 5.2 Parent Hamiltonians and their classifications

In this section, we first introduce the notion of parent Hamiltonians which formally relate quench dynamics to adiabatic pumps. After identifying the symmetries of the time-dependent parent Hamiltonians with AZ symmetries, we work out their  $K$ -theory classifications and the corresponding topological numbers. Following a case-by-case analysis, we single out all the topological numbers that can take on nontrivial values. Finally, we discuss a specific case of two-band systems.

### 5.2.1 Parent Bloch Hamiltonian

In order to perform a systematic classification, we can formally relate the problem for quench dynamics to that for adiabatic pumps by realizing that the nonequilibrium wave function  $|\Psi(t)\rangle$  in Eq. (5.1) is the ground state of

$$H(t) = e^{-iH't} H e^{iH't}, \quad (5.2)$$

which we call a *parent Hamiltonian*. This parent Hamiltonian is nothing but the prequench Hamiltonian  $H$  in the rotating frame with respect to the postquench Hamiltonian  $H'$ . We note that  $H(t)$  is not unique since the quench dynamics stay unchanged if  $H$  is deformed in a way such that the gap stays open and the ground state stays unchanged. Unlike the time-dependent Hamiltonian of an adiabatic pump, the parent Hamiltonian is not periodic in time. To make it time periodic, the postquench Hamiltonian should have even level spacings. For free-fermion systems, on which we focus throughout this chapter, this is always the case if the postquench Hamiltonian is flattened. The topological classifications will be performed for such a flat-band case, but we believe that some crucial dynamical signatures can still be observed even for nontrivial band dispersions.<sup>1</sup>

In 1D, if we further assume translation invariance, we can define the parent Bloch Hamiltonian  $h(k, t)$  from

$$H(t) = \sum_k \mathbf{c}_k^\dagger h(k, t) \mathbf{c}_k, \quad (5.3)$$

where  $\mathbf{c}_k \equiv [c_{ka}]_a^T$  is a vector consisting of fermion annihilation operators with the same wave number  $k$  and different internal states  $a$  such as spins and sublattices. Denoting  $h(k)$  and  $h'(k)$  as the Bloch Hamiltonians of  $H$  and  $H'$ , i.e.,

$$H = \sum_k \mathbf{c}_k^\dagger h(k) \mathbf{c}_k, \quad H' = \sum_k \mathbf{c}_k^\dagger h'(k) \mathbf{c}_k, \quad (5.4)$$

we can show that  $h(k, t)$  is given by

$$h(k, t) = e^{-ih'(k)t} h(k) e^{ih'(k)t}. \quad (5.5)$$

The derivation is rather straightforward. First, according to the general definition in Eq. (5.2), the equation of motion for  $H(t)$  reads

$$i\partial_t H(t) = [H', H(t)], \quad H(0) = H. \quad (5.6)$$

With translation invariance imposed, Eq. (5.6) can be decomposed into independent blocks having different wave numbers:

$$i\partial_t \mathbf{c}_k^\dagger h(k, t) \mathbf{c}_k = [\mathbf{c}_k^\dagger h'(k) \mathbf{c}_k, \mathbf{c}_k^\dagger h(k, t) \mathbf{c}_k] = \mathbf{c}_k^\dagger [h'(k), h(k, t)] \mathbf{c}_k, \quad h(k, 0) = h(k). \quad (5.7)$$

Here we have used the fermion-operator identity:

$$[c_{k\alpha}^\dagger c_{k\beta}, c_{k\gamma}^\dagger c_{k\delta}] = \delta_{\beta\gamma} c_{k\alpha}^\dagger c_{k\delta} - \delta_{\alpha\delta} c_{k\gamma}^\dagger c_{k\beta}. \quad (5.8)$$

Note that Eq. (5.7) implies Eq. (5.5). It is worth mentioning that the above derivation is not specific to 1D but applies to an arbitrary spatial dimension.

<sup>1</sup>While we will see that there are indeed some observable signatures according to the numerical results in several specific models, whether the dynamical topology is stable against band dispersions is not a trivial problem at all. See Ref. [340] for some recent discussions on this subtle issue.

As mentioned in the beginning of this subsection, to make  $h(k, t)$  in Eq. (5.5) time periodic, we can flatten  $h(k)$  and  $h'(k)$  into  $h_1(k)$  and  $h'_1(k)$ , which satisfy

$$h_1(k)^2 = h'_1(k)^2 = J^2, \quad (5.9)$$

and share the same symmetry as  $h(k)$  and  $h'(k)$  [40]. The corresponding parent Bloch Hamiltonian is also flattened, taking the form

$$\tilde{h}(k, t) = e^{-ih'_1(k)t} h_1(k) e^{ih_1(k)t}, \quad (5.10)$$

which satisfies

$$\tilde{h}(k, t)^2 = J^2, \quad \tilde{h}\left(k, t + \frac{\pi}{J}\right) = \tilde{h}(k, t). \quad (5.11)$$

We can actually write down its explicit expression as

$$\begin{aligned} \tilde{h}(k, t) = & \frac{1}{2}[h_1(k) + J^{-2}h'_1(k)h_1(k)h'_1(k) + (h_1(k) - J^{-2}h'_1(k)h_1(k)h'_1(k)) \cos(2Jt) \\ & + iJ^{-1}[h_1(k), h'_1(k)] \sin(2Jt)]. \end{aligned} \quad (5.12)$$

In the following, we will focus on the  $K$ -theory classification of  $\tilde{h}(k, t)$ . The same topological feature should be inherited by those parent Hamiltonians (5.2) that are continuously connected to  $\tilde{H}(t) = \sum_k \mathbf{c}_k^\dagger \tilde{h}(k, t) \mathbf{c}_k$  but without translation invariance (or/and time periodicity).

### 5.2.2 Symmetry constraints and the maximal $K$ -groups

Let us discuss the symmetry properties of  $\tilde{h}(k, t)$  in detail. Recalling both  $h_1(k)$  and  $h'_1(k)$  belong to the same AZ class, we have

$$Sh_1(k)S^{-1} = \eta_S h_1(\epsilon_S k), \quad Sh'_1(k)S^{-1} = \eta_S h'_1(\epsilon_S k), \quad \eta_S, \epsilon_S \in \{\pm 1\}, \quad (5.13)$$

where  $S = T$  (anti-unitary,  $\eta_T = 1$ ,  $\epsilon_T = -1$ ),  $C$  (anti-unitary,  $\eta_C = -1$ ,  $\epsilon_C = -1$ ) or/and  $\Gamma$  (unitary,  $\eta_\Gamma = -1$ ,  $\epsilon_\Gamma = 1$ ). If  $S$  is anti-unitary, we have  $SiS^{-1} = -i$ , leading to

$$S\tilde{h}(k, t)S^{-1} = \eta_S \tilde{h}(\epsilon_S k, -\eta_S t). \quad (5.14)$$

Otherwise, if  $S$  is unitary, we have

$$S\tilde{h}(k, t)S^{-1} = \eta_S \tilde{h}(\epsilon_S k, \eta_S t). \quad (5.15)$$

Here the crucial point is that while  $k$  in  $\tilde{h}(k, t)$  changes in the same way as that in the pre- and postquench Hamiltonians upon the symmetry actions,  $t$  may either change its sign or not depending on whether the (anti-)symmetry is unitary or anti-unitary.

With the symmetry constraints on  $\tilde{h}(k, t)$  clarified, we are ready to perform a systematic classification based on the  $K$ -theory (cf. Sec. 4.3.2 in the previous chapter). We emphasize that this classification relies on the symmetry constraints alone and does not take into account the specific structure of  $\tilde{h}(k, t)$  in Eq. (5.10) for quench dynamics. Identifying the nontrivial topological invariants realizable in quench dynamics will be the main focus of the next subsection.

We start from the simplest case without any symmetry requirement. In this case,  $\tilde{h}(k, t)$  simply belongs to class A in 2D and is characterized by  $K_{\mathbb{C}}(0; 2) = \pi_0(\mathcal{C}_0) = \mathbb{Z}$ .

We now turn to the case of TRS alone, i.e.,  $S = T$ . In this case, we have

$$T\tilde{h}(k, t)T^{-1} = \tilde{h}(-k, -t), \quad (5.16)$$

Table 5.1: Topological classification of  $\tilde{h}(k, t)$  subject to the symmetry constraints given in Eq. (5.14) (or Eq. (5.15) for class AIII) with  $S = T$  or/and  $C$  ( $S = \Gamma$ ). The last column shows a subset of the maximal  $K$ -group (Max.) that can be realized in quench dynamics (Dyn.), i.e., in the form of Eq. (5.10).

AZ class	$T$	$C$	$\Gamma$	Symmetry constraints on $\tilde{h}(k, t)$	Max.	Dyn.
A	0	0	0	None	$\mathbb{Z}$	0
AIII	0	0	1	$\Gamma\tilde{h}(k, t)\Gamma^{-1} = -\tilde{h}(k, -t)$	$\mathbb{Z} \oplus \mathbb{Z}$	$\mathbb{Z}$
AI	+	0	0	$T\tilde{h}(k, t)T^{-1} = \tilde{h}(-k, -t)$	0	0
BDI	+	+	1	$T\tilde{h}(k, t)T^{-1} = \tilde{h}(-k, -t), C\tilde{h}(k, t)C^{-1} = -\tilde{h}(-k, t)$	$\mathbb{Z}$	$\mathbb{Z}$
D	0	+	0	$C\tilde{h}(k, t)C^{-1} = -\tilde{h}(-k, t)$	$\mathbb{Z}_2$	$\mathbb{Z}_2$
DIII	-	+	1	$T\tilde{h}(k, t)T^{-1} = \tilde{h}(-k, -t), C\tilde{h}(k, t)C^{-1} = -\tilde{h}(-k, t)$	$\mathbb{Z}_2 \oplus \mathbb{Z}_2$	$\mathbb{Z}_2$
AII	-	0	0	$T\tilde{h}(k, t)T^{-1} = \tilde{h}(-k, -t)$	$\mathbb{Z}_2$	0
CII	-	-	1	$T\tilde{h}(k, t)T^{-1} = \tilde{h}(-k, -t), C\tilde{h}(k, t)C^{-1} = -\tilde{h}(-k, t)$	$\mathbb{Z}$	$\mathbb{Z}$
C	0	-	0	$C\tilde{h}(k, t)C^{-1} = -\tilde{h}(-k, t)$	0	0
CI	+	-	1	$T\tilde{h}(k, t)T^{-1} = \tilde{h}(-k, -t), C\tilde{h}(k, t)C^{-1} = -\tilde{h}(-k, t)$	0	0

which turns out to be the standard symmetry constraints of classes AI or AII in 2D. Therefore, the classification is  $K_{\mathbb{R}}(0; 2) = \pi_0(\mathcal{R}_6) = 0$  (trivial) for  $T^2 = 1$  (class AI), and is  $K_{\mathbb{R}}(4; 2) = \pi_0(\mathcal{R}_2) = \mathbb{Z}_2$  for  $T^2 = -1$  (class AII).

We then move on to the case of PHS alone, i.e.,  $S = C$ . The symmetry constraint on  $\tilde{h}(k, t)$  reads

$$C\tilde{h}(k, t)C^{-1} = -\tilde{h}(-k, t), \quad (5.17)$$

which coincides with that of an adiabatic fermion-parity pump [195]. To calculate the  $K$ -group, we can use the formula developed in Ref. [195]:

$$K_{\mathbb{F}}(s; d, D) = K_{\mathbb{F}}(s - d + D; 0, 0), \quad (5.18)$$

where  $\mathbb{F}$  can be either  $\mathbb{C}$  or  $\mathbb{R}$  and  $d$  ( $D$ ) corresponds to the number of momentum-like (position-like) variables that (do not) flip their signs upon the operation of an anti-unitary symmetry. For Eq. (5.17), we have  $d = D = 1$  and thus the classifications are given by  $K_{\mathbb{R}}(2; 0) = \pi_0(\mathcal{R}_2) = \mathbb{Z}_2$  for  $C^2 = 1$  (class D) and  $K_{\mathbb{R}}(6; 0) = \pi_0(\mathcal{R}_6) = 0$  for  $C^2 = -1$  (class C), respectively.

Now let us consider the case in which there are both TRS and PHS. Recalling Eq. (5.16), which means that  $t$  behaves like the wave number with respect to the TRS, we can treat this case as if we add an anti-unitary anti-symmetry  $C$  with  $d_{\parallel} = 1$  (the number of momentum components that do not flip under the symmetry operation) into class AI or AII. We can thus apply the formula developed in Ref. [200]:

$$K_{\mathbb{R}}(s, r; d, d_{\parallel}) = K_{\mathbb{R}}(s - d, r - d_{\parallel}; 0, 0), \quad (5.19)$$

where  $d = 2$ ,  $d_{\parallel} = 1$ , and  $s$  and  $r$  are determined by the base system (real AZ class, here it is either class AI or AII) and the additional two-fold symmetries. For class BDI, we have  $s = 0$  and  $r = 3$ , leading to  $\pi_0(\mathcal{C}_{-2}) = \mathbb{Z}$ . For class CI, we have  $s = 0$  and  $r = 1$ , leading to  $\pi_0(\mathcal{R}_6 \times \mathcal{R}_6) = 0$ . For class DIII, we have  $s = 4$  and  $r = 1$ , leading to  $\pi_0(\mathcal{R}_2 \times \mathcal{R}_2) = \mathbb{Z}_2 \oplus \mathbb{Z}_2$ . For class CII, we have  $s = 4$  and  $r = 3$ , leading to  $\pi_0(\mathcal{C}_2) = \mathbb{Z}$ .

For the remaining class AIII, we have to use another formula in Ref. [200]:

$$K_{\mathbb{C}}^{\text{U}}(s, r; d, d_{\parallel}) = K_{\mathbb{C}}^{\text{U}}(s - d, r - d_{\parallel}; 0, 0), \quad (5.20)$$

where  $d = 2$ ,  $d_{\parallel} = 1$ , and  $s$  and  $r$  are determined by the base system (complex AZ class) and the additional two-fold symmetry. This formula (5.20) formally coincides with Eq. (5.19) only if the additional symmetry is unitary; this explains why the superscript “U” is added. Since we start from class A, we have  $s = 0, r = 1$ , leading to  $\pi_0(\mathcal{C}_{-2} \times \mathcal{C}_{-2}) = \mathbb{Z} \oplus \mathbb{Z}$ .

We summarize all the results in the second rightmost column in Table 5.1. Remarkably, all the AZ classes characterized by a trivial maximal  $K$ -group turn out to be trivial classes in 1D [39, 40, 194]. The converse is not true, since classes A and AII are trivial in 1D, whereas the maximal groups are not. It is worthwhile to mention that the formulas developed in Ref. [200] are applicable to arbitrary dimensions and arbitrary two-fold-symmetry classes, which can be represented by certain Clifford-algebra extensions.

### 5.2.3 Topological numbers and the dynamical realizations

In this subsection, we identify all the topological numbers indicated by the  $K$ -groups and demonstrate that only some of them can be nontrivial for quench dynamics, while the others always vanish. We also provide some examples to realize these nontrivial topological numbers.

#### Complex AZ classes

We start from class A. Since there is no symmetry constraint, the topological number  $\mathbb{Z}$  is nothing but the Chern number:

$$C = \iint \frac{dtdk}{16\pi i J^3} \text{Tr}[\tilde{h}(k, t)[\partial_k \tilde{h}(k, t), \partial_t \tilde{h}(k, t)]], \quad (5.21)$$

where the double integral is carried out over  $[0, \pi J^{-1}] \times [-\pi, \pi]$ . Without specifying the form of  $\tilde{h}(k, t)$ , the generator of the maximal  $K$ -group  $\mathbb{Z}$  can be exemplified by a Thouless pump with a unit Chern number.

As for class AIII, the classification  $\mathbb{Z} \oplus \mathbb{Z}$  differs significantly from the trivial result for the conventional AZ class [39]. This is due to the fact that, unlike the wave number, the time variable changes its sign upon being acted on by the chiral operator  $\Gamma$ . The Chern number can thus be nonzero. This is to be contrasted with the conventional class AIII, where both wave numbers are not reversed so that the chiral symmetry enforces the Chern number to be zero.

In addition to the Chern number, the other topological number for class AIII can be identified as follows. Due to the reversion of  $t$ , the chiral symmetry is similar to a reflection (crystalline) symmetry and determines two high symmetry points  $t = 0, \pi/(2J)$ , where the Hamiltonian  $h(k, t)$  is chirally symmetric, i.e.,

$$\{\tilde{h}(k, 0), \Gamma\} = 0, \quad \left\{ \tilde{h}\left(k, \frac{\pi}{2J}\right), \Gamma \right\} = 0. \quad (5.22)$$

While we can define two winding numbers for these two Hamiltonians, only the *difference*  $\Delta W$  between the two winding numbers at the high symmetry points is a genuine 2D topological number [198, 200]. Indeed, a system with  $\Delta W = 0$  can be created by stacking a 1D chain along the time direction and thus the system does not possess a nontrivial 2D topology. In fact, we have  $(\Delta W + C)/2 \in \mathbb{Z}$ , due to the quantization of the Chern number over *half* of the momentum-time space with the boundaries at  $t = 0$  and  $\pi/(2J)$  contracted to lead to a boundary contribution  $\Delta W/2$ .<sup>2</sup> The two generators of the  $K$ -group can thus be exemplified by

<sup>2</sup>Here by contraction we mean that the boundary Bloch Hamiltonian is continuously deformed into a single point through a semi-sphere, as illustrated in Fig. 5.1. By stacking an appropriate trivial 2D Hamiltonian followed by a continuous deformation, we can always make  $\tilde{h}(k, 0) = \Sigma_x$  and  $\tilde{h}(k, \pi/(2J)) = \Sigma_x \cos(k\Delta W) + \Sigma_y \sin(k\Delta W)$  ( $\{\Sigma_x, \Gamma\} = \{\Sigma_y, \Gamma\} = \{\Sigma_x, \Sigma_y\} = 0$ ) so that the former is already contracted and the latter can be contracted into  $\Gamma$  through half of the standard construction in Ref. [195], which establishes an isomorphism between  $K_{\mathbb{C}}(0; 2)$  and  $K_{\mathbb{C}}(1; 1)$ . Therefore, the boundary contribution is  $\Delta W/2$ .



the Rice-Mele-Thouless pump [341, 342] ( $C = 1, \Delta W = 1$ ) and the quench dynamics in the SSH model across the phase boundary ( $C = 0, \Delta W = 2$ ), the latter of which will be studied in detail in the next subsection.

So far we only impose the symmetry requirement and have not yet specified the form of the Bloch Hamiltonian. If we confine ourselves to the quench dynamics, the flattened parent Hamiltonian takes the form of Eq. (5.10). The integrand in Eq. (5.21) can thus be calculated explicitly, giving

$$\begin{aligned}
i \operatorname{Tr}[\tilde{h}(k, t)[\partial_k \tilde{h}(k, t), \partial_t \tilde{h}(k, t)]] &= \operatorname{Tr}[h_1(k)[[A(k, t), h_1(k)] + \partial_k h_1(k), [h'_1(k), h_1(k)]]] \\
&= \operatorname{Tr}([(A(k, t), h_1(k)) + \partial_k h_1(k)][h'_1(k), h_1(k)], h_1(k))] \\
&= 2 \operatorname{Tr}[[A(k, t), h_1(k)](h'_1(k) - h_1(k)h'_1(k)h_1(k))] \\
&\quad + 2 \operatorname{Tr}[\partial_k h_1(k)(h'_1(k) - h_1(k)h'_1(k)h_1(k))] \\
&= 4J^2(\operatorname{Tr}[A(k, t)[h_1(k), h'_1(k)]] + \operatorname{Tr}[h'_1(k)\partial_k h_1(k)]),
\end{aligned} \tag{5.23}$$

where  $A(k, t) = e^{ih'_1(k)t}\partial_k(e^{-ih'_1(k)t})$  and we have used  $h_1(k)\partial_k h_1(k) + (\partial_k h_1(k))h_1(k) = 0$  and

$$\begin{aligned}
\partial_k \tilde{h}(k, t) &= e^{-ih'_1(k)t}[A(k, t), h_1(k)]e^{ih'_1(k)t} + e^{-ih'_1(k)t}\partial_k h_1(k)e^{ih'_1(k)t}, \\
\partial_t \tilde{h}(k, t) &= -ie^{-ih'_1(k)t}[h'_1(k), h_1(k)]e^{ih'_1(k)t}.
\end{aligned} \tag{5.24}$$

Noting that  $h'_1(k)^2 = J^2$ , we find that  $A(k, t)$  can be expressed as

$$A(k, t) = \left[ \frac{\sin^2 Jt}{J^2} h'_1(k) - i \frac{\sin(2Jt)}{2J} \right] \partial_k h'_1(k), \tag{5.25}$$

and its time integral gives

$$\int_0^{\frac{\pi}{J}} dt A(k, t) = \frac{\pi}{2J^3} h'_1(k) \partial_k h'_1(k). \tag{5.26}$$

Combining Eqs. (5.23) and (5.26), we obtain a vanishing Chern number:

$$C = -\frac{1}{4J^2} \int_{-\pi}^{\pi} dk \partial_k \operatorname{Tr}[h'_1(k)h_1(k)] = 0. \tag{5.27}$$

As mentioned in the beginning of this chapter, we actually have a more elegant interpretation to the vanishing Chern number, at least for two-band systems. In this case, we can easily write down the ground Bloch state  $\psi(k, t) = e^{-ih'_1(k)t}\psi(k)$ , where  $\psi(k)$  is the ground state of  $h_1(k)$ . Since  $\psi(k, t)$  is continuous in both  $k$  and  $t$ , there is no obstruction for choosing a global  $U(1)$  gauge over the momentum-time manifold, and thus the Chern number is necessarily zero.

As for parent Hamiltonians in class AIII, the Chern number must vanish as well. On the other hand,  $\Delta W$  can be nonzero, so that a subset  $\{(C, \Delta W) : C = 0, \Delta W \in 2\mathbb{Z}\}$ , which is isomorphic to  $\mathbb{Z}$ , can be realized. Furthermore, we have

$$\Delta W = 2(w' - w), \tag{5.28}$$

where  $w'$  ( $w$ ) is the winding numbers of  $h'_1(k)$  ( $h_1(k)$ ). Let us show Eq. (5.28) as follows. According to Eq. (5.10), the Bloch Hamiltonians at high symmetry points read

$$\tilde{h}(k, 0) = h_1(k), \quad \tilde{h}\left(k, \frac{\pi}{2J}\right) = h'_1(k)h_1(k)h'_1(k), \tag{5.29}$$

where, under the choice of  $\Gamma = \sigma^z \otimes 1$ ,  $h_1(k)$  and  $h'_1(k)$  take following the forms:

$$h_1(k) = \begin{bmatrix} 0 & u(k) \\ u(k)^\dagger & 0 \end{bmatrix}, \quad h'_1(k) = \begin{bmatrix} 0 & u'(k) \\ u'(k)^\dagger & 0 \end{bmatrix}. \quad (5.30)$$

Therefore, we have

$$h'_1(k)h_1(k)h'_1(k) = \begin{bmatrix} 0 & u'(k)u(k)^\dagger u'(k) \\ u'(k)^\dagger u(k)u'(k)^\dagger & 0 \end{bmatrix}, \quad (5.31)$$

implying  $w_{t=\frac{\pi}{2J}} = 2w' - w$ , where the winding numbers are given by

$$w = \int_{-\pi}^{\pi} \frac{dk}{2\pi i} \partial_k \ln \det u(k), \quad w' = \int_{-\pi}^{\pi} \frac{dk}{2\pi i} \partial_k \ln \det u'(k). \quad (5.32)$$

Since  $w_{t=0} = w$ , we finally obtain Eq. (5.28).

### Real AZ classes

According to the  $K$ -theory, there are five possibly nontrivial real AZ classes: BDI, D, DIII, AII and CII (see Table 5.1), which are nontrivial in the sense of the maximal  $K$ -group. We discuss them one by one.

The simplest case is class AII, of which the maximal  $K$ -group is exactly the same as the conventional result  $\mathbb{Z}_2$ . According to the seminal work by Moore and Balents [343], such a  $\mathbb{Z}_2$  can be determined from the parity (odd or even) of the Chern number of *half* of the Brillouin zone (which is the momentum-time manifold here) after contracting the boundaries while keeping TRS. See Fig. 5.1 for a schematic illustration of this approach. For class AII, the contraction of boundaries is always possible because class AII is trivial in 1D [39]. As for quench dynamics, since class AII is also trivial in 0D [194], we can always find two continuous paths of flattened Hamiltonians  $h_{L,R}(\gamma)$  parameterized by  $\gamma \in [0, 1]$ , which satisfy

$$h'_L(\gamma = 0) = h_1(0), \quad h'_L(\gamma = 1) = h'_1(0); \quad h'_R(\gamma = 0) = h'_1(\pi), \quad h'_R(\gamma = 1) = h_1(\pi). \quad (5.33)$$

The parent Hamiltonians are thus given by

$$\tilde{h}_{L,R}(\gamma, t) = e^{-ih'_{L,R}(\gamma)t} h_1(k_{L,R}) e^{ih'_{L,R}(\gamma)t}, \quad (5.34)$$

where  $k_L = 0$  and  $k_R = \pi$ . Using Eq. (5.27), we have

$$C = \frac{1}{4J^2} (\text{Tr}[h_1(0)^2] - \text{Tr}[h_1(\pi)^2]) = 0, \quad (5.35)$$

so that the  $\mathbb{Z}_2$  index for a quench dynamics generated by two class AII Hamiltonians is always trivial. On the other hand, with the symmetry constraint alone, the maximal  $K$ -group can be generated by the Fu-Kane pump [329], which is built upon two copies of the Rice-Mele-Thouless pump with opposite spins. Such a  $\mathbb{Z}_2$  index stays well-defined in the presence of spin-orbit coupling terms that respect the TRS.

We move on to class D, which is similar to class AII due to the same  $\mathbb{Z}_2$  characterization. Indeed, we can again use the Moore-Balents approach, since the Bloch Hamiltonians at  $k = 0, \pi$  are classified by 0 due to the fact that the effective dimension is  $\delta = 0 - 1 = -1$ , in which class D is trivial [195]. As for quench dynamics, however, a matrix (0D Hamiltonian) in class D is characterized by  $\pi_0(\mathcal{R}_2) = \mathbb{Z}_2$ , so that it is not always possible to deform  $h'_1(k = 0, \pi)$  into  $h_1(k = 0, \pi)$ . Nevertheless, we can always deform  $h'_1(k = 0, \pi)$  and  $h_1(k = 0, \pi)$  to make them

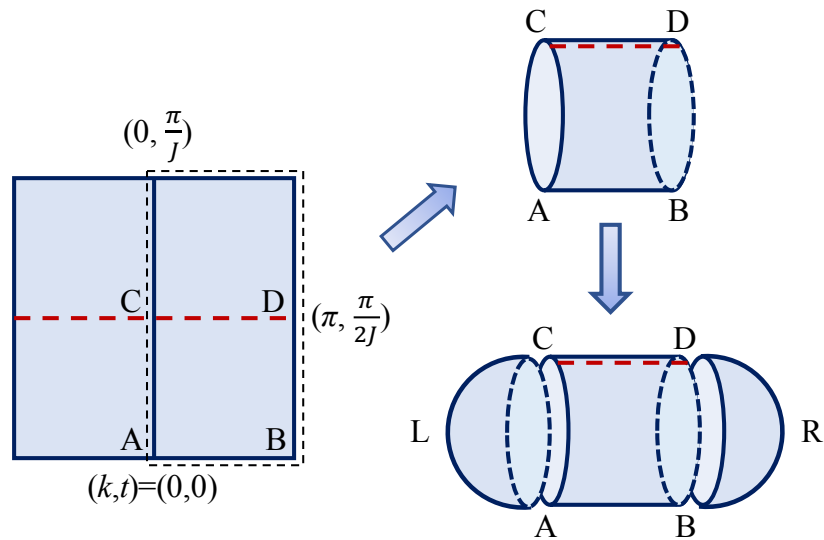


Figure 5.1: Moore-Balents approach for calculating the  $\mathbb{Z}_2$  index [343]. The right half (delimited by the dashed rectangle) of a 2D Brillouin zone is equivalent to a cylinder. By contracting the two boundaries of the cylinder while keeping the symmetry (e.g., TRS), we can compactify the manifold, on which a Chern number is well-defined. Provided that the ambiguity of contraction leads to an even-integer difference, the parity (even or odd) of the Chern number should be a well-defined  $\mathbb{Z}_2$  topological index. Reproduced from Supplementary Fig. 1 of Ref. [46]. Copyright © 2018 by the American Physical Society.

commute with each other, even if their  $\mathbb{Z}_2$  indices are different. That is, under the basis for which  $C = K$  (complex conjugation), we can always deform a  $2n \times 2n$  class D matrix  $h$ , which satisfies

$$h^* = -h, \quad h^\dagger = h \Leftrightarrow (ih)^* = ih, \quad (ih)^\top = -ih, \quad (5.36)$$

into either  $\bigoplus_{j=1}^n \sigma^y$  or  $(-\sigma^y) \oplus \bigoplus_{j=1}^{n-1} \sigma^y$ , depending on the sign of the Pfaffian of  $ih$ , which is an anti-symmetric real matrix. Neglecting the  $2\mathbb{Z}$  ambiguity (class D is characterized by  $2\mathbb{Z}$  in the effective dimension  $\delta = 0 - 2 = -2$  [195]) of contraction, and using Eq. (5.27), we can explicitly write down the  $\mathbb{Z}_2$  index as

$$\begin{aligned} v &= \frac{1}{2} (|\text{sgn Pf}[ih'_1(0)] - \text{sgn Pf}[ih_1(0)]| - |\text{sgn Pf}[ih'_1(\pi)] - \text{sgn Pf}[ih_1(\pi)]|) \bmod 2 \\ &= |\mathcal{N}' - \mathcal{N}|, \end{aligned} \quad (5.37)$$

where  $\text{sgn } x \equiv \frac{x}{|x|}$  and

$$\mathcal{N} = \frac{1}{2} |\text{sgn Pf}[ih_1(\pi)] - \text{sgn Pf}[ih_1(0)]|, \quad \mathcal{N}' = \frac{1}{2} |\text{sgn Pf}[ih'_1(\pi)] - \text{sgn Pf}[ih'_1(0)]|. \quad (5.38)$$

It is worth mentioning that, in general, this  $\mathbb{Z}_2$  index (5.37) is difficult to calculate due to the PHS constraint upon the boundary contraction [195]. Nevertheless, due to the specific form of the parent Hamiltonians for quench dynamics (5.10), obtaining the explicit expression (5.37) now becomes possible.

Let us turn to the real AZ classes with chiral symmetries. We first consider class BDI, which can be obtained from class AIII by adding an involutory ( $T^2 = 1$ ) and commutative ( $[T, \Gamma] = 0$ ) TRS. In the presence of TRS, we can show that the Chern number must vanish. On the other hand, the difference between the winding number at high-symmetry lines  $t = 0, \frac{\pi}{2J}$  can still be nonzero, even if the Hamiltonian takes the form of Eq. (5.10). Moreover, since the PHS-protected weak  $\mathbb{Z}_2$  number for the spatial degree of freedom conserves along the  $t$  direction,  $\Delta W$  must be even and we can define an integer

$$\Delta w = \frac{1}{2} \Delta W, \quad (5.39)$$

no matter whether or not  $h(k, t)$  is generated by quench dynamics. This explains why the maximal  $K$ -group and the dynamical realization are both given by  $\mathbb{Z}$ .

Using a similar argument, we can explain why the maximal  $K$ -group of class CII also reduces from  $\mathbb{Z} \oplus \mathbb{Z}$  to  $\mathbb{Z}$  when adding an anti-involutory (i.e.,  $T^2 = -1$ ) and commutative TRS. Just like class BDI, the remaining  $\mathbb{Z}$  corresponds to the difference of winding numbers at high symmetry lines, which is twice the winding-number difference between the pre- and postquench Hamiltonians. To realize the generator, we can construct a spin-orbit-coupled SSH-like model

$$h(k) = -[(J_1 + J_2 \cos k)\sigma^z \otimes \sigma^y + J_2 \sin k \sigma^x \otimes \sigma^0], \quad (5.40)$$

for which we quench the parameters as

$$(J_1, J_2) = (J, 0) \rightarrow (0, J). \quad (5.41)$$

Here  $T = i\sigma^y \otimes \sigma^0 K$  and  $C = i\sigma^0 \otimes \sigma^y K$ .

Finally, we consider class DIII, which is characterized by  $\mathbb{Z}_2 \oplus \mathbb{Z}_2$ . The simplest way to understand this topological classification is to regard class DIII as class AIII with an additional anti-involutory and anti-commutative ( $\{T, \Gamma\} = 0$ ) TRS. Note that class AIII is characterized by  $\mathbb{Z} \oplus \mathbb{Z}$ . Due to the additional TRS, both the winding number at high symmetry lines and

the Chern number vanish. Nevertheless, it is still possible to have a nontrivial Chern number or/and a nontrivial winding number over one half of the Brillouin zone after deforming the boundary to compactify the manifold (i.e., using the Moore-Balents approach). While both the Chern number and the winding number are ambiguous, their parities are unique. Therefore, one of the  $\mathbb{Z}_2$  index should be the same as that in class AII, while the other equals to the difference of  $\mathbb{Z}_2$  index at high symmetry lines, where the 1D section belongs to class DIII.

If the Hamiltonian is generated by quench dynamics, the TRS-related  $\mathbb{Z}_2$  index vanishes, as we have proved for class AII. On the other hand, the other  $\mathbb{Z}_2$  index could be nonzero. To realize the generator, we can construct an explicit model — the spin-1/2 SSH model

$$h(k) = -\sigma^0 \otimes [(J_1 + J_2 \cos k)\sigma^x + J_2 \sin k\sigma^y], \quad (5.42)$$

which undergoes the quench

$$(J_1, J_2) = (J, 0) \rightarrow (0, J). \quad (5.43)$$

Here  $T = i\sigma^y \otimes \sigma^0 K$  and  $C = \sigma^0 \otimes \sigma^z K$ . Note that since the hopping in Eq. (5.42) does not flip the spin, it is obvious that the TRS is respected. The PHS inherits simply from that of the spinless SSH model. While the other  $\mathbb{Z}_2$  index vanishes in quench dynamics, we can make it nontrivial in an adiabatic pump like [344]

$$h(k, t) = -J_0[1 - \cos k - \cos(2Jt)]\sigma^0 \otimes \sigma^x - J_0[\sin(2Jt)\sigma^0 \otimes \sigma^y + \sin k\sigma^x \otimes \sigma^z], \quad (5.44)$$

which can be examined to respect both TRS and PHS.

So far we have identified all the nontrivial elements in the maximal  $K$ -group that are realizable in quench dynamics. As summarized in Table 5.1, the results turn out to be consistent with the classification of topological insulators and superconductors in 1D [39, 194]. However, we should again emphasize that the topology underlying 1D quench dynamics is of 2D nature. It is also worth mentioning an intuitive understanding of the reason why the quench dynamics in trivial AZ classes must be trivial, even if the maximal  $K$ -group is not — we can always continuously deform  $h'_1(k)$  into  $h_1(k)$ , so that the parent Bloch Hamiltonian  $\tilde{h}(k, t) = h_1(k)$  has no  $t$  dependence and thus cannot exhibit genuine 2D nontrivial topology. This argument should also be applicable to higher dimensions and other symmetry classes.

#### 5.2.4 Quench dynamics in two-band systems

In this subsection, complementary to the abstract general theory presented above, we provide a detailed analysis on the quench dynamics in two-band systems, whose bands are not necessarily flattened. We focus especially on the Su-Schrieffer-Heeger (SSH) model, which is arguably the simplest topological insulator and has strong experimental relevance.

##### *Dynamics of pseudospins in momentum space*

For general two-band systems such as a superlattice, the pre- and post-quench Bloch Hamiltonians can be expressed as

$$h(k) = d_0(k) + \mathbf{d}(k) \cdot \boldsymbol{\sigma}, \quad h'(k) = d'_0(k) + \mathbf{d}'(k) \cdot \boldsymbol{\sigma}, \quad (5.45)$$

where  $\boldsymbol{\sigma} \equiv \sum_{\mu \in \{x, y, z\}} \sigma^\mu \mathbf{e}_\mu$  is the Pauli-matrix vector with  $\mathbf{e}_\mu$  being the unit vector in the  $\mu$  direction. Denoting the parent Bloch Hamiltonian as

$$h(k, t) = d_0(k, t) + \mathbf{d}(k, t) \cdot \boldsymbol{\sigma} \quad (5.46)$$

and using Eq. (5.7) as well as the commutation relations for the Pauli matrices, we obtain

$$d_0(k, t) = d_0(k), \quad i\partial_t d_\kappa(k, t)\sigma^\kappa = [d'_\mu(k)\sigma^\mu, d_\nu(k, t)\sigma^\nu] = 2i\epsilon_{\mu\nu\kappa}d'_\mu(k)d_\nu(k, t)\sigma^\kappa, \quad (5.47)$$

where  $\mu, \nu, \kappa \in \{x, y, z\}$  and the Einstein summation convention is assumed. With the  $d_0$ -component excluded, Eq. (5.47) can be rewritten as

$$\partial_t \mathbf{d}(k, t) = 2\mathbf{d}'(k) \times \mathbf{d}(k, t), \quad (5.48)$$

Noting that  $d_0(k, t)$  plays no role in either dynamics or band topology, we assume it to vanish for simplicity. Indeed,  $d_0(k, t) = 0$  in both the SSH model and the Rice-Mele model. Intuitively, Eq. (5.48) describes the precession of  $\mathbf{d}(k, t)$  with respect to  $\mathbf{d}'(k)$  by an angular velocity  $2\mathbf{d}'(k)$  ( $d'(k) \equiv |\mathbf{d}'(k)|$ ). Thus, we can write down the following solution:

$$\mathbf{d}(k, t) = \mathbf{d}_{\parallel}(k) + \cos(2d'(k)t)\mathbf{d}_{\perp}(k) + \sin(2d'(k)t)\mathbf{d}_o(k), \quad (5.49)$$

where the parallel ( $\parallel$ ), perpendicular ( $\perp$ ) and out-of-plane (spanned by  $\mathbf{d}(k)$  and  $\mathbf{d}'(k)$ ) ( $o$ ) components are given by

$$\mathbf{d}_{\parallel}(k) = [\mathbf{d}(k) \cdot \mathbf{n}'(k)]\mathbf{n}'(k), \quad \mathbf{d}_{\perp}(k) = \mathbf{d}(k) - \mathbf{d}_{\parallel}(k), \quad \mathbf{d}_o(k) = \mathbf{d}(k) \times \mathbf{n}'(k), \quad (5.50)$$

where  $\mathbf{n}'(k) \equiv -\mathbf{d}'(k)/d'(k)$ .

As a concrete illustration, let us consider a quench in the SSH model starting from the trivial dimerized state (see Fig. 5.4(a)). In real space, the Hamiltonian of the SSH model reads [345]

$$H = -\sum_j (J_1 b_j^\dagger a_j + J_2 a_{j+1}^\dagger b_j + \text{H.c.}), \quad (5.51)$$

where  $J_1$  and  $J_2$  are the intra- and inter-unit-cell hopping amplitudes, respectively. By Fourier transforming Eq. (5.51) into the momentum space, we obtain the following quench protocol:

$$\mathbf{d}(k) = -(J, 0, 0), \quad \mathbf{d}'(k) = -(J' + J \cos k, J \sin k, 0). \quad (5.52)$$

Substituting Eq. (5.52) into Eqs. (5.49) and (5.50) yields

$$\begin{aligned} d_x(k, t) &= -J + 2J \left[ \frac{J \sin k \sin(d'(k)t)}{d'(k)} \right]^2, \\ d_y(k, t) &= -2(J' + J \cos k) \sin k \left[ \frac{J \sin(d'(k)t)}{d'(k)} \right]^2, \\ d_z(k, t) &= -\frac{J^2}{d(k)} \sin k \sin(2d'(k)t), \end{aligned} \quad (5.53)$$

where

$$d'(k) = \sqrt{J^2 + J'^2 + 2J'J \cos k}. \quad (5.54)$$

Note that  $d_z(k, t)$  is generally nonzero, though  $d_z(k) = d'_z(k) = 0$ . We can then obtain the pseudospin texture

$$\mathbf{n}(k, t) \equiv -\frac{\mathbf{d}(k, t)}{|\mathbf{d}(k, t)|} = -\frac{\mathbf{d}(k, t)}{J}, \quad (5.55)$$

from Eq. (5.53).

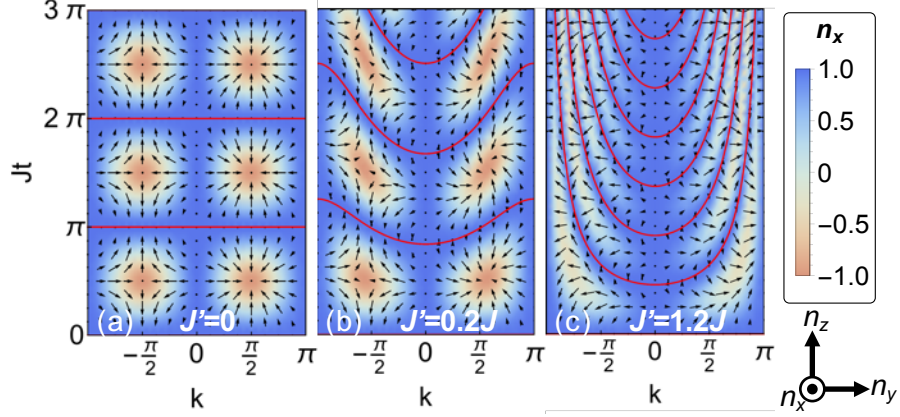


Figure 5.2: Pseudospin textures  $\mathbf{n}(k, t)$  in the  $k$ - $t$  space for the quench protocols  $(J_1, J_2) = (J, 0) \rightarrow (J', J)$  with (a)  $J' = 0$ , (b)  $J' = 0.2J$  and (c)  $J' = 1.2J$ . Momentum-time skyrmions emerge in (a) and (b), but not in (c), as explicitly shown by calculating the topological number defined in Eq. (5.56) (see also Eq. (5.63) and Fig. 5.3). Pseudospins along the red curves are polarized in the  $x$  direction. Reproduced from Supplementary Fig. 2 of Ref. [46]. Copyright © 2018 by the American Physical Society.

Figure 5.2 shows the dynamics of  $\mathbf{d}(k, t)$  for the quench in the SSH model. Remarkably, for  $J' = 0$ , the pseudospin texture  $\mathbf{n}(k, t)$  forms two rows of *skyrmion* lattices with opposite topological charges, which can be calculated from

$$C_{\text{skyrmion}} = \iint_{\text{A}} \frac{dt dk}{4\pi} \mathbf{n}(k, t) \cdot [\partial_k \mathbf{n}(k, t) \times \partial_t \mathbf{n}(k, t)], \quad (5.56)$$

with  $\text{A} = [0, \pi/J] \times [0, \pi]$  (right column) or  $[0, \pi/J] \times [-\pi, 0]$  (left). When  $0 < J' < J$ , skyrmions are still well-defined but deformed and canted. In fact, the pseudospin texture can always be mapped to two arrays of skyrmion lattices via rescaling the time axis in a  $k$ -dependent manner, or equivalently via band flattening of the postquench Hamiltonian such that  $h'(k)^2 = J^2$ . Such a continuous deformation breaks down at the critical point  $J' = J$ , above which  $\mathbf{n}(k, t)$  becomes topologically trivial since it can continuously be deformed to the pseudospin-polarized state. We note that the momentum-time skyrmions have been observed in a similar quench dynamics implemented by photonic quantum walks [346].

### Dynamical Chern number

Let us study in detail the skyrmion charge (5.56), which can alternatively be expressed as the integral of the Berry curvature  $\Omega(k, t)$  on the momentum-time manifold:

$$\Omega(k, t) \equiv 2\text{Im}[(\partial_t \mathbf{u}(k, t))^\dagger \partial_k \mathbf{u}(k, t)]. \quad (5.57)$$

Here  $\mathbf{u}(k, t)$  is the lower-band Bloch vector satisfying  $h(k, t)\mathbf{u}(k, t) = -d(k)\mathbf{u}(k, t)$ . It should be emphasized that this Berry curvature is merely a mathematical analogue, since the real physical process is a highly nonadiabatic quench dynamics.

In terms of the eigenvectors of  $h'(k)$ , which are denoted as  $\mathbf{v}_\pm(k)$  with eigenvalues  $\pm d'(k)$ ,  $\mathbf{u}(k, t)$  can explicitly be written as

$$\mathbf{u}(k, t) = e^{-id'(k)t} \mathbf{v}_+(k) (\mathbf{v}_+(k))^\dagger \mathbf{u}(k) + e^{id'(k)t} \mathbf{v}_-(k) (\mathbf{v}_-(k))^\dagger \mathbf{u}(k). \quad (5.58)$$

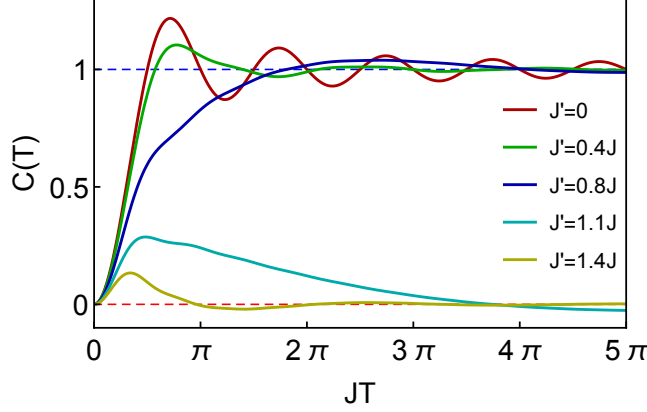


Figure 5.3:  $C(T)$  defined in Eq. (5.63) versus  $JT$  in the quench dynamics of the SSH model for different values of the parameter.  $C(T)$  converges to 1 for  $J' < J$  (dashed blue line) and 0 for  $J' > J$  (dashed red line). Reproduced from Supplementary Fig. 3 of Ref. [46]. Copyright © 2018 by the American Physical Society.

Accordingly, the inner product  $(\partial_t \mathbf{u}(k, t))^\dagger \partial_k \mathbf{u}(k, t)$  in Eq. (5.57) is calculated to be

$$\begin{aligned}
& td'(k) \partial_k d'(k) + id'(k) [\mathbf{u}(k)^\dagger \mathbf{v}_+(k) \partial_k (\mathbf{v}_+(k)^\dagger \mathbf{u}(k)) - \mathbf{u}(k)^\dagger \mathbf{v}_-(k) \partial_k (\mathbf{v}_-(k)^\dagger \mathbf{u}(k))] \\
& + id'(k) [|\mathbf{u}(k)^\dagger \mathbf{v}_+(k)|^2 (\mathbf{v}_+(k)^\dagger \partial_k \mathbf{v}_+(k)) - |\mathbf{u}(k)^\dagger \mathbf{v}_-(k)|^2 (\mathbf{v}_-(k)^\dagger \partial_k \mathbf{v}_-(k))] \\
& + id'(k) [e^{2id'(k)t} \mathbf{u}(k)^\dagger \mathbf{v}_+(k) \mathbf{v}_-(k)^\dagger \mathbf{u}(k) (\mathbf{v}_+(k)^\dagger \partial_k \mathbf{v}_-(k)) + \text{H.c.}],
\end{aligned} \tag{5.59}$$

where we have used  $\mathbf{v}_+^\dagger(k) \partial_k \mathbf{v}_-(k) + \mathbf{v}_-(k) \partial_k \mathbf{v}_+^\dagger(k) = \partial_k (\mathbf{v}_+^\dagger(k) \mathbf{v}_-(k)) = 0$ . Since  $\mathbf{v}_\pm(k)^\dagger \partial_k \mathbf{v}_\pm(k)$  is purely imaginary and  $2\text{Re}[\mathbf{u}^\dagger(k) \mathbf{v}_\pm(k) \partial_k (\mathbf{v}_\pm(k)^\dagger \mathbf{u}(k))] = \partial_k (|\mathbf{u}(k)^\dagger \mathbf{v}_\pm(k)|^2)$ , we have

$$\Omega(k, t) = 2d'(k) \partial_k (|\mathbf{u}^\dagger(k) \mathbf{v}_+(k)|^2) - 2d'(k) (e^{2id'(k)t} \text{Tr}[P(k)P_+(k) \partial_k P_+(k)] + \text{H.c.}), \tag{5.60}$$

where  $P(k) \equiv \mathbf{u}(k) \mathbf{u}^\dagger(k)$  and  $P_+(k) \equiv \mathbf{v}_+(k) \mathbf{v}_+^\dagger(k)$  are projective matrices.

Note that the second term in Eq. (5.60) oscillates with  $t$  due to the factor  $e^{2id'(k)t}$ . After integrating  $\Omega(k, t)$  over  $A = \{(k, t) : 0 < t < \frac{\pi}{d'(k)}, 0 < k < \pi\}$  in the  $k$ - $t$  plane, the contribution from this oscillating term vanishes, and we obtain a quantized *dynamical Chern number* [347]

$$C_{\text{dyn}} \equiv \iint_A \frac{dkdt}{2\pi} \Omega(k, t) = F(\pi) - F(0), \quad F(k) \equiv |\mathbf{u}^\dagger(k) \mathbf{v}_+(k)|^2. \tag{5.61}$$

The quantization of  $C_{\text{dyn}}$  is ensured by the PHS, which restricts the Bloch states of  $h(k)$  and  $h'(k)$  at  $k = 0, \pi$  to be an eigenstate of  $\sigma^x$ . Concretely, denoting the eigenvalues of  $\mathbf{u}(k = 0, \pi)$  and  $\mathbf{v}_-(k = 0, \pi)$  as  $\nu_{0,\pi}$  and  $\nu'_{0,\pi}$ , we have  $F(k = 0, \pi) = |\nu'_{0,\pi} - \nu_{0,\pi}|/2$  and thus

$$C_{\text{dyn}} = \frac{1}{2} (|\nu'_\pi - \nu_\pi| - |\nu'_0 - \nu_0|). \tag{5.62}$$

This result is consistent with Eq. (5.37), which applies to an arbitrary number of bands.

Alternatively, we can introduce

$$C(T) \equiv \int_0^\pi dk \int_0^T dt \frac{\Omega(k, t)}{2Td'(k)}, \tag{5.63}$$



and define the dynamical Chern number as

$$C_{\text{dyn}} \equiv \lim_{T \rightarrow \infty} C(T). \quad (5.64)$$

The equivalence between Eqs. (5.64) and (5.61) can be understood from the fact that the time integral of the oscillating term in Eq. (5.60) is bounded, and accordingly vanishes after being divided by an infinitely large  $T$ . For the quench dynamics in the SSH model, we have

$$\Omega(k, t) = 2 \sin k (J + J' \cos k) \left[ \frac{J \sin(d'(k)t)}{d'(k)} \right]^2, \quad (5.65)$$

where  $d'(k)$  is given in Eq. (5.54). Using the definition in Eq. (5.61), we obtain

$$C_{\text{dyn}} = \int_0^\pi \frac{dk J^2 (J + J' \cos k) \sin k}{2(J^2 + J'^2 + 2J'J \cos k)^{\frac{3}{2}}} = \int_{-1}^1 \frac{ds J^2 (J + J's)}{2(J^2 + J'^2 + 2J'J s)^{\frac{3}{2}}} = \frac{1 + \text{sgn}(J - J')}{2}. \quad (5.66)$$

We thus find  $C_{\text{dyn}} = 1$  ( $C_{\text{dyn}} = 0$ ) if  $J > J'$  ( $J < J'$ ), which is consistent with Eq. (5.62). After straightforward calculations, we obtain the expression for  $C(T)$  in Eq. (5.63):

$$C(T) = \frac{1 + \text{sgn}(J - J')}{2} - g\left(T, \frac{J'}{J}\right), \quad g(t, r) = \int_{-1}^1 ds \frac{(1 + rs) \sin(2t\sqrt{1 + r^2 + 2rs})}{4t(1 + r^2 + 2rs)^2}. \quad (5.67)$$

We plot  $C(T)$  for several different values of the quench parameter in Fig. 5.3. It seems that  $C(T)$  typically converges more quickly for a finite value  $J'$  than the flat-band case  $J' = 0$  (but this is not the case when  $J' \simeq J$ , i.e., close to the critical point). A physical explanation is that a finite bandwidth causes certain disorder in the frequency domain and washes out quantum coherent oscillations. We note that similar observations are made in Ref. [325], but in quite a different context of the asymptotic quantization of the nonequilibrium Hall conductance.

## 5.3 Entanglement-spectrum dynamics after quenches

With the spacetime topology of quench dynamics identified in the previous section, it is natural to ask how to detect it in a way that is universal, numerically tractable and experimentally accessible. Note that the momentum-time skyrmion texture in Fig. 5.2 is only applicable to two-band systems and is thus not a universal indicator. In this section, we suggest that the ES dynamics could be a promising candidate. We perform extensive numerical simulations to demonstrate that this indicator is stable against disorder and can clearly distinguish  $\mathbb{Z}_2$  topology from  $\mathbb{Z}$  topology. A possible experimental situation for measuring the ES dynamics is also discussed.

### 5.3.1 Case study on the Su-Schrieffer-Heeger model

As mentioned in the introduction of this chapter, the ES has been widely used to characterize topological systems at equilibrium. In particular, for a gapped free-fermion system (not necessarily translation-invariant) described by

$$H = \sum_{j, j', a, a'} H_{ja, j'a'} c_{ja}^\dagger c_{j'a'}, \quad (5.68)$$

where  $H_{ja, j'a'} = H_{j'a', ja}^*$  and  $c_{j\alpha}^\dagger$  creates a particle with internal degrees of freedom  $a$  at site  $j$ , we can define the *single-particle ES* for its ground state, which is necessarily a Gaussian

state. Let us outline how to define the single-particle ES for a general Gaussian state  $|\Psi\rangle$ . Denoting  $S$  ( $\bar{S}$ ) as the region of interest (the complementary of  $S$ ), the reduced density operator  $\rho_S \equiv \text{Tr}_{\bar{S}}[|\Psi\rangle\langle\Psi|]$  can be rewritten as

$$\rho_S = Z_E^{-1} e^{-H_E}, \quad H_E = \sum_n \epsilon_n f_n^\dagger f_n, \quad (5.69)$$

where  $Z_E \equiv \text{Tr} e^{-H_E}$  and  $H_E$  is the quadratic *entanglement Hamiltonian* [348] and its eigenmodes  $\{f_n\}$  are linear combinations of  $\{c_{ja}\}$ . The single-particle ES is then given by [349]

$$\xi_n \equiv \frac{1}{e^{\epsilon_n} + 1}. \quad (5.70)$$

Returning to the case of ground states of free-fermion systems, one can show that the single-particle energy eigenvalues  $\{\epsilon_n\}$  give the *exact* open-boundary spectrum of the flattened Hamiltonian [205]. Therefore, an entanglement zero mode with  $\epsilon_n = 0$  corresponds to  $\xi_n = 1/2$  in the ES.

For quench dynamics in free-fermion systems, the nonequilibrium wave function stays Gaussian as can be understood from the fact that the parent Hamiltonian is again quadratic. Accordingly, the single-particle ES stays well-defined even out of equilibrium. Recalling the equivalence between the ES and the open-boundary energy spectrum, we know that the *time evolution of ES* faithfully simulates the edge spectral flow under open-boundary conditions in real space. Given the *bulk-edge correspondence* [350], we expect that the spacetime topology of quench dynamics can directly be read out from the ES dynamics. Moreover, the converse use of this idea can be practically useful for recovering the Hamiltonian topology from quench dynamics, provided that the many-body tomography for  $|\Psi(t)\rangle$  [336, 339] or the direct measurement of the ES [151, 351] is achievable.

To illustrate the power of ES dynamics as a dynamical topological indicator, we again take the SSH model given in Eq. (5.51) as a prototypical example (see Fig. 5.4(a)). In real systems, such as polyacetylene [352] and ultracold atoms in optical superlattices [171, 341, 342], we generally have  $J_1, J_2 > 0$ , and a topological phase transition from  $w = \mathcal{N} = 0$  to  $w = \mathcal{N} = 1$  (cf. Eqs. (5.32) and (5.38) for the definitions of  $w$  and  $\mathcal{N}$ ) occurs upon crossing the boundary  $J_1 = J_2$  (see Fig. 5.4(c)). If we quench the parameters as (same as Eq. (5.52))

$$(J_1, J_2) = (J, 0) \rightarrow (J', J), \quad (5.71)$$

$|\Psi(t)\rangle$  will remain in the same trivial phase as the dimerized state with  $\mathcal{N} = 0$ . Hence, topological entanglement edge modes in  $|\Psi(t)\rangle$  are absent in general. This is confirmed numerically (see Appendix D.1 for details), i.e., the half-chain (see Fig. 5.4 (b)) ES  $\xi_n \neq 1/2$  for almost all the time in Figs. 5.4(d) and (e). However, in the flat-band case  $J' = 0$ , we find periodic oscillations of  $\{\xi_n\}$ , which cross each other at  $t_m = (m - 1/2)\pi/J$  with  $m \in \mathbb{Z}^+$ , where the system instantaneously becomes class BDI with winding number 2. Remarkably, the crossings stay robust as  $J'$  increases as long as  $J' < J$  with  $t_1$  gradually diverging. This should be understood as the robustness of the nontrivial (1 + 1)D topology characterized by  $\Delta w = 1$  (cf. Eq. (5.39)), although the temporal periodicity disappears. When  $J$  exceeds  $J'$ , no crossings occur. This sharp transition in the ES dynamics distinguishes the quenches across different topological phases from those within the same phase. The ES crossings in Fig. 5.4(d) can alternatively be interpreted as a result of the nontrivial PHS-protected index  $v = 1$  in Eq. (5.37), which has been shown in Sec. 5.2.4 to be equal to the skyrmion charge (5.56) or the dynamical Chern number (5.61) of the  $\mathbf{d}$ -vector textures in one half of the momentum-time space. Indeed, the ES crossings resemble the Dirac-cone dispersion of edge (entanglement) modes in 2D topological insulators [167, 353].

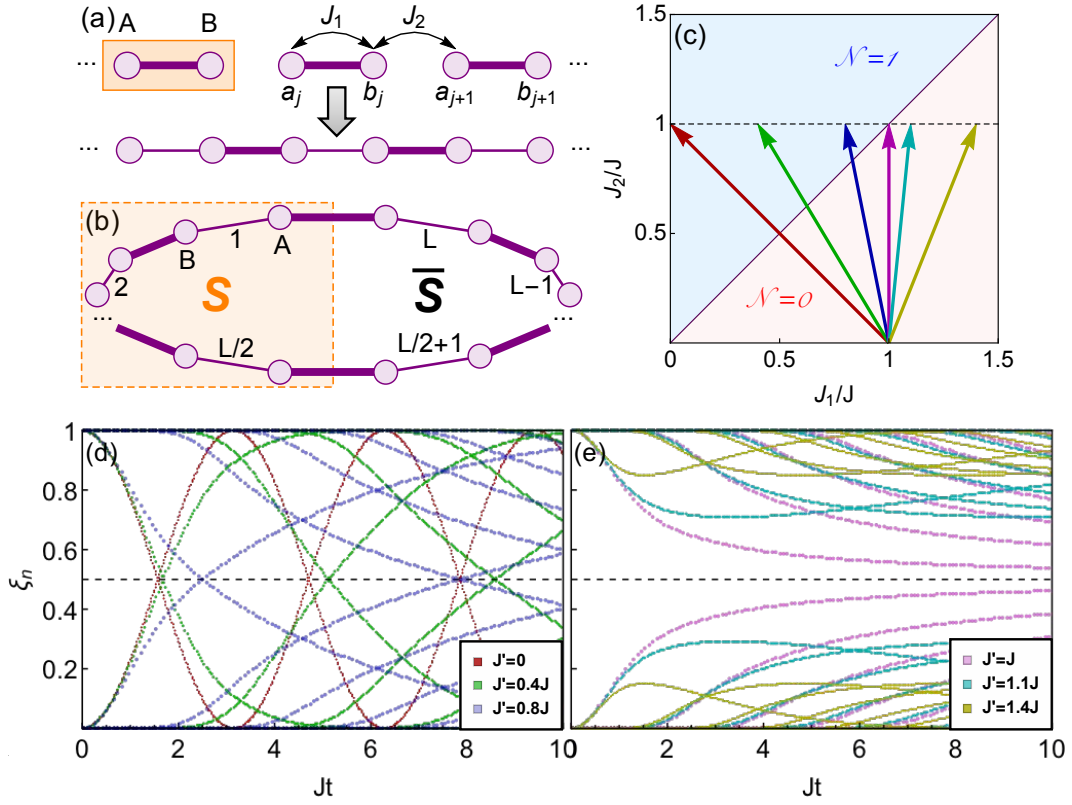


Figure 5.4: (a) Quench in the SSH model (5.51) from a dimerized state. The orange rectangle marks a unit cell. (b) Half-chain entanglement cut (shaded region  $S$ ) of a periodic chain. (c) Quench protocols. The leftmost three arrows show quenches across the topological phase boundary. (d) Dynamics of the single-particle ES (5.70) after quenches across the phase boundary, showing crossings at  $\xi_n = 1/2$ . The total number of  $\{\xi_n\}$  is  $L$  and most of them are very close to 0 or 1. (e) Single-particle ES dynamics after quenches within the same phase and to the critical point, showing no crossings at  $\xi_n = 1/2$ . The system size is  $L = 100$ . Reproduced from Fig. 1 of Ref. [46]. Copyright © 2018 by the American Physical Society.

### 5.3.2 Distinguishing $\mathbb{Z}$ and $\mathbb{Z}_2$ topology

While we have seen that the ES crossings can signal a nontrivial topology underlying the quench dynamics of the specific two-band SSH model, it is unclear whether the topology is of  $\mathbb{Z}_2$  or  $\mathbb{Z}$  nature. In this subsection, we distinguish these two kind of topological numbers by studying the quench dynamics in coupled SSH model. Depending on the form of inter-chain coupling, the system falls into either class BDI characterized by  $\mathbb{Z}$  or class D characterized by  $\mathbb{Z}_2$ . We demonstrate that the difference can indeed be readout from the ES dynamics. We also provide an example in class DIII, which is also characterized by a  $\mathbb{Z}_2$  index.

#### *Class BDI*

According to Table 5.1, the quench dynamics in class BDI systems are characterized by  $\mathbb{Z}$ . Since the addition operation on a  $K$ -group is the direct sum up to continuous deformation, we expect the number of ES crossings to be multiplied by  $M$  if we quench  $M$  copies of the system coupled to each other without breaking the symmetries, at least for the flat-band case. Also, we would like to demonstrate the robustness of ES crossings against spatial disorder. For these purposes, we consider an assembly of SSH chains and deform each chain by introducing randomness in the hopping amplitudes:

$$H_\alpha = - \sum_j (J_{1,j\alpha} b_{j\alpha}^\dagger a_{j\alpha} + J_{2,j\alpha} a_{j+1,\alpha}^\dagger b_{j\alpha} + \text{H.c.}). \quad (5.72)$$

We further randomly couple these SSH chains in a symmetry-preserving way (see Fig. 5.5(a)):

$$H_{\text{BDI}} = \sum_{\alpha=1}^M H_\alpha - \sum_{\alpha=1}^{M-1} \sum_j (J_{c,j\alpha} b_{j,\alpha+1}^\dagger a_{j\alpha} + \text{H.c.}), \quad (5.73)$$

where  $a_{j\alpha}$  ( $b_{j\alpha}$ ) is the annihilation operator of a particle at sublattice A in the  $j$ th unit cell of the  $\alpha$ th SSH chain. For  $M = 3$  chains and an appropriately chosen quench protocol, the numerically obtained ES dynamics is shown in Fig. 5.5(c). As expected, we see  $(2M = 6)$ -fold degenerate ES crossings (indicated by the blue circle) in the flat-band limit (blue curves), with the factor of 2 coming from the periodic-boundary condition. Here the degree of degeneracy is obtained by counting the number of crossings (indicated by the red arrows) in the absence of band flatness (red curves). Further numerical results shown in the first and third columns of Fig. 5.6 confirm the expectation for SSH chains with  $M = 1 \sim 4$  and with or without hopping disorder.

#### *Class D*

If we break the TRS alone, the symmetry class changes from BDI to D and the  $K$ -theory classification gives  $\mathbb{Z}_2$  (see Table 5.1), over which  $1 + 1 = 0 \pmod{2}$ . As a result, we expect the presence (absence<sup>3</sup>) of ES crossings if we quench an odd (even) number of copies of SSH chains with coupling amplitudes respecting PHS but breaking TRS. Such a situation can be realized by changing the inter-chain coupling in Eq. (5.73) into (see Fig. 5.5(b))

$$H_{\text{D}} = \sum_{\alpha=1}^M H_\alpha + \sum_{\alpha=1}^{M-1} \sum_j (iJ_{c,j\alpha} a_{j,\alpha+1}^\dagger a_{j\alpha} + \text{H.c.}). \quad (5.74)$$

---

<sup>3</sup>We do not rule out the possibility of finding accidental ES crossings without topological origin. Note that edge states may also exist in topologically trivial systems.

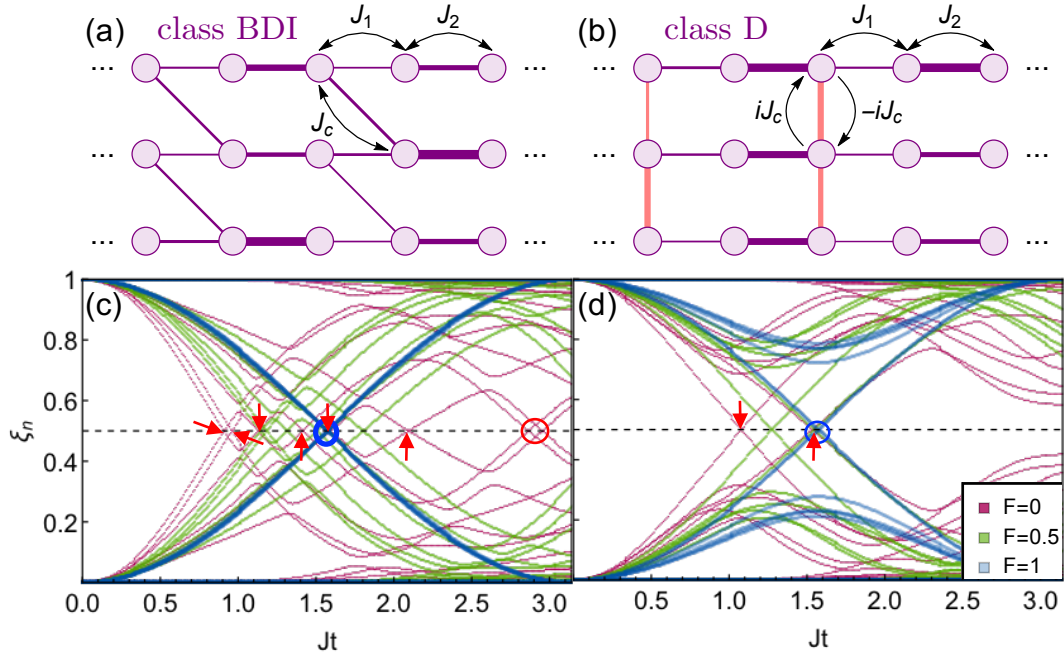


Figure 5.5: Three coupled SSH chains in (a) class BDI and (b) class D. Hopping amplitudes  $J_\alpha$  ( $\alpha = 1, 2, c$ ) are randomly sampled from a uniform distribution over  $[0.6\bar{J}_\alpha, 1.4\bar{J}_\alpha]$ . (c) ES dynamics after quench  $(\bar{J}_1, \bar{J}_2, \bar{J}_c) = (0, 1.5J, 0) \rightarrow (1.5J, 0.5J, 0.5J)$  in (a) with  $L = 40$  and the periodic-boundary condition. The result ( $F = 0$ ) is compared with those after partial ( $F = 0.5$ ) and complete ( $F = 1$ ) band flattening  $H'$ . A partially flattened Hamiltonian  $H'_F$  ( $F \in (0, 1)$ ) is related to the original one  $H'_0 = H'$  and the completely flattened one  $H'_1$  via  $H'_F = FH'_1 + (1 - F)H'_0$ . The ES crossings in the blue circle split into those marked by red arrows when  $F$  changes from 1 to 0. The remaining two crossings in the red circle stem from the second period. (d) Same as (c) but for the system in (b) with a different quench protocol  $(\bar{J}_1, \bar{J}_2, \bar{J}_c) = (0, 1.5J, 0) \rightarrow (1.5J, 0.5J, J)$ . Reproduced from Fig. 2 of Ref. [46]. Copyright © 2018 by the American Physical Society.

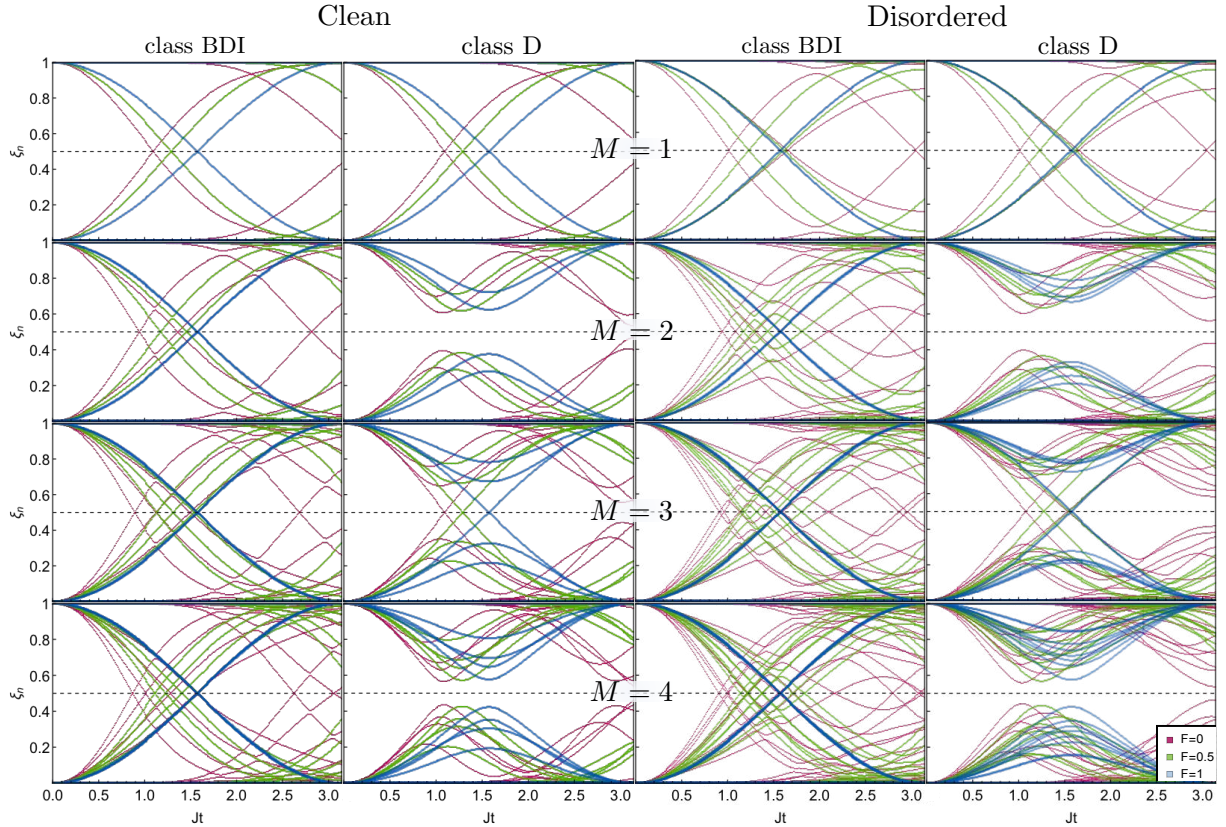


Figure 5.6: Single-particle ES dynamics in  $M$  copies of SSH chains with interchain couplings (cf. Fig. 5.5(a) and (b)) that either respect both TRS and PHS (class BDI, see Eq. (5.73)) or break the TRS alone (class D, see Eq. (5.74)). The quench parameters are chosen to be the same as those in Fig. 5.5, i.e.,  $(\bar{J}_1, \bar{J}_2, \bar{J}_c) = (0, 1.5J, 0) \rightarrow (1.5J, 0.5J, 0.5J)$  for class BDI and  $(\bar{J}_1, \bar{J}_2, \bar{J}_c) = (0, 1.5J, 0) \rightarrow (1.5J, 0.5J, J)$  for class D. The disorder realization of  $J_1$  and  $J_2$  is set to be the same for class BDI and class D, so that their ES dynamics agree with each other for  $M = 1$  in the disordered case. The length of a single chain is chosen to be  $L = 120/M$ . Reproduced from Supplementary Fig. 9 of Ref. [46]. Copyright © 2018 by the American Physical Society.

In Fig. 5.5(d), we present the numerical results of ES dynamics for  $M = 3$  chains. We find that only a single pair of crossings survive in a period in the flat-band limit (blue curves), and the crossings persist when introducing band nonflatness (red curves).<sup>4</sup> This observation strongly suggests reduction of the topological number  $\mathbb{Z} \rightarrow \mathbb{Z}_2$ . To further support such a dynamical  $\mathbb{Z}_2$  reduction, we perform extensive numerical calculations for coupled SSH chains  $M = 1 \sim 4$  in class D. As shown in the second and fourth columns of Fig. 5.6, we clearly find  $2(M \bmod 2)$  ES crossings in the flat band limit (blue curves), no matter whether the system is clean or disordered.

### *Class DIII*

We numerically demonstrate that the  $\mathbb{Z}_2$  topological index for class DIII also has an intuitive implication on the ES dynamics. In fact, by preparing two copies (with opposite spins) of the

<sup>4</sup>See Ref. [340] for a detailed explanation on the stability of this ES crossing against band nonflatness.

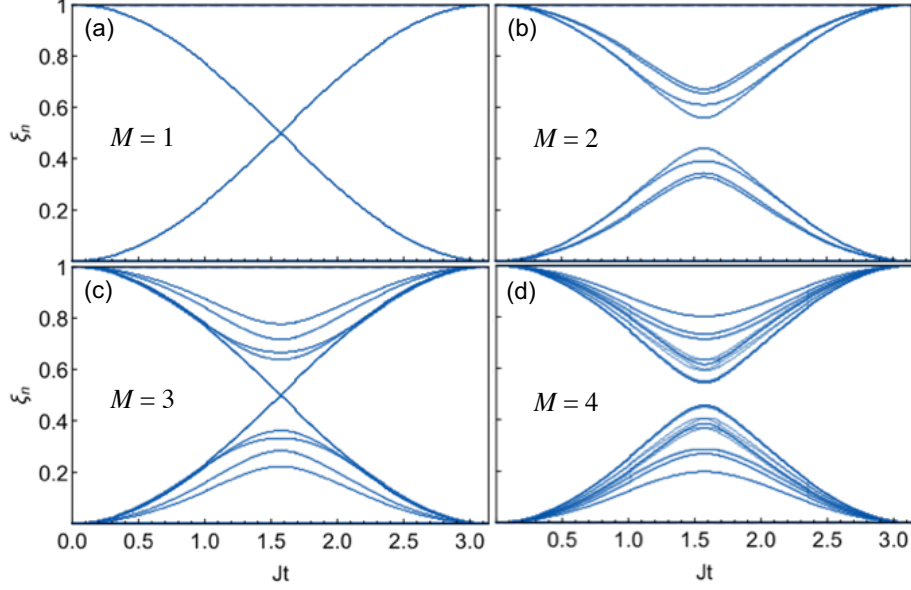


Figure 5.7: Single-particle ES dynamics in a disordered class DIII system (5.77) after band flattening. (a)-(d) correspond to the case of coupled four-band class DIII chains with  $M = 1 \sim 4$  (5.75). Note that a four-fold-degenerate (no) crossing survives for an odd (even)  $M$ , implying a robust  $\mathbb{Z}_2$  topological characterization. The length of a single chain is chosen to be  $L = 96/M$ . Reproduced from Supplementary Fig. 10 of Ref. [46]. Copyright © 2018 by the American Physical Society.

class D SSH chains, we have already obtained a model in class DIII, which certainly exhibits the  $\mathbb{Z}_2$  reduction with doubled degeneracies in the ES crossings (due to the Kramers degeneracy). Note that once the TRS alone is broken, the system reduces to class D and is always trivial.

To make the demonstration nontrivial, we can add a spin-orbit coupling term that respects both TRS and PHS:

$$H_\alpha = - \sum_{j,s} (J_{1,j\alpha} b_{j\alpha s}^\dagger a_{j\alpha s} + J_{2,j\alpha} a_{j+1,\alpha s}^\dagger b_{j\alpha s} + \text{H.c.}) + \sum_j [J_{c,j\alpha} (b_{j\alpha\downarrow}^\dagger a_{j\alpha\uparrow} - a_{j\alpha\downarrow}^\dagger b_{j\alpha\uparrow}) + \text{H.c.}], \quad (5.75)$$

where  $s = \uparrow, \downarrow$  denotes the spin degree of freedom. Denoting  $\mathbf{c}_j \equiv [a_{j\uparrow}, b_{j\uparrow}, a_{j\downarrow}, b_{j\downarrow}]^T$ , the anti-unitary TRS and PHS act like

$$T(\mathbf{c}_j)T^{-1} = (i\sigma^y \otimes \sigma^0)\mathbf{c}_j, \quad C(\mathbf{c}_j)C^{-1} = (\sigma^0 \otimes \sigma^z)\mathbf{c}_j. \quad (5.76)$$

We can couple  $M$  copies of such class DIII chains as

$$H = \sum_{\alpha=1}^M H_\alpha + \sum_{\alpha=1}^{M-1} \sum_j [(iJ_{cc,j\alpha} a_{j,\alpha+1,\uparrow}^\dagger a_{j\alpha\uparrow} - iJ_{cc,j\alpha} a_{j,\alpha+1,\downarrow}^\dagger a_{j\alpha\downarrow}) + \text{H.c.}], \quad (5.77)$$

which respects both TRS and PHS.

We calculate the ES dynamics after a quench in the model given in Eq. (5.77). All the parameters are randomly sampled from  $J_\mu \in [0.6\bar{J}_\mu, 1.4\bar{J}_\mu]$ , and the quench protocol is chosen to be

$$(\bar{J}_1, \bar{J}_2, \bar{J}_c, \bar{J}_{cc}) = (1.5J, 0, 0, 0) \rightarrow (0, 1.5J, 0.4J, 0.8J). \quad (5.78)$$

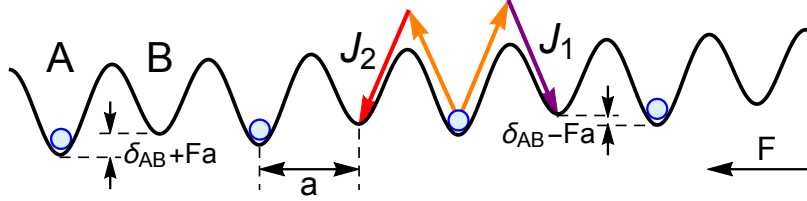


Figure 5.8: Implementation of the SSH model based on laser-assistant tunneling with ultracold atoms in a tilted optical superlattice. The intra- and inter-unit-cell hoppings  $J_1$  and  $J_2$  can independently be controlled by using two pairs of Raman lasers with detunings  $\delta_{AB} \pm Fa$ . Reproduced from Supplementary Fig. 12 of Ref. [46]. Copyright © 2018 by the American Physical Society.

The numerical results are shown in Fig. 5.7 for coupled chains  $M = 1 \sim 4$ . Remarkably, we find that there is a four-fold-degenerate crossing (which comes from the periodic-boundary condition and the Kramers degeneracy) for  $M = 1, 3$  while no crossing for  $M = 2, 4$ . Such an observation is consistent with the  $\mathbb{Z}_2$  classification predicted by the  $K$ -theory (see Table 5.1).

### 5.3.3 Experimental situation

We briefly discuss how to experimentally measure the ES dynamics in the SSH model simulated by ultracold atoms, which provide an ideal platform to explore nonequilibrium quantum dynamics. Indeed, sudden quench and Bloch-state tomography have been achieved in the Haldane model [328, 338]. Here we apply these ideas and techniques to the SSH model. It is worth mentioning that an interferometric scheme to directly measure the ES in an interacting ultracold atomic system has been proposed in Ref. [151], but has not yet been realized experimentally. Such a scheme is a generalization of Ref. [331], which describes a method of measuring the Rényi entropy and has recently been realized in an optical lattice [332].

While the SSH model has been realized in Refs. [171, 341, 342], these realizations are not suitable for studying quench dynamics since the Wannier functions change considerably after deforming the optical lattice, leading to unwanted excitations in higher bands. Also, an energy difference between A and B sublattices is needed to perform tomography [336]. Therefore, we use a superlattice with large energy offset  $\delta_{AB}$  between nearest neighbors (separated by  $a$ ) and subjected to a uniform potential gradient  $Fa \sum_j [(2j-1)a_j^\dagger a_j + 2jb_j^\dagger b_j]$  (see Fig. 5.8). Thanks to the potential gradient, it is possible to independently control the hopping parameters  $J_1$  and  $J_2$  by two pairs of Raman lasers with detunings  $\delta_{AB} \pm Fa$ . For example, to realize the quench  $(J_0, 0) \rightarrow (0, J)$ , we can suddenly switch off one laser assistant tunneling  $J_1 = J_0$  and switch on the other tunneling  $J_2 = J$ . Note that it is easy to generalize to the Rice-Mele model by choosing imperfect Raman-laser detunings  $\delta_{AB} \pm Fa \mp \Delta$ .

As for Bloch-state tomography, we follow the method in Ref. [337] to suddenly switch off the potential gradient and Raman lasers and then perform time-of-flight measurements after waiting for a varying time up to a few times of  $2\pi\delta_{AB}^{-1}$ . Unlike the case in Ref. [337], the potential gradient continuously shifts the quasimomenta during the quench dynamics, so that the measured Bloch state at  $k$  should be replaced by  $k + Ft_q$ , with  $t_q$  being the time duration of the quench dynamics. In practice, we can apply an opposite potential gradient during time  $t_q$  to compensate for this effect. If the gradient comes from inhomogeneous Zeeman splitting, this can be done by globally flipping the atomic spin [171]. With the full information of Bloch states in hand, we can calculate the half-chain ES following the standard method (see Appendix D.1).



## Chapter 6

# Summary and outlook

In this Thesis, we have focused on the dynamical generalization of order and topology in quantum systems out of equilibrium. We have considered three of the most common nonequilibrium situations — periodic driving, dissipation and quench.

In particular, in Chapter 2, we have predicted the DTC order in Floquet open quantum systems, and proposed a simple scheme for realizing it in cavity and circuit QED systems via switching on and off of the atom-light coupling. Technically, we have focused on the modulated open Dicke model both in the thermodynamic limit and in the deep quantum regime. In the former case, we have found rich dynamical phases caused by various bifurcations. In the latter case, we have shown that the interplay between dissipation and strong coupling gives rise to a clear transient DTC behavior. Moreover, we have demonstrated an exponentially long lifetime of the DTC behavior in the Floquet-GKSL-Landau theory.

Our model can readily be generalized by taking into account the atomic motional degrees of freedom [354], interactions between atoms [355], local decoherence, and spontaneous emission [106, 356, 357]. Indeed, there have already appeared several follow-up works on these topics. In particular, our study raises an intriguing question as to whether an intrinsically nonunitary DTC can possess absolute stability [69] against arbitrary nonunitary perturbation. Further studies along this line should give valuable hints for realizing a persistent DTC in the presence of realistic uncontrollable dissipation and decoherence. Another direction of research is to understand the mechanisms of the dynamical phases other than the DTC phase from their Floquet-GKSL spectra, especially the scaling behavior of these dynamical orders with respect to the system size. Note that some preliminary results on the asymmetric DTC behavior have been reported in Sec. 2.4.2 in Chapter 2.

In Chapter 3, we have focused on the classification of symmetric MPUs, for which the symmetry representation can be arbitrary or fixed. In the former case, we have achieved a complete classification based on the index and the cohomology class. In the latter case, we have unveiled a set of experimentally accessible SPIs that enrich the classification and lead to the discovery of a new class of intrinsic Floquet SPT phases in 2D.

On the other hand, the complete classification of MPUs with fixed symmetry representations stays an open problem. In addition, the current study concerns only on the locality-preserving unitaries in 1D bosonic (spin) systems with unitary symmetries, so that the directions of future studies may include the generalization to anti-unitary [35] and continuous symmetries, fermionic systems [358] or/and higher dimensions [359]. Moreover, since both SPIs and cohomology classes apply to inhomogeneous unitaries, it would also be interesting to study the impact of topology on information scrambling in random circuits [360–366]. In particular, we would like to ask whether nontrivial SPIs can set some lower bounds on the speed of thermalization [37], as might be quantified by the growth of entanglement entropy [367].

In Chapter 4, we have established a fundamental framework for a systematic study of topological non-Hermitian systems. This framework is based on a dynamical viewpoint on non-Hermitian topological systems and a generalization of the energy gap for complex energy spectra. We have studied in detail 1D non-Hermitian lattices in class A, identified the topological winding number, unveiled a novel bulk-edge correspondence, and discussed the possible experimental relevance. We have then performed a systematic classification based on the  $K$ -theory and obtained the periodic table for non-Hermitian AZ classes. All the nontrivial classes in 0D and 1D have been exemplified.

Our framework opens up many possibilities for future studies. Even if we confine ourselves to non-Hermitian AZ classes, physical properties of topological phases in higher than two dimensions are yet to be explored. Note that the topological phases in four or even higher dimensions are also physically relevant since they might be realized by making use of the time degree of freedom [368, 369] or the synthetic dimensions [370, 371]. Compatible with the  $K$ -theory, our framework can readily be extended to including Bernard-LeClair symmetries, as has been done in Ref. [257, 258]. There should be no difficulty in principle for a further generalization to crystalline symmetries [199, 200], such as the  $PT$  symmetry. Moreover, in analogy with Hermitian systems for which the  $K$ -theory approach has been applied to classify bulk-gapless topological phases [296], our framework has a potential to be generalized to non-Hermitian systems with exceptional points in the bulk [210, 212–214]. This has also been done recently in Ref. [318]. We can even go beyond the  $K$ -theory classification to seek for homotopically distinguishable (like the Hopf insulator [147]) non-Hermitian topological phases with a definite Hilbert-space dimension. See some recent progress along this line in Refs. [372–374]. Last but not the least, it would be an intriguing theoretical issue to consider the topological characterization for interacting many-body non-Hermitian systems [238, 239], which are expected to be accessible in near-future atomic, molecular and optical experiments in light of the rapid development in reservoir engineering [26].

In Chapter 5, we have identified the nontrivial spacetime topological structures for all the one-dimensional quench dynamics within the same AZ class. We have proposed using the ES dynamics to detect the dynamical topology and performed extensive numerical studies in several prototypical models. In particular, we have demonstrated how to distinguish  $\mathbb{Z}$  and  $\mathbb{Z}_2$  topology from the ES dynamics in coupled SSH chains. These phenomena can be explored in state-of-the-art AMO experiments.

In higher dimensions [375] and/or with additional symmetries, there remains an open problem as to whether a nontrivial  $(d+1)$ D topological structure emerges in quench dynamics, and, if yes, how the single-particle ES dynamics looks like. Even in 1D, it is not fully clear whether the ES crossing is robust against band nonflatness. See Ref. [376] for some recent progress on this issue. We also note that Ref. [377] has discovered similar ES crossing phenomena in free-fermion systems with long-range hoppings. Finally, the influence of interaction could be yet another important issue, which might be tackled from the dynamics of the many-body ES. In 1D, this can directly be readout from the MPS representation [153], which is accessible in cutting-edge trapped-ion experiments [150].

In short, this Thesis contributes to the emergent subject on exploring novel phenomena in nonequilibrium quantum dynamics, especially exotic dynamical phases in Floquet, open and quenched systems. We hope that this Thesis could provide some valuable pieces of information and pave the way towards a complete understanding on nonequilibrium phases.

# Appendix A

## Topological invariants for inhomogenous locality-preserving unitaries

In this appendix, we rigorously derive the factorization relation for the evolved symmetry string operator solely from the symmetry and the (strict) locality-preserving requirement without assuming the translation invariance. In analogy with the SPIs for MPUs, we prove that the (relative) SPIs defined from  $L_g$  and  $R_g$  in the factorization relation are topological invariants. The same technique also allows the generalization of the cohomology class to inhomogeneous locality-preserving unitaries.

### A.1 Factorization relation

We first introduce two useful lemmas:

**Lemma 3** *Given a unitary  $U$  acting on a bipartite system  $A \cup B$ , then  $U = U_A \otimes U_B$  for some subsystem unitaries  $U_A$  and  $U_B$  if and only if*

$$[U^\dagger(O_A \otimes \mathbb{1}_B)U, \mathbb{1}_A \otimes O_B] = [O_A \otimes \mathbb{1}_B, U^\dagger(\mathbb{1}_A \otimes O_B)U] = 0 \quad (\text{A.1})$$

for any subsystem operators  $O_A$  and  $O_B$ .

*Proof:* “Only if” is trivial. To show “if”, we first note that

$$[U^\dagger(O_A \otimes \mathbb{1}_B)U, \mathbb{1}_A \otimes O_B] = 0 \quad (\text{A.2})$$

for arbitrary  $O_B$  acting on  $B$  is equivalent to

$$U^\dagger(O_A \otimes \mathbb{1}_B)U = f_A(O_A) \otimes \mathbb{1}_B. \quad (\text{A.3})$$

See, e.g., Lemma 1.5 in Ref. [378]. Moreover,  $f_A$  is a ring automorphism on  $M_{d_A}(\mathbb{C})$  (ring of  $d_A \times d_A$  complex matrices), since it is a ring homomorphism and is bijective due to  $U(O_A \otimes \mathbb{1}_B)U^\dagger = f_A^{-1}(O_A) \otimes \mathbb{1}_B$ . According to the Skolem-Noether theorem, we must have

$$f_A(O_A) = V_A^{-1}O_A V_A, \quad (\text{A.4})$$

where  $V_A \in M_{d_A}(\mathbb{C})$  is invertible. Similarly, we must have

$$U^\dagger(\mathbb{1}_A \otimes O_B)U = \mathbb{1}_A \otimes V_B^{-1}O_B V_B. \quad (\text{A.5})$$

Therefore, for an arbitrary operator  $O = \sum_j O_{A,j} \otimes O_{B,j}$  acting on the entire system, we have

$$U^\dagger O U = \sum_j U^\dagger (O_{A,j} \otimes \mathbb{1}_B) U U^\dagger (\mathbb{1}_A \otimes O_{B,j}) U = (V_A \otimes V_B)^{-1} O (V_A \otimes V_B), \quad (\text{A.6})$$

which leads to

$$(V_A \otimes V_B) U^\dagger = c \mathbb{1}_{AB} \quad c \neq 0. \quad (\text{A.7})$$

Absorbing  $c^{-1}$  into  $V_A$  or  $V_B$  followed by choosing a proper  $\mathbb{C}^\times$  gauge, we end up with  $U = U_A \otimes U_B$ , where  $U_A$  and  $U_B$  are subsystem unitaries.  $\square$

**Lemma 4** *Given a unitary  $U$  acting on an  $M$ -partite system  $S = \bigcup_{m=1}^M S_j$ , then  $U = \bigotimes_{m=1}^M U_j$  if and only if  $U = U_m \otimes U_{\bar{m}}$  for  $m = 1, 2, \dots, M-1$ , where  $U_m$  and  $U_{\bar{m}}$  are unitaries acting only on  $S_m$  and  $S_{\bar{m}} \equiv S \setminus S_m$ , respectively.*

*Proof:* ‘‘Only if’’ is trivial. To show ‘‘if’’, we start from  $U = U_1 \otimes U_{\bar{1}}$  and prove  $U_{\bar{1}} = U_2 \otimes U_{\bar{12}}$ . Focusing on the singular-value decomposition with respect to the bipartition  $S = S_2 \cup S_{\bar{2}}$ , we know from  $U = U_2 \otimes U_{\bar{2}}$  that the bond dimension is one, implying  $U_{\bar{1}} = V_2 \otimes V_{\bar{12}}$ . Moreover, from the fact that

$$\mathbb{1}_S = U^\dagger U = U_2^\dagger V_2 \otimes [U_{\bar{2}}^\dagger (U_1 \otimes V_{\bar{12}})], \quad (\text{A.8})$$

we can properly choose the  $\mathbb{C}^\times$  gauge such that  $V_2 = U_2$ , which in turn implies  $U_{\bar{12}} \equiv V_{\bar{12}}$  is unitary. Following a similar analysis, we can factorize  $U_{\bar{12}}$  into  $U_3 \otimes U_{\bar{123}}$  and so on, and end up with  $U = \bigotimes_{m=1}^M U_m$ .  $\square$

Before deriving the factorization relation, we list a few fundamental properties of locality-preserving unitaries:

**Proposition 6** *For a locality-preserving unitary  $U_{\text{LP}}$  acting on a ring of  $L$  spins and with the Lieb-Robinson length  $l_{\text{LR}}$ , we have*

- (i) *If  $O$  acts nontrivially only on  $[j_l, j_r] \subset \mathbb{Z}_L$ , then  $U_{\text{LP}}^\dagger O U_{\text{LP}}$  is nontrivial at most on  $[j_l - l_{\text{LR}}, j_r + l_{\text{LR}}]$ ;*
- (ii) *If  $U_{\text{LP}} = U_{\text{LP},1} U_{\text{LP},2}$ , where the Lieb-Robinson length of  $U_{\text{LP},a}$  is  $l_{\text{LR},a}$  ( $a = 1, 2$ ), then  $l_{\text{LR}} \leq l_{\text{LR},1} + l_{\text{LR},2}$ ;*
- (iii)  *$U_{\text{LP}}^\dagger$  has the same Lieb-Robinson length  $l_{\text{LR}}$ .*

*Proof:* From a general expansion

$$O = \sum_{\{n_j\}_{j=j_l}^{j_r}} \bigotimes_{j=j_l}^{j_r} O_j^{[n_j]}, \quad (\text{A.9})$$

where  $O_j^{[n_j]}$  acts nontrivially only on the  $j$ th site, we obtain (i). Taking  $O = U_{\text{LP},1}^\dagger O_j U_{\text{LP},1}$  in (i) for an arbitrary operator  $O_j$  acting nontrivially only on the  $j$ th site, we know that  $U_{\text{LP},2}^\dagger U_{\text{LP},1}^\dagger O_j U_{\text{LP},1} U_{\text{LP},2}$  is nontrivial at most on  $[j - l_{\text{LR},1} - l_{\text{LR},2}, j + l_{\text{LR},1} + l_{\text{LR},2}]$  for  $\forall j \in \mathbb{Z}_L$  and (ii) follows. To show (iii), we consider all the operators  $O$  acting nontrivially only on  $\mathbb{Z}_L \setminus [j - l_{\text{LR}}, j + l_{\text{LR}}]$ , so that

$$[U_{\text{LP}}^\dagger O U_{\text{LP}}, O_j] = [O, U_{\text{LP}} O_j U_{\text{LP}}^\dagger] = 0 \quad (\text{A.10})$$

due to (i), where  $O_j$  follows the previous notation. The arbitrariness of  $O$  implies that  $U_{\text{LP}} O_j U_{\text{LP}}^\dagger$  acts nontrivially at most on  $[j - l_{\text{LR}}, j + l_{\text{LR}}]$ . Hence, denoting the Lieb-Robinson length of  $U_{\text{LP}}^\dagger$  as  $\tilde{l}_{\text{LR}}$ , we have  $\tilde{l}_{\text{LR}} \leq l_{\text{LR}}$ . Similarly, we can derive  $l_{\text{LR}} \leq \tilde{l}_{\text{LR}}$  from  $(U_{\text{LP}}^\dagger)^\dagger = U_{\text{LP}}$ . Combining these two relations, we obtain (iii).  $\square$

With all the previous results in hand, we are ready to prove the following theorem:

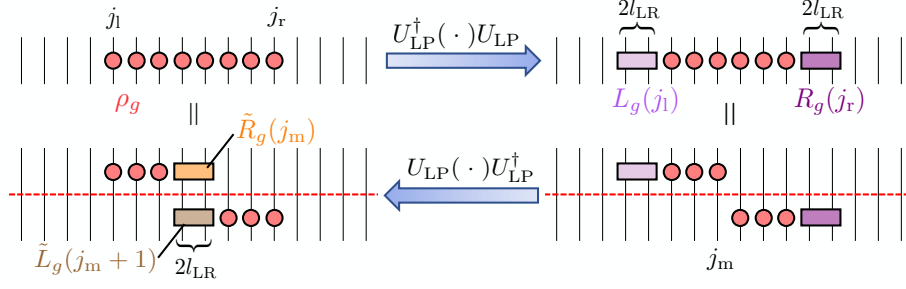


Figure A.1: Relations between  $g$ ,  $L_g$ ,  $R_g$ ,  $\tilde{L}_g$  and  $\tilde{R}_g$  through a symmetric inhomogeneous locality-preserving unitary  $U_{\text{LP}}$  with  $l_{\text{LR}} = 1$ , which is always the case after sufficient blocking. Trace preservation under unitary transformation implies  $\text{Tr } L_g(j_l) = \text{Tr } \tilde{R}_g(j_m)$  and  $\text{Tr } R_g(j_r) = \text{Tr } \tilde{L}_g(j_m + 1)$ . Note that the parts above and below the red dashed line are transformed separately. Reproduced from Supplementary Fig. 6 of Ref. [38]. Copyright © 2020 by the American Physical Society.

**Theorem 5 (Factorization relation)** *Given a  $G$ -symmetric locality-preserving unitary  $U_{\text{LP}}$  with the Lieb-Robinson length  $l_{\text{LR}}$ , for  $\forall g \in G$  defining a  $g$ -string operator  $\rho_{g[j_l, j_r]} \equiv \bigotimes_{j \in [j_l, j_r]} \rho_g$  with  $|j_l - j_r| \geq 4l_{\text{LR}}$ , we have (with  $\mathbb{1}$  omitted for simplicity)*

$$U_{\text{LP}}^\dagger \rho_{g[j_l, j_r]} U_{\text{LP}} = L_g(j_l) \otimes \rho_{g[j_l + l_{\text{LR}}, j_r - l_{\text{LR}}]} \otimes R_g(j_r), \quad (\text{A.11})$$

where  $L_g(j_l)$  and  $R_g(j_r)$  are unitary operators acting nontrivially (at most) on  $I_L = [j_l - l_{\text{LR}}, j_l + l_{\text{LR}} - 1]$  and  $I_R = [j_r - l_{\text{LR}} + 1, j_r + l_{\text{LR}}]$ , respectively.

*Proof:* We divide the lattice  $\mathbb{Z}_L$  into three subsystems:

$$S_1 \equiv \mathbb{Z}_L \setminus [j_l - l_{\text{LR}}, j_r + l_{\text{LR}}], \quad S_2 \equiv [j_l + l_{\text{LR}}, j_r - l_{\text{LR}}], \quad S_3 \equiv I_L \cup I_R. \quad (\text{A.12})$$

Applying Proposition 6(i) directly to the lhs of Eq. (A.11), we obtain

$$U_{\text{LP}}^\dagger \rho_{g[j_l, j_r]} U_{\text{LP}} = U_1 \otimes U_{\bar{1}} \quad (\text{A.13})$$

with  $U_1 = \mathbb{1}_{S_1}$ . Since  $U_{\text{LP}}$  is  $G$ -symmetric, we can rewrite the evolved  $g$ -string operator into

$$U_{\text{LP}}^\dagger \rho_{g[j_l, j_r]} U_{\text{LP}} = \rho_g^{\otimes L} U_{\text{LP}}^\dagger \rho_{g[\mathbb{Z}_L \setminus [j_l, j_r]]} U_{\text{LP}}. \quad (\text{A.14})$$

Applying Proposition 6(i) to the rhs of Eq. (A.14), we obtain

$$U_{\text{LP}}^\dagger \rho_{g[j_l, j_r]} U_{\text{LP}} = U_2 \otimes U_2 \quad (\text{A.15})$$

with  $U_2 = \rho_g^{\otimes (j_r - j_l - 2l_{\text{LR}} + 1)}$ . According to Lemma D.15, there exists a unitary  $U_3$  acting on  $S_3$  such that

$$U_{\text{LP}}^\dagger \rho_{g[j_l, j_r]} U_{\text{LP}} = \bigotimes_{m=1}^3 U_m. \quad (\text{A.16})$$

We move on to show that  $U_3$  can further be factorized. According to Props. 6(ii) and (iii), the Lieb-Robinson length of  $U_{\text{LP}}^\dagger \rho_{g[j_l, j_r]} U_{\text{LP}}$  is no more than  $2l_{\text{LR}}$ . Since  $|j_l - j_r| \geq 4l_{\text{LR}}$ , given any two operators  $O_{I_L}$  and  $O_{I_R}$  acting nontrivially only on  $I_L$  and  $I_R$ , respectively, we have

$$[U_3^\dagger (O_{I_L} \otimes \mathbb{1}_{I_R}) U_3, \mathbb{1}_{I_L} \otimes O_{I_R}] = [O_{I_L} \otimes \mathbb{1}_{I_R}, U_3^\dagger (\mathbb{1}_{I_L} \otimes O_{I_R}) U_3] = 0. \quad (\text{A.17})$$

It follows from Lemma 3 that  $U_3 = L_g(j_l) \otimes R_g(j_r)$  for two unitaries  $L_g(j_l)$  and  $R_g(j_r)$  acting on  $I_L$  and  $I_R$ , respectively. Substituting the expressions of  $U_m$  ( $m = 1, 2, 3$ ) into  $\bigotimes_{m=1}^3 U_m$  yields the rhs of Eq. (A.11).  $\square$

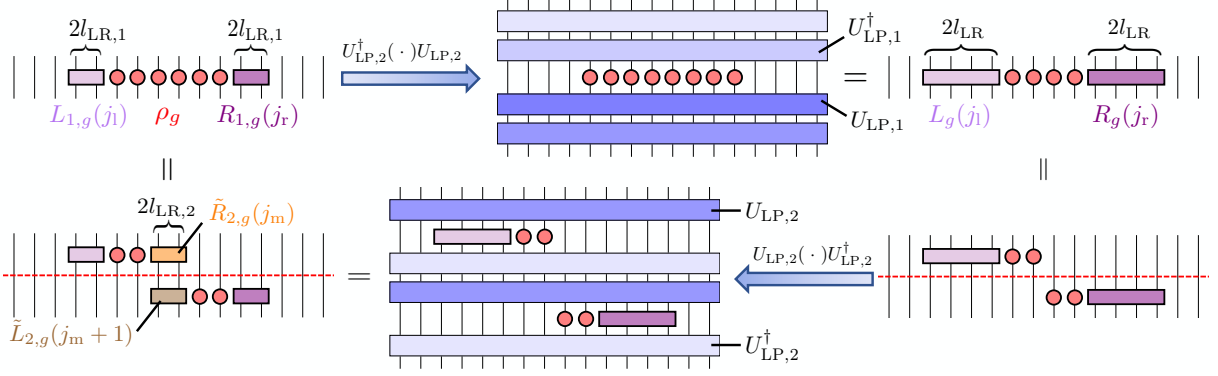


Figure A.2: Schematic illustration of the additivity of the relative SPI and the cohomology class. Up to tensoring with (equal numbers of)  $\mathbb{1}$  and  $\rho_g$ ,  $L_g(j_l)$  and  $R_g(j_r)$  of  $U_{LP} = U_{LP,1}U_{LP,2}$  are unitarily equivalent to  $L_{1,g}(j_l) \otimes \tilde{R}_{2,g}(j_m)$  and  $\tilde{L}_{2,g}(j_m+1) \otimes R_{1,g}(j_r)$ , respectively. Reproduced from Supplementary Fig. 7 of Ref. [38]. Copyright © 2020 by the American Physical Society.

## A.2 Topological invariants

We first mention that the robustness of  $\text{ind}$  defined in Eq. (3.20) against disorder and its additivity are well established in Ref. [37], so it is sufficient to focus on the relative SPI  $\text{ind}_g - \text{ind}$ . By sufficient we mean that if the relative SPI is an additive topological invariant, so is the SPI.

**Proposition 7** *The relative SPI*

$$\text{ind}_g - \text{ind} \equiv \frac{1}{2} \ln \left| \frac{\text{Tr } L_g}{\text{Tr } R_g} \right| \quad (\text{A.18})$$

is a well-defined global character, although  $L_g$  and  $R_g$  are generally site-dependent.

*Proof:* To prove the site-independence of  $|\text{Tr } L_g|$  and  $|\text{Tr } R_g|$ , we only have to show

$$\text{Tr } L_g(j_l) = \text{Tr } \tilde{R}_g(j_m), \quad \text{Tr } R_g(j_r) = \text{Tr } \tilde{L}_g(j_m+1), \quad \forall j_m \in (j_l + l_{LR}, j_r - l_{LR}), \quad (\text{A.19})$$

where  $\tilde{L}_g$  and  $\tilde{R}_g$  are determined from evolving the  $g$ -string operator by  $U_{LP}^\dagger$ . These two identities stem simply from the preservation of trace under unitary conjugation (see Fig. A.1). As  $j_l$  and  $j_r$  are variable for a fixed  $j_m$ ,  $|\text{Tr } L_g|$  and  $|\text{Tr } R_g|$  should be site-independent and  $\text{ind}_g - \text{ind}$  in Eq. (A.18) is a well-defined global character for  $U_{LP}$ .

It remains to derive the relations in Fig. A.1, where the upper half is nothing but Theorem 5, so that we only have to rigorously derive the lower half. To show the relation above the red dashed line, which explicitly reads

$$U_{LP} L_g(j_l) \otimes \rho_{g[j_l+l_{LR}, j_m]} U_{LP}^\dagger = \rho_{g[j_l, j_m-l_{LR}]} \otimes \tilde{R}_g(j_m), \quad (\text{A.20})$$

we divide  $\mathbb{Z}_L$  into

$$S_1 = \mathbb{Z}_L \setminus [j_l - 2l_{LR}, j_m + l_{LR}], \quad S_2 = [j_l - 2l_{LR}, j_m - l_{LR}], \quad S_3 = [j_m - l_{LR} + 1, j_m + l_{LR}]. \quad (\text{A.21})$$

Applying Proposition 6(i) directly to the lhs of Eq. (A.20), we obtain the factorization  $U_1 \otimes U_{\bar{1}}$  with  $U_1 = \mathbb{1}_{S_1}$ . Moreover, rewriting Eq. (A.11) into

$$U_{LP} L_g(j_l) \otimes \rho_{g[j_l+l_{LR}, j_m]} U_{LP}^\dagger = \rho_{g[j_l, j_r]} U_{LP} \rho_{g[j_m+1, j_r-l_{LR}]}^\dagger \otimes R_g(j_r)^\dagger U_{LP}^\dagger \quad (\text{A.22})$$

and applying Proposition 6(i) directly to the rhs, we obtain the factorization  $U_2 \otimes U_{\bar{2}}$  with  $U_2 = \rho_{g[j_1-2l_{\text{LR}}, j_m-l_{\text{LR}}]}$ . According to Lemma D.15, Eq. (A.20) follows. Similarly, by choosing

$$\begin{aligned} S_1 &= \mathbb{Z}_L \setminus [j_m - l_{\text{LR}} + 1, j_r + 2l_{\text{LR}}], & S_2 &= [j_m + l_{\text{LR}} + 1, j_r + 2l_{\text{LR}}], \\ S_3 &= [j_m - l_{\text{LR}} + 1, j_m + l_{\text{LR}}], \end{aligned} \quad (\text{A.23})$$

we can derive

$$U_{\text{LP}} \rho_{g[j_m+1, j_r-l_{\text{LR}}]} \otimes R_g(j_r) U_{\text{LP}}^\dagger = \tilde{L}_g(j_m + 1) \otimes \rho_{g[j_m+l_{\text{LR}}+1, j_r]}. \quad (\text{A.24})$$

The independence of  $\tilde{R}_g(j_m)$  and  $\tilde{L}_g(j_m + 1)$  on  $j_l$  and  $j_r$  with  $\min\{|j_l - j_m|, |j_r - j_m|\} \geq l_{\text{LR}}$  is again a direct consequence of Proposition 6(i), i.e., a local modification far from subsystem  $S_3$  cannot propagate to  $S_3$  through  $U_{\text{LP}}^\dagger$ .  $\square$

Similarly to the SPI, we can also generalize the cohomology character to inhomogeneous locality-preserving unitaries by realizing that  $L_g(j_l) \otimes R_g(j_r)$  is a linear representation, as can be seen from the top of Fig. A.1.

**Proposition 8** *The cohomology class of  $L_g$ , which is opposite to that of  $R_g$ , is a well-defined global character.*

To see this, note that  $L_g(j_l)$  and  $\tilde{R}_g(j_m)$  are equivalent projective representations (see Fig. A.1 bottom) and the cohomology class cannot depend on  $j_l$ .  $\square$

Just as in the case of MPUs, we have

**Theorem 6** *The relative SPI is a topological invariant, which is additive by tensoring and composition.*

*Proof:* We consider a continuous path of  $G$ -symmetric locality-preserving unitaries  $U_{\text{LP}}(\lambda)$ , along which the maximal Lieb-Robinson length is denoted as  $l_{\text{max}} \equiv \max_\lambda l_{\text{LR}}(\lambda)$ . For a fixed  $g$ -string operator  $\rho_{g[j_l, j_r]}$  with  $|j_l - j_r| \geq 4l_{\text{max}}$ , we have the factorization relation

$$U_{\text{LP}}^\dagger(\lambda) \rho_{g[j_l, j_r]} U_{\text{LP}}(\lambda) = L_g(j_l; \lambda) \otimes \rho_{g[j_l+l_{\text{max}}, j_r-l_{\text{max}}]} \otimes R_g(j_r; \lambda), \quad (\text{A.25})$$

where  $L_g(j_l; \lambda)$  and  $R_g(j_r; \lambda)$  act on  $I_l \equiv [j_l - l_{\text{max}}, j_l + l_{\text{max}} - 1]$  and  $I_r \equiv [j_r - l_{\text{max}} + 1, j_r + l_{\text{max}}]$ , respectively. Note that the factorization in Eq. (A.25) may not be optimal in the sense that  $L_g(j_l; \lambda)$  and  $R_g(j_r; \lambda)$  can be reduced to  $\mathbb{1}^{\otimes \Delta l} \otimes L_g^{\text{op}}(j_l; \lambda) \otimes \rho_g^{\otimes \Delta l}$  and  $\rho_g^{\otimes \Delta l} \otimes R_g^{\text{op}}(j_r; \lambda) \otimes \mathbb{1}^{\otimes \Delta l}$  with  $\Delta l = l_{\text{max}} - l_{\text{LR}}(\lambda)$ . Nevertheless, the ratio  $|\text{Tr } L_g / \text{Tr } R_g|$  always determines the relative SPI since additional factors  $\chi_g$  and  $d$  cancel out. Inspired by the experimental scheme, we can express the relative SPI in terms of  $U_{\text{LP}}(\lambda)$  via

$$\frac{1}{4} \ln \left| \frac{\text{Tr}_{I_l} [\text{Tr}_{I_l} \rho_{g[j_l, j_r]}^{\text{H}}(\lambda) \text{Tr}_{I_l} \rho_{g[j_l, j_r]}^{\text{H}}(\lambda)^\dagger]}{\text{Tr}_{I_r} [\text{Tr}_{I_r} \rho_{g[j_l, j_r]}^{\text{H}}(\lambda) \text{Tr}_{I_r} \rho_{g[j_l, j_r]}^{\text{H}}(\lambda)^\dagger]} \right|, \quad (\text{A.26})$$

where  $\rho_{g[j_l, j_r]}^{\text{H}}(\lambda) \equiv U_{\text{LP}}^\dagger(\lambda) \rho_{g[j_l, j_r]} U_{\text{LP}}(\lambda)$  is continuous with respect to  $\lambda$ . Accordingly, the relative SPI is a continuous function of  $\lambda$ . On the other hand, since  $L_g \otimes R_g$  is a linear representation (see also the proof of Theorem 3), we know that  $\text{ind}_g - \text{ind}$  takes values over a finite set

$$\left\{ \ln \frac{|\sum_{j \in \mathbb{Z}_{d_g}} n_j \omega_{d_g}^j|}{d^{\text{max}} |\chi_g|^{l_{\text{max}}}} : \sum_{j \in \mathbb{Z}_{d_g}} n_j = d^{2l_{\text{max}}} \right\}. \quad (\text{A.27})$$

Therefore, the relative SPI must be a topological invariant.

We move on to prove the additivity. Consider two  $G$ -symmetric locality-preserving unitaries  $U_{\text{LP},1}$  and  $U_{\text{LP},2}$  with the Lieb-Robinson lengths  $l_{\text{LR},1}$  and  $l_{\text{LR},2}$ ; then their composition  $U_{\text{LP}} = U_{\text{LP},1}U_{\text{LP},2}$  is again  $G$ -symmetric and locality-preserving with  $l_{\text{LR}} = l_{\text{LR},1} + l_{\text{LR},2} - \Delta l_{12}$  ( $\Delta l_{12} \geq 0$ ). As shown in Fig. A.2, which is similar to Fig. A.1, we apply a “pull-back” technique to  $U_{\text{LP},1}^\dagger \rho_{g[j_l, j_r]} U_{\text{LP},1}$  to obtain (a rigorous derivation is parallel to the proof of Proposition 7)

$$\begin{aligned} (d\chi_g)^{\Delta l_{12}} \text{Tr } L_g(j_l) &= \text{Tr } L_{1,g}(j_l) \text{Tr } \tilde{R}_{2,g}(j_m), \\ (d\chi_g)^{\Delta l_{12}} \text{Tr } R_g(j_r) &= \text{Tr } R_{1,g}(j_r) \text{Tr } \tilde{L}_{2,g}(j_m + 1), \end{aligned} \quad (\text{A.28})$$

which implies

$$\ln \left| \frac{\text{Tr } L_g(j_l)}{\text{Tr } R_g(j_r)} \right| = \ln \left| \frac{\text{Tr } L_{1,g}(j_l)}{\text{Tr } R_{1,g}(j_r)} \right| + \ln \left| \frac{\text{Tr } \tilde{R}_{2,g}(j_m)}{\text{Tr } \tilde{L}_{2,g}(j_m + 1)} \right|, \quad (\text{A.29})$$

and thus the additivity of the relative SPI.  $\square$

In fact, the same result (Theorem 6) holds for the cohomology class. To show this, we need the following Lemma:

**Lemma 5** *Let  $U(\lambda) = U_A(\lambda) \otimes U_B(\lambda)$  be a continuous path of unitaries acting on a bipartite system  $A \cup B$ ; then we can always choose a proper  $U(1)$  gauge such that  $U_A(\lambda)$  and  $U_B(\lambda)$  are separately continuous paths.*

*Proof:* By assumption, we have

$$U_A(\lambda) \otimes \bar{U}_A(\lambda) = \langle \Phi_{B'B} | U(\lambda) \otimes \bar{U}(\lambda) | \Phi_{B'B} \rangle, \quad (\text{A.30})$$

where  $|\Phi_{BB'}\rangle = \frac{1}{\sqrt{d_B}} \sum_{j=1}^{d_B} |j_B j_{B'}\rangle$  is the maximally entangled state of subsystem  $B$  and its copy  $B'$ . Moreover,  $U_A(\lambda) \otimes \bar{U}_A(\lambda)$  must be continuous with respect to  $\lambda$  as  $U(\lambda)$  is. Decomposing the entry of  $U_A(\lambda)$  as  $[U_A(\lambda)]_{mn} = r_{mn}(\lambda) \omega_{mn}(\lambda)$  with  $r_{mn}(\lambda) \in [0, \infty)$  and  $\omega_{mn}(\lambda) \in U(1)$ , we can uniquely determine all  $r_{mn}(\lambda)$  from

$$[U_A(\lambda) \otimes \bar{U}_A(\lambda)]_{mm,nn} = r_{mn}(\lambda)^2, \quad (\text{A.31})$$

and all  $\omega_{mn}(\lambda)/\omega_{m'n'}(\lambda)$  with  $r_{mn}(\lambda)r_{m'n'}(\lambda) \neq 0$  from

$$[U_A(\lambda) \otimes \bar{U}_A(\lambda)]_{mm',nn'} = r_{mn}(\lambda)r_{m'n'}(\lambda) \frac{\omega_{mn}(\lambda)}{\omega_{m'n'}(\lambda)}, \quad (\text{A.32})$$

which are all continuous. Also, the unitarity  $\sum_m r_{mn}(\lambda)^2 = \sum_n r_{mn}(\lambda)^2 = 1$  implies at least  $d_A$  nonzero entries. Imposing continuity to (the phase of) an arbitrary nonzero entry, the continuity of the others immediately follows from the continuity of  $\omega_{mn}(\lambda)/\omega_{m'n'}(\lambda)$ , and we obtain a continuous path of  $U_A(\lambda)$ . The corresponding  $U_B(\lambda)$  can be determined from

$$U_B(\lambda) = d_A^{-1} \text{Tr}_A[(U_A^\dagger(\lambda) \otimes \mathbb{1}_B)U(\lambda)], \quad (\text{A.33})$$

which is also continuous with respect to  $\lambda$ .  $\square$

We are now ready to prove the following theorem:

**Theorem 7** *The cohomology class is a topological invariant, which is additive by tensoring and composition.*



*Proof:* According to the factorization relation (A.11), using the same notations in the proof of Theorem 6, we have

$$L_g(j_l; \lambda) \otimes R_g(j_r; \lambda) = d^{4l_{\max}-L} \text{Tr}_{\bar{I}_l \cap \bar{I}_r} [\rho_{g[j_l+l_{\max}, j_r-l_{\max}]}^\dagger \rho_{g[j_l, j_r]}^H(\lambda)], \quad (\text{A.34})$$

where  $\rho_{g[j_l, j_r]}^H(\lambda) \equiv U_{\text{LP}}^\dagger(\lambda) \rho_{g[j_l, j_r]} U_{\text{LP}}(\lambda)$  is continuous with respect to  $\lambda$ . Therefore, we can apply Lemma 5 and find two continuous paths  $L_g(j_l; \lambda)$  and  $R_g(j_r; \lambda)$ , which are projective representations belonging to the opposite cohomology classes due to the fact that  $L_g(j_l; \lambda) \otimes R_g(j_r; \lambda)$  is a linear representation. According to Ref. [139], the cohomology class must stay unchanged along the continuous path. To prove the additivity, we only have to employ the pull-back technique shown in Fig. A.2 and then use the additivity of cohomology class upon tensoring.  $\square$

Finally, we claim the following as a special case of inhomogeneous locality-preserving unitaries.

**Theorem 8** *An open-boundary locality-preserving unitary always has trivial index, SPIs and cohomology character.*

*Proof:* For the case of the (symmetry-irrelevant) index, see Ref. [37]. In the presence of symmetry, we consider a  $g$ -string operator  $\rho_{g[0, j_r]}$  starting from the left edge of an open-boundary locality-preserving unitary  $U_{\text{LP}}$  with length  $L$  and Lieb-Robinson length  $l_{\text{LR}}$  (we choose  $j_r > l_{\text{LR}}$ ). Combining the locality-preserving property and the identity

$$U_{\text{LP}}^\dagger \rho_{g[0, j_r]} U_{\text{LP}} = \rho_g^{\otimes L} U_{\text{LP}}^\dagger \rho_{g[j_r+1, L-1]}^\dagger U_{\text{LP}}, \quad (\text{A.35})$$

we know that  $L_g(0) = \mathbb{1}^{\otimes l_{\text{LR}}} \otimes \rho_g^{\otimes l_{\text{LR}}}$  (where  $\mathbb{1}^{\otimes l_{\text{LR}}}$  acts on the rightmost  $l_{\text{LR}}$  sites), implying that both the SPI and the cohomology class are trivial.  $\square$

## Appendix B

# Localization and topology in the Hatano-Nelson model

In this appendix, we explain in detail how the topological transition is related to the Anderson transition in 1D non-Hermitian systems. We first generalize the spectral winding number to disordered lattices and then provide extensive numerical and analytical results to demonstrate the topological nature of the Anderson transition in the Hatano-Nelson model. We also provide an example of a topological transition that is not accompanied by a localization transition.

### B.1 Winding number for disordered systems

For Hermitian systems belonging to class A, we know that the integer quantum Hall states in two dimensions are robust against spatial disorder. As a consequence, while the Anderson transition is forbidden in two dimensions [379] in the absence of spin-orbit interactions [380], mobility edges emerge in an integer quantum Hall state and the delocalized modes contribute to the quantized Hall conductivity  $Ce^2/h$  [381], with  $C$  being the Chern number [165]. These well-established results naturally raise a question of whether or not a topological non-Hermitian system, such as Eq. (4.9), is robust against disorder and, if yes, in what sense.

To address this question, we consider the original Hatano-Nelson model [43, 254, 382]:

$$H = \sum_j (J_R c_{j+1}^\dagger c_j + J_L c_j^\dagger c_{j+1} + V_j c_j^\dagger c_j), \quad (\text{B.1})$$

which describes a 1D ring with asymmetric hopping amplitudes and on-site disorder  $V_j$ . While a 1D Hermitian system is always localized in the presence of a random potential [379], e.g.,  $V_j \in [-W, W]$  with a uniform probability, the Hatano-Nelson model (B.1) exhibits an Anderson transition [383]. Recalling the emergence of mobility edges in quantum Hall systems, we may conjecture that the Anderson transition is ensured by the nontrivial topological winding number, which is expected to be trivial if the system is fully localized.

To verify the conjecture, we first have to generalize the definition of the winding number (4.7) to disordered systems. Following the idea of defining the Chern number for disordered quantum Hall states [206], we apply a magnetic flux  $\Phi$  through a finite non-Hermitian ring with length  $L$  such that the hopping amplitudes are multiplied by  $e^{\mp i\Phi/L}$  under a specific choice of gauge. For the Hatano-Nelson model (B.1), we have

$$H(\Phi) = \sum_{j=1}^L (J_R e^{-i\frac{\Phi}{L}} c_{j+1}^\dagger c_j + J_L e^{i\frac{\Phi}{L}} c_j^\dagger c_{j+1} + V_j c_j^\dagger c_j). \quad (\text{B.2})$$

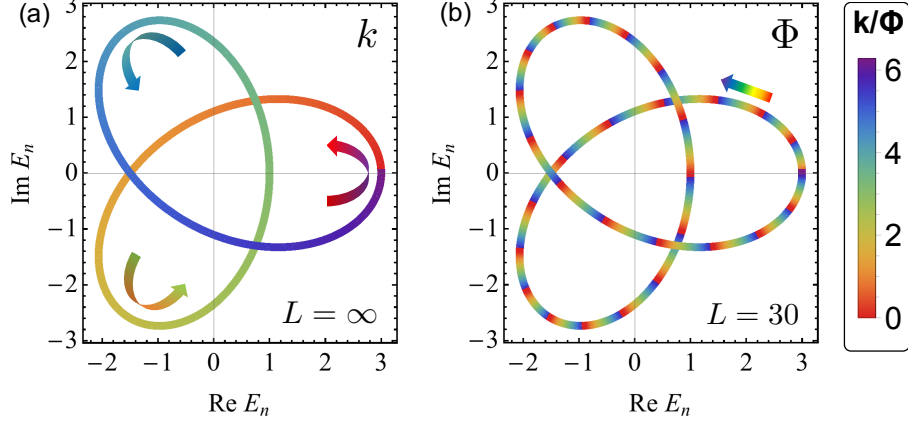


Figure B.1: (a) Energy spectrum of an infinite translation-invariant lattice described by Eq. (B.8). The arrows indicate the flow of eigenenergy as the wave number  $k$  increases from 0 to  $2\pi$ . (b) The same as in (a) but for a finite ( $L = 30$ ) ring subjected to a flux  $\Phi$ . The arrow indicates the spectral flow as  $\Phi$  changes from 0 to  $2\pi$ . Reproduced from Fig. 11 of Ref. [44]. Copyright © 2018 by the American Physical Society.

While  $H(\Phi)$  is not periodic in  $\Phi$ , there exists a large-gauge transformation  $U_{\text{LG}} = e^{\frac{2\pi i}{L} \sum_j j c_j^\dagger c_j}$  such that

$$H(\Phi + 2\pi) = U_{\text{LG}} H(\Phi) U_{\text{LG}}^\dagger. \quad (\text{B.3})$$

Therefore, the gauge-independent quantity  $\det H(\Phi)$  is periodic in  $\Phi$  and the winding number can be defined as

$$w \equiv \int_0^{2\pi} \frac{d\Phi}{2\pi i} \partial_\Phi \ln \det H(\Phi), \quad (\text{B.4})$$

which reproduces Eq. (4.7) in the presence of translation invariance. To show this, let us first distinguish the fluxed entire Hamiltonian  $H(\Phi)$  from the Bloch Hamiltonian  $H(k)$  by adding a subscript “tot” to the former. In the quasi-momentum representation, the entire Hamiltonian  $H_{\text{tot}}$  with flux  $\Phi$  can be block-diagonalized as

$$H_{\text{tot}}(\Phi) = \bigoplus_{k=\frac{2j\pi}{L}-\pi} H\left(k + \frac{\Phi}{L}\right), \quad (\text{B.5})$$

which leads to

$$\ln \det H_{\text{tot}}(\Phi) = \sum_{k=\frac{2j\pi}{L}-\pi} \ln \det H\left(k + \frac{\Phi}{L}\right). \quad (\text{B.6})$$

Therefore, we have

$$\begin{aligned} \int_0^{2\pi} \frac{d\Phi}{2\pi} \partial_\Phi \ln \det H_{\text{tot}}(\Phi) &= \sum_{k=\frac{2j\pi}{L}-\pi} \int_0^{2\pi} \frac{d\Phi}{2\pi L} \partial_k \ln \det H\left(k + \frac{\Phi}{L}\right) \\ &= \sum_{j=0}^{L-1} \int_{\frac{2j\pi}{L}-\pi}^{\frac{2(j+1)\pi}{L}-\pi} \frac{d\phi}{2\pi} \partial_k \ln \det H(k + \phi) = \int_{-\pi}^{\pi} \frac{dk}{2\pi} \partial_k \ln \det H(k). \end{aligned} \quad (\text{B.7})$$

It is instructive to illustrate the equivalence between the  $k$ -based and  $\Phi$ -based winding numbers in a concrete model, such as

$$H = \sum_j (J_1 c_{j+1}^\dagger c_j + J_2 c_{j-1}^\dagger c_{j+1}) \quad (\text{B.8})$$

with  $J_1 = 1$  and  $J_2 = 2$ . According to the dispersion relation  $H(k) = J_1 e^{-ik} + J_2 e^{2ik}$ , it is easy to know that  $\det H(k)$  encircles the origin twice when  $k$  runs over the Brillouin zone, as shown in Fig. B.1(a). Note that a given  $k$  corresponds to a single eigenenergy since there is only a single band. On the other hand, for a finite ring with length  $L$  and subjected to a flux  $\Phi$ , the Hamiltonian becomes  $H_{\text{tot}}(\Phi) = \sum_j (e^{-i\frac{\Phi}{L}} J_1 c_{j+1}^\dagger c_j + e^{2i\frac{\Phi}{L}} J_2 c_{j-1}^\dagger c_{j+1})$ , where a given  $\Phi$  corresponds to  $L$  eigenenergies that form a discretized configuration of the continuous curve  $H(k)$  (see Fig. B.1(b)). When  $\Phi$  increases from 0 to  $2\pi$ , the spectrum of  $H_{\text{tot}}(\Phi)$  returns to itself and the trajectory exactly generates the energy spectrum in the thermodynamic limit in a counterclockwise manner, leading to the same winding number  $w = 2$ . It is also clear from this example that  $w$  counts the number of times the complex spectral trajectory encircles the base point at  $E_B = 0$  when the flux is increased from 0 to  $2\pi$ .

Remarkably, the generalized winding number (B.4) also allows us to have a topological understanding on the boundary-condition sensitivity of general topologically nontrivial 1D non-Hermitian lattices such as the Hatano-Nelson model. It is clear that the winding number (B.4) should either vanish or become ill-defined in an open chain, since the flux can always be gauged out and thus  $\det H(\Phi)$  is  $\Phi$  independent. Therefore, the spectrum no longer encircles any base point inside the spectrum loop under the open boundary condition. Since the spectrum should change continuously when the boundary hopping is gradually switched on, the spectrum must be very sensitive to the boundary condition.

## B.2 Topological and localization transitions

### *Spectral flow and localization*

In the previous section, our conjecture on the topological origin of the Anderson transition in the Hatano-Nelson model is based on the intuition that a fully localized system is topologically trivial. Here, we justify this statement from the viewpoint of the potential-gradient response of wave functions. For an open chain with length  $L$  and described by the Hamiltonian  $H = \sum_{j,l} J_{jl} c_j^\dagger c_l$  subject to a perturbation  $\delta H = -\frac{V}{L} \sum_j j c_j^\dagger c_j$ , starting from an eigenstate  $|\varphi_0\rangle$  of  $H$  and assuming the adiabaticity in the interacting picture, the wave function  $|\psi_t\rangle$  at time  $t$  can well be approximated by  $e^{-i\delta H t} |\varphi_t\rangle$  with  $|\varphi_t\rangle$  being the eigenstate of  $H(t) \equiv e^{i\delta H t} H e^{-i\delta H t} = \sum_{j,l} J_{jl} e^{-i\frac{Vt}{L}(j-l)} c_j^\dagger c_l$ . Note that  $|\psi_t\rangle \simeq e^{-i\delta H t} |\varphi_t\rangle$  shares almost the same real-space profile as  $|\varphi_t\rangle$ . When the system becomes a ring, with  $Vt$  replaced by  $\Phi$  in  $H(t)$ , the obtained Hamiltonian  $H(\Phi)$  is equivalent to that of a ring with a flux  $\Phi$  inside. This correspondence can be understood from the fact that a temporally changing magnetic flux induces an electromotive force. If  $|\varphi_0\rangle$  is localized, then by definition the wave function should be rigid against the induced electric field. In contrast, a delocalized state should be flexible in response to a change of  $\Phi$ , giving rise to transport phenomena. Recalling that the spectra of  $H(\Phi)$  and  $H(\Phi + 2\pi)$  coincide, we expect the complex energy of a localized (delocalized) state to stay almost unchanged (flow to another eigenvalue) when varying  $\Phi$  from 0 to  $2\pi$ . Accordingly, the spectral trajectory of  $H(\Phi)$  cannot form any loop and is topologically trivial for a fully localized system.

We illustrate the above argument for a Hatano-Nelson ring (B.1) with a complex on-site random potential and  $L = 30$ . As shown in Fig. B.2, when changing  $\Phi$  from 0 to  $2\pi$ , 8 of the 30 eigenvalues stay almost unchanged, while the rest 22 eigenvalues flow clockwise to their nearest

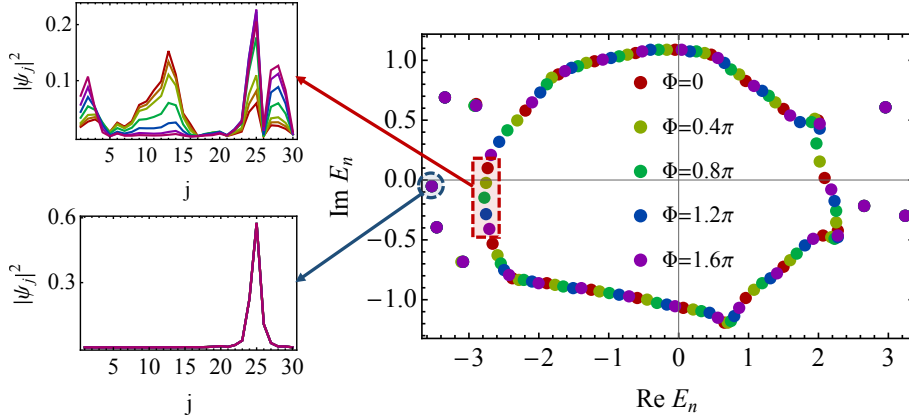


Figure B.2: Spectral flow (right) and two representative eigen wave functions (left) of a Hatano-Nelson ring with complex disorder  $W = 2.5$ ,  $L = 30$ ,  $J_L = 2$ ,  $J_R = 1$  and threaded by a varying flux  $\Phi$ . A delocalized wave function (left-upper panel) behaves flexibly, while a localized wave function (left-lower panel) exhibits rigidity. Reproduced from Fig. 12 of Ref. [44]. Copyright © 2018 by the American Physical Society.

neighbors, forming a loop. We also show the  $\Phi$ -dependence of two representative wave functions on and outside the loop. The former wave function (left-upper panel) is relatively extensive in real space and changes dramatically with respect to  $\Phi$ , while the latter one is localized and exhibits rigidity against a change in  $\Phi$ . Given a base point (e.g.,  $E_B = 0$ ) inside the loop, the spectral flow of the delocalized modes contributes to the winding number of  $w = 1$ .

### Topological Anderson transition

To study the relation between the Anderson transition and the associated topological transition, we perform an exact-diagonalization analysis of a much larger Hatano-Nelson model with  $L = 10^3$ ,  $J_R = 2$  and  $J_L = 1$  subject to the periodic boundary condition. We present the numerical results in Fig. B.3 for four different disorder strengths  $W = 1, 3, 4, 5$ . As  $W$  increases, the fraction of localized modes (indicated by the points located on the real axis in Fig. B.3(a)) increases and the mobility edges (points encircling the origin) shrink to the origin. Nevertheless, even if the fraction of delocalized modes is small, the winding number (B.4) is always quantized at  $w = -1$ . Moreover,  $\arg \det H(\Phi)$  is approximately given by  $\pi - \Phi$ , as can be seen from the following explicit expression

$$\det H(\Phi) = (-)^{L-1} (J_R^L e^{-i\Phi} + J_L^L e^{i\Phi}) + P(\{V_j\}), \quad (\text{B.9})$$

where an overwhelming majority of the random magnitudes of the polynomial  $P(\{V_j\})$ , which are independent of  $\Phi$ , should be much smaller than  $J_R^L$  before localization. With further increasing the disorder strength, an Anderson transition occurs at  $W_c \simeq 4.3$  and all the states become localized, leading to a trivial topological number.

In fact, the real parameters used in numerical calculations endows the Hatano-Nelson model with time-reversal symmetry  $T = K$  ( $K$ : complex conjugate), which makes the spectra symmetric under reflection with respect to the real axis (see Fig. B.3(a)). To demonstrate that the time-reversal symmetry is irrelevant to the winding number discussed here, we also calculate the energy spectra for complex random potentials  $V_j = |V_j|e^{i\phi_j}$ , where the magnitude  $|V_j|$  (phase  $\phi_j$ ) is randomly sampled from a uniform distribution over  $[0, W]$  ( $[0, 2\pi]$ ). Then the symmetry

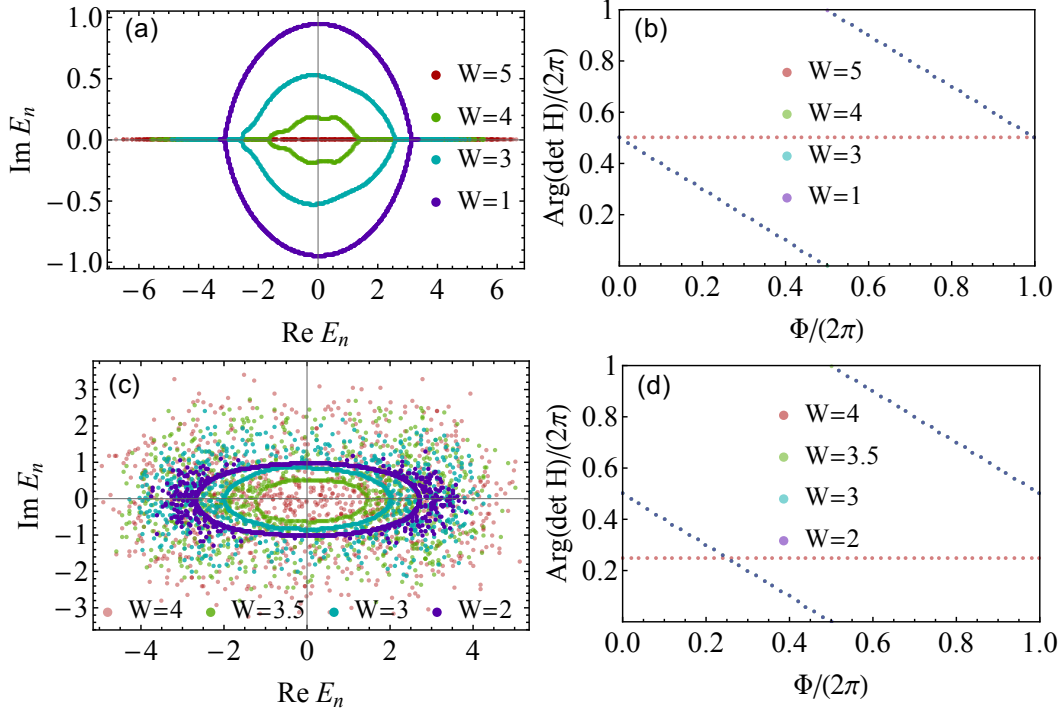


Figure B.3: (a) Complex-energy spectra and (b) flows of  $\text{Arg}(\det H)$  with respect to the flux  $\Phi$  for typical realizations of the Hatano-Nelson Hamiltonian (B.1) with  $L = 10^3$ ,  $J_R = 2$ ,  $J_L = 1$  and real on-site disorder  $V_j \in [-W, W]$ , where  $W = 1, 3, 4, 5$ . (c) and (d) correspond to (a) and (b), respectively, with the same set of parameters except for inclusion of a complex on-site disorder  $V_j = |V_j|e^{i\phi_j}$ , where  $|V_j| \in [0, W]$  with  $W = 2, 3, 3.5, 4$  and  $\phi_j \in [0, 2\pi]$ . Note that the flows of  $\text{Arg}(\det H)$  almost overlap in (b) for  $W = 1, 3, 4$  and in (d) for  $W = 2, 3, 3.5$ , and that they also overlap with each other between (b) and (d). We see that the transition occurs between  $W = 4$  and  $W = 5$  in (a) and between  $W = 3.5$  and  $W = 4$  in (c). In the nontrivial phase ( $W = 1, 3, 4$  in (a) and  $W = 2, 3, 3.5$  in (c)), the spectra encircle the base point at  $E = 0$ , giving the winding number  $w = -1$ . In the trivial phase, the data points lie on the real axis in (a) and scatter in the complex energy plane without forming a closed loop in (c). Reproduced from Fig. 14 of Ref. [44]. Copyright © 2018 by the American Physical Society.

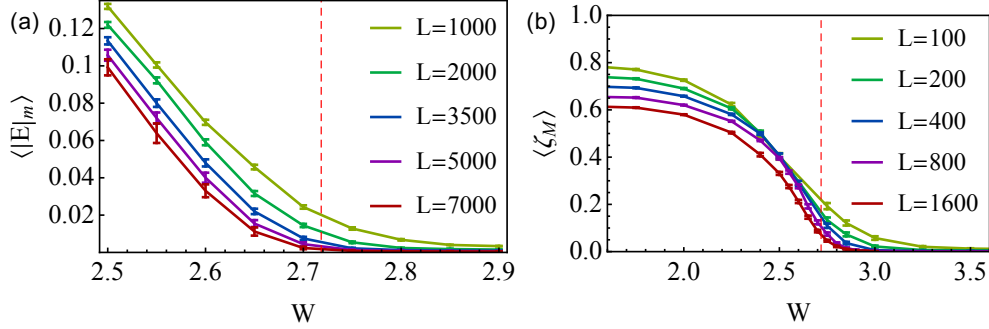


Figure B.4: (a) Disorder-averaged minimum absolute value of energy  $\langle |E|_m \rangle$  for the Hatano-Nelson model (B.1) with  $J_L = 1$ ,  $J_R = 0$ , real on-site disorder  $V_j \in [-W, W]$  and different system sizes ranging from  $L = 1000$  to  $7000$ . (b) Disorder-averaged maximum  $\zeta$  (defined in Eq. (B.11)) for the same model but with complex disorder  $V_j = |V_j|e^{i\phi_j}$ , where  $|V_j| \in [0, W]$  and  $\phi_j \in [0, 2\pi]$ , and different system sizes ranging from  $L = 100$  to  $1600$ . In both (a) and (b), the red dashed line indicates the theoretical transition point  $W_c = e = 2.718\dots$  (see the derivation below Eq. (B.10)). The number of disorder realizations ranges from thousands to hundreds, depending on the system size. The error bars denote twice the standard deviations of the mean. Reproduced from Fig. 13 of Ref. [44]. Copyright © 2018 by the American Physical Society.

with respect to the real axis is lost, yet for disorder strength  $W = 2, 3$  and  $3.5$ , we still find that the complex spectrum encircles the origin (see Fig. B.3(c)), as listed in a nontrivial winding number  $w = -1$  (see Fig. B.3(d)). When the disorder is too strong (the critical value is about  $W_c \simeq 3.9$ ), e.g., for  $W = 4$ , the winding number becomes zero. Note that  $\text{Arg}(\det H)$  in Fig. B.3(d) for  $W = 4$  does not take on special values like  $0$  or  $\pi$  unlike the Hermitian case. This is because the constant term  $P(\{V_j\})$  in Eq. (B.9) now becomes complex due to  $V_j \in \mathbb{C}$ .

As we will see in the next subsection, while the topological transition and the localization transition coincide in the above two models, this may not be the case for other forms of disorder. On the other hand, one may conjecture that the system is fully localized if and only if the winding number with respect to an arbitrary base energy vanishes, provided that the eigenvalues of robust delocalized modes always form some loops. That is to say, a topological transition is certainly not sufficient but probably necessary for a localization transition.

### Some exact results

In general, we can hardly calculate the distribution of  $P(\{V_j\})$  in Eq. (B.9) analytically. However, analytical results are available under specific choices of parameters, e.g.,  $J_L J_R = 0$  (unidirectional hopping [279]) and  $|V_j|$  obeys a uniform distribution over  $[0, W]$ . In this case,  $P(\{V_j\}) = \prod_{j=1}^L V_j$  and the distribution of  $\Xi_L \equiv -\ln(|P(\{V_j\})|/W^L) \in [0, \infty)$  can explicitly be obtained as follows. Defining  $\xi_j \equiv -\ln(|V_j|/W) \in [0, \infty)$ , we find that  $\xi_j$  obeys the standard exponential distribution, i.e.,  $\text{Prob}(\xi_j = \xi) = e^{-\xi}\theta(\xi)$ , where  $\theta(\xi)$  is the Heaviside step function. Since  $\Xi_L = \sum_{j=1}^L \xi_j$  with  $\{\xi_j\}$  being independent,  $\Xi_L$  obeys the Gamma distribution

$$\text{Prob}(\Xi_L = \Xi) = \frac{\Xi^{L-1}}{(L-1)!} e^{-\Xi}. \quad (\text{B.10})$$

For  $L \gg 1$ , we can check that  $\Xi_L/L$  approximately obeys the Gaussian distribution with mean 1 and variance  $L^{-1}$ , and thus it approaches the delta distribution at 1 in the thermodynamic limit.

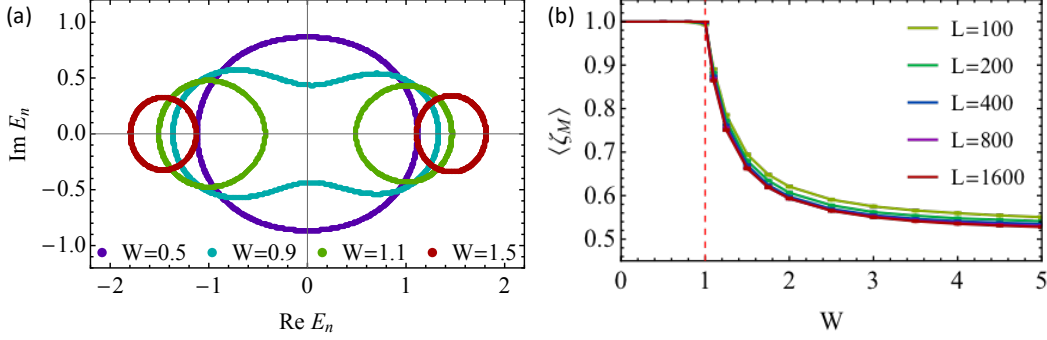


Figure B.5: (a) Complex-energy spectra of Eq. (B.1) with  $L = 10^3$ ,  $J_R = 0$ ,  $J_L = 1$  and binary on-site disorder  $V_j = \pm W$  with equal probability of occurrence for  $W$  and  $-W$ , where  $W = 0.5, 0.9, 1.1, 1.5$ . (b) Disorder-averaged maximum  $\zeta$  (see Eq. (B.11)) for the same model but with different system sizes ranging from  $L = 100$  to 1600. The red dashed line indicates the theoretical topological transition point  $W_c = 1$ . Reproduced from Fig. 14 of Ref. [44]. Copyright © 2018 by the American Physical Society.

Let us recall that the topological transition occurs at  $|P(\{V_j\})| = J^L$  with  $J \equiv \max\{|J_R|, |J_L|\}$ , or equivalently  $\Xi_L/L = -\ln(J/W)$ ; we thus obtain the critical disorder strength to be  $W_c = eJ$ . Note that this critical value does not depend on whether  $V_j$  is complex or not. However, this property should be unique to the unidirectional hopping.

In Fig. B.4, we provide numerical evidence that supports the above prediction. For real disorder, we calculate the disorder average of  $|E|_m \equiv \min\{|E| : \det(E - H) = 0, E \in \mathbb{C}\}$ , which is the minimum absolute value of the complex eigenenergies. In the thermodynamic limit, we expect a nonzero (zero)  $\langle |E|_m \rangle$  in the delocalized (localized) phase. For a finite system, as shown in Fig. B.4(a), we find a sharper and sharper crossover near  $W_c$  when increasing the system size. For complex disorder, we use the inverse participation ratio, which is defined as  $\text{IPR}(\{\rho_j\}) = \sum_{j=1}^L \rho_j^2$  for a normalized distribution  $\sum_{j=1}^L \rho_j = 1$ , where  $\rho_j \propto |\varphi_j \psi_j|$  (this quantity has been demonstrated to be a better indicator than  $|\psi_j|^2$  and  $|\varphi_j|^2$  [382]),  $\psi_j$  is a right eigen-wave function of  $H$  and  $\varphi_j$  is the corresponding left eigen-wave function. We calculate the disorder average of the maximum of a rescaled quantity

$$\zeta \equiv \frac{1}{L \times \text{IPR}(\{\rho_j\})} \in (0, 1] \quad (\text{B.11})$$

for individual realizations. In the thermodynamic limit, we have  $\zeta \neq 0$  if  $\rho_j$  decays no faster than the square-root power law and  $\zeta = 0$  otherwise, especially for an exponentially localized  $\rho_j$ . As shown in Fig. B.4(b), we find a similar crossover for  $\langle \zeta_M \rangle$  from finite to zero near  $W_c$ , and the crossover becomes sharper for larger  $L$ .

More generally, even if the analytic expression of  $\text{Prob}(\Xi_L = \Xi)$  is not available, the distribution of  $\Xi_L/L$  asymptotically approaches the Gaussian distribution with mean  $E(\xi_j)$  and variance  $\text{Var}[\xi_j]/L$  as long as the central limit theorem is applicable. For example, when  $|V_j|$  obeys the Lorentz distribution  $\text{Prob}(|V_j| = V) = \frac{2W}{\pi(V^2 + W^2)} \theta(V)$ , the rescaled variable  $\xi_j \equiv -\ln(|V_j|/W)$  obeys the hyperbolic secant distribution  $\text{Prob}(\xi_j = \xi) = (\pi \cosh \xi)^{-1}$  with mean 0 and variance  $\pi^2/4$ . Therefore, the critical disorder strength for the Lorentz distribution is  $W_c = J$ , which is consistent with that obtained by the Green's function method [279].

Finally, we provide an example which demonstrates a topological transition without a localization transition. Consider a *binary* disorder  $V_j = \pm W$  with equal probability of occurrence



for  $W$  and  $-W$  [279]. In this case,  $|P(\{V_j\})| = W^L$  in an arbitrary disorder realization, so that the critical disorder strength for the topological transition is  $W_c = J$ . On the other hand, the winding number with respect to  $E_B = \pm W$  is always one in the thermodynamic limit, no matter how large  $W$  is. This implies that there are always some delocalized modes and the system never undergoes a localization transition. Nevertheless, there is indeed a qualitative change in the spectrum when  $W$  exceeds  $W_c$  — a single loop splits into two loops (see Fig. B.5(a)). As shown in Fig. B.5(b), such a transition is accompanied by the onset of the deviation of  $\zeta_M$  from one.

## Appendix C

# Proof of the bulk-edge correspondence

In this appendix, we prove the bulk-edge correspondence between the winding number (4.7) and the number of (quasi-)edge modes for a general single-band lattice with finite-range hopping amplitudes  $\{J_j\}$ . By finite-range hopping, we mean that the hopping towards the right (left) direction is at most  $p$ -site ( $q$ -site) with  $p$  ( $q$ ) being a finite integer. Hence, with  $e^{ik}$  denoted as  $z$ , the dispersion relation, or the characteristic equation of the Schrödinger equation, can be written as

$$E = f(z) = \sum_{j=-p}^q J_j z^j, \quad (\text{C.1})$$

where  $J_{-p}$  and  $J_q$  are nonzero. Assuming that the winding number  $w$  is non-negative, we impose the right semi-infinite condition, so that the general solution of an edge state takes the form

$$\psi_j = \sum_{l=1}^S \sum_{m=1}^{n_l} c_{l,m} \frac{d^{m-1}}{dz^{m-1}} z^j \Big|_{z=z_l}, \quad (\text{C.2})$$

where  $z_l$  ( $l = 1, 2, \dots, S$ ) is the  $n_l$ th-order zero of  $f(z) = 0$  given in Eq. (C.1) and inside of the unit circle  $|z| = 1$ , i.e.,  $|z_l| < 1$ . Using the argument principle (4.21) and the assumption  $w \geq 0$ , we have  $\sum_{l=1}^S n_l = Z = p + w \geq p$ , with  $p$  being the effective number of poles for  $|z| < 1$ . Indeed, there is a single  $p$ th-order pole at  $z = 0$ , implying  $z_l \neq 0$  for all  $l = 1, 2, \dots, S$ . The initial condition reads

$$\psi_0 = \psi_{-1} = \dots = \psi_{-p+1} = 0, \quad (\text{C.3})$$

which, together with Eq. (C.2), leads to a set of homogeneous linear equations

$$M\mathbf{c} = \mathbf{0}, \quad (\text{C.4})$$

where the elements of the generalized Vandermonde matrix [384]  $M = [M_{uv}]_{p \times Z}$  and the coefficient vector  $\mathbf{c} = (c_1, c_2, \dots, c_Z)^T$  are given by

$$M_{j,\sigma(l,m)} = \frac{d^{m-1}}{dz^{m-1}} z^{-j+1} \Big|_{z=z_l}, \quad c_{\sigma(l,m)} = c_{l,m}, \quad (\text{C.5})$$

with  $\sigma(l,m) \equiv \sum_{r=1}^{l-1} n_r + m$ ,  $1 \leq l \leq S$  and  $1 \leq m \leq n_l$ . To see how many degrees of freedom survive under the condition imposed by Eq. (C.4), we have to determine the rank of  $M$ , which

equals that of  $M^T$ . Suppose that the rank of  $M^T$  does not saturate the maximum  $p$ ; then there must exist a nonzero vector  $\mathbf{a} = (a_1, a_2, \dots, a_p)^T$  that satisfies

$$M^T \mathbf{a} = \mathbf{0}. \quad (\text{C.6})$$

Defining a polynomial  $g(z) \equiv \sum_{j=1}^p a_j z^{j-1}$  with  $0 < \deg g(z) \leq p-1$  due to the fundamental theorem of algebra, Eq. (C.6) can be explicitly written down as

$$\left. \frac{d^{m-1}}{dz^{m-1}} g(z^{-1}) \right|_{z=z_l} = 0, \quad (\text{C.7})$$

implying that  $g(z)$  contains a polynomial factor  $\prod_{l=1}^S (z - z_l^{-1})^{n_l}$  and thus  $\deg g(z) \geq \sum_{l=1}^S n_l = Z$ . Recalling that  $Z \geq p$ ,  $\deg g(z) \geq Z$  contradicts  $\deg g(z) \leq p-1$ , we find that the original assumption that  $\text{rank}(M^T) < p$  must be wrong. In other words, both the rank of  $M^T$  and that of  $M$  saturate the maximum  $p$ . Therefore, the number of independent  $\{c_j\}$  satisfying Eq. (C.4), or the degeneracy of zero modes localized at the left edge, turns out to be  $Z - p = w$ . As an example with two-fold degeneracy, we can examine the model given in Eq. (B.8) and check that

$$\begin{aligned} \psi_j^{(1)} &= (-)^j \sqrt{\frac{1}{3}(1 + \beta + \beta^2)\beta^{j-1}} (1 - e^{\frac{2\pi i}{3}j}) \quad \text{and} \\ \psi_j^{(2)} &= \frac{(-)^j}{3} \sqrt{\frac{(1 - \beta^3)\beta^{j-2}}{1 + \beta}} [1 + \beta e^{\frac{2\pi i}{3}} + (\beta + e^{\frac{2\pi i}{3}})e^{\frac{2\pi i}{3}j} + (\beta + 1)e^{-\frac{2\pi i}{3}(j+1)}] \end{aligned} \quad (\text{C.8})$$

span the zero-mode space, where  $\beta = (\frac{J_1}{J_2})^{\frac{2}{3}}$ .

We move on to the case of  $w < 0$ . If we use the same boundary condition as above, we will again obtain Eq. (C.4), but there are more rows than columns in  $M$  since  $p = Z - w > Z$ . We can thus pick out the first  $Z$  rows of  $M$  to construct a square matrix  $\tilde{M}$ , such that

$$\tilde{M} \mathbf{c} = \mathbf{0} \quad (\text{C.9})$$

is necessarily satisfied. Straightforward calculations give

$$\det \tilde{M} = C \prod_{1 \leq r < s \leq l} (z_s^{-1} - z_r^{-1})^{n_r n_s} \neq 0, \quad (\text{C.10})$$

where the factor  $C = \prod_{l=1}^S (-)^{n_l-1} z_l^{-n_l(n_l-1)} \prod_{m=1}^{n_l} (m-1)!$ . Therefore, as a necessary condition of Eq. (C.4), Eq. (C.9) is sufficient to enforce  $\mathbf{c}$  to be  $\mathbf{0}$ , implying no edge modes localized at the left boundary. On the other hand, if we change the boundary condition to be left semi-infinite, we have

$$\psi_{-j} = \sum_{l=1}^R \sum_{n=1}^{m_l} c_{l,n} \left. \frac{d^{n-1}}{dz^{n-1}} z^{-j} \right|_{z=\zeta_l}, \quad (\text{C.11})$$

where  $\zeta_l$  ( $l = 1, 2, \dots, R$ ) is the  $m_l$ th zero of  $f(z)$  outside  $|z| = 1$ . Recalling that  $z^p f(z)$  is a polynomial with degree  $p + q$ , we have  $Z' \equiv \sum_{l=1}^R m_l = p + q - Z = q - w$ . This result is consistent with directly applying the argument principle to  $f(z^{-1})$ , which has a single  $q$ th-order pole  $z = 0$  inside the circle of  $|z| = 1$ , leading to

$$\oint_{|z|=1} \frac{dz}{2\pi i} \frac{\frac{d}{dz} f(z^{-1})}{f(z^{-1})} = Z' - q. \quad (\text{C.12})$$

Here we have used the fact that  $\zeta_l^{-1}$ 's are the zeros of  $f(z^{-1})$  inside the unit circle  $|z| = 1$ . Noting that the left-hand side in Eq. (C.12) can be shown to be the minus of that in Eq. (4.21) via a change of the integration variable, we obtain  $Z' = q - w$ . The initial condition

$$\psi_0 = \psi_1 = \dots = \psi_{q-1} = 0 \quad (\text{C.13})$$

can again be written in the form of Eq. (C.4), but the elements of the generalized Vandermonde matrix  $M = [M_{\mu\nu}]_{q \times Z'}$  and the coefficient vector  $\mathbf{c} = (c_1, c_2, \dots, c_{Z'})^T$  become

$$M_{j,\mu(l,n)} = \frac{d^{n-1}}{dz^{n-1}} z^{j-1} \Big|_{z=\zeta_l}, \quad c_{\mu(l,n)} = c_{l,n}, \quad (\text{C.14})$$

where  $\mu(l,n) \equiv \sum_{r=1}^{l-1} m_r + n$ ,  $1 \leq l \leq R$  and  $1 \leq n \leq m_r$ . Using the same technique as in the previous paragraph, we can prove that  $M$  takes the maximum rank  $q$ , so that the number of independent degrees of freedom, or the degeneracy of the zero modes localized at the right boundary, turns out to be  $Z' - q = -w$ .

As an application of the bulk-edge correspondence for non-Hermitian Hamiltonians, we can demonstrate the bulk-edge correspondence in Hermitian systems with a chiral symmetry (class AIII), whose Hamiltonian is given by Eq. (4.22). Such a Hamiltonian can be unitarily transformed into  $\sigma_x \otimes \sqrt{H^\dagger H}$ , so that the full spectrum reads  $\{\pm E_1, \pm E_2, \dots\}$ , with  $\{E_1, E_2, \dots\}$  being the eigenvalues of  $\sqrt{H^\dagger H}$ , which is semi-positive-definite. Therefore the statement that there are  $2|w|$  zero modes of Eq. (4.22) is equivalent to the fact that there are  $|w|$  zero modes of  $\sqrt{H^\dagger H}$ . We have already known that  $|w|$  gives the number of edge states of  $H$  at  $E = 0$  in a semi-infinite space, but it generally does not for an open chain. However, it gives the number of quasi-eigenstates at  $E = 0$ , which almost vanish after being acted on by  $H$ . Using this property, we can show that  $|w|$  does give the number of zero modes for the Hermitian operator  $\sqrt{H^\dagger H}$ .

To this end, we first prove the following lemma:

**Lemma 6** *Given  $D$  different wave functions  $|\psi_n\rangle$  ( $n = 1, 2, \dots, D$ ) satisfying  $\|H|\psi_n\rangle\| < \epsilon_1$  and  $|\langle\psi_m|\psi_n\rangle| < \epsilon_2 \ll D^{-1}$  for all  $m \neq n$ , there must be at least  $D$  different eigenstates of  $\sqrt{H^\dagger H}$  with energies less than  $E_b = D\epsilon_1/\sqrt{1 - (D-1)\epsilon_2}$ .*

*Proof:* We note that  $\{|\psi_n\rangle\}$  are linearly independent. Otherwise, we can find  $\{c_j\}_{j=1}^D$  such that  $\max_{1 \leq j \leq D} |c_j| = |c_{j_0}| > 0$  and  $\sum_{j=1}^D c_j |\psi_j\rangle = 0$ , leading to the contradiction

$$|c_{j_0}| = |c_{j_0} \langle\psi_{j_0}|\psi_{j_0}\rangle| = \left| \sum_{j \neq j_0} c_j \langle\psi_{j_0}|\psi_j\rangle \right| \leq \sum_{j \neq j_0} |c_j| |\langle\psi_{j_0}|\psi_j\rangle| < \epsilon_2 (D-1) |c_{j_0}| \ll |c_{j_0}|. \quad (\text{C.15})$$

Therefore, denoting  $V_0 \equiv \text{span}\{|\psi_j\rangle : j = 1, 2, \dots, D\}$ , we have  $\dim V_0 = D$ . For an arbitrary  $|\psi\rangle \in V_0$ , which can always be expressed as  $|\psi\rangle = \sum_{j=1}^D c_j |\psi_j\rangle / \|\sum_{j=1}^D c_j |\psi_j\rangle\|$ , we can bound  $\|H|\psi\rangle\|$  from above as

$$\begin{aligned} \|H|\psi\rangle\| &\leq \frac{\sum_{j=1}^D |c_j| \|H|\psi_j\rangle\|}{\|\sum_{j=1}^D c_j |\psi_j\rangle\|} < \frac{\epsilon_1 \sum_{j=1}^D |c_j|}{\sqrt{\sum_{j=1}^D |c_j|^2 - \sum_{m \neq n} c_m^* c_n \langle\psi_m|\psi_n\rangle}} \\ &< \frac{\epsilon_1}{\sqrt{1 - (D-1)\epsilon_2}} \frac{\sum_{j=1}^D |c_j|}{\sqrt{\sum_{j=1}^D |c_j|^2}} \leq \frac{\sqrt{D}\epsilon_1}{\sqrt{1 - (D-1)\epsilon_2}} = \frac{E_b}{\sqrt{D}}. \end{aligned} \quad (\text{C.16})$$

Consequently, we have

$$\text{Tr}_{V_0}[H^\dagger H] < E_b^2, \quad (\text{C.17})$$

where  $\text{Tr}_{V_0}[\dots]$  denotes the trace over the subspace  $V_0$ . Denoting  $P_g$  as the projector onto the Hilbert subspace  $V_g$  spanned by all the eigenstates of  $\sqrt{H^\dagger H}$  with energies less than  $E_b$ , we can construct  $H' \equiv E_b^2(1 - P_g) \leq H^\dagger H$ , leading to

$$\text{Tr}_{V_0}[H'] = E_b^2(D - \text{Tr}_{V_0}[P_g]) < E_b^2 \quad \Leftrightarrow \quad \text{Tr}_{V_0}[P_g] = \text{Tr}_{V_g}[P_0] > D - 1, \quad (\text{C.18})$$

where  $P_0$  is the projector onto  $V_0$ . Since  $\text{Tr}_{V_g}[P_0] \leq \text{Tr}_{V_g}[1] = \dim V_g$ , which should be an integer, we finally obtain  $\dim V_g \geq D$ .  $\square$

Now let us come back to the eigenvalue problem of  $\sqrt{H^\dagger H}$  for an open chain with length  $L$ . We can first work in the semi-infinite limit to determine a set of orthonormal zero modes  $\{|\phi_j\rangle\}_{j=1}^{|w|}$  of  $H$ , and then truncate and normalize them on a finite chain, obtaining  $|\psi_j\rangle$ 's. Note that  $|\psi_j\rangle$ 's are now not exact eigenstates of  $H$ , but the conditions of the theorem proved above are satisfied, with  $\epsilon_1$  and  $\epsilon_2$  exponentially small in  $L$ , since the deviations stem from the exponential tail. According to the theorem, we can find at least  $|w|$  eigenstates with exponentially small energies. We should furthermore mention the impossibility to find the  $(|w| + 1)$ th eigenstate with a small energy that eventually vanishes in the thermodynamic limit; otherwise we would have at least  $|w| + 1$  zero modes of  $H$  in a semi-infinite space, leading to a contradiction.

It is worthwhile to mention that the bulk-edge correspondence for class AIII (or BDI) alone can alternatively be proved using the Callias index theorem [385] according to Ref. [189]. However, it seems rather nontrivial whether a similar method can be applied to a single off-diagonal block in a class AIII Hamiltonian.

# Appendix D

## Calculating the entanglement-spectrum dynamics

In this appendix, we provide the details on how we numerically obtain the ES dynamics shown in Figs. 5.4 and 5.5 in Chapter 5. We also provide some analytical results on the ES dynamics in the Rice-Mele model after a flat-band quench.

### D.1 Numerical method for general noninteracting systems

We follow the method proposed in Ref. [348] to numerically calculate the single-particle ES. The basic idea is that in a particle-number-conserving free-fermion system described by a quadratic Hamiltonian in terms of  $c_j$  ( $j = 1, 2, \dots, N$ ), any reduced density operator  $\rho_S$  of the ground state  $|\Psi\rangle$ , which consists of the modes  $c_j$  with  $j \in S \subset \{1, 2, \dots, N\}$ , is a Gaussian state

$$\rho_S \propto e^{-\sum_{m,n \in S} (h_E)_{mn} c_m^\dagger c_n} \equiv e^{-H_E}, \quad (\text{D.1})$$

which can be reconstructed from its  $|S| \times |S|$  correlation matrix (where  $|S|$  denotes the cardinality of  $S$ )

$$C_{mn} \equiv \text{Tr}[c_m^\dagger c_n \rho_S] = \langle \Psi | c_m^\dagger c_n | \Psi \rangle, \quad m, n \in S \quad (\text{D.2})$$

via

$$C = \frac{1}{e^{h_E} + 1}. \quad (\text{D.3})$$

Therefore, the eigenvalues of  $C$  simply gives the single-particle ES [349]

$$\xi_n \equiv \frac{1}{e^{\epsilon_n} + 1}, \quad (\text{D.4})$$

where  $\{\epsilon_n\}$  are the eigenvalues of  $H_E$  or  $h_E$ .

In particular, for a 1D lattice system with  $L$  unit cells and subjected to the periodic boundary condition, we can utilize the translational invariance to represent the many-body wave function in a factorized form:

$$|\Psi\rangle = \prod_k \mathbf{c}_k^\dagger \mathbf{u}(k) |\text{vac}\rangle, \quad (\text{D.5})$$

where  $\mathbf{u}(k)$  is the Bloch vector and  $\mathbf{c}_k^\dagger \mathbf{u}(k) = \sum_a u_a(k) c_{ka}^\dagger$  with  $a$  being an internal degrees of freedom. In this case, the correlation matrix (D.2) turns out to be a block-Toeplitz matrix:

$$C_{ja,j'a'} \equiv \langle \Psi | c_{ja}^\dagger c_{j'a'} | \Psi \rangle = \frac{1}{L} \sum_k u_a^*(k) u_{a'}(k) e^{ik(j-j')} = C_{j-j'}^{aa'}, \quad (\text{D.6})$$

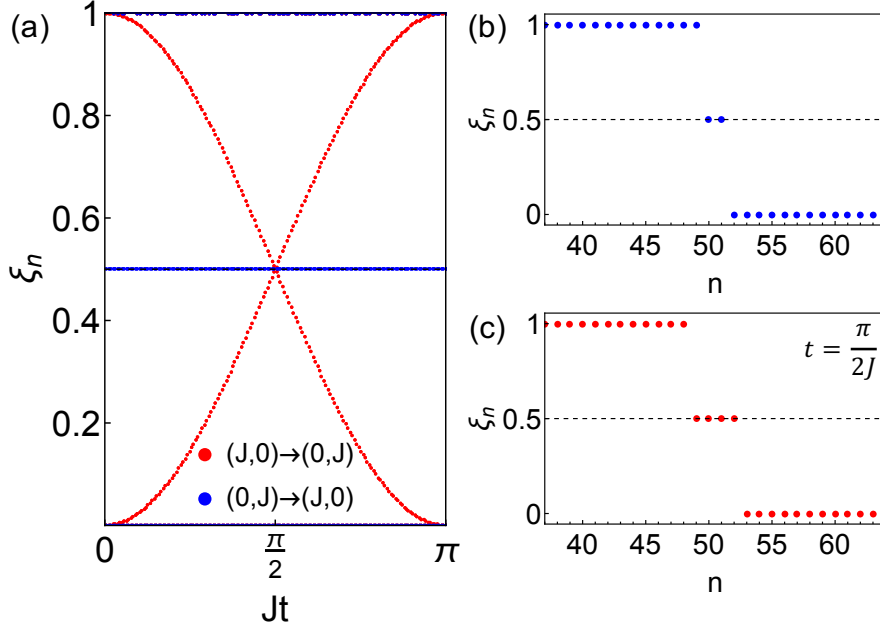


Figure D.1: (a) ES dynamics after the quenches  $(J_1, J_2) = (0, J) \rightarrow (J, 0)$  (blue) and  $(J, 0) \rightarrow (0, J)$  (red) in the SSH model. (b) In the former case, the dynamics is trivial and two degenerate entanglement edge modes at  $\xi_n = 1/2$  persist. (c) In the latter case, the dynamics is nontrivial, and the instantaneous four-fold degeneracy at  $\xi_n = 1/2$  emerges at  $t = \pi/(2J)$ . Reproduced from Supplementary Fig. 4 of Ref. [46]. Copyright © 2018 by the American Physical Society.

where  $m, n$  are the site indices. To calculate the inter-unit-cell half-chain ES, we only have to figure out the eigenvalues of the  $(LD/2) \times (LD/2)$  matrix  $C_{ja, j'a'}$  (D.6), where  $D$  is the total number of internal degrees of freedom.

In a superlattice system,  $D = 2$  and  $a$  labels the sublattices. By calculating first the dynamics of the Bloch vectors governed by Eq. (5.58) and then the correlation matrix (D.6) followed by exact diagonalization, we can obtain the dynamics of the full single-particle ES. As a benchmark, we plot in Fig. D.1(a) the ES dynamics for the quench  $(J_1, J_2) = (0, J) \rightarrow (J, 0)$  in the SSH model, after which no entanglement is generated for the entanglement cut shown in Fig. 5.4(b) in Chapter 5 so that the ES should stay unchanged. Since the initial state is topologically nontrivial ( $\mathcal{N} = 2$ ), we find two degenerate entanglement edge modes at  $\xi_n = 1/2$ , as shown in Fig. D.1(b). This is to be compared with the ES dynamics for the quench  $(J, 0) \rightarrow (0, J)$ , after which we find nontrivial dynamics and instantaneous *four*-fold degeneracy at  $\xi_n = 1/2$  at  $t = \pi/(2J)$  (see Fig. D.1(c)).

According to the notion of SPT phases, we expect that the ES crossings may disappear if the PHS is explicitly broken, for example, by adding a staggered potential  $\sum_j \Delta(b_j^\dagger b_j - a_j^\dagger a_j)$  in the SSH Hamiltonian; then the model becomes the Rice-Mele model [386] (see Fig. D.2(a)):

$$H_{\text{RM}} = - \sum_j (J_1 b_j^\dagger a_j + J_2 a_{j+1}^\dagger b_j + \text{H.c.}) + \sum_j \Delta (b_j^\dagger b_j - a_j^\dagger a_j). \quad (\text{D.7})$$

This is confirmed numerically in the flat-band case, as shown in Fig. D.2(b). An interesting observation is that the gap is as small as  $\mathcal{O}(\Delta^3/J^3)$ , as will be explained in the next section. Note that the dynamical Chern number (5.61) is no longer well-defined (quantized) in this case.

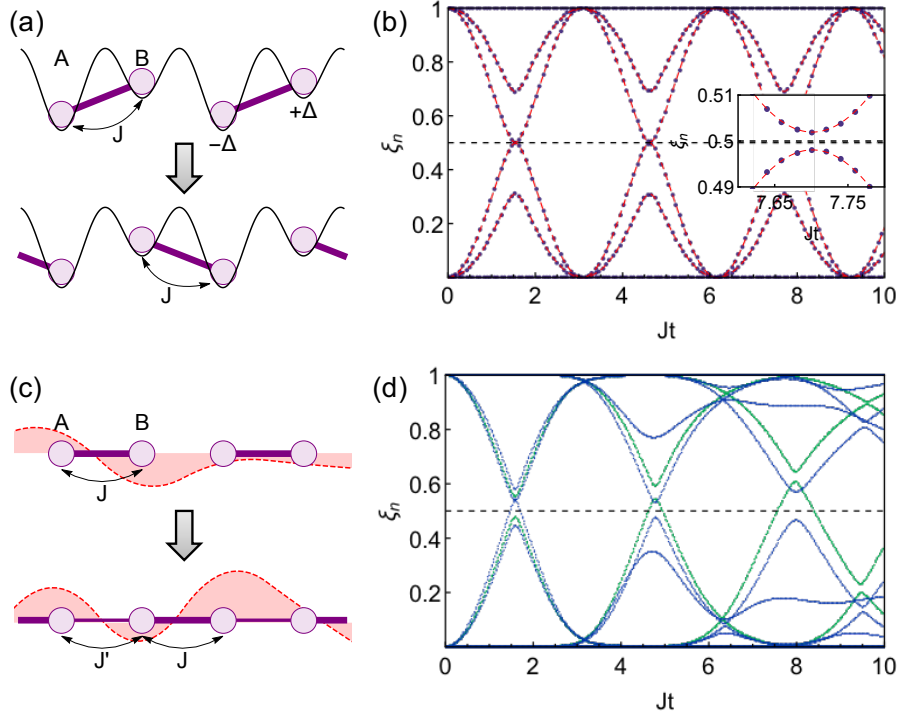


Figure D.2: (a) Quench in the flat-band Rice-Mele model (D.7) with  $\Delta = 0.2J$  and (b) the corresponding ES dynamics. The dots and dashed curves show the numerical and analytical results, respectively. The inset shows the enlarged view around  $Jt = 7.7$ , showing that the two-fold degeneracy is lifted, and crossings are gapped out, although the gap is very small (see inset). (c) Quench from a dimerized state with a random on-site potential  $V_j^{a,b}$  shown schematically by a dashed curve (see Eq. (D.8)). Here  $W = J' = 0.2J$ . (d) The corresponding ES dynamics, which no longer exhibit crossings at  $\xi_n = 1/2$  with (green) and without (blue) inversion symmetry. When  $V_j$  respects the inversion symmetry, the ES is two-fold degenerate. Reproduced from Supplementary Fig. 5 of Ref. [46]. Copyright © 2018 by the American Physical Society.



We also calculate the ES dynamics in the SSH model with a random on-site potential:

$$H_{\text{RSSH}} = - \sum_j (J_1 b_j^\dagger a_j + J_2 a_{j+1}^\dagger b_j + \text{H.c.}) + \sum_j (V_j^a a_j^\dagger a_j + V_j^b b_j^\dagger b_j), \quad (\text{D.8})$$

where  $V_j^a$  and  $V_j^b$  are randomly sampled from a uniform distribution over  $[-W, W]$ . We consider the ES dynamics after a quench that changes both the disorder configuration and the following parameters (see Fig. D.2(c)):

$$(J_1, J_2, \Delta) = (J, 0, \Delta) \rightarrow (J', J, 0). \quad (\text{D.9})$$

As shown in Fig. D.2(d), we find that ES crossings at  $\xi_n = 1/2$  disappear, even if the disorder respects the inversion symmetry, i.e.,  $V_j^a = V_{(\frac{L}{2}-j) \bmod L+1}^b$ . In contrast, we have seen in Fig. 5.6 that the ES crossings are robust against disorder in hopping amplitudes, which preserves the PHS (and also the TRS).

## D.2 Analytical results for some flat-band quenches

Since the entanglement cut is made in real space, a straightforward way to read out the ES is to represent the real-space many-body wave function in the form of MPS [132, 153]. To do this, we should first translate the picture of a 1D fermionic superlattice into that of a spin chain via the Jordan-Wigner transformation:<sup>1</sup>

$$a_j = e^{-i\frac{\pi}{2} \sum_{i=1}^{2j-2} (\sigma_i^z + 1)} \sigma_{2j-1}^-, \quad b_j = e^{-i\frac{\pi}{2} \sum_{i=1}^{2j-1} (\sigma_i^z + 1)} \sigma_{2j}^-. \quad (\text{D.10})$$

For example, the Rice-Mele Hamiltonian (D.7) in the spin representation becomes

$$H_{\text{RM}} = - \sum_j (J_1 \sigma_{2j}^+ \sigma_{2j-1}^- + J_2 \sigma_{2j+1}^+ \sigma_{2j}^- + \text{H.c.}) - \sum_j \frac{\Delta}{2} (\sigma_{2j-1}^z - \sigma_{2j}^z), \quad (\text{D.11})$$

which describes a spin chain with anisotropic spin-flip coupling and subjected to a staggered magnetic field in the  $z$  direction. Here we have used the identity  $e^{-i\frac{\pi}{2} (\sigma_j^z + 1)} \sigma_j^- = \sigma_j^-$ , since the state of the  $j$ th site must be  $|\downarrow\rangle$  or vanish after the operation  $\sigma_j^-$ . In the specific case  $(J_1, J_2, \Delta) = (J_0, 0, \Delta_0)$ , the ground state is asymmetrically dimerized:

$$|\Psi\rangle = \bigotimes_{j=1}^L \left( \cos \frac{\theta_0}{2} |\uparrow_{2j-1} \downarrow_{2j}\rangle + \sin \frac{\theta_0}{2} |\downarrow_{2j-1} \uparrow_{2j}\rangle \right), \quad (\text{D.12})$$

where  $\theta_0 \in (0, \pi)$  is determined from  $\Delta_0 = J_0 \cot \theta_0$ . Equation (D.12) can be rewritten into the following MPS form (see Fig. D.3(a)):

$$|\Psi\rangle = \sum_{\{s_j\}} \text{Tr}[\Gamma_{s_1}^A \Lambda^A \Gamma_{s_2}^B \Lambda^B \dots \Gamma_{s_{2L}}^B \Lambda^B] |s_1 s_2 \dots s_{2L}\rangle, \quad (\text{D.13})$$

where the sum runs over all the possible spin configurations  $s_j = \uparrow, \downarrow$  ( $j = 1, 2, \dots, 2L$ ) and

$$\Lambda^A = \begin{bmatrix} \cos \frac{\theta_0}{2} & 0 \\ 0 & \sin \frac{\theta_0}{2} \end{bmatrix}, \quad \Lambda^B = [1], \quad \Gamma_{\uparrow}^B = \begin{bmatrix} 0 \\ 1 \end{bmatrix}, \quad \Gamma_{\downarrow}^B = \begin{bmatrix} 1 \\ 0 \end{bmatrix}, \quad \Gamma_{\uparrow}^A = [1 \quad 0], \quad \Gamma_{\downarrow}^A = [0 \quad 1]. \quad (\text{D.14})$$

<sup>1</sup>In fact, it is also possible to directly use the fermionic MPS [387]. However, the Jordan-Wigner transformed spin picture is more convenient for practical numerical calculations.

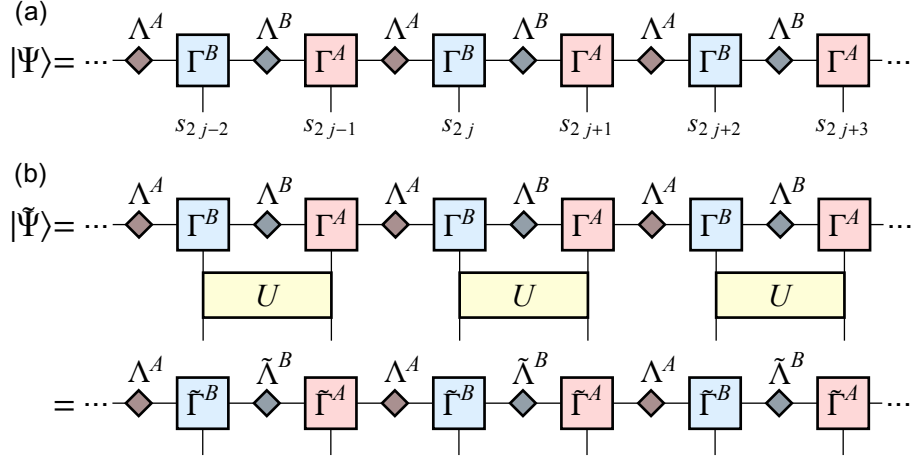


Figure D.3: (a) MPS representation of a 1D superlattice system in the spin language. (b) After a factorized unitary evolution  $U = \bigotimes_j U_j$  with translational invariance ( $\langle s_{2j} s_{2j+1} | U_j | s'_{2j} s'_{2j+1} \rangle = U_{s'_{2j} s'_{2j+1}}^{s_{2j} s_{2j+1}}$  for  $\forall j$ , where  $s, s' \in \{\uparrow, \downarrow\}$ ),  $|\tilde{\Psi}\rangle = U|\Psi\rangle$  has a different (the same) ES encoded in  $\tilde{\Lambda}^B$  ( $\Lambda^A$ ) for the intra-unit-cell (inter-unit-cell) entanglement cut. Reproduced from Supplementary Fig. 6 of Ref. [46]. Copyright © 2018 by the American Physical Society.

After the quench of the Hamiltonian, we can numerically calculate the MPS form of  $|\Psi(t)\rangle = e^{-iH't}|\Psi\rangle$  by using, e.g., the iTEBD algorithm [153] if we work in the thermodynamic limit. However, if the time-evolution operator is factorized as

$$U = \bigotimes_j U_j, \quad (\text{D.15})$$

with  $U_j$  only acting on the spins at the  $2j$ th and the  $(2j+1)$ th sites (see Fig. D.3(b)), it is possible to analytically obtain the MPS form of  $|\tilde{\Psi}\rangle = U|\Psi\rangle$ :

$$|\tilde{\Psi}\rangle = \sum_{\{s_j\}} \text{Tr}[\tilde{\Gamma}_{s_1}^A \Lambda^A \tilde{\Gamma}_{s_2}^B \tilde{\Lambda}^B \tilde{\Gamma}_{s_{2L}}^B \tilde{\Lambda}^B] |s_1 s_2 \dots s_{2L}\rangle, \quad (\text{D.16})$$

where the matrix ingredients  $\tilde{\Gamma}^{A,B}$  and  $\tilde{\Lambda}^B$  are related to those in Eq. (D.13) via [153]

$$\Lambda^A \tilde{\Gamma}_{s_1}^B \tilde{\Lambda}^B \tilde{\Gamma}_{s_2}^A \Lambda^A = U_{s'_1 s'_2}^{s_1 s_2} \Lambda^A \Gamma_{s'_1}^B \Lambda^B \Gamma_{s'_2}^A \Lambda^A, \quad (\text{D.17})$$

where  $U_{s'_1 s'_2}^{s_1 s_2}$  is the matrix element of a single block  $U_j$ . If we are only interested in the inter-unit-cell ES, it suffices to find the singular values of the left-hand side of Eq. (D.17), i.e.,

$$\begin{bmatrix} \Lambda^A \tilde{\Gamma}_{\uparrow}^B \tilde{\Lambda}^B \tilde{\Gamma}_{\uparrow}^A \Lambda^A & \Lambda^A \tilde{\Gamma}_{\downarrow}^B \tilde{\Lambda}^B \tilde{\Gamma}_{\uparrow}^A \Lambda^A \\ \Lambda^A \tilde{\Gamma}_{\downarrow}^B \tilde{\Lambda}^B \tilde{\Gamma}_{\uparrow}^A \Lambda^A & \Lambda^A \tilde{\Gamma}_{\downarrow}^B \tilde{\Lambda}^B \tilde{\Gamma}_{\downarrow}^A \Lambda^A \end{bmatrix}. \quad (\text{D.18})$$

Equation (D.15) is satisfied for a general *flat-band* quench in the Rice-Mele model:

$$(J_1, J_2, \Delta) = (J_0, 0, \Delta_0) \rightarrow (0, J, \Delta), \quad (\text{D.19})$$

which implies

$$\begin{aligned} U_{\downarrow\downarrow}^{\downarrow\downarrow} &= U_{\uparrow\uparrow}^{\uparrow\uparrow} = \phi, & U_{\downarrow\uparrow}^{\uparrow\downarrow} &= U_{\uparrow\downarrow}^{\downarrow\uparrow} = i \sin \theta \sin \phi, \\ U_{\uparrow\downarrow}^{\uparrow\downarrow} &= \cos \phi + i \cos \theta \sin \phi, & U_{\downarrow\uparrow}^{\downarrow\uparrow} &= \cos \phi - i \cos \theta \sin \phi, \end{aligned} \quad (\text{D.20})$$

where  $\phi = \sqrt{J^2 + \Delta^2}t$  and  $\theta \in (0, \pi)$  is defined from  $\Delta = J \cot \theta$ . Combining Eqs. (D.20) and (D.14), we can explicitly compute the matrix elements in Eq. (D.18) to obtain

$$\begin{bmatrix} 0 & 0 & i \cos^2 \frac{\theta_0}{2} \sin \theta \sin \phi & 0 \\ \sin \frac{\theta_0}{2} \cos \frac{\theta_0}{2} & 0 & 0 & \sin^2 \frac{\theta_0}{2} (\cos \phi + i \cos \theta \sin \phi) \\ \cos^2 \frac{\theta_0}{2} (\cos \phi - i \cos \theta \sin \phi) & 0 & 0 & \sin \frac{\theta_0}{2} \cos \frac{\theta_0}{2} \\ 0 & i \sin^2 \frac{\theta_0}{2} \sin \theta \sin \phi & 0 & 0 \end{bmatrix}. \quad (\text{D.21})$$

The four singular values of the above matrix (D.21) are found to be

$$\frac{1}{2} \left( \sqrt{1 - \sin^2 \theta \cos^2 \theta_0 \sin^2 \phi} \pm \sqrt{1 - \sin^2 \theta \sin^2 \phi} \right), \quad \frac{1}{2} \sin \theta (1 \pm \cos \theta_0) |\sin \phi|, \quad (\text{D.22})$$

which constitute the eigenvalues of  $\tilde{\Lambda}_B$ . The single-particle ES can subsequently be determined from Eq. (D.22) via the relation between many-body ES and single-particle ES [205]:

$$\lambda_{s=\{s_n\}} = \prod_n \left[ \frac{1}{2} + s_n \left( \xi_n - \frac{1}{2} \right) \right], \quad s_n = \pm 1. \quad (\text{D.23})$$

The result turns out to be

$$\xi_n = \frac{1}{2} \left[ 1 \pm \cos \theta_0 \sin^2 \theta \sin^2 \phi \pm \sqrt{(1 - \sin^2 \theta \sin^2 \phi)(1 - \cos^2 \theta_0 \sin^2 \theta \sin^2 \phi)} \right]. \quad (\text{D.24})$$

Finally, let us discuss a specific case in which  $\theta = \theta_0$ , namely the quench shown in Fig. D.2(a). In this case, the single-particle-ES gap reaches its minimum at  $\phi = \pi/2$ . Substituting  $\theta = \theta_0$  and  $\phi = \pi/2$  into Eq. (D.24), we obtain

$$\xi_n = \frac{1}{2} \left[ 1 \pm \cos \theta \left( \sin^2 \theta \pm \sqrt{1 - \cos^2 \theta \sin^2 \theta} \right) \right], \quad (\text{D.25})$$

which implies a tiny gap

$$\delta \xi = \frac{1}{2} \cos^3 \theta (1 + \cos^2 \theta) \simeq \frac{\Delta^3}{2J^3} \quad (\text{D.26})$$

for a small  $\Delta$ . This is consistent with the small gap found in the inset of Fig. D.2(b). If we further set  $\theta = \theta_0 = \frac{\pi}{2}$ , Eq. (D.24) becomes

$$\xi_n = \frac{1}{2} [1 \pm \cos(Jt)], \quad (\text{D.27})$$

which reproduces the sinusoidal oscillation observed in Fig. 5.4(c) (red curve) in Chapter 5.

# Acknowledgements

First of all, I would like to express my sincere gratitude to my advisor Prof. Masahito Ueda. He is really an outstanding teacher who provided me tremendous support for not only doing research but also writing papers, replying referee reports, presentations, and award/job applications. He always help me make the correct decisions, including but not restricted to guiding my main focus to the interdisciplinary field of AMO physics and condensed matter physics, suggesting me to consider the non-Hermitian periodic table (which eventually led the work in Chapter 4), and encouraging me to complete the projects (which are actually those presented in Chapters 2 and 5) despite of the appearance of similar works. I am indeed lucky and honored to have such a wonderful advisor, without whom my academic start dash cannot be so smooth. Of course, I should not forget to acknowledge him for carefully reading this Thesis and giving a lot of valuable comments.

It was really a wonderful experience to visit Prof. Ignacio Cirac's group at the Max-Planck Institut für Quantenoptik (MPQ). I have to thank Ueda-sensei again for his recommendation and Ignacio for his hospitality. Although I had heard about some rumors, I was still shocked by the super power of Ignacio, who can simply understand everything in just a few seconds and then provide a lot of critical advice. It is during this research visit that the work on matrix-product unitaries presented in Chapter 3 was initiated and completed.

I am indeed grateful to all of my collaborators, including Prof. Yuto Ashida, Prof. Norbert Schuch, Dr. Ryusuke Hamazaki, Dr. Sho Higashikawa, Dr. Kazuaki Takasan, Kohei Kawabata and Christoph Sünderhauf, for helping me accomplish the projects included in this Thesis. I am also deeply grateful to Prof. Masatoshi Sato, Dr. Naoto Kura, Dr. Nobuyuki Yoshioka, Kangqiao Liu, and Naoyuki Shibata for the collaborations on other works. In addition, I would like to thank Dr. Tao Liu for inviting me to join in his interesting project on second-order non-Hermitian topological insulators. Apart from the collaborations, it has been my great pleasure to discuss with Prof. Ippeï Danshita, Prof. Mikio Furuta, Prof. Naomichi Hatano, Prof. Yasuhiro Hatsugai, Prof. Masaya Nakagawa, Prof. Haitao Quan, Prof. Hal Tasaki, Prof. Takahiro Sagawa, Prof. Keiji Saito, Prof. Koichi Semba, Prof. Ken Shiozaki, Prof. Tsuneya Yoshida, Max McGinley, Kaoru Mizuta, and Hengyun Zhou.

I am really thankful to Asako Takeuchi and Kyouko Tanaka, who helped me a lot dealing with various paper works. In particular, I would like to thank Takeuchi-san for guiding me to the clinic when I accidentally became ill (and I should thank Ueda-sensei again for contacting the doctor). I would also like to thank Andrea Kluth for her powerful administrative support for my visit to the MPQ.

I would like to express my special gratitude to all the members<sup>2</sup> in Ueda group, including Prof. Kazuya Fujimoto, Prof. Shunsuke Furukawa, Dr. Taiki Haga, Dr. Yusuke Horinouchi, Dr. Yûto Murashita, Dr. Tomohiro Shitara, Dr. Shuhei Yoshida, Takumi Yoshino, Ziyin Liu, Norifumi Matsumoto, Yuki Sakamoto, Shoki Sugimoto, and Zhikang Wang, who make the office

---

<sup>2</sup>Here we include all the current and former members who have overlap with my PhD course and have not been mentioned previously.

atmosphere intellectual and comfortable. There were also many happy moments outside the office, such as watching *Psycho-Pass* with Yuto and *Weathering With You* with Hantao in Shinjuku, playing *Taiko Drum Master* and going to Karaoke with Ziyin and Zhikang in Ueno, watching *Dr. Stone* with Ziyin and Zhikang at my home, drinking with Ryusuke and Nobuyuki, and playing Nintendo Switch with Yuto, Satoken, Komoken, Zhikang and Shoki.

I would like to express my best gratitude to my mother for listening to my endless complaint every week, for encouraging me all the time, and for flying to Japan from time to time to take direct care of me. In fact, I suffered from severe depression in the last year partially because all of my papers were rejected.<sup>3</sup> Indeed, one cannot find any first-author paper published in 2019 from my publication list. I was almost going mad when I received the first e-mail in 2020, telling me that my joint submission was rejected by arXiv, probably because it was misidentified as a “double post”. I cannot imagine how many times I had gave up myself if I could not share my hyper-negative emotions with my mother.

Finally, I acknowledge the financial support from the University of Tokyo through the Graduate Research Abroad in Science Program (GRASP) and the Ministry of Education, Culture, Sports, Science and Technology (MEXT).

---

<sup>3</sup>I understand that this is a place for acknowledgement, but I just cannot help to point out that a considerable percentage of referee reports are not even an excuse for rejection but rather a kind of harassment (although some are very beneficial, even if the result is rejection). Honestly speaking, I can hardly feel any respect to the authors’ efforts from those reports, nor any efforts to try to understand the main points of the papers. For the mental health of all the researchers, especially PhD students who are typically under great pressures, I believe it is necessary to build a better review system so as to mitigate the mental damages from those rubbishy reports. This might be achieved by, e.g., adding a third party (thus not biased by the result of rejection or acceptance; and should consist of reputable experts) which plays the role of judging the quality of referee reports. Those irresponsible referee reports identified should immediately be discarded. It seems that the DAE system of PRL plays quite a similar role, but I think this is far from enough since receiving a rubbishy report is not a rare event at all (at least for me and many of my colleagues). Please note that I am not blaming the referees since everyone may (sometimes unconsciously) write a rubbishy report due to, e.g., being accidentally in a bad mood or simply too busy to go through the paper. I just think that a better review system should set hurdles to not only the papers but also the referee reports. There will certainly be a lot of new problems during the improvement, but it is a shame if we do not even think about how to break the status quo. It is really a huge pity for me to see so many energetic young researchers around, some are obviously much more talented and passionate about physics than me, to leave the academic community after experiencing their hyper-frustrating struggles with the referee reports, even though they enjoyed a lot doing research and finally their papers were published in top journals.

# Bibliography

- [1] Lev D. Landau. On the theory of phase transitions. *Zh. Eksp. Teor. Fiz.*, 7:19, 1937.
- [2] Xiao-Gang Wen. *Quantum Field Theory of Many-Body Systems*. Oxford University Press, New York, 2004.
- [3] K. v. Klitzing, G. Dorda, and M. Pepper. New method for high-accuracy determination of the fine-structure constant based on quantized hall resistance. *Phys. Rev. Lett.*, 45:494–497, Aug 1980.
- [4] Xiao-Gang Wen. Colloquium: Zoo of quantum-topological phases of matter. *Rev. Mod. Phys.*, 89:041004, Dec 2017.
- [5] F. Duncan M. Haldane. Nobel lecture: Topological quantum matter. *Rev. Mod. Phys.*, 89:040502, Oct 2017.
- [6] Zheng-Cheng Gu and Xiao-Gang Wen. Tensor-entanglement-filtering renormalization approach and symmetry-protected topological order. *Phys. Rev. B*, 80:155131, Oct 2009.
- [7] Andrej Mesaros and Ying Ran. Classification of symmetry enriched topological phases with exactly solvable models. *Phys. Rev. B*, 87:155115, Apr 2013.
- [8] Bei Zeng, Xie Chen, Duan-Lu Zhou, and Xiao-Gang Wen. *Quantum Information Meets Quantum Matter*. Springer, New York, 2019.
- [9] Ching-Kai Chiu, Jeffrey C. Y. Teo, Andreas P. Schnyder, and Shinsei Ryu. Classification of topological quantum matter with symmetries. *Rev. Mod. Phys.*, 88:035005, Aug 2016.
- [10] M. Hafezi, S. Mittal, J. Fan, A. Migdall, and J. M. Taylor. Imaging topological edge states in silicon photonics. *Nat. Photonics*, 7:1001, 2013.
- [11] Jayson Paulose, Bryan Gin ge Chen, and Vincenzo Vitelli. Topological modes bound to dislocations in mechanical metamaterials. *Nat. Phys.*, 11(4):153–156, 2015.
- [12] Markus König, Steffen Wiedmann, Christoph Brüne, Andreas Roth, Hartmut Buhmann, Laurens W. Molenkamp, Xiao-Liang Qi, and Shou-Cheng Zhang. Quantum spin hall insulator state in hgte quantum wells. *Science*, 318(5851):766, 2007.
- [13] Immanuel Bloch, Jean Dalibard, and Sylvain Nascimbène. Quantum simulations with ultracold quantum gases. *Nat. Phys.*, 8:267, 2012.
- [14] R. Blatt and C. F. Roos. Quantum simulations with trapped ions. *Nat. Phys.*, 8:277, 2012.
- [15] Andrew A. Houck, Hakan E. Türeci, and Jens Koch. On-chip quantum simulation with superconducting circuits. *Nat. Phys.*, 8:292, 2012.

- [16] I. M. Georgescu, S. Ashhab, and Franco Nori. Quantum simulation. *Rev. Mod. Phys.*, 86:153–185, Mar 2014.
- [17] N. Goldman, J. C. Budich, and P. Zoller. Topological quantum matter with ultracold gases in optical lattices. *Nat. Phys.*, 12:639, 2016.
- [18] N. R. Cooper, J. Dalibard, and I. B. Spielman. Topological bands for ultracold atoms. *Rev. Mod. Phys.*, 91:015005, Mar 2019.
- [19] Tomoki Ozawa, Hannah M. Price, Alberto Amo, Nathan Goldman, Mohammad Hafezi, Ling Lu, Mikael C. Rechtsman, David Schuster, Jonathan Simon, Oded Zilberberg, and Iacopo Carusotto. Topological photonics. *Rev. Mod. Phys.*, 91:015006, Mar 2019.
- [20] Gregor Jotzu, Michael Messer, Rémi Desbuquois, Martin Lebrat, Thomas Uehlinger, Daniel Greif, and Tilman Esslinger. Experimental realization of the topological haldane model with ultracold fermions. *Nature*, 515:237, 2014.
- [21] F. D. M. Haldane. Model for a quantum hall effect without landau levels: Condensed-matter realization of the "parity anomaly". *Phys. Rev. Lett.*, 61:2015, Oct 1988.
- [22] Takashi Oka and Sota Kitamura. Floquet engineering of quantum materials. *Annu. Rev. Cond. Matt. Phys.*, 10(1):387–408, 2019.
- [23] J. Eisert, M. Friesdorf, and C. Gogolin. Quantum many-body systems out of equilibrium. *Nat. Phys.*, 11:124, 2015.
- [24] Marin Bukov, Luca D'Alessio, and Anatoli Polkovnikov. Universal high-frequency behavior of periodically driven systems: from dynamical stabilization to floquet engineering. *Advances in Physics*, 64(2):139–226, 2015.
- [25] Fenner Harper, Rahul Roy, Mark S. Rudner, and S.L. Sondhi. Topology and broken symmetry in floquet systems. *Annu. Rev. Cond. Matt. Phys.*, 11(1):345, 2020.
- [26] Markus Müller, Sebastian Diehl, Guido Pupillo, and Peter Zoller. Engineered open systems and quantum simulations with atoms and ions. *Adv. At. Mol. Opt. Phys.*, 61:1, 2012.
- [27] Aditi Mitra. Quantum quench dynamics. *Annu. Rev. Condens. Matter Phys.*, 9(1):245, 2018.
- [28] Vedika Khemani, Achilleas Lazarides, Roderich Moessner, and S. L. Sondhi. Phase structure of driven quantum systems. *Phys. Rev. Lett.*, 116:250401, Jun 2016.
- [29] C. W. von Keyserlingk and S. L. Sondhi. Phase structure of one-dimensional interacting floquet systems. ii. symmetry-broken phases. *Phys. Rev. B*, 93:245146, Jun 2016.
- [30] Dominic V. Else, Bela Bauer, and Chetan Nayak. Floquet time crystals. *Phys. Rev. Lett.*, 117:090402, Aug 2016.
- [31] Soonwon Choi, Joonhee Choi, Renate Landig, Georg Kucsko, Hengyun Zhou, Junichi Isoya, Fedor Jelezko, Shinobu Onoda, Hitoshi Sumiya, Vedika Khemani, Curt von Keyserlingk, Norman Y. Yao, Eugene Demler, and Mikhail D. Lukin. Observation of discrete time-crystalline order in a disordered dipolar many-body system. *Nature*, 543:221, 2017.

- [32] J. Zhang, P. W. Hess, A. Kyprianidis, P. Becker, A. Lee, J. Smith, G. Pagano, I.-D. Potirniche, A. C. Potter, A. Vishwanath, N. Y. Yao, and C. Monroe. Observation of a discrete time crystal. *Nature*, 543:217, 2017.
- [33] Achilleas Lazarides and Roderich Moessner. Fate of a discrete time crystal in an open system. *Phys. Rev. B*, 95:195135, May 2017.
- [34] Zongping Gong, Ryusuke Hamazaki, and Masahito Ueda. Discrete time-crystalline order in cavity and circuit qed systems. *Phys. Rev. Lett.*, 120:040404, Jan 2018.
- [35] J Ignacio Cirac, David Pérez-García, Norbert Schuch, and Frank Verstraete. Matrix product unitaries: structure, symmetries, and topological invariants. *J. Stat. Mech.*, (8):083105, 2017.
- [36] Tobias J. Osborne. Efficient approximation of the dynamics of one-dimensional quantum spin systems. *Phys. Rev. Lett.*, 97:157202, Oct 2006.
- [37] Hoi Chun Po, Lukasz Fidkowski, Takahiro Morimoto, Andrew C. Potter, and Ashvin Vishwanath. Chiral floquet phases of many-body localized bosons. *Phys. Rev. X*, 6:041070, Dec 2016.
- [38] Zongping Gong, Christoph Sünderhauf, Norbert Schuch, and J. Ignacio Cirac. Classification of matrix-product unitaries with symmetries. *Phys. Rev. Lett.*, 124:100402, Mar 2020.
- [39] Andreas P. Schnyder, Shinsei Ryu, Akira Furusaki, and Andreas W. W. Ludwig. Classification of topological insulators and superconductors in three spatial dimensions. *Phys. Rev. B*, 78:195125, Nov 2008.
- [40] A. Kitaev. Periodic table for topological insulators and superconductors. *AIP Conf. Proc.*, 1134:22, 2009.
- [41] Alexander Altland and Martin R. Zirnbauer. Nonstandard symmetry classes in mesoscopic normal-superconducting hybrid structures. *Phys. Rev. B*, 55:1142–1161, Jan 1997.
- [42] B. Andrei Bernevig, Taylor L. Hughes, and Shou-Cheng Zhang. Quantum spin hall effect and topological phase transition in hgte quantum wells. *Science*, 314(5806):1757, 2006.
- [43] Naomichi Hatano and David R. Nelson. Localization transitions in non-hermitian quantum mechanics. *Phys. Rev. Lett.*, 77:570, Jul 1996.
- [44] Zongping Gong, Yuto Ashida, Kohei Kawabata, Kazuaki Takasan, Sho Higashikawa, and Masahito Ueda. Topological phases of non-hermitian systems. *Phys. Rev. X*, 8:031079, Sep 2018.
- [45] Ce Wang, Pengfei Zhang, Xin Chen, Jinlong Yu, and Hui Zhai. Scheme to measure the topological number of a chern insulator from quench dynamics. *Phys. Rev. Lett.*, 118:185701, May 2017.
- [46] Zongping Gong and Masahito Ueda. Topological entanglement-spectrum crossing in quench dynamics. *Phys. Rev. Lett.*, 121:250601, Dec 2018.
- [47] Paul M. Chaikin and Tom C. Lubensky. *Principles of condensed matter physics*. Cambridge University Press, Cambridge, 2000.



- [48] Subir Sachdev. *Quantum Phase Transitions*. Cambridge University Press, Cambridge, 2011.
- [49] Frank Wilczek. Quantum time crystals. *Phys. Rev. Lett.*, 109:160401, Oct 2012.
- [50] Alfred Shapere and Frank Wilczek. Classical time crystals. *Phys. Rev. Lett.*, 109:160402, Oct 2012.
- [51] Tongcang Li, Zhe-Xuan Gong, Zhang-Qi Yin, H. T. Quan, Xiaobo Yin, Peng Zhang, L.-M. Duan, and Xiang Zhang. Space-time crystals of trapped ions. *Phys. Rev. Lett.*, 109:163001, Oct 2012.
- [52] Patrick Bruno. Impossibility of spontaneously rotating time crystals: A no-go theorem. *Phys. Rev. Lett.*, 111:070402, Aug 2013.
- [53] Haruki Watanabe and Masaki Oshikawa. Absence of quantum time crystals. *Phys. Rev. Lett.*, 114:251603, Jun 2015.
- [54] Immanuel Bloch, Jean Dalibard, and Wilhelm Zwerger. Many-body physics with ultracold gases. *Rev. Mod. Phys.*, 80:885, 2008.
- [55] D. Leibfried, R. Blatt, C. Monroe, and D. Wineland. Quantum dynamics of single trapped ions. *Rev. Mod. Phys.*, 75:281–324, Mar 2003.
- [56] M. H. Devoret and R. J. Schoelkopf. Superconducting circuits for quantum information: An outlook. *Science*, 339:1169, 2013.
- [57] Anatoli Polkovnikov, Krishnendu Sengupta, Alessandro Silva, and Mukund Vengalattore. Colloquium: Nonequilibrium dynamics of closed interacting quantum systems. *Rev. Mod. Phys.*, 83:863, Aug 2011.
- [58] R. Moessner and S. L. Sondhi. Equilibration and order in quantum floquet matter. *Nat. Phys.*, 13:424, 2017.
- [59] Arijeet Pal and David A. Huse. Many-body localization phase transition. *Phys. Rev. B*, 82:174411, Nov 2010.
- [60] Ehud Altman and Ronen Vosk. Universal dynamics and renormalization in many-body-localized systems. *Annu. Rev. Cond. Matt. Phys.*, 6(1):383, 2015.
- [61] Rahul Nandkishore and David A. Huse. Many-body localization and thermalization in quantum statistical mechanics. *Annu. Rev. Cond. Matt. Phys.*, 6:201, 2015.
- [62] Pedro Ponte, Z. Papić, François Huveneers, and Dmitry A. Abanin. Many-body localization in periodically driven systems. *Phys. Rev. Lett.*, 114:140401, Apr 2015.
- [63] Achilleas Lazarides, Arnab Das, and Roderich Moessner. Fate of many-body localization under periodic driving. *Phys. Rev. Lett.*, 115:030402, Jul 2015.
- [64] Jae-yoon Choi, Sebastian Hild, Johannes Zeiher, Peter Schauß, Antonio Rubio-Abadal, Tarik Yefsah, Vedika Khemani, David A. Huse, Immanuel Bloch, and Christian Gross. Exploring the many-body localization transition in two dimensions. *Science*, 352(6293):1547–1552, 2016.
- [65] Takuya Kitagawa, Erez Berg, Mark Rudner, and Eugene Demler. Topological characterization of periodically driven quantum systems. *Phys. Rev. B*, 82:235114, Dec 2010.

- [66] Liang Jiang, Takuya Kitagawa, Jason Alicea, A. R. Akhmerov, David Pekker, Gil Refael, J. Ignacio Cirac, Eugene Demler, Mikhail D. Lukin, and Peter Zoller. Majorana fermions in equilibrium and in driven cold-atom quantum wires. *Phys. Rev. Lett.*, 106:220402, Jun 2011.
- [67] Mark S. Rudner, Netanel H. Lindner, Erez Berg, and Michael Levin. Anomalous edge states and the bulk-edge correspondence for periodically driven two-dimensional systems. *Phys. Rev. X*, 3:031005, Jul 2013.
- [68] Paraj Titum, Erez Berg, Mark S. Rudner, Gil Refael, and Netanel H. Lindner. Anomalous floquet-anderson insulator as a nonadiabatic quantized charge pump. *Phys. Rev. X*, 6:021013, May 2016.
- [69] C. W. von Keyserlingk and S. L. Sondhi. Phase structure of one-dimensional interacting floquet systems. i. abelian symmetry-protected topological phases. *Phys. Rev. B*, 93:245145, Jun 2016.
- [70] Dominic V. Else and Chetan Nayak. Classification of topological phases in periodically driven interacting systems. *Phys. Rev. B*, 93:201103(R), May 2016.
- [71] Andrew C. Potter, Takahiro Morimoto, and Ashvin Vishwanath. Classification of interacting topological floquet phases in one dimension. *Phys. Rev. X*, 6:041001, Oct 2016.
- [72] Andrzej Syrwid, Jakub Zakrzewski, and Krzysztof Sacha. Time crystal behavior of excited eigenstates. *Phys. Rev. Lett.*, 119:250602, Dec 2017.
- [73] Dominic V. Else, Bela Bauer, and Chetan Nayak. Floquet time crystals. *Phys. Rev. Lett.*, 117:090402, Aug 2016.
- [74] N. Y. Yao, A. C. Potter, I.-D. Potirniche, and A. Vishwanath. Discrete time crystals: Rigidity, criticality, and realizations. *Phys. Rev. Lett.*, 118:030401, Jan 2017.
- [75] Krzysztof Sacha and Jakub Zakrzewski. Time crystals: a review. *Rep. Prog. Phys.*, 81(1):016401, nov 2017.
- [76] Valerii K. Kozin and Oleksandr Kyriienko. Quantum time crystals from hamiltonians with long-range interactions. *Phys. Rev. Lett.*, 123:210602, Nov 2019.
- [77] Luca D'Alessio and Marcos Rigol. Long-time behavior of isolated periodically driven interacting lattice systems. *Phys. Rev. X*, 4:041048, Dec 2014.
- [78] Achilleas Lazarides, Arnab Das, and Roderich Moessner. Equilibrium states of generic quantum systems subject to periodic driving. *Phys. Rev. E*, 90:012110, Jul 2014.
- [79] Hyungwon Kim, Tatsuhiko N. Ikeda, and David A. Huse. Testing whether all eigenstates obey the eigenstate thermalization hypothesis. *Phys. Rev. E*, 90:052105, Nov 2014.
- [80] Wen Wei Ho, Soonwon Choi, Mikhail D. Lukin, and Dmitry A. Abanin. Critical time crystals in dipolar systems. *Phys. Rev. Lett.*, 119:010602, Jul 2017.
- [81] Krzysztof Sacha. Modeling spontaneous breaking of time-translation symmetry. *Phys. Rev. A*, 91:033617, Mar 2015.
- [82] Angelo Russomanno, Fernando Iemini, Marcello Dalmonte, and Rosario Fazio. Floquet time crystal in the lipkin-meshkov-glick model. *Phys. Rev. B*, 95:214307, Jun 2017.

- [83] Dominic V. Else, Bela Bauer, and Chetan Nayak. Prethermal phases of matter protected by time-translation symmetry. *Phys. Rev. X*, 7:011026, Mar 2017.
- [84] Tian-Sheng Zeng and D. N. Sheng. Prethermal time crystals in a one-dimensional periodically driven floquet system. *Phys. Rev. B*, 96:094202, Sep 2017.
- [85] Frank Verstraete, Michael M. Wolf, and J. Ignacio Cirac. Quantum computation and quantum-state engineering driven by dissipation. *Nat. Phys.*, 5:633, 2009.
- [86] M. Beau and A. del Campo. Nonlinear quantum metrology of many-body open systems. *Phys. Rev. Lett.*, 119:010403, Jul 2017.
- [87] F. Petruccione and H. P. Breuer. *The theory of open quantum systems*. Oxford University Press, London, 2002.
- [88] R. H. Dicke. Coherence in spontaneous radiation processes. *Phys. Rev.*, 93:99, 1954.
- [89] K. Rzażewski, K. Wódkiewicz, and W. Żakowicz. Phase transitions, two-level atoms, and the  $A^2$  term. *Phys. Rev. Lett.*, 35:432–434, Aug 1975.
- [90] Clive Emary and Tobias Brandes. Chaos and the quantum phase transition in the dicke model. *Phys. Rev. E*, 67:066203, 2003.
- [91] Kristian Baumann, Christine Guerlin, Ferdinand Brennecke, and Tilman Esslinger. Dicke quantum phase transition with a superfluid gas in an optical cavity. *Nature*, 464:1301–1306, 2010.
- [92] K. Baumann, R. Mottl, F. Brennecke, and T. Esslinger. Exploring symmetry breaking at the dicke quantum phase transition. *Phys. Rev. Lett.*, 107:140402, Sep 2011.
- [93] Helmut Ritsch, Peter Domokos, Ferdinand Brennecke, and Tilman Esslinger. Cold atoms in cavity-generated dynamical optical potentials. *Rev. Mod. Phys.*, 85:553–601, Apr 2013.
- [94] Markus P. Baden, Kyle J. Arnold, Arne L. Grimsmo, Scott Parkins, and Murray D. Barrett. Realization of the dicke model using cavity-assisted raman transitions. *Phys. Rev. Lett.*, 113:020408, Jul 2014.
- [95] Alexandre Blais, Ren-Shou Huang, Andreas Wallraff, S. M. Girvin, and R. J. Schoelkopf. Cavity quantum electrodynamics for superconducting electrical circuits: An architecture for quantum computation. *Phys. Rev. A*, 69:062320, Jun 2004.
- [96] Pierre Nataf and Cristiano Ciuti. No-go theorem for superradiant quantum phase transitions in cavity qed and counter-example in circuit qed. *Nat. Commun.*, 1:72, 2010.
- [97] Oliver Viehmann, Jan von Delft, and Florian Marquardt. Superradiant phase transitions and the standard description of circuit qed. *Phys. Rev. Lett.*, 107:113602, Sep 2011.
- [98] J. A. Mlynek, A. A. Abdumalikov, C. Eichler, and A. Wallraff. Observation of dicke superradiance for two artificial atoms in a cavity with high decay rate. *Nat. Commun.*, 5:5186, Nov 2014.
- [99] Tuomas Jaako, Ze-Liang Xiang, Juan José Garcia-Ripoll, and Peter Rabl. Ultrastrong-coupling phenomena beyond the dicke model. *Phys. Rev. A*, 94:033850, Sep 2016.

- [100] Motoaki Bamba, Kunihiro Inomata, and Yasunobu Nakamura. Superradiant phase transition in a superconducting circuit in thermal equilibrium. *Phys. Rev. Lett.*, 117:173601, Oct 2016.
- [101] Fumiki Yoshihara, Tomoko Fuse, Sahel Ashhab, Kosuke Kakuyanagi, Shiro Saito, and Kouichi Semba. Superconducting qubit–oscillator circuit beyond the ultrastrong-coupling regime. *Nat. Phys.*, 13:44–47, 2017.
- [102] F. Dimer, B. Estienne, A. S. Parkins, and H. J. Carmichael. Proposed realization of the dicke-model quantum phase transition in an optical cavity qed system. *Phys. Rev. A*, 75:013804, 2007.
- [103] V. M. Bastidas, C. Emary, B. Regler, and T. Brandes. Nonequilibrium quantum phase transitions in the dicke model. *Phys. Rev. Lett.*, 108:043003, Jan 2012.
- [104] M. J. Bhaseen, J. Mayoh, B. D. Simons, and J. Keeling. Dynamics of nonequilibrium dicke models. *Phys. Rev. A*, 85:013817, Jan 2012.
- [105] R. Chitra and O. Zilberberg. Dynamical many-body phases of the parametrically driven, dissipative dicke model. *Phys. Rev. A*, 92:023815, Aug 2015.
- [106] Peter Kirton and Jonathan Keeling. Suppressing and restoring the dicke superradiance transition by dephasing and decay. *Phys. Rev. Lett.*, 118:123602, Mar 2017.
- [107] E. M. Kessler. Generalized schrieffer-wolff formalism for dissipative systems. *Phys. Rev. A*, 86:012126, Jul 2012.
- [108] Tony E. Lee and H. R. Sadeghpour. Quantum synchronization of quantum van der pol oscillators with trapped ions. *Phys. Rev. Lett.*, 111:234101, Dec 2013.
- [109] Michael R. Hush, Weibin Li, Sam Genway, Igor Lesanovsky, and Andrew D. Armour. Spin correlations as a probe of quantum synchronization in trapped-ion phonon lasers. *Phys. Rev. A*, 91:061401, Jun 2015.
- [110] Niels Lörch, Simon E. Nigg, Andreas Nunnenkamp, Rakesh P. Tiwari, and Christoph Bruder. Quantum synchronization blockade: Energy quantization hinders synchronization of identical oscillators. *Phys. Rev. Lett.*, 118:243602, Jun 2017.
- [111] Robert M. May. Simple mathematical models with very complicated dynamics. *Nature*, 261:459–467, Jun 1976.
- [112] John Guckenheimer and Philip Holmes. *Nonlinear Oscillations, Dynamical Systems, and Bifurcations of Vector Fields*. Springer, New York, 1983.
- [113] Yuri A. Kuznetsov. *Elements of Applied Bifurcation Theory*. Springer, New York, 1998.
- [114] Xiaoli Liu and Dongmei Xiao. Complex dynamic behaviors of a discrete-time predator–prey system. *Chaos, Solitons & Fractals*, 32(1):80 – 94, 2007.
- [115] Felix Flicker. Time Quasilattices in Dissipative Dynamical Systems. *SciPost Phys.*, 5:1, 2018.
- [116] W. Casteels, R. Fazio, and C. Ciuti. Critical dynamical properties of a first-order dissipative phase transition. *Phys. Rev. A*, 95:012128, Jan 2017.

- [117] Mattias Fitzpatrick, Neereja M. Sundaresan, Andy C. Y. Li, Jens Koch, and Andrew A. Houck. Observation of a dissipative phase transition in a one-dimensional circuit qed lattice. *Phys. Rev. X*, 7:011016, Feb 2017.
- [118] C.-E. Bardyn, M. A. Baranov, C. V. Kraus, E. Rico, A. İmamoğlu, P. Zoller, and S. Diehl. Topology by dissipation. *New J. Phys.*, 15:085001, 2013.
- [119] Rahul Roy and Fenner Harper. Periodic table for floquet topological insulators. *Phys. Rev. B*, 96:155118, Oct 2017.
- [120] Shunyu Yao, Zhongbo Yan, and Zhong Wang. Topological invariants of floquet systems: General formulation, special properties, and floquet topological defects. *Phys. Rev. B*, 96:195303, Nov 2017.
- [121] Sho Higashikawa, Masaya Nakagawa, and Masahito Ueda. Floquet chiral magnetic effect. *Phys. Rev. Lett.*, 123:066403, Aug 2019.
- [122] Max McGinley and Nigel R. Cooper. Topology of one-dimensional quantum systems out of equilibrium. *Phys. Rev. Lett.*, 121:090401, Aug 2018.
- [123] Max McGinley and Nigel R. Cooper. Classification of topological insulators and superconductors out of equilibrium. *Phys. Rev. B*, 99:075148, Feb 2019.
- [124] Max McGinley and Nigel R. Cooper. Interacting symmetry-protected topological phases out of equilibrium. *Phys. Rev. Research*, 1:033204, Dec 2019.
- [125] Andrea Coser and David Pérez-García. Classification of phases for mixed states via fast dissipative evolution. *Quantum*, 3:174, August 2019.
- [126] Julio T. Barreiro, Markus Müller, Philipp Schindler, Daniel Nigg, Thomas Monz, Michael Chwalla, Markus Hennrich, Christian F. Roos, Peter Zoller, and Rainer Blatt. An open-system quantum simulator with trapped ions. *Nature*, 470:486, 2011.
- [127] P. Schindler, M. Müller, D. Nigg, J. T. Barreiro, E. A. Martinez, M. Hennrich, T. Monz, S. Diehl, P. Zoller, and R. Blatt. Quantum simulation of dynamical maps with trapped ions. *Nat. Phys.*, 9:361, 2013.
- [128] Hannes Bernien, Sylvain Schwartz, Alexander Keesling, Harry Levine, Ahmed Omran, Hannes Pichler, Soonwon Choi, Alexander S. Zibrov, Manuel Endres, Markus Greiner, Vladan Vuletić, and Mikhail D. Lukin. Probing many-body dynamics on a 51-atom quantum simulator. *Nature*, 551:579, 2017.
- [129] J. Zhang, G. Pagano, P. W. Hess, A. Kyprianidis, P. Becker, H. Kaplan, A. V. Gorshkov, Z.-X. Gong, and C. Monroe. Observation of a many-body dynamical phase transition with a 53-qubit quantum simulator. *Nature*, 551:601, 2017.
- [130] F. D. M. Haldane. Nonlinear field theory of large-spin heisenberg antiferromagnets: Semi-classically quantized solitons of the one-dimensional easy-axis néel state. *Phys. Rev. Lett.*, 50:1153–1156, Apr 1983.
- [131] Ian Affleck, Tom Kennedy, Elliott H. Lieb, and Hal Tasaki. Rigorous results on valence-bond ground states in antiferromagnets. *Phys. Rev. Lett.*, 59:799–802, Aug 1987.
- [132] Frank Pollmann, Ari M. Turner, Erez Berg, and Masaki Oshikawa. Entanglement spectrum of a topological phase in one dimension. *Phys. Rev. B*, 81:064439, Feb 2010.

- [133] M. B. Hastings. An area law for one-dimensional quantum systems. *J. Stat. Mech.*, page P08024, August 2007.
- [134] M. Fannes, B. Nachtergaele, and R. F. Werner. Finitely correlated states on quantum spin chains. *Commun. Math. Phys.*, 144(3):443, Mar 1992.
- [135] F. Verstraete and J. I. Cirac. Matrix product states represent ground states faithfully. *Phys. Rev. B*, 73:094423, Mar 2006.
- [136] D. Pérez-García, F. Verstraete, M. M. Wolf, and J. I. Cirac. Matrix product state representations. *Quantum Inf. Comput.*, 7:401, 2007.
- [137] F. Verstraete, V. Murg, and J. I. Cirac. Matrix product states, projected entangled pair states, and variational renormalization group methods for quantum spin systems. *Adv. Phys.*, 57(2):143, 2008.
- [138] D. Pérez-García, M. M. Wolf, M. Sanz, F. Verstraete, and J. I. Cirac. String order and symmetries in quantum spin lattices. *Phys. Rev. Lett.*, 100:167202, Apr 2008.
- [139] Norbert Schuch, David Pérez-García, and Ignacio Cirac. Classifying quantum phases using matrix product states and projected entangled pair states. *Phys. Rev. B*, 84:165139, Oct 2011.
- [140] Xie Chen, Zheng-Cheng Gu, and Xiao-Gang Wen. Classification of gapped symmetric phases in one-dimensional spin systems. *Phys. Rev. B*, 83:035107, Jan 2011.
- [141] Xie Chen, Zheng-Cheng Gu, and Xiao-Gang Wen. Complete classification of one-dimensional gapped quantum phases in interacting spin systems. *Phys. Rev. B*, 84:235128, Dec 2011.
- [142] M. Burak Şahinoğlu, Sujeet K. Shukla, Feng Bi, and Xie Chen. Matrix product representation of locality preserving unitaries. *Phys. Rev. B*, 98:245122, Dec 2018.
- [143] Elliott H. Lieb and Derek W. Robinson. The finite group velocity of quantum spin systems. *Commun. Math. Phys.*, 28:251, 1972.
- [144] D. Gross, V. Nesme, H. Vogts, and R. F. Werner. Index theory of one dimensional quantum walks and cellular automata. *Commun. Math. Phys.*, 310(2):419–454, Mar 2012.
- [145] Amos Chan and Thorsten B Wahl. Classification of symmetry-protected topological many-body localized phases in one dimension. *J. Phys.: Condens. Matter*, 32(30):305601, may 2020.
- [146] M. B. Hastings. Classifying quantum phases with the kirby torus trick. *Phys. Rev. B*, 88:165114, Oct 2013.
- [147] Joel E. Moore, Ying Ran, and Xiao-Gang Wen. Topological surface states in three-dimensional magnetic insulators. *Phys. Rev. Lett.*, 101:186805, 2008.
- [148] Andrew C. Potter and Takahiro Morimoto. Dynamically enriched topological orders in driven two-dimensional systems. *Phys. Rev. B*, 95:155126, Apr 2017.
- [149] Rahul Roy and Fenner Harper. Floquet topological phases with symmetry in all dimensions. *Phys. Rev. B*, 95:195128, May 2017.

- [150] B. P. Lanyon, C. Maier, M. Holzäpfel, T. Baumgratz, C. Hempel, P. Jurcevic, I. Dhand, A. S. Buyskikh, A. J. Daley, M. Cramer, M. B. Plenio, R. Blatt, and C. F. Roos. Efficient tomography of a quantum many-body system. *Nat. Phys.*, 13:1158, 2017.
- [151] Hannes Pichler, Guanyu Zhu, Alireza Seif, Peter Zoller, and Mohammad Hafezi. Measurement protocol for the entanglement spectrum of cold atoms. *Phys. Rev. X*, 6:041033, Nov 2016.
- [152] Jean-Pierre Serre. *Linear Representations of Finite Groups*. Springer, New York, 1977.
- [153] G. Vidal. Classical simulation of infinite-size quantum lattice systems in one spatial dimension. *Phys. Rev. Lett.*, 98:070201, Feb 2007.
- [154] D. L. Zhou, B. Zeng, Z. Xu, and C. P. Sun. Quantum computation based on d-level cluster state. *Phys. Rev. A*, 68:062303, Dec 2003.
- [155] Xie Chen, Zheng-Cheng Gu, Zheng-Xin Liu, and Xiao-Gang Wen. Symmetry protected topological orders and the group cohomology of their symmetry group. *Phys. Rev. B*, 87:155114, Apr 2013.
- [156] Robbert Dijkgraaf and Edward Witten. Topological gauge theories and group cohomology. *Commun. Math. Phys.*, 129(2):393–429, Apr 1990.
- [157] Chuangxun Cheng. A character theory for projective representations of finite groups. *Linear Alg. Appl.*, 469:230, 2015.
- [158] Dominic V. Else and Chetan Nayak. Classifying symmetry-protected topological phases through the anomalous action of the symmetry on the edge. *Phys. Rev. B*, 90:235137, Dec 2014.
- [159] R. Dorner, S. R. Clark, L. Heaney, R. Fazio, J. Goold, and V. Vedral. Extracting quantum work statistics and fluctuation theorems by single-qubit interferometry. *Phys. Rev. Lett.*, 110:230601, Jun 2013.
- [160] Brian Swingle, Gregory Bentsen, Monika Schleier-Smith, and Patrick Hayden. Measuring the scrambling of quantum information. *Phys. Rev. A*, 94:040302(R), Oct 2016.
- [161] Guanyu Zhu, Mohammad Hafezi, and Tarun Grover. Measurement of many-body chaos using a quantum clock. *Phys. Rev. A*, 94:062329, Dec 2016.
- [162] Norman Y. Yao, Fabian Grusdt, Brian Swingle, Mikhail D. Lukin, Dan M. Stamper-Kurn, Joel E. Moore, and Eugene A. Demler. Interferometric approach to probing fast scrambling. arXiv:1607.01801, 2016.
- [163] Andrew C. Potter and Ashvin Vishwanath. Protection of topological order by symmetry and many-body localization. arXiv:1506.00592, 2015.
- [164] Fenner Harper and Rahul Roy. Floquet topological order in interacting systems of bosons and fermions. *Phys. Rev. Lett.*, 118:115301, Mar 2017.
- [165] D. J. Thouless, M. Kohmoto, M. P. Nightingale, and M. den Nijs. Quantized hall conductance in a two-dimensional periodic potential. *Phys. Rev. Lett.*, 49:405, Aug 1982.
- [166] Xiao-Gang Wen. Topological orders and edge excitations in fractional quantum hall states. *Adv. Phys.*, 44(5):405, 1995.

- [167] C. L. Kane and E. J. Mele. Quantum spin hall effect in graphene. *Phys. Rev. Lett.*, 95:226801, Nov 2005.
- [168] M. Z. Hasan and C. L. Kane. Colloquium: Topological insulators. *Rev. Mod. Phys.*, 82:3045–3067, Nov 2010.
- [169] Xiao-Liang Qi and Shou-Cheng Zhang. Topological insulators and superconductors. *Rev. Mod. Phys.*, 83:1057–1110, Oct 2011.
- [170] C. W. J. Beenakker. Random-matrix theory of majorana fermions and topological superconductors. *Rev. Mod. Phys.*, 87:1037, Sep 2015.
- [171] Marcos Atala, Monika Aidelsburger, Julio T. Barreiro, Dmitry Abanin, Takuya Kitagawa, Eugene Demler, and Immanuel Bloch. Direct measurement of the zak phase in topological bloch bands. *Nat. Phys.*, 9:795, 2013.
- [172] M. Aidelsburger, M. Lohse, C. Schweizer, M. Atala, J. T. Barreiro, S. Nascimbène, N. R. Cooper, I. Bloch, and N. Goldman. Measuring the chern number of hofstadter bands with ultracold bosonic atoms. *Nat. Phys.*, 11:162, 2015.
- [173] B. K. Stuhl, H.-I. Lu, L. M. Ayccock, D. Genkina, and I. B. Spielman. Visualizing edge states with an atomic bose gas in the quantum hall regime. *Science*, 349(6255):1514, 2015.
- [174] M. Mancini, G. Pagano, G. Cappellini, L. Livi, M. Rider, J. Catani, C. Sias, P. Zoller, M. Inguscio, M. Dalmonte, and L. Fallani. Observation of chiral edge states with neutral fermions in synthetic hall ribbons. *Science*, 349(6255):1510, 2015.
- [175] Zhan Wu, Long Zhang, Wei Sun, Xiao-Tian Xu, Bao-Zong Wang, Si-Cong Ji, Youjin Deng, Shuai Chen, Xiong-Jun Liu, and Jian-Wei Pan. Realization of two-dimensional spin-orbit coupling for bose-einstein condensates. *Science*, 354:83, 2016.
- [176] Han-Ning Dai, Bing Yang, Andreas Reingruber, Hui Sun, Xiao-Fan Xu, Yu-Ao Chen, Zhen-Sheng Yuan, and Jian-Wei Pan. Four-body ring-exchange interactions and anyonic statistics within a minimal toric-code hamiltonian. *Nat. Phys.*, 13:1195, 2017.
- [177] A. Y. Kitaev. Fault-tolerant quantum computation by anyons. *Ann. Phys.*, 303:2, 2003.
- [178] Chetan Nayak, Steven H. Simon, Ady Stern, Michael Freedman, and Sankar Das Sarma. Non-abelian anyons and topological quantum computation. *Rev. Mod. Phys.*, 80:1083–1159, Sep 2008.
- [179] Jason Alicea, Yuval Oreg, Gil Refael, Felix von Oppen, and Matthew P. A. Fisher. Non-abelian statistics and topological quantum information processing in 1d wire networks. *Nat. Phys.*, 7:412, 2011.
- [180] R. Barends, J. Kelly, A. Megrant, A. Veitia, D. Sank, E. Jeffrey, T. C. White, J. Mutus, A. G. Fowler, B. Campbell, Y. Chen, Z. Chen, B. Chiaro, A. Dunsworth, C. Neill, P. O’Malley, P. Roushan, A. Vainsencher, J. Wenner, A. N. Korotkov, A. N. Cleland, and John M. Martinis. Superconducting quantum circuits at the surface code threshold for fault tolerance. *Nature*, 508:500, 2014.
- [181] F. D. M. Haldane and S. Raghu. Possible realization of directional optical waveguides in photonic crystals with broken time-reversal symmetry. *Phys. Rev. Lett.*, 100:013904, Jan 2008.



- [182] Mohammad Hafezi, Eugene A. Demler, Mikhail D. Lukin, and Jacob M. Taylor. Robust optical delay lines with topological protection. *Nat. Phys.*, 7:907, 2011.
- [183] Kejie Fang, Zongfu Yu, and Shanhui Fan. Realizing effective magnetic field for photons by controlling the phase of dynamic modulation. *Nat. Photonics*, 6:782, 2012.
- [184] Alexander B. Khanikaev, S. Hossein Mousavi, Wang-Kong Tse, Mehdi Kargarian, Allan H. MacDonald, and Gennady Shvets. Photonic topological insulators. *Nat. Mater.*, 12:233, 2013.
- [185] Iacopo Carusotto and Cristiano Ciuti. Quantum fluids of light. *Rev. Mod. Phys.*, 85:299, Feb 2013.
- [186] Mikael C. Rechtsman, Julia M. Zeuner, Yonatan Plotnik, Yaakov Lumer, Daniel Podolsky, Felix Dreisow, Stefan Nolte, Mordechai Segev, and Alexander Szameit. Photonic floquet topological insulators. *Nature*, 496:196, 2013.
- [187] Ling Lu, John D. Joannopoulos, and Marin Soljačić. Topological photonics. *Nat. Photonics*, 8:821, 2014.
- [188] Torsten Karzig, Charles-Edouard Bardyn, Netanel H. Lindner, and Gil Refael. Topological polaritons. *Phys. Rev. X*, 5:031001, Jul 2015.
- [189] C. L. Kane and T. C. Lubensky. Topological boundary modes in isostatic lattices. *Nat. Phys.*, 10:39, 2014.
- [190] Taofiq K. Paraïso, Mahmoud Kalaei, Leyun Zang, Hannes Pfeifer, Florian Marquardt, and Oskar Painter. Position-squared coupling in a tunable photonic crystal optomechanical cavity. *Phys. Rev. X*, 5:041024, Nov 2015.
- [191] Roman Süsstrunk and Sebastian D. Huber. Observation of phononic helical edge states in a mechanical topological insulator. *Science*, 349(6243):47, 2015.
- [192] Cheng He, Xu Ni, Hao Ge, Xiao-Chen Sun, Yan-Bin Chen, Ming-Hui Lu, Xiao-Ping Liu, and Yan-Feng Chen. Acoustic topological insulator and robust one-way sound transport. *Nat. Phys.*, 12:1124, 2016.
- [193] B. A. Bernevig and T. L. Hughes. *Topological Insulators and Topological Superconductors*. Princeton University Press, Princeton, NJ, 2013.
- [194] Shinsei Ryu, Andreas P. Schnyder, Akira Furusaki, and Andreas W. W. Ludwig. Topological insulators and superconductors: tenfold way and dimensional hierarchy. *New J. Phys.*, 12:065010, 2010.
- [195] Jeffrey C. Y. Teo and C. L. Kane. Topological defects and gapless modes in insulators and superconductors. *Phys. Rev. B*, 82:115120, Sep 2010.
- [196] Liang Fu. Topological crystalline insulators. *Phys. Rev. Lett.*, 106:106802, Mar 2011.
- [197] Robert-Jan Slager, Andrej Mesaros, Vladimir Juričić, and Jan Zaanen. The space group classification of topological band-insulators. *Nat. Phys.*, 9:98, 2013.
- [198] Ching-Kai Chiu, Hong Yao, and Shinsei Ryu. Classification of topological insulators and superconductors in the presence of reflection symmetry. *Phys. Rev. B*, 88:075142, Aug 2013.

- [199] Takahiro Morimoto and Akira Furusaki. Topological classification with additional symmetries from clifford algebras. *Phys. Rev. B*, 88:125129, Sep 2013.
- [200] Ken Shiozaki and Masatoshi Sato. Topology of crystalline insulators and superconductors. *Phys. Rev. B*, 90:165114, Oct 2014.
- [201] Yoichi Ando and Liang Fu. Topological crystalline insulators and topological superconductors: From concepts to materials. *Annu. Rev. of Cond. Matt. Phys.*, 6(1):361–381, 2015.
- [202] Jorrit Kruthoff, Jan de Boer, Jasper van Wezel, Charles L. Kane, and Robert-Jan Slager. Topological classification of crystalline insulators through band structure combinatorics. *Phys. Rev. X*, 7:041069, Dec 2017.
- [203] Yasuhiro Hatsugai. Chern number and edge states in the integer quantum hall effect. *Phys. Rev. Lett.*, 71:3697–3700, Nov 1993.
- [204] A. Y. Kitaev. Unpaired majorana fermions in quantum wires. *Phys. Usp.*, 44:131, 2001.
- [205] Lukasz Fidkowski. Entanglement spectrum of topological insulators and superconductors. *Phys. Rev. Lett.*, 104:130502, Apr 2010.
- [206] Qian Niu, D. J. Thouless, and Yong-Shi Wu. Quantized hall conductance as a topological invariant. *Phys. Rev. B*, 31:3372–3377, Mar 1985.
- [207] Yi Chen Hu and Taylor L. Hughes. Absence of topological insulator phases in non-hermitian  $pt$ -symmetric hamiltonians. *Phys. Rev. B*, 84:153101, Oct 2011.
- [208] Kenta Esaki, Masatoshi Sato, Kazuki Hasebe, and Mahito Kohmoto. Edge states and topological phases in non-hermitian systems. *Phys. Rev. B*, 84:205128, Nov 2011.
- [209] Henning Schomerus. Topologically protected midgap states in complex photonic lattices. *Opt. Lett.*, 38(11):1912, Jun 2013.
- [210] Simon Malzard, Charles Poli, and Henning Schomerus. Topologically protected defect states in open photonic systems with non-hermitian charge-conjugation and parity-time symmetry. *Phys. Rev. Lett.*, 115:200402, Nov 2015.
- [211] Pablo San-Jose, Jorge Cayao, Elsa Prada, and Ramón Aguado. Majorana bound states from exceptional points in non-topological superconductors. *Sci. Rep.*, 6:21427, 2016.
- [212] Tony E. Lee. Anomalous edge state in a non-hermitian lattice. *Phys. Rev. Lett.*, 116:133903, Apr 2016.
- [213] Daniel Leykam, Konstantin Y. Bliokh, Chunli Huang, Y. D. Chong, and Franco Nori. Edge modes, degeneracies, and topological numbers in non-hermitian systems. *Phys. Rev. Lett.*, 118:040401, Jan 2017.
- [214] Yong Xu, Sheng-Tao Wang, and L.-M. Duan. Weyl exceptional rings in a three-dimensional dissipative cold atomic gas. *Phys. Rev. Lett.*, 118:045701, Jan 2017.
- [215] Kohei Kawabata, Yuto Ashida, Hosho Katsura, and Masahito Ueda. Parity-time-symmetric topological superconductor. *Phys. Rev. B*, 98:085116, Aug 2018.

- [216] G. Barontini, R. Labouvie, F. Stubenrauch, A. Vogler, V. Guarrera, and H. Ott. Controlling the dynamics of an open many-body quantum system with localized dissipation. *Phys. Rev. Lett.*, 110:035302, 2013.
- [217] Markus Aspelmeyer, Tobias J. Kippenberg, and Florian Marquardt. Cavity optomechanics. *Rev. Mod. Phys.*, 86:1391–1452, Dec 2014.
- [218] Hui Cao and Jan Wiersig. Dielectric microcavities: Model systems for wave chaos and non-hermitian physics. *Rev. Mod. Phys.*, 87:61, Jan 2015.
- [219] Peng Peng, Wanxia Cao, Ce Shen, Weizhi Qu, Jianming Wen, Liang Jiang, and Yanhong Xiao. Anti-parity-time symmetry with flying atoms. *Nat. Phys.*, 12:1139, 2016.
- [220] H. Xu, D. Mason, Luyao Jiang, and J. G. E. Harris. Topological energy transfer in an optomechanical system with exceptional points. *Nature*, 537:80, 2016.
- [221] Bo Peng, Şahin Kaya Özdemir, Matthias Liertzer, Weijian Chen, Johannes Kramer, Huzeyfe Yilmaz, Jan Wiersig, Stefan Rotter, and Lan Yang. Chiral modes and directional lasing at exceptional points. *Proc. Natl. Acad. Sci. USA*, 113(25):6845, 2016.
- [222] Weijian Chen, Şahin Kaya Özdemir, Guangming Zhao, Jan Wiersig, and Lan Yang. Exceptional points enhance sensing in an optical microcavity. *Nature*, 548:192, 2017.
- [223] Hengyun Zhou, Chao Peng, Yoseob Yoon, Chia Wei Hsu, Keith A. Nelson, Liang Fu, John D. Joannopoulos, Marin Soljačić, and Bo Zhen. Observation of bulk fermi arc and polarization half charge from paired exceptional points. *Science*, 359:1009, 2018.
- [224] Miguel A. Bandres, Steffen Wittek, Gal Harari, Midya Parto, Jinhan Ren, Mordechai Segev, Demetrios N. Christodoulides, and Mercedeh Khajavikhan. Topological insulator laser: Experiments. *Science*, 359(6381), 2018.
- [225] Christian E. Rüter, Konstantinos G. Makris, Ramy El-Ganainy, Demetrios N. Christodoulides, Mordechai Segev, and Detlef Kip. Observation of parity-time symmetry in optics. *Nat. Phys.*, 6:192, 2010.
- [226] Bo Peng, Şahin Kaya Özdemir, Fuchuan Lei, Faraz Monifi, Mariagiovanna Gianfreda, Gui Lu Long, Shanhui Fan, Franco Nori, Carl M. Bender, and Lan Yang. Parity-time-symmetric whispering-gallery microcavities. *Nat. Phys.*, 10:394, 2014.
- [227] Liang Feng, Zi Jing Wong, Ren-Min Ma, Yuan Wang, and Xiang Zhang. Single-mode laser by parity-time symmetry breaking. *Science*, 346(6212):972, 2014.
- [228] Vladimir V. Konotop, Jianke Yang, and Dmitry A. Zezyulin. Nonlinear waves in  $\mathcal{PT}$ -symmetric systems. *Rev. Mod. Phys.*, 88:035002, Jul 2016.
- [229] L. Xiao, X. Zhan, Z. H. Bian, K. K. Wang, X. Zhang, X. P. Wang, J. Li, K. Mochizuki, D. Kim, N. Kawakami, W. Yi, H. Obuse, B. C. Sanders, and P. Xue. Observation of topological edge states in parity-time-symmetric quantum walks. *Nat. Phys.*, 13:1117, 2017.
- [230] S. Weimann, M. Kremer, Y. Plotnik, Y. Lumer, S. Nolte, K. G. Makris, M. Segev, M. C. Rechtsman, and A. Szameit. Topologically protected bound states in photonic parity-time-symmetric crystals. *Nat. Mater.*, 16:433, 2017.

- [231] Ramy El-Ganainy, Konstantinos G. Makris, Mercedeh Khajavikhan, Ziad H. Musslimani, Stefan Rotter, and Demetrios N. Christodoulides. Non-hermitian physics and pt symmetry. *Nat. Phys.*, 14:11, 2018.
- [232] Carl M. Bender and Stefan Boettcher. Real spectra in non-hermitian hamiltonians having  $\mathcal{PT}$  symmetry. *Phys. Rev. Lett.*, 80:5243, Jun 1998.
- [233] Carl M. Bender. Making sense of non-hermitian hamiltonians. *Rep. Prog. Phys.*, 70:947, 2007.
- [234] W. D. Heiss. The physics of exceptional points. *J. Phys. A: Math. Theor.*, 45:444016, 2012.
- [235] M. S. Rudner and L. S. Levitov. Topological transition in a non-hermitian quantum walk. *Phys. Rev. Lett.*, 102:065703, Feb 2009.
- [236] Tony E. Lee and Ching-Kit Chan. Heralded magnetism in non-hermitian atomic systems. *Phys. Rev. X*, 4:041001, Oct 2014.
- [237] Tony E. Lee, Florentin Reiter, and Nimrod Moiseyev. Entanglement and spin squeezing in non-hermitian phase transitions. *Phys. Rev. Lett.*, 113:250401, Dec 2014.
- [238] Yuto Ashida, Shunsuke Furukawa, and Masahito Ueda. Quantum critical behavior influenced by measurement backaction in ultracold gases. *Phys. Rev. A*, 94:053615, Nov 2016.
- [239] Yuto Ashida, Shunsuke Furukawa, and Masahito Ueda. Parity-time-symmetric quantum critical phenomena. *Nat. Commun.*, 8:15791, 2017.
- [240] Masaya Nakagawa, Norio Kawakami, and Masahito Ueda. Non-hermitian kondo effect in ultracold alkaline-earth atoms. *Phys. Rev. Lett.*, 121:203001, Nov 2018.
- [241] Zongping Gong, Sho Higashikawa, and Masahito Ueda. Zeno hall effect. *Phys. Rev. Lett.*, 118:200401, May 2017.
- [242] Kohei Kawabata, Yuto Ashida, and Masahito Ueda. Information retrieval and criticality in parity-time-symmetric systems. *Phys. Rev. Lett.*, 119:190401, Nov 2017.
- [243] M. Esposito, U. Harbola, and S. Mukamel. Nonequilibrium fluctuations, fluctuation theorems, and counting statistics in quantum systems. *Rev. Mod. Phys.*, 81:1665, 2009.
- [244] Jie Ren, Peter Hänggi, and Baowen Li. Berry-phase-induced heat pumping and its impact on the fluctuation theorem. *Phys. Rev. Lett.*, 104:170601, Apr 2010.
- [245] Takahiro Sagawa and Hisao Hayakawa. Geometrical expression of excess entropy production. *Phys. Rev. E*, 84:051110, Nov 2011.
- [246] David R. Nelson and Nadav M. Shnerb. Non-hermitian localization and population biology. *Phys. Rev. E*, 58:1383, Aug 1998.
- [247] Ariel Amir, Naomichi Hatano, and David R. Nelson. Non-hermitian localization in biological networks. *Phys. Rev. E*, 93:042310, Apr 2016.
- [248] Arvind Murugan and Suriyanarayanan Vaikuntanathan. Topologically protected modes in non-equilibrium stochastic systems. *Nat. Commun.*, 8:13881, 2017.

- [249] Jie Ren and N. A. Sinitsyn. Braid group and topological phase transitions in nonequilibrium stochastic dynamics. *Phys. Rev. E*, 87:050101(R), May 2013.
- [250] Yuansheng Cao, Zongping Gong, and H. T. Quan. Thermodynamics of information processing based on enzyme kinetics: An exactly solvable model of an information pump. *Phys. Rev. E*, 91:062117, Jun 2015.
- [251] Thomas McGrath, Nick S. Jones, Pieter Rein ten Wolde, and Thomas E. Ouldridge. Biochemical machines for the interconversion of mutual information and work. *Phys. Rev. Lett.*, 118:028101, Jan 2017.
- [252] Mark S. Rudner, Michael Levin, and Leonid S. Levitov. Survival, decay, and topological protection in non-hermitian quantum transport. arXiv:1605.07652, 2016.
- [253] Huitao Shen, Bo Zhen, and Liang Fu. Topological band theory for non-hermitian hamiltonians. *Phys. Rev. Lett.*, 120:146402, Apr 2018.
- [254] Naomichi Hatano and David R. Nelson. Vortex pinning and non-hermitian quantum mechanics. *Phys. Rev. B*, 56:8651, Oct 1997.
- [255] Max Karoubi. *K-theory: An Introduction*. Springer, Berlin, 2008.
- [256] Denis Bernard and André LeClair. A classification of non-hermitian random matrices. arXiv:cond-mat/0110649, 2001.
- [257] Kohei Kawabata, Ken Shiozaki, Masahito Ueda, and Masatoshi Sato. Symmetry and topology in non-hermitian physics. *Phys. Rev. X*, 9:041015, Oct 2019.
- [258] Hengyun Zhou and Jong Yeon Lee. Periodic table for topological bands with non-hermitian symmetries. *Phys. Rev. B*, 99:235112, Jun 2019.
- [259] Roman Süsstrunk and Sebastian D. Huber. Classification of topological phonons in linear mechanical metamaterials. *Proceedings of the National Academy of Sciences*, 113(33):E4767–E4775, 2016.
- [260] Tsuneya Yoshida and Yasuhiro Hatsugai. Exceptional rings protected by emergent symmetry for mechanical systems. *Phys. Rev. B*, 100:054109, Aug 2019.
- [261] Ananya Ghatak, Martin Brandenbourger, Jasper van Wezel, and Corentin Coulais. Observation of non-hermitian topology and its bulk-edge correspondence. arXiv:1907.11619, 2019.
- [262] Joseph Schindler, Ang Li, Mei C. Zheng, F. M. Ellis, and Tsampikos Kottos. Experimental study of active lrc circuits with  $\mathcal{PT}$  symmetries. *Phys. Rev. A*, 84:040101, Oct 2011.
- [263]
- [264] T. Helbig, T. Hofmann, S. Imhof, M. Abdelghany, T. Kiessling, L. W. Molenkamp, C. H. Lee, A. Szameit, M. Greiter, and R. Thomale. Generalized bulk–boundary correspondence in non-hermitian topoelectrical circuits. *Nat. Phys.*, 16:747, Jun 2020.
- [265] Yuto Ashida, Zongping Gong, and Masahito Ueda. Non-hermitian physics. arXiv:2006.01837, 2020.
- [266] J. F. Poyatos, J. I. Cirac, and P. Zoller. Quantum reservoir engineering with laser cooled trapped ions. *Phys. Rev. Lett.*, 77:4728, 1996.

- [267] B. Kraus, H. P. Büchler, S. Diehl, A. Kantian, A. Micheli, and P. Zoller. Preparation of entangled states by quantum markov process. *Phys. Rev. A*, 78:042307, 2008.
- [268] S. Diehl, A. Micheli, A. Kantian, B. Kraus, H. P. Büchler, and P. Zoller. Quantum states and phases in driven open quantum systems with cold atoms. *Nat. Phys.*, 4:878, 2008.
- [269] Sebastian Diehl, Enrique Rico, Mikhail A. Baranov, and Peter Zoller. Topology by dissipation in atomic quantum wires. *Nat. Phys.*, 7:971, 2011.
- [270] G. Lindblad. On the generators of quantum dynamical semigroups. *Commun. Math. Phys.*, 48(2):119–130, Jun 1976.
- [271] Vittorio Gorini, Andrzej Kossakowski, and E. C. G. Sudarshan. Completely positive dynamical semigroups of n-level systems. *J. Math. Phys.*, 17(5):821–825, 1976.
- [272] Yuto Ashida and Masahito Ueda. Full-counting many-particle dynamics: Nonlocal and chiral propagation of correlations. *Phys. Rev. Lett.*, 120:185301, May 2018.
- [273] Lars V. Ahlfors. *Complex Analysis*. McGraw-Hill, New York, 1979.
- [274] Fritz Haake. *Quantum Signatures of Chaos*. Springer, Berlin, 2010.
- [275] N. G. Van Kampen. *Stochastic Processes in Physics and Chemistry*. Elsevier, New York, 2007.
- [276] Victor V. Albert, Barry Bradlyn, Martin Fraas, and Liang Jiang. Geometry and response of lindbladians. *Phys. Rev. X*, 6:041031, 2016.
- [277] Dakyeong Kim, Mochizuki Ken, Norio Kawakami, and Hideaki Obuse. Floquet topological phases driven by  $\mathcal{PT}$  symmetric nonunitary time evolution. arXiv:1609.09650, 2016.
- [278] M. A. Nielsen and I. L. Chuang. *Quantum Computation and Information*. Cambridge University Press, Cambridge, 2010.
- [279] Joshua Feinberg and A. Zee. Non-hermitian localization and delocalization. *Phys. Rev. E*, 59:6433, Jun 1999.
- [280] D. J. Thouless. Quantization of particle transport. *Phys. Rev. B*, 27:6083–6087, May 1983.
- [281] Ye Xiong. Why does bulk boundary correspondence fail in some non-hermitian topological models. *J. Phys. Commun.*, 2:035043, 2018.
- [282] L. Reichel and L. N. Trefethen. Eigenvalues and pseudo-eigenvalues of toeplitz matrices. *Linear Algebra Appl.*, 162-164:153, 1992.
- [283] Di Xiao, Ming-Che Chang, and Qian Niu. Berry phase effects on electronic properties. *Rev. Mod. Phys.*, 82:1959, 2010.
- [284] Maksym Serbyn, Z. Papić, and Dmitry A. Abanin. Universal slow growth of entanglement in interacting strongly disordered systems. *Phys. Rev. Lett.*, 110:260601, Jun 2013.
- [285] S. Longhi. Bloch oscillations in complex crystals with  $\mathcal{PT}$  symmetry. *Phys. Rev. Lett.*, 103:123601, Sep 2009.

- [286] Stefano Longhi. Bloch oscillations in non-hermitian lattices with trajectories in the complex plane. *Phys. Rev. A*, 92:042116, Oct 2015.
- [287] Martin Wimmer, Hannah M. Price, Iacopo Carusotto, and Ulf Peschel. Experimental measurement of the berry curvature from anomalous transport. *Nat. Phys.*, 13:545, 2017.
- [288] Stefano Longhi, Davide Gatti, and Giuseppe Della Valle. Robust light transport in non-hermitian photonic lattices. *Sci. Rep.*, 5:13376, 2015.
- [289] Stefano Longhi, Davide Gatti, and Giuseppe Della Valle. Non-hermitian transparency and one-way transport in low-dimensional lattices by an imaginary gauge field. *Phys. Rev. B*, 92:094204, Sep 2015.
- [290] E. M. Graefe, H. J. Korsch, and A. Rush. Quasiclassical analysis of bloch oscillations in non-hermitian tight-binding lattices. *New J. Phys.*, 18:075009, 2016.
- [291] Florentin Reiter and Anders S. Sørensen. Effective operator formalism for open quantum systems. *Phys. Rev. A*, 85:032111, Mar 2012.
- [292] Fabrice Gerbier and Jean Dalibard. Gauge fields for ultracold atoms in optical superlattices. *New J. Phys.*, 12:033007, 2010.
- [293] Z. W. Barber, C. W. Hoyt, C. W. Oates, L. Hollberg, A. V. Taichenachev, and V. I. Yudin. Direct excitation of the forbidden clock transition in neutral  $^{174}\text{Yb}$  atoms confined to an optical lattice. *Phys. Rev. Lett.*, 96:083002, Mar 2006.
- [294] Martin Miranda, Ryotaro Inoue, Yuki Okuyama, Akimasa Nakamoto, and Mikio Kozuma. Site-resolved imaging of ytterbium atoms in a two-dimensional optical lattice. *Phys. Rev. A*, 91:063414, Jun 2015.
- [295] Pranjal Bordia, Henrik P. Lüschen, Sean S. Hodgman, Michael Schreiber, Immanuel Bloch, and Ulrich Schneider. Coupling identical one-dimensional many-body localized systems. *Phys. Rev. Lett.*, 116:140401, Apr 2016.
- [296] Ken Shiozaki, Masatoshi Sato, and Kiyonori Gomi. Topological crystalline materials: General formulation, module structure, and wallpaper groups. *Phys. Rev. B*, 95:235425, Jun 2017.
- [297] Ken Shiozaki, Masatoshi Sato, and Kiyonori Gomi. Atiyah-hirzebruch spectral sequence in band topology: General formalism and topological invariants for 230 space groups. arXiv:1802.06694, 2018.
- [298] Raoul Bott. The stable homotopy of the classical groups. *Proc. Natl. Acad. Sci. U. S. A.*, 43(10):933 – 935, 1957.
- [299] Kohei Kawabata, Sho Higashikawa, Zongping Gong, Yuto Ashida, and Masahito Ueda. Topological unification of time-reversal and particle-hole symmetries in non-hermitian physics. *Nat. Commun.*, 10:297, 2019.
- [300] Eugene P. Wigner. Normal form of antiunitary operators. *J. Math. Phys.*, 1(5):409, 1960.
- [301] K. Kraus. General state changes in quantum theory. *Ann. Phys.*, 64:311, 1972.
- [302] Michael M. Wolf, Frank Verstraete, Matthew B. Hastings, and J. Ignacio Cirac. Area laws in quantum systems: Mutual information and correlations. *Phys. Rev. Lett.*, 100:070502, Feb 2008.

- [303] Heinz-Peter Breuer, Elsi-Mari Laine, Jyrki Piilo, and Bassano Vacchini. Colloquium: Non-markovian dynamics in open quantum systems. *Rev. Mod. Phys.*, 88:021002, 2016.
- [304] Charles H. Bennett, Gilles Brassard, Sandu Popescu, Benjamin Schumacher, John A. Smolin, and William K. Wootters. Purification of noisy entanglement and faithful teleportation via noisy channels. *Phys. Rev. Lett.*, 76:722, Jan 1996.
- [305] Katarzyna Macieszczak, Mădălin Guță, Igor Lesanovsky, and Juan P. Garrahan. Towards a theory of metastability in open quantum dynamics. *Phys. Rev. Lett.*, 116:240404, Jun 2016.
- [306] C. W. von Keyserlingk, Vedika Khemani, and S. L. Sondhi. Absolute stability and spatiotemporal long-range order in floquet systems. *Phys. Rev. B*, 94:085112, Aug 2016.
- [307] Masatoshi Sato, Yoshiro Takahashi, and Satoshi Fujimoto. Non-abelian topological order in  $s$ -wave superfluids of ultracold fermionic atoms. *Phys. Rev. Lett.*, 103:020401, Jul 2009.
- [308] Jay D. Sau, Roman M. Lutchyn, Sumanta Tewari, and S. Das Sarma. Generic new platform for topological quantum computation using semiconductor heterostructures. *Phys. Rev. Lett.*, 104:040502, Jan 2010.
- [309] Ken Shiozaki, Masatoshi Sato, and Kiyonori Gomi. Topology of nonsymmorphic crystalline insulators and superconductors. *Phys. Rev. B*, 93:195413, May 2016.
- [310] Hui Li and F. D. M. Haldane. Entanglement spectrum as a generalization of entanglement entropy: Identification of topological order in non-abelian fractional quantum hall effect states. *Phys. Rev. Lett.*, 101:010504, Jul 2008.
- [311] Alexei Kitaev and John Preskill. Topological entanglement entropy. *Phys. Rev. Lett.*, 96:110404, Mar 2006.
- [312] Michael Levin and Xiao-Gang Wen. Detecting topological order in a ground state wave function. *Phys. Rev. Lett.*, 96:110405, Mar 2006.
- [313] Steven T. Flammia, Alioscia Hamma, Taylor L. Hughes, and Xiao-Gang Wen. Topological entanglement rényi entropy and reduced density matrix structure. *Phys. Rev. Lett.*, 103:261601, Dec 2009.
- [314] Emil J Bergholtz, Jan Carl Budich, and Flore K Kunst. Exceptional topology of non-hermitian systems. arXiv:1912.10048, 2019.
- [315] Alexander Cerjan, Meng Xiao, Luqi Yuan, and Shanhui Fan. Effects of non-hermitian perturbations on weyl hamiltonians with arbitrary topological charges. *Phys. Rev. B*, 97:075128, Feb 2018.
- [316] Jan Carl Budich, Johan Carlström, Flore K. Kunst, and Emil J. Bergholtz. Symmetry-protected nodal phases in non-hermitian systems. *Phys. Rev. B*, 99:041406, Jan 2019.
- [317] Zhesen Yang and Jiangping Hu. Non-hermitian hopf-link exceptional line semimetals. *Phys. Rev. B*, 99:081102, Feb 2019.
- [318] Kohei Kawabata, Takumi Bessho, and Masatoshi Sato. Classification of exceptional points and non-hermitian topological semimetals. *Phys. Rev. Lett.*, 123:066405, Aug 2019.



- [319] Matthew S. Foster, Maxim Dzero, Victor Gurarie, and Emil A. Yuzbashyan. Quantum quench in a  $p+ip$  superfluid: Winding numbers and topological states far from equilibrium. *Phys. Rev. B*, 88:104511, Sep 2013.
- [320] M. D. Caio, N. R. Cooper, and M. J. Bhaseen. Quantum quenches in chern insulators. *Phys. Rev. Lett.*, 115:236403, Dec 2015.
- [321] Luca D’Alessio and Marcos Rigol. Dynamical preparation of floquet chern insulators. *Nat. Commun.*, 6:8336, 2015.
- [322] Szabolcs Vajna and Balázs Dóra. Topological classification of dynamical phase transitions. *Phys. Rev. B*, 91:155127, Apr 2015.
- [323] Jan Carl Budich and Markus Heyl. Dynamical topological order parameters far from equilibrium. *Phys. Rev. B*, 93:085416, 2016.
- [324] Zhoushen Huang and Alexander V. Balatsky. Dynamical quantum phase transitions: Role of topological nodes in wave function overlaps. *Phys. Rev. Lett.*, 117:086802, 2016.
- [325] Ying Hu, Peter Zoller, and Jan Carl Budich. Dynamical buildup of a quantized hall response from nontopological states. *Phys. Rev. Lett.*, 117:126803, Sep 2016.
- [326] Justin H. Wilson, Justin C. W. Song, and Gil Refael. Remnant geometric hall response in a quantum quench. *Phys. Rev. Lett.*, 117:235302, Nov 2016.
- [327] M. D. Caio, N. R. Cooper, and M. J. Bhaseen. Hall response and edge current dynamics in chern insulators out of equilibrium. *Phys. Rev. B*, 94:155104, Oct 2016.
- [328] Matthias Tarnowski, F. Nur Ünal, Nick Fläschner, Benno S. Rem, André Eckardt, Klaus Sengstock, and Christof Weitenberg. Measuring topology from dynamics by obtaining the chern number from a linking number. *Nat. Commun.*, 10:1728, 2019.
- [329] Liang Fu and C. L. Kane. Time reversal polarization and a  $z_2$  adiabatic spin pump. *Phys. Rev. B*, 74:195312, 2006.
- [330] Tim Langen, Remi Geiger, and Jörg Schmiedmayer. Ultracold atoms out of equilibrium. *Annu. Rev. Cond. Matt. Phys.*, 6:201, 2015.
- [331] A. J. Daley, H. Pichler, J. Schachenmayer, and P. Zoller. Measuring entanglement growth in quench dynamics of bosons in an optical lattice. *Phys. Rev. Lett.*, 109:020505, Jul 2012.
- [332] Rajibul Islam, Ruichao Ma, Philipp M. Preiss, M. Eric Tai, Alexander Lukin, Matthew Rispoli, and Markus Greiner. Measuring entanglement entropy in a quantum many-body system. *Nature*, 528:77, 2015.
- [333] S. Korenblit, D. Kafri, W. C. Campbell, R. Islam, E. E. Edwards, Z.-X. Gong, G.-D. Lin, L.-M. Duan, J. Kim, K. Kim, and C. Monroe. Quantum simulation of spin models on an arbitrary lattice with trapped ions. *New J. Phys.*, 14:095024, 2012.
- [334] J. Smith, A. Lee, P. Richerme, B. Neyenhuis, P. W. Hess, P. Hauke, M. Heyl, D. A. Huse, and C. Monroe. Many-body localization in a quantum simulator with programmable random disorder. *Nat. Phys.*, 12:907, 2016.
- [335] P. Jurcevic, H. Shen, P. Hauke, C. Maier, T. Brydges, C. Hempel, B. P. Lanyon, M. Heyl, R. Blatt, and C. F. Roos. Direct observation of dynamical quantum phase transitions in an interacting many-body system. *Phys. Rev. Lett.*, 119:080501, Aug 2017.

- [336] Philipp Hauke, Maciej Lewenstein, and André Eckardt. Tomography of band insulators from quench dynamics. *Phys. Rev. Lett.*, 113:045303, Jul 2014.
- [337] N. Fläschner, B. S. Rem, M. Tarnowski, D. Vogel, D.-S. Lühmann, K. Sengstock, and C. Weitenberg. Experimental reconstruction of the berry curvature in a floquet bloch band. *Science*, 352(6289):1091–1094, 2016.
- [338] N. Fläschner, D. Vogel, M. Tarnowski, B. S. Rem, D.-S. Lühmann, M. Heyl, J. C. Budich, L. Mathey, K. Sengstock, and C. Weitenberg. Observation of dynamical vortices after quenches in a system with topology. *Nat. Phys.*, 14:265, 2018.
- [339] Marcus Cramer, Martin B. Plenio, Steven T. Flammia, Rolando Somma, David Gross, Stephen D. Bartlett, Olivier Landon-Cardinal, David Poulin, and Yi-Kai Liu. Efficient quantum state tomography. *Nat. Commun.*, 1:149, 2010.
- [340] Shuangyuan Lu and Jinlong Yu. Stability of entanglement-spectrum crossing in quench dynamics of one-dimensional gapped free-fermion systems. *Phys. Rev. A*, 99:033621, Mar 2019.
- [341] M. Lohse, C. Schweizer, O. Zilberberg, M. Aidelsburger, and I. Bloch. A thouless quantum pump with ultracold bosonic atoms in an optical superlattice. *Nat. Phys.*, 12:350, 2016.
- [342] Shuta Nakajima, Takafumi Tomita, Shintaro Taie, Tomohiro Ichinose, Hideki Ozawa, Lei Wang, Matthias Troyer, and Yoshiro Takahashi. Topological thouless pumping of ultracold fermions. *Nat. Phys.*, 12:296, 2016.
- [343] J. E. Moore and L. Balents. Topological invariants of time-reversal-invariant band structures. *Phys. Rev. B*, 75:121306(R), Mar 2007.
- [344] Liang Fu and C. L. Kane. Topological insulators with inversion symmetry. *Phys. Rev. B*, 76:045302, Jul 2007.
- [345] W. P. Su, J. R. Schrieffer, and A. J. Heeger. Solitons in polyacetylene. *Phys. Rev. Lett.*, 42:1698–1701, Jun 1979.
- [346] Kunkun Wang, Xingze Qiu, Lei Xiao, Xiang Zhan, Zhihao Bian, Barry C. Sanders, Wei Yi, and Peng Xue. Observation of emergent momentum–time skyrmions in parity–time-symmetric non-unitary quench dynamics. *Nat. Commun.*, 10:2293, 2019.
- [347] Chao Yang, Linhu Li, and Shu Chen. Dynamical topological invariant after a quantum quench. *Phys. Rev. B*, 97:060304(R), Feb 2018.
- [348] Ingo Peschel. Calculation of reduced density matrices from correlation functions. *J. Phys. A*, 36:L205, 2003.
- [349] Taylor L. Hughes, Emil Prodan, and B. Andrei Bernevig. Inversion-symmetric topological insulators. *Phys. Rev. B*, 83:245132, Jun 2011.
- [350] Emil Prodan and Hermann Schulz-Baldes. *Bulk and Boundary Invariants for Complex Topological Insulators: From K-Theory to Physics*. Springer, Berlin, 2016.
- [351] M. Dalmonte, B. Vermersch, and P. Zoller. Quantum simulation and spectroscopy of entanglement hamiltonians. *Nat. Phys.*, 14:827, 2018.

- [352] H. Shirakawa, E. J. Louis, A. G. MacDiarmid, C. K. Chiang, and A. J. Heeger. Synthesis of electrically conducting organic polymers: halogen derivatives of polyacetylene, (ch)x. *J. Chem. Soc. Chem. Comm.*, page 578, 1977.
- [353] Ari M. Turner, Yi Zhang, and Ashvin Vishwanath. Entanglement and inversion symmetry in topological insulators. *Phys. Rev. B*, 82:241102(R), Dec 2010.
- [354] Peter Domokos and Helmut Ritsch. Collective cooling and self-organization of atoms in a cavity. *Phys. Rev. Lett.*, 89:253003, Dec 2002.
- [355] Jonas Larson, Bogdan Damski, Giovanna Morigi, and Maciej Lewenstein. Mott-insulator states of ultracold atoms in optical resonators. *Phys. Rev. Lett.*, 100:050401, Feb 2008.
- [356] Emanuele G. Dalla Torre, Sebastian Diehl, Mikhail D. Lukin, Subir Sachdev, and Philipp Strack. Keldysh approach for nonequilibrium phase transitions in quantum optics: Beyond the dicke model in optical cavities. *Phys. Rev. A*, 87:023831, Feb 2013.
- [357] Emanuele G. Dalla Torre, Yulia Shchadilova, Eli Y. Wilner, Mikhail D. Lukin, and Eugene Demler. Dicke phase transition without total spin conservation. *Phys. Rev. A*, 94:061802, Dec 2016.
- [358] Lukasz Fidkowski, Hoi Chun Po, Andrew C. Potter, and Ashvin Vishwanath. Interacting invariants for floquet phases of fermions in two dimensions. *Phys. Rev. B*, 99:085115, Feb 2019.
- [359] Jeongwan Haah, Lukasz Fidkowski, and Matthew B. Hastings. Nontrivial quantum cellular automata in higher dimensions. arXiv:1812.01625, 2018.
- [360] C. W. von Keyserlingk, Tibor Rakovszky, Frank Pollmann, and S. L. Sondhi. Operator hydrodynamics, otopcs, and entanglement growth in systems without conservation laws. *Phys. Rev. X*, 8:021013, Apr 2018.
- [361] Tibor Rakovszky, Frank Pollmann, and C. W. von Keyserlingk. Diffusive hydrodynamics of out-of-time-ordered correlators with charge conservation. *Phys. Rev. X*, 8:031058, Sep 2018.
- [362] Adam Nahum, Sagar Vijay, and Jeongwan Haah. Operator spreading in random unitary circuits. *Phys. Rev. X*, 8:021014, Apr 2018.
- [363] Vedika Khemani, Ashvin Vishwanath, and David A. Huse. Operator spreading and the emergence of dissipative hydrodynamics under unitary evolution with conservation laws. *Phys. Rev. X*, 8:031057, Sep 2018.
- [364] Christoph Sündershauf, David Pérez-García, David A. Huse, Norbert Schuch, and J. Ignacio Cirac. Localization with random time-periodic quantum circuits. *Phys. Rev. B*, 98:134204, Oct 2018.
- [365] Amos Chan, Andrea De Luca, and J. T. Chalker. Spectral statistics in spatially extended chaotic quantum many-body systems. *Phys. Rev. Lett.*, 121:060601, Aug 2018.
- [366] Amos Chan, Andrea De Luca, and J. T. Chalker. Solution of a minimal model for many-body quantum chaos. *Phys. Rev. X*, 8:041019, Nov 2018.
- [367] Tianci Zhou and David J. Luitz. Operator entanglement entropy of the time evolution operator in chaotic systems. *Phys. Rev. B*, 95:094206, Mar 2017.

- [368] Oded Zilberberg, Sheng Huang, Jonathan Guglielmon, Mohan Wang, Kevin P. Chen, Yaacov E. Kraus, and Mikael C. Rechtsman. Photonic topological boundary pumping as a probe of 4d quantum hall physics. *Nature*, 553:59, 2018.
- [369] Michael Lohse, Christian Schweizer, Hannah M. Price, Oded Zilberberg, and Immanuel Bloch. Exploring 4d quantum hall physics with a 2d topological charge pump. *Nature*, 553:55, 2018.
- [370] A. Celi, P. Massignan, J. Ruseckas, N. Goldman, I. B. Spielman, G. Juzeliūnas, and M. Lewenstein. Synthetic gauge fields in synthetic dimensions. *Phys. Rev. Lett.*, 112:043001, Jan 2014.
- [371] H. M. Price, O. Zilberberg, T. Ozawa, I. Carusotto, and N. Goldman. Four-dimensional quantum hall effect with ultracold atoms. *Phys. Rev. Lett.*, 115:195303, Nov 2015.
- [372] Krishanu Roychowdhury and Michael J. Lawler. Classification of magnetic frustration and metamaterials from topology. *Phys. Rev. B*, 98:094432, Sep 2018.
- [373] Zhi Li and Roger S. K. Mong. Homotopical classification of non-hermitian band structures. *arXiv:1911.02697*, 2019.
- [374] Charles C. Wojcik, Xiao-Qi Sun, Tomá š Bzdušek, and Shanhui Fan. Homotopy characterization of non-hermitian hamiltonians. *Phys. Rev. B*, 101:205417, May 2020.
- [375] Po-Yao Chang. Topology and entanglement in quench dynamics. *Phys. Rev. B*, 97:224304, Jun 2018.
- [376] Shuangyuan Lu and Jinlong Yu. Stability of entanglement-spectrum crossing in quench dynamics of one-dimensional gapped free-fermion systems. *Phys. Rev. A*, 99:033621, Mar 2019.
- [377] Kaixiang Su, Zheng-Hang Sun, and Heng Fan. Quench dynamics of entanglement spectra and topological superconducting phases in a long-range hamiltonian. *Phys. Rev. A*, 101:063613, Jun 2020.
- [378] Matthias Christandl. The structure of bipartite quantum states - insights from group theory and cryptography. *arXiv:0604183*, 2006.
- [379] E. Abrahams, P. W. Anderson, D. C. Licciardello, and T. V. Ramakrishnan. Scaling theory of localization: Absence of quantum diffusion in two dimensions. *Phys. Rev. Lett.*, 42:673, Mar 1979.
- [380] Yoichi Asada, Keith Slevin, and Tomi Ohtsuki. Anderson transition in two-dimensional systems with spin-orbit coupling. *Phys. Rev. Lett.*, 89:256601, Dec 2002.
- [381] H. Aoki and T. Ando. Effect of localization on the hall conductivity in the two-dimensional system in strong magnetic fields. *Solid State Commun.*, 38:1079, 1981.
- [382] Naomichi Hatano and David R. Nelson. Non-hermitian delocalization and eigenfunctions. *Phys. Rev. B*, 58:8384, Oct 1998.
- [383] P. W. Anderson. Absence of diffusion in certain random lattices. *Phys. Rev.*, 109:1492, Mar 1958.

- [384] C. D. Meyer. *Matrix Analysis and Applied Linear Algebra*. Society for Industrial and Applied Mathematics, Philadelphia, 2000.
- [385] Constantine Callias. Axial anomalies and index theorems on open spaces. *Commun. Math. Phys.*, 62:213, 1978.
- [386] M. J. Rice and E. J. Mele. Elementary excitations of a linearly conjugated diatomic polymer. *Phys. Rev. Lett.*, 49:1455–1459, Nov 1982.
- [387] Nick Bultinck, Dominic J. Williamson, Jutho Haegeman, and Frank Verstraete. Fermionic matrix product states and one-dimensional topological phases. *Phys. Rev. B*, 95:075108, Feb 2017.